Functional identification and investigation of genes initiating chromosomal instability using CRISPR activation and high-throughput automated image analysis.

Katie Dale

A thesis submitted for the degree of:
Doctor of Philosophy
University College London

Primary Supervisor: Dr Elina Vladimirou
Secondary Supervisor: Dr. Rob Hynds
September 2021

Declaration

I, Katie Dale, confirm that the work presented in this thesis is my own. Where information has been derived from other sources, I confirm that this has been indicated in the thesis.

Abstract

Chromosomal instability (CIN), the dynamic state where cells experience increased structural and/or numerical chromosome segregation errors, is prevalent in cancer, where it contributes to aneuploidy and tumour evolution. Despite its profound consequences on human health, initiation of CIN in the early stages of tumourigenesis is not well understood. In this work multiple strategies were employed to investigate the effects of gene upregulation, as well as upregulation of the PIK3CA signalling pathway, a frequently altered pathway in many cancer types (Jamal-Hanjani *et al*. 2017; Teixeira *et al*. 2019).

Combining CRISPR gene upregulation to model overexpression, high content imaging (HCS), and automated high-throughput image analysis, a pipeline was developed to screen for CIN and aneuploidy in a normal human cell line, RPE1. This provides a readout of micronuclei and centromere counts. Using this pipeline, upregulation of *KIF11* was found to increase the proportion of cells exhibiting micronuclei, and cause significant deviation from the modal centromere count, indicating CIN and aneuploidy. Further investigation of this phenotype revealed that *KIF11* upregulation causes spindle pole fragmentation, mitotic catastrophe, and chromosome congression defects. Centric and acentric lagging chromosomes were observed in cells that exhibited both normal and fragmented spindle poles. Mechanistically, *KIF11* was shown to generate a force imbalance in the early stages, which could be partially rescued upon upregulation of *HSET*.

MCF10A cell lines expressing *PIK3CA*^{H1047R} at the endogenous genetic loci as a result of CRISPR genome editing were used to investigate the impact of increased signalling through the PIK3CA pathway on CIN, aneuploidy, and centrosome biology. This showed that *PIK3CA*^{H1047R} increased the incidence of supernumerary centrosomes, and may play a role in structural CIN, but failed to identify any effect on numerical CIN. Finally, by chemically modulating PIK3CA activity, microtubule dynamics in response to PIK3CA pathway activation and inhibition were investigated.

Impact Statement

The work in this thesis has aimed to develop methods to screen for CIN using high throughput automated image analysis. Using a machine learning approach, an accurate method to detect micronuclei has been developed. This method could be applied to rapidly identify micronuclei and conditions that cause CIN in other types of screening such as siRNA or small molecule studies, in cell lines derived from cancer patients, or any other disease where a cell line exhibits micronuclei. It could also be adapted to other samples such as tissue sections by simply retraining the algorithm using a set of manually labelled images of the sample type in question, further extending its applications and impact on the field.

The work in this thesis will impact the mitosis field, providing a mechanistic understanding of the effects of KIF11 upregulation in cells, building on current literature and providing a more detailed insight into the phenotype. The field has mostly relied on siRNA knockdown or chemical inhibition to study the function of proteins within the mitotic spindle, however this study demonstrates the importance of protein overexpression. It shows that cells can be sensitive to protein upregulation, with only 2- to 3-fold upregulation of KIF11 causing severe defects in mitosis. This will inspire further investigation of other mitotic proteins and the effects of their upregulation, which may elucidate additional functions that aid in the understanding of the mechanical regulation of mitosis.

The work in this thesis will also impact the PIK3CA field, demonstrating that PIK3CA pathway activation as an early event in tumourigenesis is unlikely to contribute to CIN and aneuploidy, while suggesting a role in the development and/or maintenance of supernumerary centrosomes. While disproving the hypothesis that pathway activation causes CIN, this work provides progression towards understanding the impact of altered PIK3CA signalling in cancer. A better understanding of this may aid in patient stratification or treatment choice, ultimately providing an increase to life expectancy. In addition, once patenting and licensing is complete, the chemical activator 1938 will provide a useful tool to the field for research into PIK3CA signalling. This work contributes to the understanding of the function of this drug, potential toxicity in cells, and how it can be applied experimentally.

Acknowledgements

I would firstly like to thank my supervisor, Elina, I am immensely grateful for the opportunity to complete this project, and everything I have learned along the way. Thank you for your constant support, enthusiasm, and guidance.

Secondly, I would like to thank the many individuals at the UCL Cancer Institute that helped me with data analysis, laboratory techniques, and boosting morale during these testing times. In particular, I would like to thank Bart Vanhaesbroek for the opportunity to work on exciting projects involving PIK3CA. I would like to thank Benoit Bilanges, Sarah Conduit, and Evelyn Lau from the Vanhaesbroek lab, who have all provided support and guidance throughout this project. I would like to thank Jonathan Armond for all his computational efforts, which were integral to this project. I would like to thank Rob Hynds for his support and advice throughout, and for his critical reading of this thesis. I would like to thank the network of PhD students at the cancer institute, and in particular Maria Vila de Mucha for taking charge of the PhD committee and bringing us all together. I would also like to thank Jo Clancy for rescuing my cells on occasion, and for keeping me motivated when difficult working restrictions were put in place in response to the COVID-19 pandemic.

I would like to thank all staff running the CI core facilities, without whom I would not have been able to learn the techniques required to complete this project. I would like to thank Jiten Manji, Dumisile Lumkwana, and Christin Luft for the microscopy training and technical support they provided - I can only hope the spinning disk is on better behaviour since I have left! I would like to thank Alex McLatchie for the training in qPCR, and virus production. I would like to thank all the staff in the flow cytometry facility for performing cell sorting for me and providing support.

Finally, I would like to thank my family for being supportive and understanding, and my partner Owen, for his critical reading of this thesis and for keeping me sane while working from home. Thank you for all that late night washing up!

Abbreviations

APC/C - Anaphase Promoting Complex/Cyclosome

CATD - CENPA Targeting Domain

CCAN - Constitutive Centromere Associated Network

CIN - Chromosome Instability

CIS - Carcinoma *in Situ*

DDR - DNA Damage response

DSB - Double Strand Break

EMT - Epithelial to Mesenchymal Transition

FISH - Fluorescence in situ Hybridisation

HAC - Human Artificial Chromosome

HCS - High Content Screening

HPV - Human Papillomavirus

KT - Kinetochore

MAP - Microtubule Associated Protein

MCC - Mitotic Checkpoint Complex

MD - Modal Deviation

ML - Machine Learning

MN - Micronuclei

MT - Microtubule

MTOC Microtubule Organising Centre

NEB - Nuclear Envelope Breakdown

NLS - Nuclear Localisation Sequence

NSCLC - Non-Small Cell Lung Cancer

PCM - Pericentriolar Matrix

ROI - Region of Interest

SAC - Spindle Assembly Checkpoint

SAM - Synergistic Activation Mediators

SCC - Squamous Cell Carcinoma

scWGS – Single Cell Whole Genome Sequencing

SCNA - Somatic Copy Number Amplification

Table of Contents

List of Figures

List of Tables

Chapter 2: Materials & Methods

Chapter 3: High Throughput Automated Image Analysis Pipeline to Screen for CIN & Aneuploidy

Chapter 1: Introduction

1.1 The Cell Cycle & Mitosis

1.1.1 An Overview of the Cell Cycle

Cells pass through the cell cycle to ensure mitosis occurs in a timely fashion, only after they have grown to a sufficient size and faithfully replicated their genome (Cooper 2000). The first phase is known as Gap 1 (G1) and is important for production of key proteins and cellular machinery required for DNA replication, such as histones (Figure 1.1a). In this phase cells are responsive to external stimuli, such as nutrient availability and space to grow, and decide whether to continue through the cell cycle or enter a quiescent resting state known as Gap 0 (G0). The restriction point is the stage at which cells either enter G0 or commit to progression into S phase, also known as the G1/S checkpoint (Pardee 1974). In the second phase, Synthesis (S), the DNA and centrosomes are replicated in an ordered and timely manner, with the intra-S checkpoint preserving genomic integrity by promoting the repair of any DNA damage. Once DNA replication is complete cells progress into Gap 2 (G2), a further stage of growth and protein synthesis, which has been proposed to have a role in regulating cell size. Finally, after the G2/M checkpoint ensures DNA replication and DNA damage repair is complete (Taylor and Stark 2001), the cell will progress into mitosis.

In mitosis the cell must condense each chromosome, assemble the mitotic spindle, segregate each set of chromosomes into a daughter cell, and reform the nuclear and cellular membranes to form two separate daughter cells. These processes function to preserve genomic integrity during mitosis, preventing chromosome segregation errors. In addition, the spindle assembly checkpoint (SAC) plays an essential role in mitosis, regulating the onset of chromosome segregation. The SAC is formed by a number of proteins that interact to ensure the cell undergoes chromosome segregation only when it is ready.

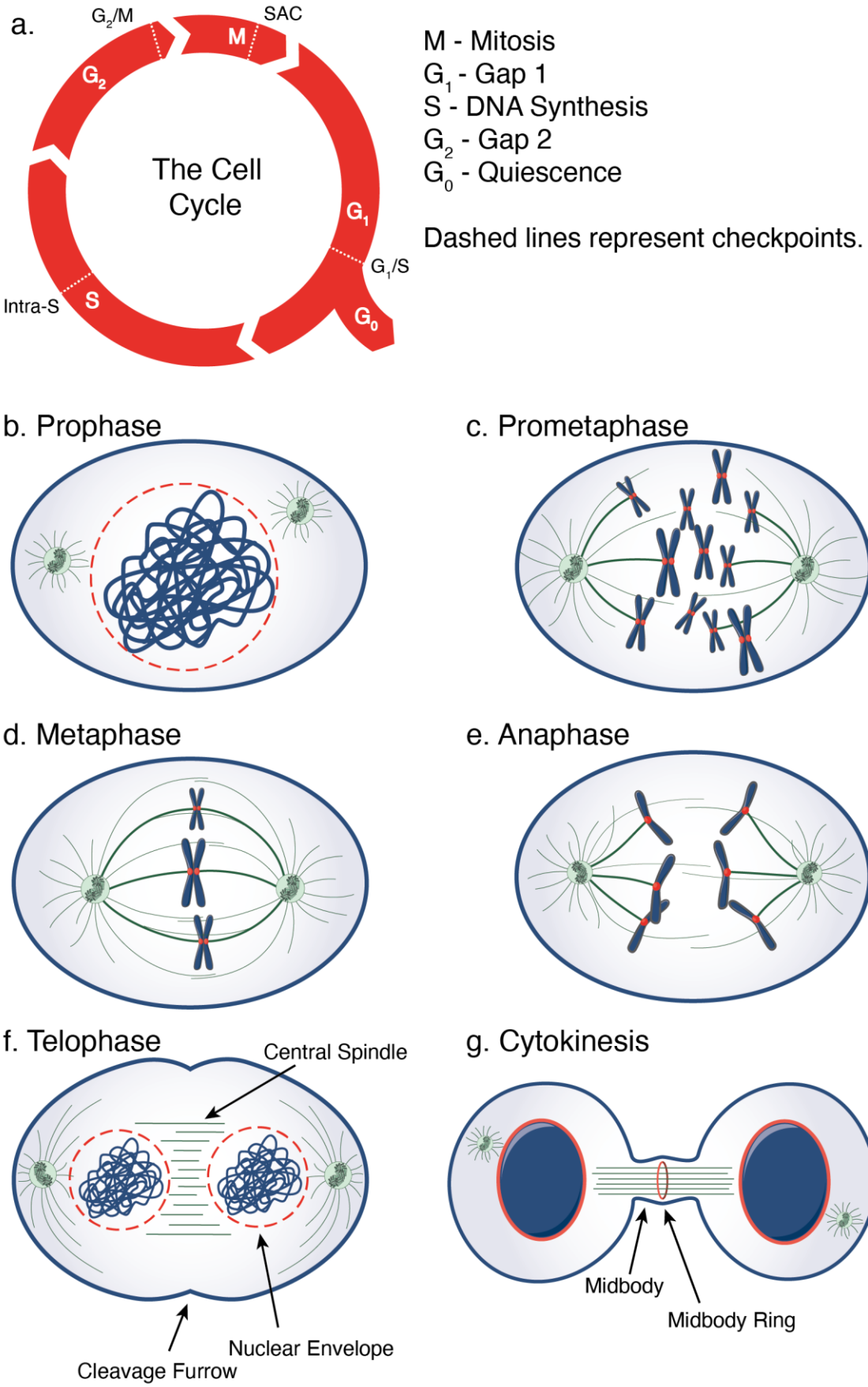

Figure 1.1 Stages of the Cell Cylce & Mitosis **a.** Digram of the cell cycle. Graphics showing nuclear morphology and spindle organisation during **b.** prophase (before NEB) **c.** prometaphase, **d.** metaphase, **e.** anaphase, **f.** telophase, and **g.** cytokinesis.

The cell cycle is driven by cyclin dependant kinases (CDKs), and their protein ligands cyclins (Malumbres 2014). Differential temporal expression and degradation of the different types of cyclins and CDKs drives the cell through the different stages of the cell cycle, for example, degradation of cyclin B by the anaphase promoting complex/cyclosome APC/C is essential for anaphase onset (Clute and Pines 1999). The various cell cycle checkpoints often function by modulating CDK activity, for example, DNA damage in G1 activates a signalling cascade resulting in the inhibition of cyclin D/CDK4/6 by p21, which arrests the cell in G1 allowing for time to repair the DNA damage. The transcription factor p53 also plays a particularly important role in the G1/S checkpoint, becoming activated by the various proteins involved in sensing DNA damage, and inducing a cell cycle arrest (Senturk and Manfredi 2013).

1.1.2 The Stages of Mitosis

Mitosis takes approximately 30 minutes and is the shortest phase of the cell cycle. The first stage of mitosis is prophase: the nuclear envelope remains intact while chromosomes are condensed (Antonin and Neumann 2016), and microtubule (MT) nucleation at centrosomes increases five times in comparison to interphase (Figure 1.1b). Centrosome separation can begin at this stage, with molecular motor proteins including dynein utilising the nuclear envelope to exert the forces required (Tanenbaum and Medema 2010). Breakdown of the nuclear envelope (NEB) signals the transition to prometaphase.

1.1.3 Prometaphase

Centrosome separation usually begins in prophase and is completed in prometaphase, after NEB. Cells begin assembling the spindle, and congress chromosomes toward the metaphase plate (Baudoin and Cimini 2018; Figure 1.1c). This requires an attachment to form between spindle microtubules and the kinetochore (KT), the multiprotein complex that assembles on chromosomes, known as a kinetochore microtubule attachment (kMT). Chromosomes exhibit dynamic oscillations during prometaphase, some moving towards and some away from the spindle poles. This process is essential for congression of chromosomes to the metaphase plate; it is mediated by MT growth and shrinkage

and the action of molecular motor proteins. Perturbation of motor activity can cause a congression delay which is dangerous to cells, as it greatly increases the rate of chromosome segregation errors. For example, inhibition of centromere protein E (CENPE) prevents the congression of polar chromosomes (chromosomes stuck at or behind the spindle poles), from the centrosome to the metaphase plate. RPE1 cells, used extensively in the mitosis field and throughout this thesis, spend around 18 minutes in prometaphase (Uetake and Sluder 2010).

1.1.4 Metaphase

Metaphase begins when all chromosomes are aligned at the spindle equator, and all chromosomes are bioriented, with sister KTs forming end-on attachments with MTs from opposite spindle poles (Figure 1.1d). Metaphase is highly important in ensuring cells faithfully and accurately segregate chromosomes during anaphase, as the spindle assembly checkpoint (SAC) functions at this stage. In RPE1 cells, metaphase usually lasts around 5 to 10 minutes, and delays observed are likely due to SAC activity at erroneously attached kinetochores. Cells can spend hours arrested at metaphase, however as the duration increases the likelihood of mitotic slippage increases, where the cell re-enters interphase without dividing as a tetraploid.

1.1.5 Anaphase

Anaphase occurs once the SAC is satisfied, and the cohesin rings linking sister chromatids are released (Figure 1.1e). Anaphase occurs in two stages, firstly anaphase A, where chromosomes move towards the spindle poles, catalysed by the depolymerisation and shortening of MTs. In the second stage, anaphase B, the centrosomes move apart and the spindle elongates, further separating the chromosomes (Vukušić *et al*. 2019). At this stage molecular motors on the interpolar MTs (the MTs that form the central spindle, Figure 1.2a), generate pushing forces that slide the MTs apart. Astral MTs also begin to depolymerise, pulling the centrosomes closer to the cell cortex. Historically, these mechanisms have been known as ‘the midzone pushing’ and ‘the cortical pulling’ models, respectively.

RPE1 cells usually spend 5 to 10 minutes completing anaphase, the duration of which is controlled spatially by an Aurora B phosphorylation gradient emanating from the central spindle (Afonso *et al*. 2014), and temporally by the reduction in CDK1 activity observed at the metaphase to anaphase transition. This regulation allows time for lagging chromosomes to be segregated and incorporated into the main nucleus, rather than forming a separate micronucleus (MN; Orr *et al*. 2021).

Cells begin mitotic exit upon anaphase onset, the process of spindle disassembly and the re-establishment of interphase cell structures. The phosphatases PP1 and PP2A play important roles in dephosphorylating a plethora of proteins during mitosis to enable these cellular changes. For example, during mitosis CDK1 phosphorylation of lamin filaments promote breakdown of the nuclear membrane. While a direct function has not yet been demonstrated, PP1 and PP2A family phosphatases have been shown to be required for reassembly of the nuclear lamina (Wurzenberger and Gerlich 2011).

1.1.6 Telophase & Cytokinesis

Telophase is the final stage of mitosis, where the chromosomes begin to decondense, the nuclear envelope begins to reform, and the spindle begins to disassemble (Figure 1.1f). This is driven by the deactivation of the CDKs that drive the cell through early mitosis, through the action of multiple signalling pathways. The cleavage furrow forms during telophase at the cell equator, specified by the astral and central spindle MTs, and begins to progress inwards where eventually the two daughter cells will separate by abscission (Lens and Medema 2019).

Cytokinesis occurs after telophase, the process of a cell dividing its cytoplasm and separating the cell membrane to form to equal daughter cells (Figure 1.1g). It is driven by a contractile actin-myosin ring regulated by RhoA signalling, which activates myosin II motor activity, allowing it to use ATP hydrolysis to walk along the actin filaments. The cleavage furrow ingresses until reaching the condensed midbody structure, which is thought to act as a signalling platform that recruits the cellular machinery required to perform abscission. Cells remain connected through this cytokinetic bridge for 1-2 hours after mitosis, until the midbody is

physically cut and the daughter cells physically separate (Lens and Medema 2019).

1.2 An Overview of the Mitotic Machinery

During mitosis cells must faithfully segregate the two sets of chromosomes to each daughter cell, ensuring both receive a complete, diploid set of the genome, carrying a maternal and paternal version of each chromosome. When this goes wrong, cells can lose or gain whole chromosomes, fragments of chromosomes, or undergo mutatgenic events such as chromothrypsis, where a chromosome is shattered and incorporated into other chromosomes. These are examples of CIN, a cellular state where there is an increased rate of chromosome segregation errors. Many types of cancer exhibit CIN, which can accelerate tumour evolution and lead to the development of drug resistance. Normal, healthy cells coordinate a variety of cellular machinery to execute mitosis in a timely fashion without errors, including centrosomes, MTs, kinetochores (KTs), and molecular motor proteins.

1.2.1 The Mitotic Spindle

The mitotic spindle is a MT-based, bipolar structure that carries out chromosome segregation in mitosis (Figure 1.2a). During prophase the two poles of the spindle are formed by the centrosomes, a cellular organelle that functions as a MT organizing centre (MTOC). Centrosomes consist of two centrioles connected by tether proteins, surrounded by a pericentriolar matrix (PCM), which contains two to three hundred proteins including pericentrin (PCNT; Figure 1.2b). The core of the centriole displays a cylindrical structure with nine-fold symmetry, which is

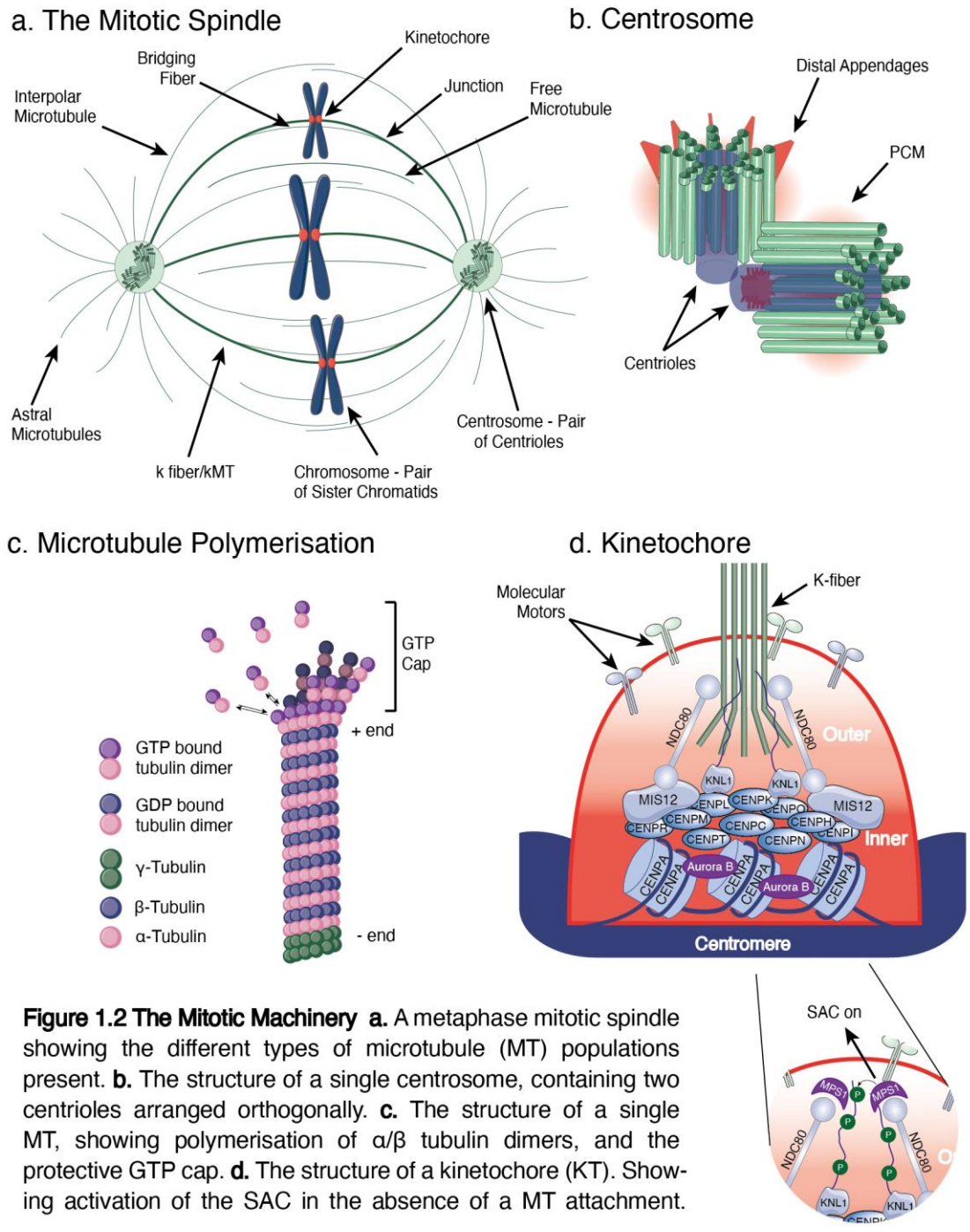

Figure 1.2 The Mitotic Machinery **a.** A metaphase mitotic spindle showing the different types of microtubule (MT) populations present. **b.** The structure of a single centrosome, containing two centrioles arranged orthogonally. **c.** The structure of a single MT, showing polymerisation of α/β tubulin dimers, and the protective GTP cap. **d.** The structure of a kinetochore (KT). Showing activation of the SAC in the absence of a MT attachment.

established by the cartwheel complex, and maintained by the proteins centrin 1 and centrin 2. The PCM contains concentrated amounts of proteins that nucleate and stabilize MTs, allowing centrosomes to act as the predominant MTOC within mammalian cells. In particular, high levels of γ-tubulin ring complexes (γTuRCs) are present, which nucleate MT polymerization (Moritz *et al*. 1995); the minus end is embedded within the PCM, and the MT grows out from the MTOC with the plus end towards the centre of the spindle. In addition to centrosomes, nucleation

of MTs can also be initiated by chromatin, existing MTs, and fragments of PCM that form MTOCs (Petry 2016).

There are different types of MTs that fulfil different roles within the mitotic spindle, including astral, KT, interpolar, free, and bridging MTs (Figure 1.2a). Astral MTs are important for mediating physical interactions between centrosomes and the cell cortex and controlling spindle positioning. Kinetochore-MTs (kMTs) are found in bundles of up to 30 individual MTs in human cells that connect the spindle pole to chromosomes at the KT. These bundles of MTs are termed k fibers.

Interpolar MTs are those that do not directly interact with KTs. These can have their minus ends embedded at the centrosome, with their plus ends reaching out into the central region of the spindle, where they will often form an antiparallel configuration with MTs emanating from the opposite spindle pole. However, it was observed that free spindle MTs often have their minus ends located on k fibers (Mastronarde *et al*. 1993). Further studies identified that in human cells, each k fiber is supported by a bridging fibre, comprising of antiparallel MTs emanating from each k fiber connected to the sister KT pair (Figure 1.2a). The bridging fiber helps to balance the forces exerted on the KT pair, increasing the tension the kMT is under in the region between the KT and the junction with the bridging fiber (Kajtez *et al*. 2016). Finally, free microtubules are not nucleated by the centrosome, and form a cross-linking meshwork which other MTs can interact with.

1.2.2 MT Instability

MTs undergo dynamic instability, continually growing and shrinking, resulting in many unstable MTs probing the cellular space at any one time. This forms the basis of the search-and-capture mechanism in prometaphase, where MTs search the cellular space for KTs, eventually forming kMT attachments (Cheeseman and Desai 2008), initiating the formation of a k fiber (McEwen *et al*. 1997). Different MT populations have different dynamicity, with the kinetochore MTs being the most stable, as they are anchored at their plus end by proteins assembled at the KT (Howard and Hyman 2003). MT instability is essential for mitosis as it facilitates the cytoskeletal transition from interphase to mitosis, allows for the

search-and-capture of chromosomes, and allows for correction of erroneous kMT attachments.

The dynamic nature of MTs is an inherent feature of their molecular structure (Figure 1.2c). MTs consist of α- and β-tubulin dimers, arranged into 13 protofilaments that form a negatively charged cylindrical polymer. When in a polymerizing state GTP-bound α/β tubulin dimers bind to the plus end, generating a stabilising GTP cap, while the minus end is protected by a γTuRC cap. If the GTP is hydrolysed to GDP the stability of the MT reduces, leaving it susceptible to catastrophe, where there is rapid disassembly of the subunits. Conversely, if GTP bound tubulin dimers are added to the depolymerising tip, this can stabilise and rescue the MT. Cells exist in an equilibrium of MT growth and shrinkage based on this cycle of GTP hydrolysis, which provides the MT instability required for a successful mitosis (Howard and Hyman 2003).

In mitotic spindles kMTs exhibit poleward flux, a constant turnover of tubulin towards the spindle poles. This is achieved by depolymerisation at the minus end combined with polymerisation at the plus end. WD repeat containing protein 62 (WDR62) has been demonstrated to be important for recruiting the katanin complex to spindle poles, which severs MT minus ends, promoting poleward flux (Guerreiro *et al*. 2021). The role of poleward flux may differ between organisms, but in mammalian cells it is thought to play a role in chromosome congression, and correcting kMT attachment errors, with a minor contribution to poleward chromosome movement during anaphase (Ganem and Compton 2006).

1.2.3 Centromeres & Kinetochores

Centromeres are the part of the chromosome where the KT assembles and are involved in sister chromatid cohesion. Centromeric DNA is composed of repetitive α-satellite DNA sequences (alphoid DNA), that associate with the histone H3 variant CENPA (Lamb and Birchler 2003). In mammals, the length of α-satellite repeats varies between chromosome, but do not necessarily correlate with chromosome size. Human centromeres typically contain hundreds of CENPA nucleosomes, organised within 20-100 Mb of alphoid DNA. These regions of chromatin are arranged into specialized structures, with distinct epigenetic

modifications, which enable KT assembly (McKinley and Cheeseman 2016). Within the centromere CENPA has been shown to recruit additional centromeric proteins and provide key interactions with inner KT components. The CENPA targeting domain (CATD) is responsible for associating with CENPC, required for KT assembly, and the chaperone protein HJURP which facilitates CENPA loading (McKinley and Cheeseman 2016). Together, CENPA and CENPC recruit the 15 subunits of the constitutively centromere-associated network (CCAN), including CENP-H/I/K/L/M/N/O/P/Q/R/S/ T/U/W/X (McAinsh and Meraldi 2011) (Figure 1.2d).

The CCAN proteins form the inner KT, forming a bridge between the centromere and the outer KT (Figure 1.2d), and providing structural integrity to accommodate intrakinetochore stretching (Suzuki *et al*. 2014). The KMN network, a set of three multiprotein complexes including KNL1, MIS12 and NDC80 forms the outer KT. This functions as a landing site for spindle assembly checkpoint (SAC) proteins, and specifically via NDC80, mediates the interaction with the plus end of MTs forming a kMT (Cheeseman and Desai 2008; Verdaasdonk and Bloom 2011). The KT is decorated with a variety of molecular motors and MAPs that regulate the stability of kMT attachments and contribute to the enhanced stability and reduced turnover rate of kMTs.

1.2.4 Kinetochore-MT Attachments

kMT attachments must be stable enough to allow progression through mitosis, yet dynamic enough to ensure erroneous attachments can be corrected. There are a number of different attachment configurations that can be achieved during prometaphase and metaphase (Gregan *et al*. 2011; Gay *et al*. 2012), the correct of which is known as amphitelic (Figure 1.3a), where each kinetochore within a pair of sister chromatids is bound by a k fiber originating from opposite ends of the spindle pole. In a syntelic attachment (Figure 1.3b), both KTs are attached to k fibers originating from the same spindle pole, whereas in a monotelic a

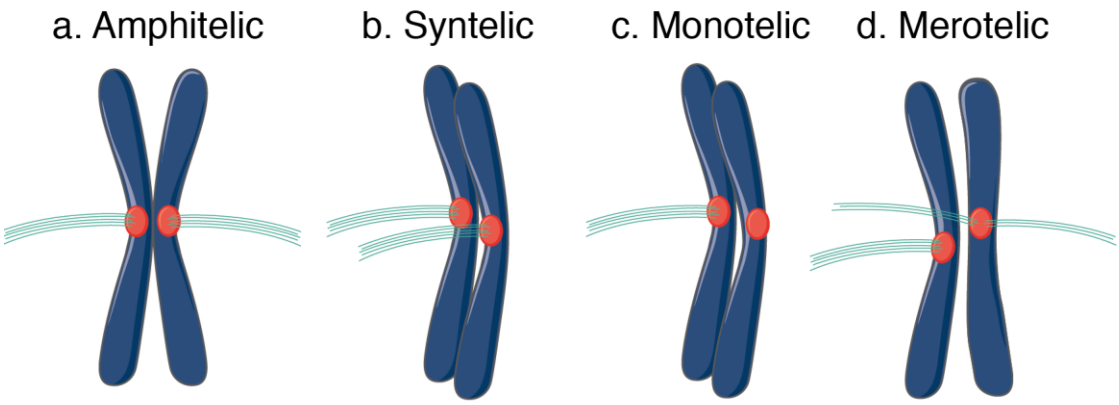

Figure 1.3 The Different Types of Kinetochore-Microtubule Attachments a. Amphiltelic, the correct configuration where each kinetochore (KT) is attached to a single K-fiber emanating from opposite spindle poles, resulting in tension across the sister-KT pair. **.** Syntelic, where both KTs are attached to K-fibers from the same spindle pole. **c.** Monotelic, where only one KT is attached to a K-fiber. **d.** Merotelic, where a single KT is attached to K-fibers emanating from both spindle poles.

ttachment only one KT is attached to a k fiber, (Figure 1.3c). Finally, in a merotelic attachment a single KT is attached to MTs emanating from both spindle poles, (Figure 1.3d).

The spindle assembly checkpoint (SAC) ensures all chromosomes are amphitelically attached, such that faithful chromosome segregation can occur. The SAC operates by sensing unattached kinetochores within a sister chromatid pair, detecting monotelic attachments and preventing progression to anaphase (Lara-Gonzalez *et al*. 2021). Syntelic attachments are also detected by the SAC, and corrected through an alternative mechanism involving Aurora B. One hypothesis within the field is that the lack of tension across the sister KT reduces MT occupancy generating an intermediate monotelic attachment that activates the SAC, however the exact mechanism is not understood (Manic *et al*. 2017). Merotelic attachments can be corrected through the same mechanism involving Aurora B, but do not activate the SAC, as both kinetochores exhibit correct MT attachments that maintain a normal MT occupancy. When merotelic attachments persist to anaphase, MT occupancy within k fibers has been shown to ensure segregation of lagging chromosomes to the correct pole (Dudka *et al*. 2018). In fact, one individual MT can generate sufficient force to move a human chromosome, however it is well established across multiple organisms that k fibers contain multiple MTs. A higher MT occupancy within the correctly attached

k fiber generates a force differential, favouring segregation of the chromosome to the correct pole (Dudka *et al*. 2018).

1.2.5 Molecular Motors and MT-Associated Proteins

The forces required to assemble a bipolar spindle with chromosomes aligned at the metaphase plate are generated by KTs, MTs, and motor proteins that act upon them, known as kinesins and dyneins (Prosser and Pelletier 2017). Generally, kinesins move towards the MT plus end while dyneins move towards the minus end. The mechanism of action of molecular motors involves ATPase driven conformational changes, often combined with a high processivity, allowing them to undergo consecutive conformational changes while remaining bound to a MT. This generates the processive stepping motion of the motor head domains along an MT.

Motor proteins are involved in all stages of mitosis. In prophase/prometaphase, centrosome separation is performed by KIF11-mediated outward pushing forces on antiparallel MTs located between the centrosomes, and nuclear envelope localized dynein pulling on astral MTs (Raaijmakers *et al*. 2012). KIF15 in complex with TPX2 also generates outward sliding force, and when ectopically overexpressed, it can rescue centrosome separation upon KIF11 is inhibition (Tanenbaum *et al*. 2009). In prometaphase chromosomes must congress to the metaphase plate. A major driver of this is KIF18A, which when depleted causes a complete failure of chromosome alignment in cells. KIF18A localizes to the plus ends of MTs and KTs, where it dampens MT dynamics, negatively regulating MT length (Du *et al*. 2010). KIF18A shows minus end directed motor activity, but also functions as a MT depolymerase. In addition to other depolymerases, such as MCAK, KIF18A utilises diffusion to move along the MT lattice. CENPE at KTs is particularly important for congression of polar chromosomes localized behind the spindle poles (Barisic *et al*. 2014). Finally, polar ejection forces are also important for congression, referring to the pushing of chromosomes away from the spindle poles and towards the metaphase plate (Rieder and Salmon 1994). The chromokinesins KID; Funabiki and Murray 2000) and KIF4A (Mazumdar *et al*. 2004) contribute to polar ejection force, binding on the chromosome arms they

interact with non-kMTs and move towards the plus ends located in the central spindle.

In metaphase, motor proteins are required to maintain the spindle structure and MT poleward flux, correct erroneously attached KTs, and promote KT oscillations. Outward forces from KIF11 and KIF15 are balanced by inward forces from dynein and HSET to maintain spindle length, while cortex localized dynein pulling on astral MTs maintains spindle pole position.

During anaphase A, motor activity at the KTs promotes MT depolymerisation and shortening to move the chromosomes towards the spindle poles, while the kMT attachments remain intact. This is known as plus-tip coupling and has been referred to historically as KT pac-man activity, as many hypothesized that proteins at the KT 'ate away' at the plus-tip, promoting depolymerization. While no single protein has been identified as responsible for anaphase A, many have been implicated. KIF18A was found to slow anaphase B when depleted and accelerate poleward movement of chromosomes when overexpressed (Stumpff *et al*. 2008). Other relevant players include CENPE (Lombillo *et al*. 1995) and CENPF (Auckland *et al*. 2020), which are able to bind to actively depolymerising MT plus-tips; CLASP2, where knockout MEFs showed reduced poleward chromosome velocities (Pereira *et al*. 2006); and dynein-dynactin, where knockdown reduced poleward chromosome velocities (Yang *et al*. 2007). During anaphase B a combination of KIF11 and KIF4A localised to antiparallel MTs via PRC1 drive the sliding filament mechanism that elongates the spindle pole (Vukušić *et al*. 2021).

MT-associated proteins (MAPs) are essential proteins that lack motor activity, but play important roles in localising motor proteins, regulating MT dynamics, and stabilising kMT attachments (Maiato *et al*. 2004). Dynactin is a MAP that binds dynein and MTs and is essential for the majority of dynein activity. TPX2 is required for binding of KIF15 to MTs, and its antiparallel sliding motion. PRC1 promotes MT bundling in the spindle midzone by crosslinking antiparallel MTs within bridging fibres (Polak *et al*. 2017), and associates with KIF4A during anaphase B. Cytoplasmic linker-associated proteins (CLASPs) regulate MTs, showing dynamic localization to centrosomes, kinetochores, the spindle midbody,

and MT plus ends throughout mitosis. EB1 is a widely conserved MAP that localizes to growing MT plus ends, where it regulates MT dynamics, promoting MT growth and reducing the frequency of catastrophe (Tirnauer *et al*. 2002).

1.2.6 Kinetochore Oscillations

MT dynamics at the kinetochore cause chromosomes to oscillate during prometaphase and metaphase, undergoing poleward and anti-poleward movements (Skibbens *et al*. 1993). Just before anaphase onset oscillations are dampened and reduced, to ensure the metaphase plate is tightly ordered (Häfner *et al*. 2014). Periods of poleward movement are associated with MT depolymerisation, while anti-poleward movement is associated with polymerisation at the plus end embedded within the KT (Mitchison and Salmon 1992). Many studies have aimed to investigate why KTs oscillate, and identify key proteins involved in regulating the process, however the exact function of oscillations is not well understood. KIF18A has been identified as a key regulator of KT oscillations; depletion significantly increased oscillation speed, resulting in congression defects, disordered metaphase plates and SAC-dependent mitotic arrest (Stumpff *et al*. 2008; Jaqaman *et al*. 2010).

Depletion of CENPH, which is required for the loading of CENP-H/I/K/L/M/N/O/P/Q/R/S/X to kinetochores, completely abrogates regular KT oscillations. The amplitude of KT oscillations is significantly reduced, resembling that of fixed cells, however this causes congression defects similar to those observed in KIF18A depleted cells. CENPH depletion led to a reduction in CLASP1, CLASP2, and EB1 at the KT, due to changes in MT dynamics. MTs were stabilised and showed reduced poleward flux, however increased turnover of tubulin at MT plus ends was observed. This results in rapid switching between a polymerising and depolymerising state, explaining why KTs do not oscillate upon depletion (Amaro *et al*. 2010).

It has been demonstrated that the movements of neighbouring sister-KT pairs are correlated, which depends on transmission of the poleward and anti-poleward forces through crosslinked MTs. Interestingly, perturbation of the two motors responsible for outward pushing forces within the spindle via MT crosslinking

produces different effects on the correlation of non-sister KT movement; inhibition of KIF11 increased the correlation, while depletion of KIF15 reduced it. One hypothesis for these phenotypes is that KIF11 limits the overall forces generated upon the spindle by causing drag. Inhibition of KIF11 with both monastrol and FCTP (that induces a rigor state where KIF11 remains tightly bound) caused the same phenotype, therefore it is likely that correlation is increased due to enhanced MT crosslinking (Vladimirou *et al*. 2013).

1.2.7 The Spindle Assembly Checkpoint

The spindle assembly checkpoint (SAC) functions to ensure anaphase onset occurs only once all chromosomes are bi-oriented on the metaphase plate, with amphitelic kMT attachments. It is active during prometaphase when chromosomes are congressing and unattached KTs are present, and during metaphase when there are erroneous kMT attachments (Rieder et al. 1994; Rieder et al. 1995). Anaphase onset is achieved by the anaphase promoting complex (APC/C), a ubiquitin ligase that initiates degradation of securin and cyclin B (King *et al*. 1995, Yamano 2019). APC/C is first phosphorylated by cyclin B/CDK1 at the Apc3 and Apc1 loops, which promotes recruitment of the activator CDC20 (Fujimitsu *et al*. 2016). Degradation of securin releases and activates separase, the protease required for removing cohesin rings from sister chromatids and allowing for chromosome segregation. Degradation of cyclin B inactivates CDK1, preventing inhibitory phosphorylation events and enabling PP1 and PP2A to promote mitotic exit.

When the SAC is active, erroneously attached kinetochores activate the mitotic checkpoint complex (MCC), which prevents CDC20 from activating the APC/C. The MCC consists of ‘closed’-MAD2, MAD1, BUBR1 and BUB3, genes identified in yeast that upon mutation, did not prevent progression through mitosis in the presence of microtubule poisons (Hoyt *et al* 1991; Li and Murray 1991). Firstly, the kinetochore promotes a conformational change in MAD2 to form closed-MAD2, which accumulates at the KT and binds CDC20. This complex then associates with BUBR1 and BUB3, which sequesters CDC20 from binding to and activating the APC/C (Musacchio 2015). MPS1 localises to unattached KTs where it plays an essential role in the recruitment of SAC proteins, and

phosphorylates multiple targets including KNL1, BUB1 and MAD1, promoting MT turnover (Winey et al. 1991). MPS1 senses the attachment status of KTs through competitive binding to NDC80 with MTs (Hiruma *et al* 2015; Ji *et al* 2015; Figure 1.2d).

Alongside the MCC, Aurora B kinase plays an important role in promoting the correction of erroneous kMT attachments through a tension sensing mechanism, which can correct syntelic and monotelic kMT attachments (Cimini *et al*. 2006; Krenn and Musacchio 2015). Aurora B kinase is concentrated near the inner centromere, however when there is a lack of tension between the two sister chromatids it can reach phosphorylation substrates in the outer kinetochore. The result of these phosphorylation events is destabilisation of the kMT attachment, promoting MT turnover. For example, Aurora B mediated phosphorylation of KNL1 and NDC80 reduces their affinity for MTs, likely because of the negatively charged phosphate groups interfering with the binding to negatively charged MTs. Aurora B also targets centromeric and kinetochore localised molecular motors, which play a role in destabilising kMT attachments. For example, it controls the kinetochore localisation of the centromeric MT depolymerase MCAK, and regulates the MT binding affinity of KIF10, a kinesin involved in MT plus end elongation (Lan *et al*. 2004).

A similar mechanism has been proposed for Aurora B mediated correction of merotelic attachments during metaphase, which relies on the abnormal and distorted kinetochore orientation caused by a merotelic attachment. Within a merotelic attachment the MTs emanating from the incorrect spindle pole come into close proximity with the inner centromere, due to the orientation of the sister chromatids. This means that centromere localised SAC proteins including Aurora B and MCAK, which have indeed been found enriched at merotelic attachments, can easily access these MTs and promote detachment (Cimini 2007).

1.3 Centrosome Biology

Centrosomes, the MTOC conserved across animal species, are important for the building of a bipolar spindle during mitosis. Their duplication and separation are tightly regulated to ensure these processes do not go wrong. Emergence of

supernumerary centrosomes (more than two during G2/M phases of the cell cycle), can be extremely toxic to cells, causing multipolar spindle formation. Cells have evolved mechanisms to cluster extra centrosomes, which are often exploited by cancer cells, where supernumerary centrosomes are frequently observed.

1.3.1 Centrosome Duplication

During the late stages of mitosis and early G1 the cycle of centrosome duplication begins with centriole licensing. During mitosis a centrosome consists of a parent centriole and a procentriole that was generated in the previous cell cycle. Centriole licensing is initiated by centriole to centrosome conversion, where the procentriole acquires PCM, and centriole disengagement, the physical separation of the mature centriole and the immature procentriole. CDK1 mediated removal of the cartwheel complex is also important, as only newly growing procentrioles require this structure, it is not found in mature parent centrioles. Centriole disengagement requires separase mediated cleavage of PCNT, the main component required for maintaining centriole engagement (Lee and Rhee 2012). Centriole disengagement is sufficient to license the parent centriole for reduplication as, unlike the procentriole, it can recruit PCM. Centriole to centrosome conversion is essential for reduplication of the procentriole; it requires complete centriole disengagement, and CDK1/PLK1 activity which promotes the recruitment of the proteins involved (Nigg and Holland 2018; M and G1 phase panels in Figure 1.4a).

Each centriole is now ready for duplication, initiated at the G1-S transition alongside DNA replication, by CDK2 activity and the E2F transcription factors. The cartwheel complex is transiently recruited and a new procentriole begins to assemble perpendicularly on each centrosome, one of which contains the parent centriole (possesses distal appendages) and the other a licensed, immature parent centriole. This is controlled by asymmetrical localization of PLK4, which ensures only one procentriole assembles on each parent centriole (Habedanck *et al*. 2005). The procentrioles grow in length throughout S and G2 phase, until the cell reaches the G2/M transition, at which point PLK1 stimulates the final stage of centrosome maturation. The PCM expands in size to support the MT nucleating requirements of the centrosomes during mitosis, and distal

appendages assemble on the immature parent centriole (Nigg and Holland 2018; S and G2 phase panels in Figure 1.4a).

1.3.2 Centrosome Separation

Centrosome separation during prophase in late G2, or prometaphase in mitosis, is coordinated by a number of kinases. Firstly, centrosome disjunction occurs late during G2, where the linker disassembles (Figure 1.4a, G2 – M phase panels). This is initiated by Nek2A phosphorylation of centrosomal components. This includes centrosomal Nek2-associated protein 1 (C-Nap1) and ninein-like protein (Nlp), dissociation of which is required for the splitting of centrosomes (Fry et al. 1998b; Rapley et al. 2005). Cdk1 and Plk1 activity at the centrosome are also required to phosphorylate and recruit KIF11, and increase MT dynamic instability to allow centrosomes to move (Smith *et al*. 2011).

Mammalian cells display two mechanisms of centrosome separation, both of which are employed at different levels depending on cell type. Prophase centrosome separation has been shown to reduce the rate of chromosome segregation errors, and these cells tend to complete mitosis faster. One study found that during prophase in Hela cells, there is only around 10 minutes for centrosome separation to occur before NEB. In the remaining cells that do not complete centrosome separation within this window, the prometaphase pathway

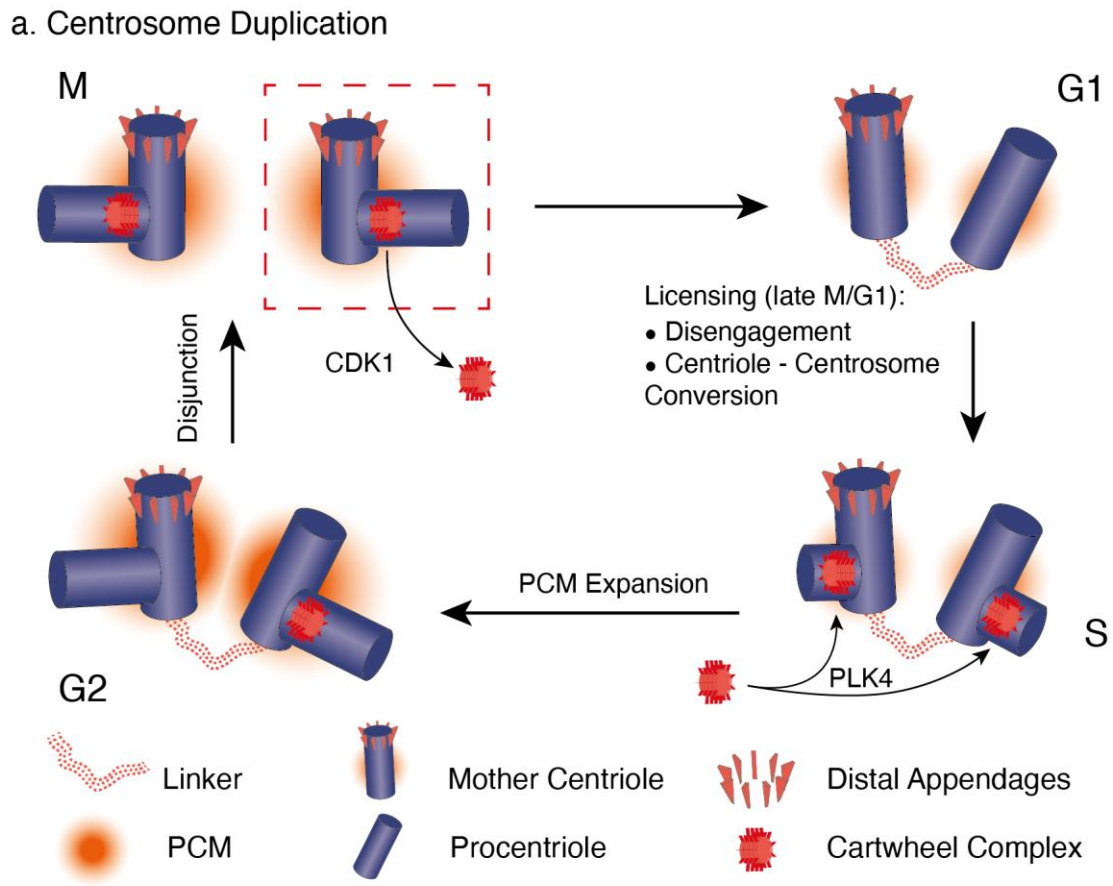

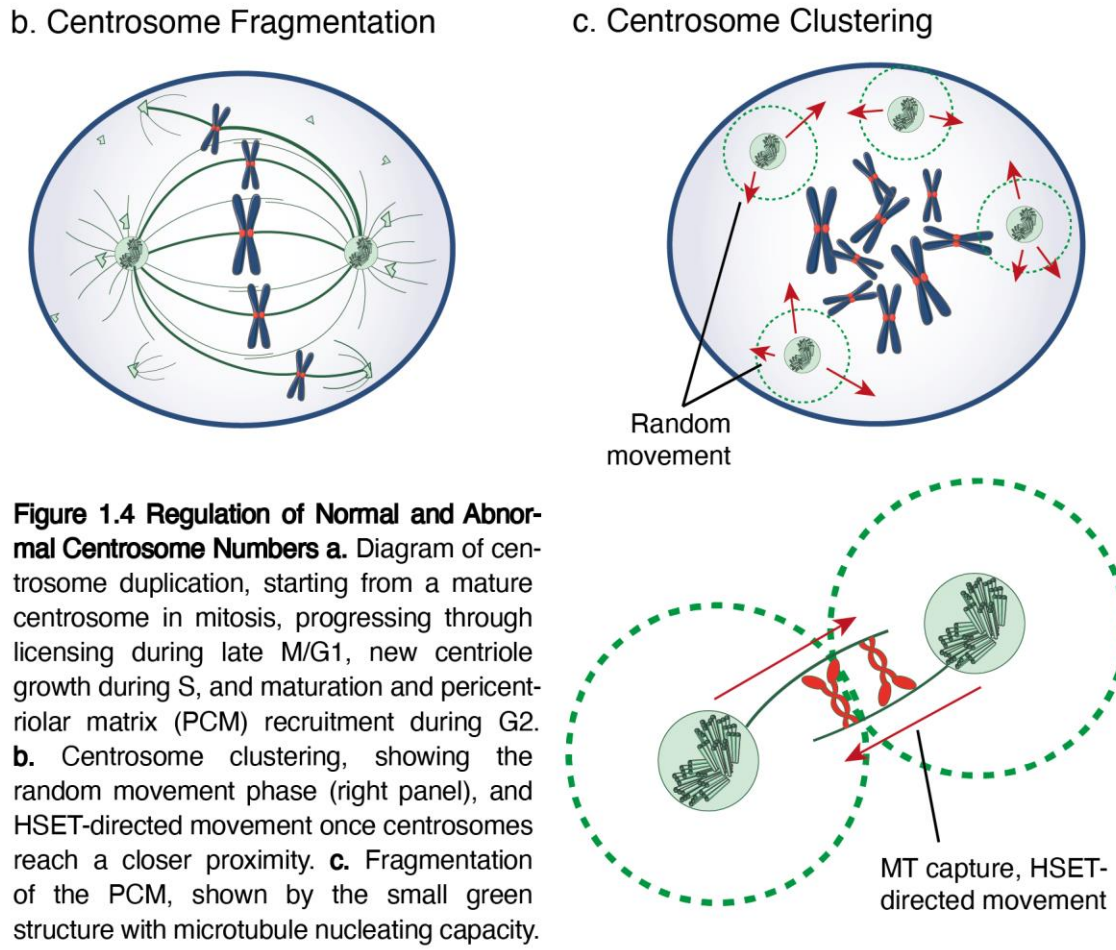

Figure 1.4 Regulation of Normal and Abnormal Centrosome Numbers a. Diagram of centrosome duplication, starting from a mature centrosome in mitosis, progressing through licensing during late M/G1, new centriole growth during S, and maturation and pericentriolar matrix (PCM) recruitment during G2. **b.** Centrosome clustering, showing the random movement phase (right panel), and HSET-directed movement once centrosomes reach a closer proximity. **c.** Fragmentation of the PCM, shown by the small green structure with microtubule nucleating capacity.

is used, where separation occurs post NEB (Kaseda *et al*. 2011). In RPE1 cells, another study showed that centrosome separation always began during prophase, however the spatial orientation of the centrosomes was not always consistent. In 73% of cases centrosomes separated vertically, producing a ring-like formation of chromosomes arranged around the axis. In the remaining cases centrosomes were separated to opposite ends of the nucleus horizontally, and upon NEB chromosomes form a H-like shape (Magidson *et al*. 2011).

1.3.3 Centrosome Amplification

Centrosome amplification can occur when the duplication cycle becomes deregulated. Overexpression of various regulators of centrosome duplication have been shown to cause amplification, including PLK4, which is often found overexpressed in cancer (Shinmura *et al*. 2014). A detailed insight into the mechanism of PLK4 mediated centrosome amplification was provided by a study investigating the link between human papillomavirus type 16 (HPV-16) and centrosome amplification (Korzeniewski *et al*. 2011), which is frequently observed in HPV positive tumours. HPV-16 encodes an oncoprotein E7 that disrupts the G1/S checkpoint, promoting entry into S phase by degrading the retinoblastoma tumour suppressor pRB, inactivating histone deacetylases HDAC-1 and HDAC-2, and interacting with E2F transcription factors and CDKs. Expression of *PLK4* was significantly increased in cells transduced to expressed HPV-16 E7, which is known to cause centrosome amplification (Duensing *et al*. 2000). This study also suggests that *PLK4* is transcriptionally controlled by a complex of E2F1 and SP1. Alongside findings that it is transcriptionally repressed by HDAC1 (Li *et al*. 2005), these data demonstrate how HPV-16 E7 promotes centrosome amplification via upregulating *PLK4* at the transcriptional level.

One study screened the NCI-60 panel of cancer cell lines using a semi-automated image analysis approach to detect centriole elongation, identifying 22 cell lines out of the 60 that showed significantly longer centrioles compared to normal tissue control cell lines (Marteil *et al*. 2018). These cell lines showed an increased incidence of centrosome amplification, caused by a deregulation of centriole duplication. Elongated centrioles promoted the assembly of an ectopic centriole

on the mother centriole, which often then fragmented, giving rise to aberrant but functional additional centrosomes.

1.3.4 Supernumerary Centrosomes Without Amplification

Cells can also acquire supernumerary centrosomes when becoming tetraploid, through the mechanisms of cytokinesis failure, mitotic slippage, and cell-cell fusion. However, one study found that extra centrosomes could only be propagated in a non-transformed setting when p53 was knocked out. RPE1 cells were treated with blebbistatin to block cytokinesis, resulting in binucleated G1 cells with two centrosomes (as opposed to one). These binucleated cells were able to proliferate for up to three mitoses, reforming mononucleated daughter cells after the first division, but eventually by the fourth division all cells had arrested in interphase, despite previously undergoing bipolar divisions. Interestingly, when the same experiment was performed with cytochalasin D, only 60% of binucleated cells entered mitosis compared to 90% with blebbistatin treatment, suggesting residual cytochalasin D can cause cell cycle arrest independent of the induced tetraploid/supernumerary centrosome phenotype (Krzywicka-Racka and Sluder 2011). These results suggest that in a non-transformed setting, p53 limits the proliferation of cells with supernumerary centrosomes.

1.3.5 Centrosome Fragmentation

Centrosome fragmentation can cause similar phenotypes to supernumerary centrosomes, but instead involves breakdown of the PCM, releasing acentriolar fragments with MT nucleating capabilities. The centrioles are not essential for anchoring and nucleating MTs, as other proteins that perform these functions such as ninein, γ-TURCs, and CLASPs localize to the PCM. The PCM is a highly ordered structure and perturbing the proteins that regulate this can often lead to fragmentation, such as ninein or CEP90 knockdown (Kim and Rhee 2011; Maiato and Logarinho 2014). Under normal conditions, these proteins exist in pericentriolar satellites surrounding the centrosomes, which aid in their recruitment. Interestingly, pericentriolar satellites are regulated by autophagy. This targets PCM1 for degradation, in turn limiting the size and number of

pericentriolar satellites. Inhibition of autophagy by knockdown of specific regulators resulted in accumulation of large pericentriolar satellites, centrosome fragmentation, and chromosome segregation errors (Holdgaard *et al*. 2019).

Centrosomes must retain their structural integrity while experiencing pushing and pulling forces exerted upon them during establishment of a bipolar spindle. These forces are generated by molecular motors at the centrosome, KT, and chromosome arms, including KIF11, dynein-dynactin, KIF4a, CENPE, and Kid. Centrosome fragmentation is often associated with chromosome alignment errors and mitotic delays, leading to speculation that misaligned chromosomes cause fragmentation, rather than the more intuitive reverse hypothesis. However, there is only direct evidence for fragmentation causing misaligned chromosomes, after chemically induced mitotic arrest (Karki *et al*. 2017), or after depletion of PCM components (Kim and Rhee 2011). CLASPs play an important role in resisting these poleward forces and maintaining spindle pole integrity via a scaffolding function, which promotes recruitment of ninein. Depletion of CLASP1/2 increased multipolar spindle formation, which was rescued upon CENPE depletion (Logarinho *et al*. 2012).

1.3.6 Premature Centriole Disengagement

Multipolar spindles can also be generated by premature centriole disengagement, where the mother centriole and daughter centriole become separated before chromosome segregation is complete. During a prolonged metaphase arrest where chromosomes experience cohesion fatigue, the leaky separase activity is also able to initiate premature centriole disengagement. Mitotic arrest induced by monastrol treatment causes a time-dependent increase in centrosome fragmentation and centriole disengagement in RPE1 cells, due to separase activity. HSET was required for clustering of the centrosome fragments and disengaged centrioles, and chemical inhibition resulted in a large increase in the number of multipolar spindles after 8 hrs mitotic arrest. Interestingly, pre-treatment with nocodazole to depolymerize MTs was able to rescue the fragmentation phenotype, proving it is dependent on MT pushing/pulling forces (Karki *et al*. 2017).

1.3.7 Cellular Response to Supernumerary Centrosomes

Investigating the requirement of p53 to prevent the proliferation of cells with supernumerary centrosomes was performed in RPE1 cells. Cells were treated with blebbistatin to block cytokinesis, resulting in binucleated G1 cells with two centrosomes. These binucleated cells were able to proliferate for up to three mitoses, reforming mononucleated daughter cells after the first division, but eventually by the fourth division all cells had arrested in interphase, despite previously undergoing bipolar divisions. Interestingly, when the same experiment was performed with cytochalasin D, only 60% of binucleated cells entered mitosis compared to 90% with blebbistatin treatment, suggesting residual cytochalasin D can cause cell cycle arrest independent of the tetraploid/supernumerary centrosome phenotype induced (Krzywicka-Racka and Sluder 2011). These results suggest that in a non-transformed setting, p53 limits the proliferation of cells with supernumerary centrosomes.

Supernumerary centrosomes have been shown to activate p53 through the hippo pathway serine/threonine protein kinase LATS2 in RPE1 cells, after the induction of tetraploidy by Dihydrochlorocytochalasin-B (DCB; Ganem *et al*. 2014). Cytokinesis failure and induction of tetraploidy was also shown to result in cell cycle arrest due to activation of the PIDDosome and caspase-2 in RPE1 cells (Fava *et al*. 2017). These pathways show how normal non-transformed cells tightly control proliferation of cells with supernumerary centrosomes.

1.3.8 Centrosome Clustering

Supernumerary centrosomes can be extremely toxic to cells, causing multipolar divisions and large-scale aneuploidy and p53 activation. To prevent this, cells possess mechanisms to cluster extra centrosomes and form a pseudobipolar spindle. It is well established that the molecular motor HSET is important for clustering, which binds MTs emanating from different centrosomes and pulls them towards each other (Kwon *et al*. 2008). Another study showed that centrosome clustering occurs in a biphasic mechanism. There is first a ‘search and capture’ phase (Figure 1.4c), characterized by slow movement of centrosomes, that is dependent on cell cortex contractility. Centrosomes move

randomly during this phase, and the degree of cortical contractility determines how restricted this movement is. Cells with increased cortical contractility exhibit reduced centrosome movement, meaning there is a greater likelihood of extra centrosomes becoming spatially close. A 'motorized' phase then follows once the centrosomes come within a certain distance of each other (Figure 1.4c), where centrosomes move in a rapid, directional manner due to the activity of HSET on overlapping antiparallel MTs in between the centrosomes (Rhys *et al*. 2017).

While many cell types, even when non-transformed, show the ability to cluster extra centrosomes, and the degree to which they are able to do so varies. Epithelial cells show a reduced clustering ability dependent on E-cadherin; upon loss of E-cadherin MCF10A were able to cluster extra centrosomes more efficiently, after the induction of tetraploidy by dihydrocytochalasin B (DCB). E-cadherin decreases cortical contractility via a signalling cascade that modulate adherens junctions, resulting in greater movement of centrosomes during the search and capture phase, leaving them more frequently out of range of HSET (Rhys *et al*. 2017).

When generating tetraploid cells in culture, they often lose supernumerary centrosomes and show a normal centrosome number. It has been demonstrated that this is due to asymmetrical clustering of centrosomes, with the cell that inherits a single centrosome showing increased survival and proliferation, while the cell that inherits 2 or more centrosomes is prone to multipolar divisions and cell death. Experiments were performed in $p53^{-/-}$ RPE1 cells, due to the p53 induced cell cycle arrest after tetraploidisation with DCB (Baudoin *et al*. 2020).

1.4 KIF11

KIF11 (also known as Eg5, Kinesin 5), is a homotetrameric plus end directed kinesin that crosslinks antiparallel MTs, generating an outward pushing force, as discussed in section 1.2.5. Structurally, each monomer contains a globular motor domain and a helical stalk domain, and when associated this provides KIF11 with two functional motor domains at either end of the long stalk domain. KIF11 localises across the entire spindle and is enriched at the poles (Sawin *et al*. 1992; Uteng *et al*. 2008), however it is also found on antiparallel interpolar MTs within

the central spindle region, including within bridging fibers (Kajtez *et al*. 2016). Its functions are important throughout mitosis (Figure 1.5a).

KIF11 inhibitors have proved extremely useful for investigating mitosis and the functions of KIF11, as in contrast to siRNA, once washed out cells can proceed through mitosis normally. Monastrol was the first KIF11 inhibitor to be identified and has been widely used within the field to induce monopolar spindle formation (Mayer *et al*. 1999; Kapoor *et al*. 2000). S-trityl-L-cysteine (STLC) is a more potent inhibitor compared to monastrol (Skoufias *et al*. 2006). Inhibition of KIF11 by FCTP is used to lock the motor in a rigor state, where it remains bound to MTs but cannot perform its stepwise motion towards the plus end.

1.4.1 Post-Translational Regulation of KIF11 Activity

KIF11, like many other mitotic proteins is spatially and post-translationally regulated to ensure its correct function during mitosis. A cytoplasmic protein, it requires phosphorylation by CDK1 at T926 (human, T937 *Xenopus laevis*) to interact with MTs during mitosis, which prevents its interaction with MTs during interphase (Sawin and Mitchison 1995). While unphosphorylated KIF11 retains near-normal motor activity, it has a much weaker affinity for MTs, and phosphorylation is required such that loading of KIF11 onto MTs exceeds a threshold necessary for spindle assembly (Cahu *et al*. 2008).

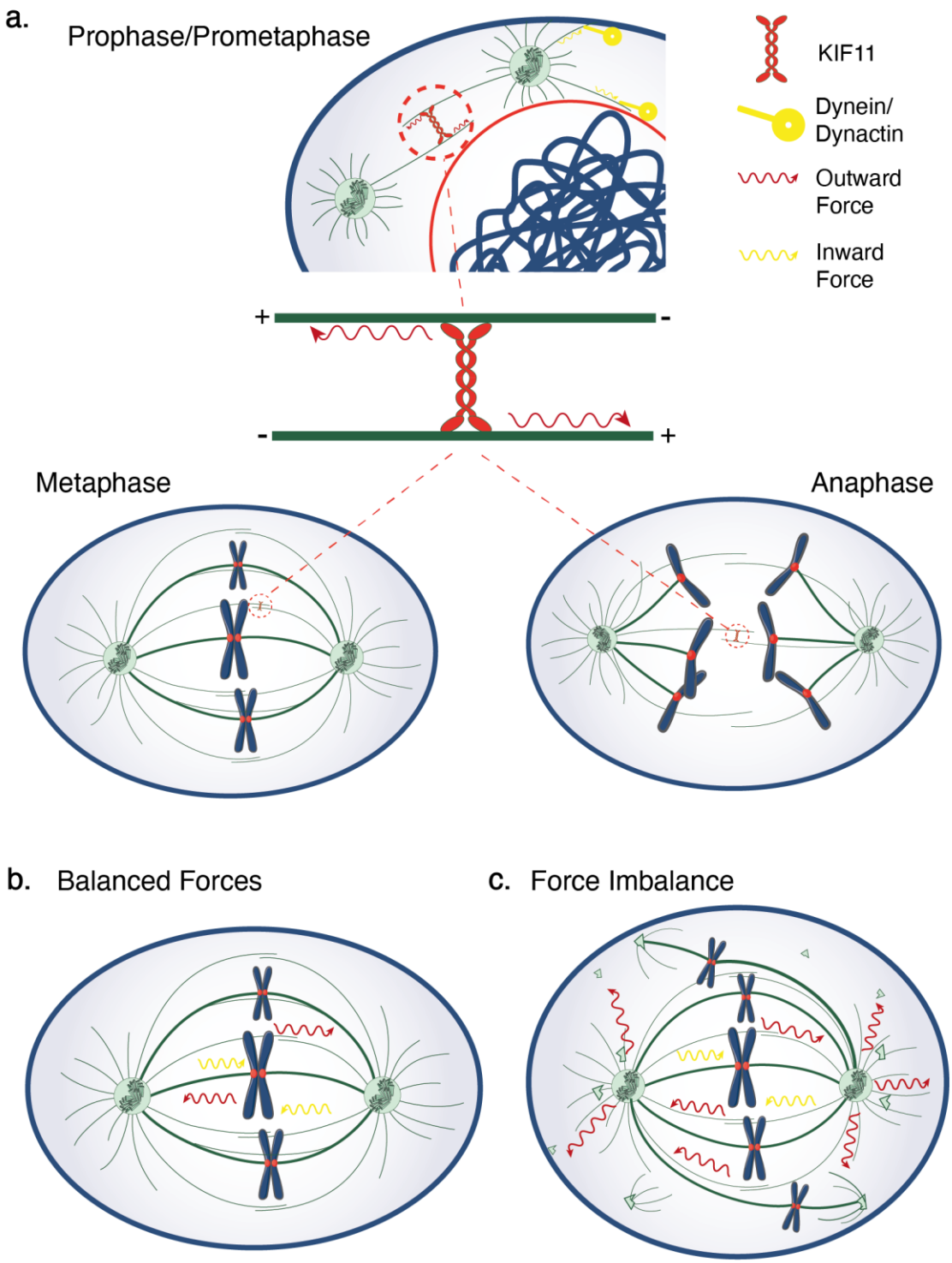

Figure 1.5 Functions of KIF11 in Mitosis a. Diagram showing KIF11 motor activity (centre), and its functions during the various stages of mitosis. **b.** Diagram representing a normal mitotic spindle, with balanced inward and outward forces. **c.** Model for how imbalanced forces and increased outward forces mediated by KIF11 upregulation could lead to spindle pole fragmentation.

There is also evidence suggesting KIF11 is phosphorylated by Src family kinases in human cells, at Y125, Y211, and Y231 (Bickel *et al*. 2017), residues found in the motor domain. Phosphomimetic mutants showed significantly decreased ATPase activity and MT sliding velocities *in vitro*, suggesting phosphorylation at this site negatively regulates KIF11 function. *In vivo*, expression of the Y211 phosphomimetic mutant caused an increase in monopolar spindle formation, while expression of a non-phosphorylatable mutant caused disorganized spindle formation. Neither mutant effected multipolar spindle formation, however, and spindle pole integrity was not examined.

KIF11 phosphorylation is in turn regulated by phosphatases. Both PP2A (Liu *et al*. 2017) and PTEN (He *et al*. 2016) have been identified as negative regulators of phosphorylation at T926. Interestingly, PTEN depletion and a resultant hyperphosphorylation of KIF11 was shown to reduce spindle localization, delay mitosis and increase errors, suggesting an interplay between CDK1 and PTEN is important to finely tune the activity of KIF11. PP2A dephosphorylation was found to occur from metaphase; depletion caused significant accumulation of pKIF11 in metaphase cells, and these cells took significantly longer to transition into anaphase.

1.4.2 KIF11 Mediated Outward Pushing Force in Mitosis

Precise regulation of KIF11 activity is important for coordinating its various functions throughout mitosis. As mentioned in section 1.2.5, one of the most important functions of KIF11 is centrosome separation during prophase and prometaphase, achieved by the outward pushing force exerted on MTs (Kapitein *et al*. 2005). These forces also play a role in maintaining the spindle structure in metaphase and anaphase (Figure 1.5a). While KIF11 is essential in most organisms, it is dispensable for mitotic spindle elongation in *C. elegans* and *Dictyostelium* (Saunders et al. 2007; Tikhonenko et al. 2008).

In *Xenopus laevis* extracts treated with 50 μM monastrol during metaphase, spindle disassembly was observed after 20 minutes (Kapoor *et al*. 2000). Similarly, addition of 40 μM STLC to RPE1 cells during metaphase caused rapid spindle collapse, within 10 minutes of drug addition (Vukušić *et al*. 2021). While

these studies suggest KIF11 is the predominant driver of outward force during metaphase, KIF11 inhibition alone in other cellular systems does not cause spindle collapse, suggesting there are other factors involved. PTK1 cells treated with 200 μM monastrol did not experience any degeneration of spindle structure in the 30 minutes following drug addition (Cameron *et al*. 2006), and U2OS only formed monopolar spindles after around 5 hours, when arrested at metaphase with MG132 and treated with 40 μM STLC (van Heesbeen *et al*. 2014).

There is an established interplay between pushing forces from KIF11 and KIF15, and pulling forces from dynein at the KTs, that maintain spindle structure during metaphase (Figure 1.5b). When KIF15 is knocked down, the sensitivity of U2OS cells to STLC greatly increases, and collapse to a monopolar spindle is observed around 30 minutes after addition of STLC. This phenotype is rescued when dynein is also knocked down, although most cells die in mitosis. These data suggest that spindle structure in metaphase is maintained by the net force generated by a combination of KIF11, KIF15 and dynein activity (van Heesbeen *et al*. 2014).

The differences observed in the sensitivity to KIF11 inhibition during metaphase could be due to differences in the balance of these molecular motors; perhaps RPE1 rely more on KIF11 for outward pushing force, whereas U2OS have more redundancy between KIF11 and KIF15. As U2OS is a highly genetically altered cancer cell line (Ozaki *et al*. 2003), it is possible that mitotic gene expression has been altered compared to the normal, near-diploid RPE1 cell line.

The picture is similar in anaphase: a number of different motor proteins contribute to the forces required to separate spindle poles, and the precise mechanisms differ between organisms. However, there is a consensus that KIF11 is dispensable for anaphase B centrosome separation (Collins *et al*. 2014a; Vukušić *et al*. 2021). Inhibition of KIF11 with STLC added at anaphase onset resulted in a significant increase in the rate of spindle elongation, consistent with a model where KIF11 functions as a brake during anaphase, due to its MT crosslinking ability. Inhibition with STLC reduces the affinity of KIF11 for MTs, reducing its crosslinking ability. In support of this treatment with FCPT, which induces the

rigor state in KIF11 and increases MT crosslinking, slows down spindle elongation.

A recent study has shed light on the mechanism of spindle elongation, using extensive single and double ablations of kinesins and MAPs (Vukušić et al. 2021, pp.1-). Knockdown of PRC1 or KIF4A in combination with KIF11 inhibition was found to completely block spindle elongation, while KIF11 inhibition, KIF4A knockdown, and PRC1 knockdown alone had no significant effects. The authors also examined the contribution from astral MTs, to determine whether cortical pulling is affected by KIF11 inhibition and KIF4A knockdown. There was no change in the length of astral MTs or the number of EB3 comets present at the cell cortex, and hence the authors conclude that spindle elongation during anaphase B depends solely on MT sliding within the central spindle, mediated by KIF11 and KIF4A.

1.4.3 Counteracting KIF11 Activity

The outward pushing forces generated by KIF11 are antagonized in various ways. KT localised dynein generates an antagonistic inward pulling force, and simultaneous ablation in cell free systems restored spindle formation, in comparison to the defects observed after single depletions (Gaglio *et al*. 1996). There is similar evidence suggesting HSET [OM1]also antagonizes KIF11 activity. HSET is dispensable for mitosis under normal conditions, however it was essential for spindle assembly in acentrosomal cells. The inward pulling forces it generates (Figure 1.3b), were required for the clustering of MT minus ends to form asters. In addition, knockdown of HSET in cells treated with KIF11 inhibitors restores bipolar spindle formation in a variety of experimental systems including human cells, suggesting it is the predominant antagonist of KIF11 mediated outward pushing forces (Mountain *et al*. 1999).

1.4.4 KIF11 and Poleward MT Flux

The outward sliding force generated by KIF11 has also been implicated in promoting MT poleward flux. While older work found that flux was independent of KIF11 in *Xenopus laevis* extracts (Sawin and Mitchison 1994; Kapoor and

Mitchison 2001; Cameron *et al*. 2006), developments in image analysis techniques revealed a dose dependent reduction in flux rate in response to KIF11 inhibition with monastrol or (S)-quinazolinone.

More recently, Steblyanko *et al* performed extensive investigation into the coordinated regulation of MT flux by KIF11, KIF15, CENPE and KIF4A (Steblyanko *et al*. 2020). Depletions identified KIF4A as the predominant driver of MT flux in bipolar and monopolar spindles, through force generation on non-kMTs from chromosome arms. These forces were distributed to kMTs through coupling, dependent on MT crosslinking proteins HSET and NuMA. While KIF11 inhibition alone did not affect MT flux rate, inhibition in combination with KIF15 knockdown caused a significant reduction, and KIF4A depletion in addition to these inactivations caused an even stronger reduction in flux rate. These results suggest KIF15 and KIF11 play a minor role in metaphase MT flux, while this is predominantly driven by KIF4A motor activity.

The contribution of KIF11 to MT flux may be regulated by its position-dependent function within the spindle. KIF11 was identified to remain static within the spindle midzone in *Xenopus laevis* extracts, while MTs fluxed towards the spindle poles. Motor activity on the antiparallel MTs in this region could be contributing to flux. In the half spindle region, however, KIF11 was actively transported to the spindle poles by dynein-dynactin, at a rate faster than MT flux. This activity is likely dependent on a physical interaction with dynein-dynactin, and its subsequent minus end directed motor activity (Uteng *et al*. 2008).

1.4.5 KIF11 and MT Dynamics

Work in yeast identified that the KIF11 homologue Cin8p exhibited an MT depolymerization function (Gardner *et al*. 2008). This study demonstrated the function is mediated at MT plus ends, where it promotes MT shortening to regulate spindle length. The model put forward predicts that longer MTs are preferentially shortened by Cin8p, as they have more binding sites and recruit more Cin8p molecules. Interestingly, expression of an NLS-mutant Cin8p that remained localized in the cytoplasm was also found to promote depolymerization of astral MTs. The authors hypothesise that ~~the~~ mechanistically, the motor activity

of KIF11 walking along MTs could stress the bonds between tubulin dimers causing destabilization, or that alternatively KIF11 works in conjunction with a binding partner that induces destabilization.

In contradiction to these results, a study (Chen and Hancock 2015) employing a transgenic form of KIF11 containing the motor domain from *Xenopus laevis* KIF11, the *Drosophila* KIF11 heavy chain, and a GFP tag (called Kin5-14), showed MT stabilization and increased polymerization *in vitro*. Kin5-14 was found to pause at the MT plus end before being released, remaining bound 40-fold longer than the normal duration of a step. The authors hypothesise that binding of Kin5-14 stabilises the bonds between tubulin dimers longitudinally and promotes recruitment of the next tubulin dimer.

1.4.6 Investigating MT Dynamics and Spindle Formation with KIF11 Inhibitors

Both monastrol and STLC are allosteric inhibitors that bind to loop 5 and induce a conformational change in KIF11, reducing its affinity for MTs. The atomic interactions within the binding site differ between the two, however. One study investigating the differences between the two drugs identified a previously unknown function of mammalian KIF11 in promoting MT depolymerization, a function that was inhibited by STLC but not monastrol (Kim *et al*. 2019). Given that monastrol bound KIF11 interacts with MTs more weakly than free KIF11, it is interesting that there was no significant change to the MT depolymerization rate measured compared with KIF11 alone. One explanation could be differential affinity for the GTP-rich tubulin found at MT plus ends, as there is evidence of other kinesins binding here preferentially (Nakata, 2011).

The authors also examined monopolar spindles generated by either monastrol or STLC treatment in Hela cells. Analysis of the area and tubulin signal intensity suggested that STLC treatment does indeed prevent KIF11-induced MT depolymerisation, as spindles were significantly larger and brighter (Kim *et al*. 2019). This study suggests that motor activity and MT depolymerizing function of KIF11 are caused by distinct mechanisms that can be uncoupled. The MT depolymerization observed in this study is consistent with observations from

yeast expressing different Cin8p mutants, however it contradicts the data presented by Chen and Hancock, which suggests KIF11 promotes MT stability and polymerization at the plus end.

BRD9876 and FCTP are examples of competitive inhibitors of KIF11 that preferentially target MT-bound KIF11, inducing a rigor state in which KIF11 cannot slide MTs (Chattopadhyay *et al*. 2015; Chen *et al*. 2017). One study investigating the function of KIF11 inhibitors on KIF11 induced MT stabilization showed that treatment of MTs with KIF11 alone modestly reduced the depolymerization rate, while KIF11 + BRD9876 reduced the depolymerization rate to near zero (Chen *et al*. 2017). In contrast, KIF11 + monastrol treated MTs showed no difference in depolymerization rate compared to control, in the absence of KIF11. These results suggest that active KIF11 stabilises MTs, a function that is due to MT binding rather than motor activity. Enhancing MT binding with BRD9876 increases MT stability, whereas treatment with monastrol weakens MT binding, preventing stabilization.

This study was performed in the same laboratory as Chen and Hancock. In their model systems KIF11 behaves to promote MT stability, while in other studies the opposite has been demonstrated. To further complicate the picture, another study found no significant changes to the rate of MT poleward flux in after monastrol treatment in Hela cells, suggesting KIF11 does not affect MT dynamics (Vladimirou *et al*. 2013). Therefore, there is contradicting evidence for how KIF11 functions in the regulation of MT polymerisation and stability, and its function may be organism or cell type specific.

1.4.7 KIF11 Inhibitors in Cancer Therapy

The anti-mitotic effect of KIF11 inhibition is analogous to that of MT poisons and could be useful in a chemotherapeutic setting. KIF11 is overexpressed in several cancers, where expression is higher than in normal tissue. However, it is unclear whether this reflects true upregulation of KIF11 at the protein or mRNA level, or whether it reflects the increased proliferation rate of cancer cells, and therefore the increased number of mitotic proteins in general. Nonetheless, work in cell lines has demonstrated that KIF11 inhibitors can selectively kill cancer cells

compared to normal cells (Orth *et al*. 2008), and these drugs were subsequently brought to the clinic.

While KIF11 inhibitors showed less toxicity in patients than MT poisons, responses were poor, with some studies reporting partial responses in a small proportion of individuals (Lee *et al*. 2008), and others reporting no responses (Beer *et al*. 2008). The problem with these regimens was most likely due to the drug half-life and the proliferation rate paradox. The drug must remain in the patient at a therapeutic dose long enough for all cells within the tumour to enter mitosis for killing to be observed, which is highly unlikely based on the drug half-life. In support of this theory, the most successful KIF11 inhibitor in the clinic has been Arry-520 (Owens 2013), which has a much longer half-life and was used for the treatment of a highly aggressive and proliferative type of cancer (relapsed multiple myeloma).

Resistance to KIF11 inhibitors rapidly develops in cultured cells. This occurs through a mechanism involving KIF15. Under normal circumstances KIF15 localises to kMTs (containing bundled MTs), where it generates an outward pushing force. In response to KIF11 inhibition a spontaneous mutation can arise (G286V) known as the KIF11 rigor mutant, as it causes similar effects to FCTP. This promotes MT bundling throughout the spindle, promoting redistribution of KIF15 such that it is able to perform centrosome separation in the absence of KIF11 (Sturgill *et al*. 2016). This mechanism is an example of the functional overlap often seen with kinesins.

1.4.8 KIF11 Knockdown

KIF11 knockdown has the same consequences as inhibition: monopolar spindle formation. Knockdown of KIF11 in cancer cell lines that show overexpression reduced cell motility in triple negative breast cancer (Jiang *et al*. 2017), and inhibited growth in oral cancer cells (Daigo *et al*. 2017). Knockdown experiments are not as useful in the study of mitosis as they do not have the same reversibility as chemical inhibitors, however they have provided an insight on the role of KIF11 in cell migration. While one study found that KIF11 inhibition does not affect cell

motility (Even-Ram *et al*. 2007), another reported that knockdown specifically reduced cell migration towards a chemotactic signal, EGF (Wang and Lin 2014).

1.4.9 KIF11 Overexpression

Defective spindle formation has been observed in a mouse study, in which a KIF11 transgene was overexpressed using genetic engineering. Cultured fibroblast cell lines generated from some of the mice showed a 4- to 9-fold overexpression of KIF11, and increased incidence of both monopolar and multipolar spindles. Castillo *et al* show a 25% increase in the number of monopolar spindles, however these have been poorly characterized as cells were only stained for tubulin and DAPI, and no consideration has been given to discriminating prometaphase cells from monopolar spindles. FACS analysis revealed increased tetraploid and octoploid populations in the KIF11 transgenic MEFs, which they suggest are the cause of the ~3% increase in multipolar spindles based on increased DAPI staining in these cells. Due to the absence of any centrosome stain, it is unclear whether these spindles are formed from fragmented or supernumerary centrosomes, and mechanistic investigation was not performed. (Castillo *et al*. 2007).

1.4.10 KIF11-Mediated Spindle Pole Fragmentation

More recent studies have provided better evidence for a role of KIF11 in spindle pole fragmentation (Figure 1.5c). Clift & Schuh identified a role for KIF11 in driving the intrinsic fragmentation of MT organizing centres (MTOCs) during mouse oocyte development. MTOCs were first stretched before NEB, which was shown to be dependent on dynein anchored to the nuclear membrane by Bicaudal D2 (BicD2). In some cases, the MTOC stretching resulted in fragmentation before NEB, with the fragments colocalizing with α-Tubulin on the nuclear membrane, however KIF11 was dispensable during this stage. After NEB, KIF11 was shown to drive further fragmentation events and push the fragments further apart. (Clift and Schuh 2015).

Further compelling evidence for KIF11-mediated spindle pole fragmentation was shown by Huechsen *et al*, whereby knock-out of dynein or NuMA induced

turbulent spindles, with numerous poles. Inhibition of KIF11 with 5 μM STLC rescued the phenotype, confirming it is KIF11-dependent. Cells with turbulent spindles were found to have increased motility during mitosis compared to control cells arrested with MG132, a phenotype that was again rescued by KIF11 inhibition. (Hueschen *et al*. 2019).

Interestingly, another study has found a link between centrosome fragmentation and KIF11, specifically through its regulation by PTEN. Loss of PTEN-mediated dephosphorylation of KIF11 increased the number of cells with fragmented centrosomes, by ~5%. PTEN has been shown to colocalize with KIF11 during mitosis, where it is thought to function in balancing the level of KIF11 phosphorylation required for proper spindle formation. Knockdown of PTEN in HeLa cells induced congression errors which delayed mitosis, resulting in a ~25% increase in the number of cells experiencing mitotic catastrophe. This phenotype manifests as cells that do not enter anaphase and instead further condense their DNA, likely becoming apoptotic. Using a phospho-mimetic KIF11 variant, He *et al* demonstrated the same centrosome fragmentation and congression delay phenotypes observed after PTEN knockdown (He *et al*. 2016).

1.5 Defective Mitosis & Chromosome Instability

1.5.1 Defective Spindle Formation

Defects in centrosome regulation, replication, and separation can compromise the mitotic spindle geometry. An imbalance in the motor proteins required to separate centrosomes during prophase can result in the formation of a monopolar spindle (Figure 1.6a), for example by knockdown of KIF2A (Ganem and Compton 2004) and inhibition or overexpression of KIF11 (Castillo *et al*. 2007). The polo-like kinases, which regulate CDKs and control mitotic entry, play an important role in centrosome maturation and separation. Inhibition of PLK1 or PLK4 is sufficient to induce monopolar spindles, whilst overexpression of PLK1 promotes centrosome amplification and the formation of multipolar spindles (Ganem *et al*. 2009; Tillement *et al*. 2009; Cárcer *et al*. 2018; Figure 1.4). Cells with monopolar spindles become arrested at prometaphase, due to the activity of the SAC, which allows more time for centrosome separation. In the event of a persistent

monopolar spindle, cells can undergo mitotic slippage and re-enter G1 with a 4N (tetraploid) genome.

Deregulated centrosome duplication can result in supernumerary centrosomes that cause multipolar spindle geometries (Figure 1.6b), for example, by overexpression of PLK1. Fragmentation of centrosomes can lead to the formation of multipolar spindles, as the pericentriolar matrix retains its MT nucleating ability, acting as an additional spindle pole (Karki *et al*. 2017). In these cases, cells can undergo a multipolar anaphase, resulting in segregation of chromosomes into >2 daughter cells. This is a highly toxic process for cells as chromosome loss can be detrimental to cell viability, causing gene imbalances and loss of essential genes, therefore often the daughter cells undergo apoptosis.

Cancer cells show very high rates of multipolar spindle formation, as perturbation of a variety of genes can impact centrosome function. For example, centrosome amplification was identified in mammary tissue upon inhibition of BRCA1, due to a loss of regulatory ubiquitination of gamma-tubulin (Starita *et al*. 2004). Expression of the oncogenic PIK3CA H1047R variant has also been shown to promote centrosome duplication in mouse models (Berenjeno *et al*. 2017). There is a large amount of evidence showing that cancer cells utilise centrosome clustering to evade the toxicity associated with multipolar divisions.

Whilst multipolar anaphases inherently cause CIN, they also increase the number of erroneous merotelic kMT attachments, resulting in an increased number of lagging chromosomes during anaphase (Figure 1.6b). When supernumerary centrosomes are present, there is an increase in the number of MTs available to make kMT attachments, and the non-canonical spindle geometry allows access of MTs from different poles to the same chromatid (Ganem *et al*. 2009). This therefore increases the likelihood of merotelic attachments forming and persisting through to anaphase, resulting in lagging chromosomes. This is also true of cells that cluster supernumerary centrosomes into a pseudobipolar spindle, as often there is a transient period of multipolarity, providing a window for erroneous kMT attachments to form (Silkworth and Cimini 2012).

1.5.2 Numerical Chromosome Segregation Errors

Numerical chromosome segregation errors occur when whole chromosomes or chromatids are segregated to the incorrect daughter cell. Numerical CIN has been attributed to mitotic defects such as compromised centromere geometry, supernumerary centrosomes, impaired spindle assembly checkpoint and sister chromatid cohesion. These processes increase or allow the formation of erroneous kMT attachments, which generate lagging chromosomes that often mis-segregate into the wrong daughter cell (Bakhoum *et al*. 2009b; Thompson and Compton 2011; Figure 1.6c). The result of a division with chromosome segregation errors is aneuploid daughter cells, one with 46+n, and the other 46-n, where n is the number of mis-segregated chromosomes.

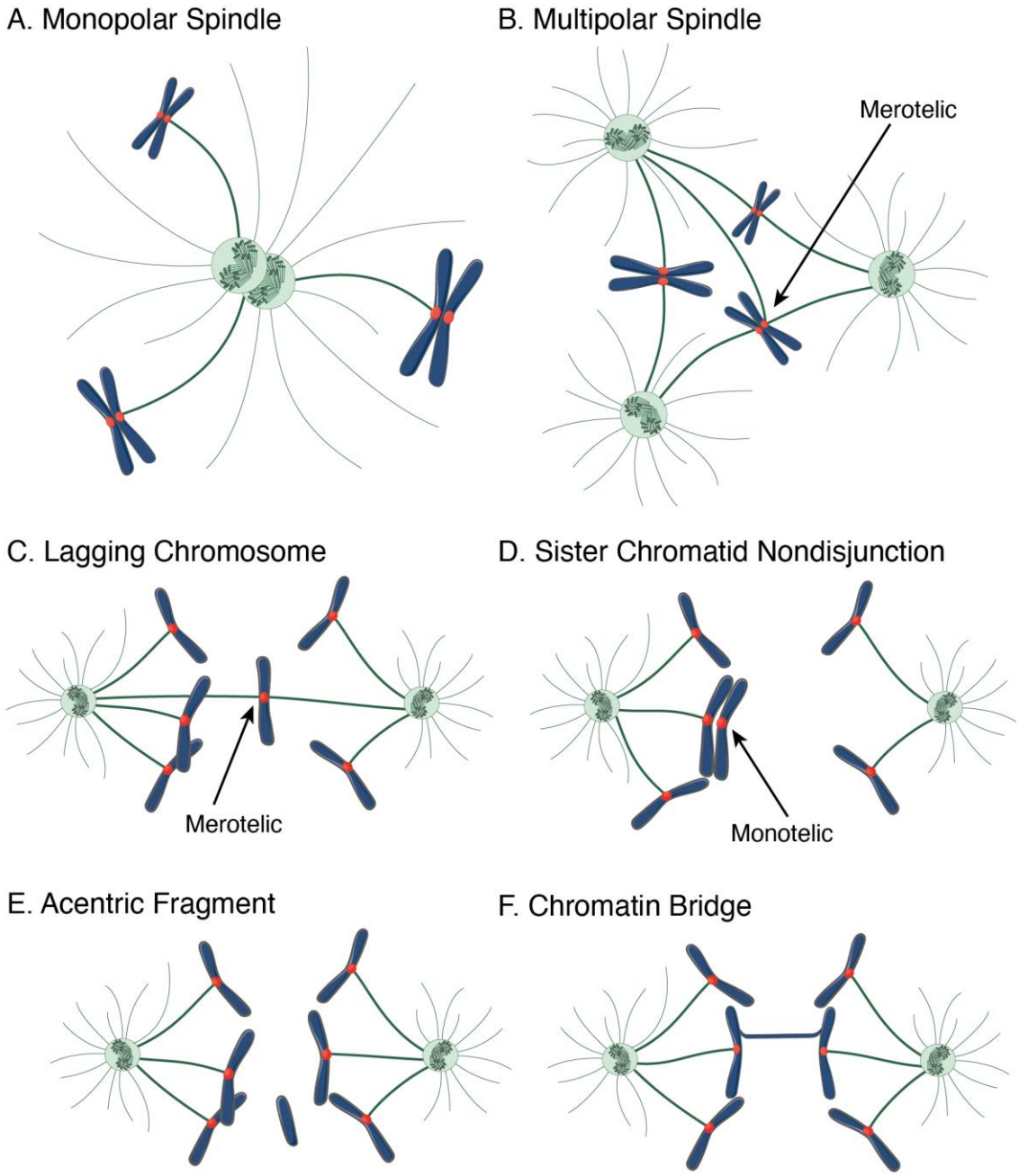

Figure 1.6 Types of Mitotic Errors **A.** Monopolar spindle formation, caused by failure of centrosome separation. **B.** Multipolar spindle formation (tripolar), caused by the presence of an extra centrosome. **C.** Lagging chromosome, caused by merotely. **D.** Acentric fragment, lagging behind during anaphase due to an absence of kMT attachments. **E.** Chromatin bridge.

Perturbation of MT dynamics can affect the stability of kMT attachments, thereby reducing the rate of correction of merotelics during prometaphase/metaphase. This can be achieved by interfering with kinetochore components, such as Aurora B kinase, Hec1, or MCAK, or motor proteins such as KIF18A (DeLuca *et al*. 2006; Cimini 2007; Bakhoum *et al*. 2009a). Aurora B kinase is a component of the SAC and functions to destabilize kMTs, therefore chemical inhibition induces the

opposite effect; kMT attachment stabilisation (Cimini *et al*. 2006). MCAK also promotes MT depolymerisation resulting in destabilisation kMT attachments.

Another mechanism of numerical CIN that generates aneuploidy is sister chromatid nondisjunction, where chromatids fail to separate and are segregated into the same daughter cell (Figure 1.6d). These can result from monotelic kMT attachments and subsequent failure of the SAC to detect and allow for correction of the error. In some cases, they cannot be detected by looking at mitotic cells, as they are segregated at the same time as the main bulk of chromosomes, without experiencing 'lagging'. Inhibition of DNA topoisomerases was also shown to increase sister chromatid nondisjunction, as DNA remained supercoiled after replication, with the sister chromatid strands tangled (Holm *et al*. 1989). In this case, when kMT attachments are amphitelic, nondisjunction results in lagging chromosomes.

1.5.3 Fates of Lagging Chromosomes

Lagging chromosomes do not always result in chromosome segregation errors, they can often be resolved during anaphase and segregated to the correct daughter cell. One theory is that MT occupancy at merotelic attachments can determine segregation of a lagging chromosome. At a human KT there are 20-30 individual MTs binding to form a k fiber, which exerts a strong mechanical force during anaphase. Evidence suggests that cells are able to distinguish between high occupancy kMT attachments, often correct, and low occupancy attachments, often incorrect/merotelic (Dudka *et al*. 2018). It has also been shown that in RPE1 cells, chromosomes 1 and 2 are more susceptible to mis-segregation events than others (Worrall *et al*. 2018). These chromosomes are more susceptible to cohesion fatigue after an 8 hour treatment with nocodazole, followed by a 2 hour MG132 treatment. The mechanism behind this phenotype was not shown, however the authors hypothesize it could be related to centromere and KT size. Despite the lack of correlation between chromosome size and length of α-satellite DNA at the centromere, there is a significant correlation with the amount of CENPA protein (Irvine *et al*. 2004). Larger chromosomes with more CENPA may be predisposed to forming merotelic kMT attachments and exhibiting mis-segregation.

The importance of Aurora B kinase in correcting lagging chromosomes and ensuring their segregation to the correct daughter cell was highlighted in a recent study (Sen *et al*. 2021). Lattice light sheet imaging combined with automated image analysis using KiT to track KTs were employed to track the fates of lagging KTs through anaphase. The authors coin the term ‘laziness’ to quantitatively examine the kinetics of the lagging KTs, including those that mis-segregate and those that are resolved. In RPE1 cells treated with DMSO, only a small number of KTs exhibited laziness. Of these, 93% were segregated to the correct daughter cell, and 7% were mis-segregated. A short nocodazole treatment was used to increase the number of KTs exhibiting laziness, which also increased the proportion that mis-segregated. For both DMSO and nocodazole treated cells, treatment with an Aurora B inhibitor more than doubled the proportion of lazy KTs that underwent mis-segregation compared to resolution.

There are multiple outcomes which result in mis-segregation of a lagging chromosome. Depending on the forces exerted on the KT pair by the opposing k fibers, the lagging chromosome can segregate to the wrong daughter nuclei or become stranded in the centre of the spindle. Stranded chromosomes most commonly form micronuclei, which segregate to either daughter cell. Micronuclei can propagate further genomic and chromosomal instability, as DNA replication and repair processes are less efficient within micronuclei, and they are susceptible to chromothripsis (Zhang *et al*. 2015). They are also more likely to mis-segregate in the subsequent mitosis, as KT construction is also less efficient, resulting in a reduced ability to bind MTs and align on the metaphase plate (Soto *et al*. 2018). Chromosomes that remain stranded during cytokinesis also present a threat to genomic integrity, as if they become trapped in the cleavage furrow, they are prone to DNA damage that is carried through to the next cell cycle (Funk *et al*. 2016).

Lagging chromosomes also increase the likelihood of cytokinesis failure (Lens and Medema 2019). Work in yeast showed that lagging chromosomes trapped in the spindle midzone prevent abscission, resulting in cytokinesis failure, via an Aurora kinase signalling pathway. This was named the ‘NoCut’ pathway, and was

shown to function to prevent DNA damage (Norden *et al*. 2006). Aurora B is involved in a similar pathway in mammalian cells (Amaral *et al*. 2016).

1.5.4 Mechanisms of Genome Doubling

Cytokinesis failure results in the formation of a single binucleated daughter cell, which can progress through another cell cycle becoming a mononucleated tetraploid cell. Tetraploidy can also be caused by mitotic slippage, endoreplication, or cell fusion. Improper spindle geometries and kMT attachment errors can lead to SAC-induced mitotic arrest during metaphase and if the cell cannot correct the errors, it can 'slip' through mitosis, reforming a nuclear membrane without dividing chromosomes. The cell re-enters G1 and chromosomes decondense, and the cell becomes tetraploid (Zielke *et al*. 2013). Endoreplication is where cells complete S phase but do not enter mitosis, instead re-entering G1 with a 4N DNA content.

Tetraploidisation provides a 'gene dosage buffer' allowing the accumulation of otherwise deleterious chromosome losses or gains, therefore this phenotype is more likely to be maintained as it is advantageous to CIN positive cancer cells (Dewhurst *et al*. 2014). However, the timing of genome doubling is variable across different human cancers, and classification of the clonality of SCNAs across multiple cancer types showed that a similar number were clonal compared to subclonal, suggesting they frequently arise pre-genome doubling (Watkins *et al*. 2020).

1.6 Chromosome Instability & Pre-Mitotic Errors

1.6.1 Structural CIN

Chromatin bridges, acentric fragments, and chromosome rearrangements are types of CIN classified as 'structural' as they do not involve whole chromosomes (Baudoin and Cimini 2018). These are mostly caused by pre-mitotic errors in G1, S and G2, rather than faults in mitosis itself. Acentric fragments are parts of whole chromosomes that do not contain centromeric DNA, and therefore cannot build a kinetochore during mitosis (Figure 1.6e). MTs cannot attach to acentric fragments

and they often either do not align on a metaphase plate, or do not segregate during anaphase, which can result in micronuclei formation.

Chromatin bridges consist of chromatin from a single sister chromatid, or a pair, that cannot separate, and therefore stretches between each set of daughter chromosomes during anaphase (Figure 1.6f). DNA within a chromatin bridge remains condensed and visible by DAPI staining, however there are also ultra-fine DNA bridges formed of single strands of DNA. Dicentric chromosomes are one mechanism that causes chromatin bridges, as each KT could be pulled in opposite directions if their k fibers originate from opposite spindle poles.

A third type of error, chromosome rearrangements, are caused when DNA double strand break (DSB) repair mechanisms fail, joining fragments from different chromosomes. This can be a very mutagenic event, resulting in the expression of fusion proteins with abnormal functions, and is widespread in cancer (Thompson *et al*. 2010).

1.6.2 Replication Stress & Structural CIN

Replication stress, where DNA polymerase experiences barriers to replication during S phase, and DNA damage, are two of the most common causes of structural CIN. Replication stress results from a depletion of the nucleotide pool, regions of chromosomes with low numbers of replication origins or highly heterochromatic structure, and DNA damage such as inter-strand cross links. When there are non-replicated regions of chromosomes and a cell enters mitosis, the two sister chromatids will be interjoined, causing a chromatin bridge during anaphase (Zeman and Cimprich 2014). These bridges can have different fates; they can persist into the next cell cycle, form micronuclei, or become resolved (Umbreit *et al*. 2020). In mammalian cells, bridges caused by replication stress were shown to activate an Aurora B dependent NoCut pathway, while bridges caused by dicentric chromosomes did not (Amaral *et al*. 2016).

One study identified CIN-suppressor genes that when knocked down, caused replication stress, structural CIN, and numerical CIN in a CIN negative cell line, HCT116. While nucleoside supplementation to relieve replication stress caused

a significant reduction in overall chromosome segregation errors, rescuing the phenotype, it was not clear how this effected specifically numerical CIN (Burrell *et al*. 2013). Another study more recently found that mild replication stress caused premature centriole disengagement in RPE1 cells, generating transient multipolar spindles that caused numerical CIN. Replication stress likely deregulates the cell cycle promoting early centriole disengagement, as partial inhibition of PLK1 (a key regulator of centriole disengagement and duplication) partially rescued the phenotype (Wilhelm *et al*. 2019).

1.6.3 DNA Damage & CIN

DNA damage that is not repaired properly during S/G2 phases of the cell cycle can cause chromosome segregation errors in mitosis, for example, DSBs can lead to acentric fragments. If repair pathways go wrong, then chromosome rearrangements can result in one acentric chromosome and one dicentric chromosome. Crosslinked DNA formed by treatments such as cisplatin can lead to ultra-fine bridges in anaphase, like those formed by incomplete replication or topological entanglement.

In addition to directly causing chromatin bridges and chromosome rearrangements, DSBs have been identified to induce numerical CIN (Bakhoum *et al*. 2014; Bakhoum *et al*. 2015), through an indirect mechanism. During mitosis DSB repair mechanisms are downregulated, due to the difficulty of repair on condensed chromosomes, and the break is instead repaired in the following cell cycle. There is still some DNA damage response (DDR) signalling however, and activation of CHK2 and ATM has been shown to have a downstream effect on MT dynamics, through phosphorylation and activation of Aurora Kinase A and PLK1 (Bakhoum *et al*. 2014). PLK1 has been shown to increase kMT attachment stability during prometaphase (Liu *et al*. 2012), which reduces the rate of correction of erroneous attachments, increasing the likelihood of merotelic KTs at anaphase.

1.6.4 Mitotic Catastrophe

Large scale chromosome segregation errors or DNA damage can lead to mitotic catastrophe, a form of cell death during or just after mitosis. This is commonly caused by a failure of cell cycle checkpoints, or after a prolonged mitotic arrest. Failure of the G2/M checkpoints allows entry into mitosis with damaged DNA, and combined with failure of the spindle assembly checkpoint, results in severe errors in mitosis that generate inviable daughter cells. Mitotic catastrophe results in cell death through the same biochemical pathways as apoptosis, however it can proceed via two mechanisms: during metaphase, or once the cell has completed mitosis (Castedo *et al*. 2004a).

In metaphase, mitotic catastrophe can induce cell death via activation of caspase-2 through ATR and ATM signalling, in response to DNA damage (Sidi *et al*. 2008). Caspase-2 activation is independent of p53, and activates matrix metalloproteinases which go on to activate the general caspase cascade observed in standard apoptosis (Castedo *et al*. 2004b). When cells undergo this type of mitotic catastrophe, they often show chromatin condensation before the completion of mitosis, which can be observed under a microscope as a dense mass of DNA that brightens and shrivels, often while the cell detaches from the cover slip.

Conversely, if mitotic catastrophe occurs due to chromosome segregation errors, cells will complete mitosis before undergoing apoptosis in a p53-dependent manner. This has been referred to as the polyploidy checkpoint, where activation of p53 in response to chromosome segregation errors is employed to suppress the proliferation of aneuploid cells (Castedo *et al*. 2004a). This type of mitotic catastrophe is characterised by p53 induction of the caspase cascade after a period of G1 cell cycle arrest.

1.7 Aneuploidy

Aneuploidy is the consequence of CIN, referring to an abnormal number of chromosomes in cells. Whereas CIN refers to a dynamic phenotype cells experience over continual divisions, aneuploid cells can maintain a stable karyotype over time, such as trisomy 21 that is maintained in individuals with downs syndrome.

1.7.1 Aneuploidy in Cancer

Aneuploidy is widespread in cancer however the relationship is complex, with chromosome losses or gains having both tumour suppressive and proliferative effects. These are dependent on cellular context, for example, the stage of tumourigenesis, and microenvironmental conditions. In advanced cancers aneuploidy and ongoing CIN provide tumour cells a mechanism to rapidly alter their genome, allowing beneficial phenotypes to be selected which, for example, confer drug resistance, or have metastatic potential. In patients, metastatic tumours often show a higher degree of aneuploidy compared to the primary tumour, and aneuploidy is correlated with poor prognosis in various cancer types (Kheir *et al*. 1988; Stopsack *et al*. 2019).

In some cancers there are specific aneuploidies that occur at high frequencies among patients, suggesting the genes they contain play a direct role in tumourigenesis. For example, one study found amplification of the chromosome arm 3q by around 3-15 copies in 94% of lung squamous cell carcinoma (SCC), and 20% of lung adenocarcinoma samples (Björkqvist *et al*. 1998). Various driver genes are located in this chromosomal region, including *SOX2* and *PIK3CA*, as well as the CIN-associated gene *ECT2*. Multi-region sequencing of lung cancers revealed that 3q amplification was often a clonal event, indicating that it happened early on during tumour evolution, and that it could play a role in initiating transformation (Jamal-Hanjani *et al*. 2017). Investigation of pre-cancerous lesions revealed a similar prevalence of this alteration, further supporting its role in tumourigenesis (Teixeira *et al*. 2019). Among these pre-cancerous lesions, those that progressed to invasive cancer exhibited a higher somatic copy number amplification (SCNA) burden, and a CIN gene expression signature, suggesting these are important processes for transformation. More research is required to understand the link between 3q amplification and CIN, the differential prevalence of this amplification in lung SCC vs lung adenocarcinoma, and how it contributes to tumourigenesis within a pre-cancerous lesion.

1.7.2 Context Dependence of Aneuploidy

In most systems aneuploidy confers a reduction in cell fitness, slowing proliferation due to cell cycle defects and proteotoxic stress. However, when cells are grown under certain conditions of stress, aneuploidy can provide a survival benefit. One study generated MEF cell lines trisomic for particular chromosomes and found these all grew poorly compared to their euploid control lines *in vitro*. Inhibition of p53 in these cell lines induced some cancer-like phenotypes in the euploid lines such as loss of contact inhibition, however the aneuploid lines remained normal and still grew poorly (Sheltzer *et al*. 2017). The same results were observed in HCT116 cell lines engineered to contain specific trisomies/tetrasomies. These results were confirmed in another study investigating DLD1 cells lines (cancerous, pseudodiploid phenotype with microsatellite instability) with an extra copy of chromosome 7 or 13, where the trisomic cell lines grew slower in normal conditions compared to the parental cell line. However, when grown in serum-free medium, 5-fluorouracil, or hypoxic conditions, the trisomic cell lines grew significantly better (Rutledge *et al*. 2016). These data suggest that aneuploidy is utilized in cancer cells to rapidly adapt and confer a survival advantage in response to changing environmental conditions.

Nonetheless, aneuploidies have been identified in pre-cancerous lesions in multiple tissue types, suggesting this can be an early event during tumorigenesis, alongside CIN. It is not well understood, however, how CIN is initiated in pre-cancerous lesions. Studies in mice show that perturbation of various mitotic genes can initiate CIN, and subsequently tumorigenesis (Schvartzman *et al*. 2010). While mutation of mitotic checkpoint genes and key factors involved in mitosis is rare in cancer, a favoured hypothesis is that their deregulation and in particular overexpression causes CIN initiation and aneuploidy. This has been difficult to investigate, however, as matched controls of normal tissue for comparison of gene expression levels are hard to obtain, and thus evidence for this theory is limited.

1.7.3 Tolerance of Aneuploidy

In the later stages of tumorigenesis aneuploidy becomes increasingly more prevalent, as tumours acquire the means to tolerate the cytotoxic effects of aneuploidy. For example, whole genome doubling acts to buffer the effects of

whole chromosome losses and gains (López *et al*. 2020). Firstly, it protects against loss of heterozygosity, which could have deleterious effects if a gene exhibits haploinsufficiency. Secondly, it protects against the proteotoxic effects of aneuploidy, as there are smaller changes in stoichiometries when chromosomes are lost or gained in a tetraploid background compared to diploid. In support of this, tetraploid colorectal cancer cell lines were found to possess a higher variance in chromosome number compared to their diploid counterparts (Dewhurst *et al*. 2014). Other mechanisms include evasion of the immune response to aneuploidy (Wang *et al*. 2020), and dysfunction of BCL9L and aneuploidy induced apoptosis (López-García *et al*. 2017).

Genome doubling itself however is a toxic phenotype to cells, that must be tolerated (Quinton *et al*. 2021). One study found that expression of oncogenic *PIK3CA* harbouring the activating H1047R point mutation provided tolerance to genome doubling in MEFs. When diploid MEFs were treated with DCB to induce binucleation, the proportion of $PIK3CA^{H1047R}$ cells that divided was much higher than WT, suggesting $PIK3CA^{H1047R}$ cells can overcome a G1 cell cycle block experienced in response to supernumerary centrosomes and/or tetraploidy. *PIK3CA* mutations in breast cancers and NSCLC are often clonal events that precede whole genome doubling, further supporting this hypothesis (Berenjeno *et al*. 2017). *In silico* modelling has demonstrated that cancer cells that undergo whole genome doubling will often evolve towards a triploid state, which increases the cellular fitness compared with compared to cells that undergo genome doubling. This state was shown to balance the fitness cost of aneuploidy with the beneficial gain of oncogenes and loss of tumour suppressors associated with chromosome gains and losses (Laughney *et al*. 2015).

CIN, tetraploidization, and aneuploidy have all been found to increase the propagation of these same errors. For example, trisomic DLD1 cell lines were shown to undergo tetraploidization at higher rates than euploid controls, suggesting that this phenotype is selected for and provides a growth advantage to aneuploid cells (Nicholson *et al*. 2015). Despite the growth disadvantage experienced by HCT116 cells with trisomy 3/5 and tetrasomy 5, after several passages the growth rates of some of the aneuploid cell lines reached that of the euploid cell lines. Sequencing of these clones revealed they had acquired

multiple chromosome abnormalities, which had subsequently been selected for as they provided increased tolerance to the aneuploid phenotype compared to the initial karyotype (Sheltzer *et al*. 2017).

One study performed a genome wide siRNA screen for genes that increased tolerance of CIN using a readout of cell proliferation (Sansregret *et al*. 2017). Cells were treated with reversine to induce chromosome segregation errors, and hit genes were identified that increased survival compared to control. This work identified that partial knockdown of the APC/C component CDC16 impairs APC/C function, reducing the rate of segregation errors and conferring CIN tolerance by increasing mitotic duration.

1.7.4 Immune Recognition of Aneuploid Cells

Under normal conditions in healthy tissue, aneuploid cells are destroyed by the immune system, a mechanism that has likely evolved to suppress tumourigenesis during the early stages of cellular transformation. In a co-culture system, aneuploid RPE1 cells generated by MPS1 inhibition were destroyed by natural killer cells (Santaguida *et al*. 2017). In more developed cancers, bioinformatic analysis showed that tumours with a higher degree of aneuploidy had less infiltrating cytotoxic immune cells, suggesting that immune evasion is another factor required for tolerance of aneuploidy (Davoli *et al*. 2017). Cells also have a pathway for sensing cytosolic DNA, such as MN, and triggering an immune response. The cyclic GMP-AMP synthase (cGAS) localises to MN and produces cyclic GMP-AMP, which binds to and activates stimulator of interferon genes (STING). STING in turn induces production of type I interferon, causing an inflammatory response to destroy the cell. This pathway promotes the killing of cells infected with intracellular pathogens, however the finding that it is also activated by MN establishes its importance in cancer prevention (Mackenzie *et al*. 2017).

1.7.5 CIN, Aneuploidy, & p53

CIN and aneuploidy are tightly regulated by p53; p53 is the only gene mutated significantly more frequently in CIN^+ tumours and cell lines compared to CIN^-

(Burrell *et al*. 2013). It is well established that structural CIN and mutagenic events such as chromothripsis activate a p53 response through classical DNA damage response signalling (Soto *et al*. 2017). DNA within micronuclei is also more likely to become damaged and elicit a p53 response, as it is susceptible to replication stress and improper KT assembly (Soto *et al*. 2018). Large scale chromosome changes cause cellular stress that activates the p38 stress response kinase, resulting in a p53-dependent G1 arrest (Simões-Sousa *et al*. 2018). However, recent work has demonstrated that the response to smaller changes in whole chromosome number is more complex.

One study using HCT116 and RPE1 cells found robust p53 responses after chromosome mis-segregation was induced by monastrol treatment or MCAK depletion, resulting in around a third of cells mis-segregating one or more chromosomes (Thompson and Compton 2010). However, more recently a combination of an MPS1 inhibitor to block the SAC and a CENPE inhibitor to generate polar chromosomes was used to generate aneuploidy, without causing a mitotic arrest. This method resulted in a subset of cells developing micronuclei, and these were used to select cells positive for aneuploidy (Soto *et al*. 2017). Long term live imaging of these cells revealed that >40% were able to undergo a second mitosis, despite >80% of cells being aneuploid, demonstrating that aneuploidy does not always lead to p53 activation. These mis-segregation events that do activate p53 could be more dangerous in the early stages of tumorigenesis, while in the later stages once the tumour has evolved to tolerate aneuploidy through immune evasion and loss of p53, larger scale mis-segregation events become more dangerous.

In the context of cancer, it is unclear whether loss of p53 alone is sufficient to induce tolerance of CIN/aneuploidy; some studies report increased proliferation of aneuploid cells upon p53 loss (Thompson and Compton 2010; Soto *et al*. 2017), while others do not (Sheltzer *et al*. 2017). It is likely that multiple factors are involved which the cancer cell acquires over time, and as such it can tolerate increasing levels of aneuploidy. For example, early/clonal loss of *TP53* (Jamal-Hanjani *et al*. 2017) may allow for low levels of CIN, followed by increased immune evasion, followed by modification of the microenvironment in the later stages of tumourigenesis (e.g. hypoxia).

1.7.6 Screening for CIN/Aneuploidy

Given the importance of aneuploidy and CIN in cancer, there have been many efforts to design screens that identify either causative genes or genes involved in tolerance to aneuploidy. Due to the vast number of genetic abnormalities in cancer it has been difficult to elucidate the function of individual genes in these processes, hence these studies employed chromosomally stable experimental systems combined with RNAi or overexpression libraries.

Various methods have been developed to assay for CIN and aneuploidy, as manually identifying mitotic cells and then classifying chromosome segregation errors is a time-consuming process, meaning limited n numbers. Early methods employed the Lac operon to label single chromosomes, introducing an array of LacO repeats into a specific chromosome where GFP tagged Lac repressor binds, generating a focus in live cells (Straight *et al*. 1996). In fixed cells, FISH has been used to provide information on multiple chromosomes simultaneously (Godek and Compton 2018). An adaptation of this method uses DCB to inhibit cytokinesis, generating binucleated cells where the two daughter nuclei can be identified, showing the phenotypes of both daughter cells after erroneous chromosome segregation (Fenech 2007).

Another tool used to measure CIN is the human artificial chromosome (HAC), which has a functional centromere and is replicated and segregated similar to endogenous human chromosomes. By constitutively expressing GFP, cells that mis-segregate and lose the HAC can be easily identified by FACS. However, HACs were found to be 10-fold more likely to be lost than endogenous chromosomes, and more likely to be lost as lagging chromosomes rather than through nondisjunction. This system therefore may be susceptible to false positives and bias when used to screen for CIN/aneuploidy. One study employed the HAC system to investigate the frequency at which cells experienced chromosome segregation errors in response to 9 anti-mitotic drugs, demonstrating its ability to identify conditions that give rise to CIN/aneuploidy (Lee *et al*. 2013). Another utilized it to perform an siRNA screen for human

kinases important for faithful chromosome segregation, alongside high-content imaging and automated image analysis (Liskovykh *et al*. 2019).

Recently, a method combining imaging flow cytometry and FISH was used to analyse the karyotype of individual chromosomes (Worrall *et al*. 2018). This method was advantageous in that the cells are not perturbed in any way, centromeres can be automatically counted, and thousands of cells can be analysed in one experiment. However, only two different chromosomes can be analysed at one time, and not all human chromosomes have unique sequences within the centromeric DNA for targeting of FISH probes.

One of the largest screening efforts for mitotic regulators was performed by the Mitocheck consortium (Neumann *et al*. 2010). Genome-wide siRNA knockdowns were performed, and cells were imaged for 2 days with fluorescently labelled DNA. This revealed regulators of mitosis, migration, and survival. The time-lapse data was fed into an image analysis pipeline that used machine learning to segment and classify the cells based on the nuclear morphology, identifying polylobed, binucleated and mis-shapen nuclei, and nuclei in different mitotic stages. This screen identified phenotypes such as increased cell death upon TPX2 and CENPE knockdown, but in terms of chromosome segregation errors, the ML algorithm was only able to identify extreme cases that resulted in many micronuclei. Information regarding more subtle phenotypes where mis-segregated chromosomes either formed very few or no MN were therefore lost.

1.8 PIK3CA Signalling

1.8.1 Overview of the PIK3CA Pathway

Phosphatidylinositol 3-kinases (PI3K) are a family of lipid kinases activated by mitogenic signalling at the plasma membrane, where they convert phosphatidylinositol 4,5-bisphosphate (PIP_2) to phosphatidylinositol 3,4,5-trisphosphate (PIP_3). There are various types of PI3Ks, of which the catalytic subunit alpha (PIK3CA, also known as p110α) has a well-established role in cancer. PIK3CA dimerises with a regulatory subunit p85, that interacts with the adaptor protein IRS1 at receptors (Figure 1.7a). PIP_3 functions as a docking site

for protein kinase B (AKT), which upon binding is phosphorylated by mTORC2 and PKD1, before being released back into the cytosol to phosphorylate downstream targets. AKT has many substrates which are often involved in promoting cell survival and proliferation, including mTORC1 which promotes protein synthesis, and MYC which induces transcriptional changes. Glycogen synthase kinase 3 (GSK3) is an AKT substrate inhibited by phosphorylation, causing metabolic reprogramming in response to growth factors, promoting glycolysis. The PI3K pathway is negatively regulated by the phosphatase PTEN, which converts PIP_3 back to PIP_2, and through feedback loops such as negative

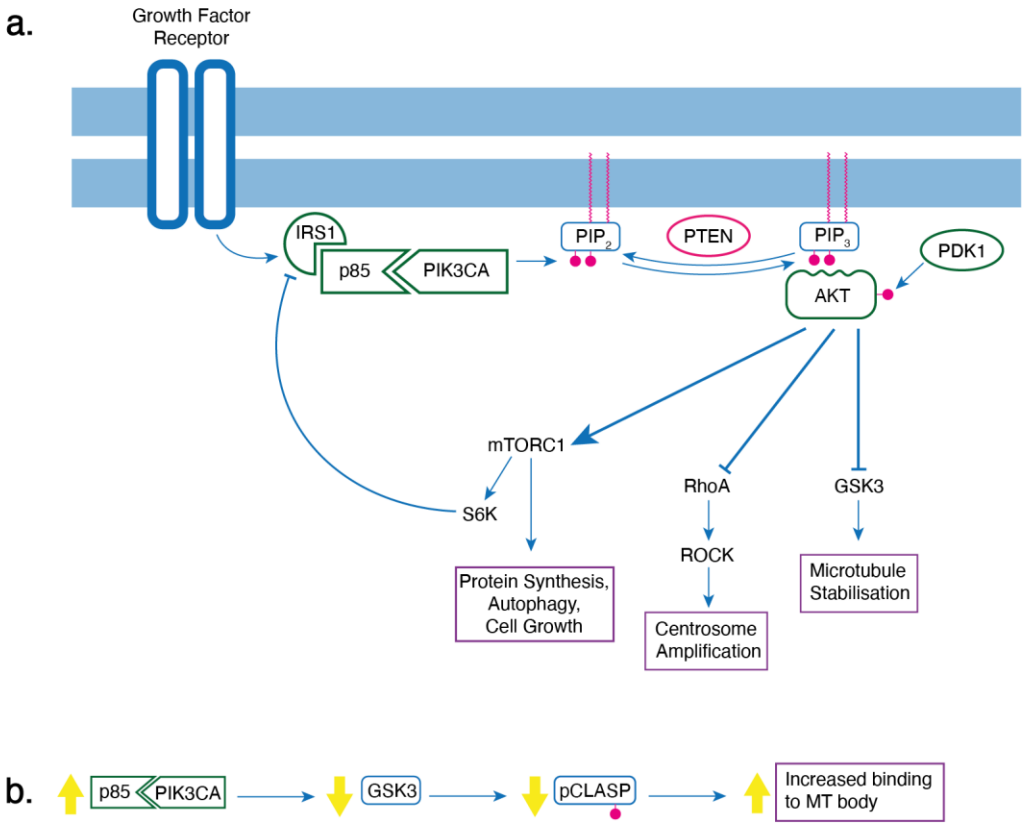

Figure 1.7 PIK3CA Signalling Pathway and Downstream Processes a. Upon activation of receptor tyrosine kinases, such as the insulin growth factor receptor, PIK3CA/p85 is recruited to the plasma membran via the adaptor protein IRS1. PIK3CA converts phosphatidylinositol 4,5-bisphosphate (PIP_2) to phosphatidylinositol 3,4,5-trisphosphate (PIP_3). AKT is recruited to PIP_3 and phsophorylated by phosphoinositide-dependent kinase 1 (PDK1), and then goes on to phosphorylate various downstream effectors. GSK3 has been demonstrated to modulate microtubule stability, while ROCK plays a role in centrosome amplification. **b.** Model of PIK3CA pathway regulation of CLASP activity. Increased PIK3CA signalling reduces GSK3 activity, reducing GSK3-mediated phosphorylation of CLASPs, increasing their affinity for binding to the body of MTs (as opposed to the plus tip).

regulation of IRS1 by the p90 ribosomal S6 kinase (S6K; Figure 1.7a; Hoxhaj and Manning 2020).

The regulatory subunit p85 is multifunctional, having both positive and negative effects on PIK3CA activation. Dimerisation of PIK3CA with p85 enhances its stability, preventing degradation. P85 is also required for recruitment and activation of PIK3CA at the plasma membrane in response to growth factor receptor activation, through its interaction with the adaptor protein IRS1. However, monomeric p85 also competes and binds to this adaptor protein, negatively regulating the pathway. Cells finely tune p85 expression to ensure these positive and negative regulatory effects are sufficiently balanced. (Luo and Cantley 2005).

1.8.2 PIK3CA Pathway Alterations in Cancer

The PIK3CA pathway is the most frequently altered pathway in cancer, where it is modulated to suit the metabolic needs of rapidly dividing cancer cells. Alterations manifest as activating point mutations in the catalytic p110α subunit, amplification of WT or activated *PIK3CA*, loss of *PTEN*, and upregulation of pAKT. Based on TCGA data from cBioPortal, amplification events involve the WT allele over 75% of the time, while the remaining cases involve amplification of a mutant allele. One study found that the majority of alterations were mutually exclusive is gastric and colorectal cancers (Chong *et al*. 2014). Another study showed that PIK3CA activating mutations alone are weakly oncogenic in mice, however, but when combined with other alterations such as *PTEN* loss, will sufficiently drive tumourigenesis (Kinross *et al*. 2012). In lung SCC, *PIK3CA* is commonly amplified via 3q gain, where it is co-amplified with *SOX2*, a direct target of AKT. Together *PIK3CA* and *SOX2* amplification promote a squamous injury response in lung SCC precursor cells (basal cells, a stem cell lineage), which is likely a protumourigenic event in the majority of lung SCC patients (Kim *et al*. 2016).

The most common point mutations are at residues E545 and H1047, in the helical and kinase domains of PIK3CA, respectively. E545 is substituted to an amino acid with the opposite charge (often lysine) which disrupts interaction of the regulatory subunit p85 with the helical domain. This relieves an inhibitory interaction with the activation loop of PIK3CA, allowing it to adopt an active

conformation (Leontiadou *et al*. 2018). In contrast, H1047 mutations do not affect the interaction with p85. Mutations at H1047 also affect the activation loop, but do not disrupt interactions with p85. Switching the residue to arginine at position 1047 results in a conformational change in two loops that mediate interactions with plasma membrane lipids, promoting recruitment of PIK3CA and generation of PIP_3 in the absence of growth factor receptor activation. (Mandelker *et al*. 2009).

1.8.3 PIK3CA Signalling & Mitosis

PIK3CA mutations were found to occur before genome doubling, with a tendency to show mutual exclusivity with *TP53* loss. Given that *TP53* loss provides tolerance to genome doubling and CIN, this suggests PIK3CA pathway signalling could be an alternative tolerance mechanism. One study demonstrated this *in vivo*, showing that MEFs conditionally expressing $PIK3CA^{H1047R}$ showed higher proportions of tetraploid and aneuploid chromosome counts at 3 and 5 days after induction of expression (Berenjeno *et al*. 2017). No defects were observed in cytokinesis failure, and therefore it was determined that $PIK3CA^{H1047R}$ expression promoted survival of tetraploid cells that are formed stochastically.

Expression of $PIK3CA^{H1047R}$ in MEFs was also shown to cause centrosome amplification. This finding was backed up by observation of supernumerary centrosomes in MCF10A overexpressing $PIK3CA^{H1047R}$, $PIK3CA^{E545K}$, and WT *PIK3CA*, as well as in fibroblasts from a patient with a human overgrowth syndrome caused by $PIK3CA^{H1047R}$. To confirm this phenotype was due to amplification, centrosomes were counted in MEFs that were serum starved and arrested in G1, before $PIK3CA^{H1047R}$ expression induced. This experiment showed that supernumerary centrosomes appeared between 20-25 hours after induction, when cells had entered S phase following cell cycle arrest. This data demonstrates that $PIK3CA^{H1047R}$ deregulates centrosome duplication, as it is known to occur alongside DNA replication. Treatment with inhibitors of AKT or Rho-associated coiled-coil kinase (ROCK) during this period identified that centrosome amplification was dependent on both these signalling pathways. ROCK also promotes transformation of primary MEFs upon expression of $PIK3CA^{H1047R}$. (Berenjeno *et al*. 2017).

Another study demonstrated centrosome amplification in HCT116 upon expression of constitutively active Met kinase, which was dependent on AKT, as AKT inhibitors and siRNA knockdown caused a full or partial rescue, respectively (Nam 2010). In this system, aneuploidy was only observed after Met-induced centrosome amplification in $p53^{-/-}$ cells, suggesting that PI3K pathway activation alone is not sufficient to induce or provide tolerance to aneuploidy/CIN.

Oncogenic PIK3CA was also shown to promote centrosome clustering in cells with supernumerary centrosomes, forming a pseudobipolar spindle where one or more pole contained two or more centrosomes. Of the cells with extra centrosomes, 94% of *PIK3CA*^{H1047R} cells were able to exit mitosis, compared to 65% of WT cells. The tolerance to tetraploidy in *PIK3CA*^{H1047R} cells was therefore attributed to the ability to cluster supernumerary centrosomes. Interestingly, despite centrosome amplification, *PIK3CA*^{H1047R} cells did not exhibit increased chromosome segregation errors. Analysis of fixed cells revealed a lower incidence of multipolar spindles, suggesting that *PIK3CA*^{H1047R} reduces the number of multipolar intermediates experienced, reducing the likelihood of erroneous kMT attachments that could lead to segregation errors. (Berenjeno *et al*. 2017).

1.8.4 PIK3CA Signalling & MT Dynamics

Dynamic growth and shrinkage of MTs is essential in both mitosis and cell migration, contributing to the remodelling of the cytoskeleton to form the mitotic spindle or cell membrane protrusions such as lamella, respectively. The PI3K pathway has an established role in cell migration, promoting polarization of cells in response to chemokines (such as platelet derived growth factor (PDGF), insulin). This generates a leading edge and a rear edge. At the leading edge PIK3CA activates the Rac GTPase, which promotes actin filament assembly and lamella/lamellapodium formation (Rappel and Edelstein-Keshet 2017). Actin filaments promote protrusion of lamella/lamellipodia and MTs allow the transport of cellular cargo, while at the rear edge MTs in combination with myosin cause contraction of the cytoskeleton, promoting directionality (Ganguly *et al*. 2012).

One study using NIH 3T3 fibroblasts showed that PI3K signalling regulated MT stability at the leading edge (Onishi *et al*. 2007). PDGF stimulation of cells increased the stability of MTs at the leading edge, dependent on PIK3CA and AKT signalling. The mechanism by which MT stabilization is achieved is unclear, however inhibition of GSK3 but not mTOR was shown to induce the phenotype.

1.8.5 PIK3CA Signalling & CLASPs

PIK3CA signalling has been implicated in the regulation of CLASP activity. CLASPs regulate the dynamics of kMTs during mitosis, as well as cytoplasmic MTs involved in cell migration. CLASPs are well conserved across different species, with a KT-binding domain and a separate unstructured region with phosphorylation sites that regulate its interaction with EB1 and MT plus ends (Kumar *et al*. 2012). CLASP1 has a major function in mitosis; antibody ablation of CLASP1 causes monopolar spindles with short MTs, that do not exhibit dynamic behavior (Maiato *et al*. 2003a; Maiato *et al*. 2003b). In comparison, while the paralogue CLASP2 shows a similar localization in mitosis, knockout cells can progress through mitosis normally, albeit with higher rates of spindle defects and lagging chromosomes. Overexpression of either CLASP1 or CLASP2 partially rescues these defects, suggesting a degree of redundancy in their functions (Pereira *et al*. 2006). Both CLASPs also bind to EB1 at cytoplasmic MT plus ends at the leading edge of the cell, where they stabilize MTs and reduce catastrophe rates (Akhmanova *et al*. 2001).

CLASP association with MTs was assessed in PTK1 cells, which form lamella containing MT lattices when migrating. While in the cell body and during mitosis CLASPs localize to the plus tips of MTs, in lamella they also localize to the body of the MT. It has been shown that CLASP function is regulated by the GSK3β kinase, which is involved in determining their MT affinity within different subcellular locations. In PTK1 cells expressing a constitutively active variant of GSK3β, CLASP binding to MT lattices within lamella was completely abolished, and plus end tracking within the cell body was reduced. The data from this study fits a model where GSK3β directly phosphorylates CLASPs and modulates their affinity for MTs; inhibition of GSK3β, perhaps by PIK3CA signalling, results in

increased binding of CLASPs to lattice MTs within the lamella (Figure 1.7b; Wittmann and Waterman-Storer 2005).

In further support of the regulation of CLASP activity by the PIK3CA pathway, CLASP2 relocalisation to the leading edge was observed upon serum stimulation. PIK3CA inhibitors reduced the level of CLASP2 relocalisation upon serum stimulation (Akhmanova *et al*. 2001). Considering it is known that PIK3CA activation results in GSK3 inhibition, these data suggest that the PI3K pathway could regulate phosphorylation of CLASPs, increasing their affinity for MTs. This is consistent with the observation that GSK3 inhibition increased MT stability at the leading edge in NIH 3T3 fibroblasts (Onishi *et al*. 2007), and the role of CLASPs in stabilising MTs.

Regulation of the mitotic function of CLASPs by GSK3 has also been observed, but its effects are not well understood. In mitosis, CLASP2 phosphorylation is mediated by CDK1 and PLK1; CDK1 phosphorylation on S1234 promoted recruitment of PLK1, which further phosphorylated CLASP2 and increased binding at KTs. This phosphorylation was essential for maintenance of a bipolar spindle; expression of a non-phosphorylatable mutant caused spindles to collapse to monopolar (Maia *et al*. 2012). Interestingly, one study found that *in vitro* phosphorylation of a CLASP2 peptide (residues 497 – 794, containing only the EB1 binding domain), by cyclin B/CDK1 was a priming event for phosphorylation by GSK3β, indicating that there could be a functional interplay between different kinases *in vivo* (Kumar *et al*. 2012). CLASP2 phosphorylation by GSK3β prevents its interaction with EB1 at the plus tip of MTs, and may instead be important for anchoring CLASP2 at the KT.

1.9 Aims of the Project

The first aim of this project was to design a screen to measure numerical chromosome instability and aneuploidy in monolayer cells cultured *in vitro*. The project aimed to develop a methodology that was sensitive to low levels of CIN, easy to perform and higher throughput than current methods, and applicable to a wide range of experimental hypotheses.

The second aim was to implement the methodology developed to investigate whether upregulation of specific genes can cause CIN and aneuploidy in RPE1 cells. A gene list was collated based on pre-existing knowledge of alterations that occur early during tumourigenesis and may therefore initiate CIN. This included genes involved in SCNAs (Jamal-Hanjani *et al*. 2017), genes identified to be upregulated at the protein level through microarray profiling (Teixeira *et al*. 2019), and some mitotic genes that are frequently upregulated in cancer.

The third aim was to follow up on any hits identified during the screening processes, employing high spatiotemporal imaging techniques to determine the mechanism by which CIN is caused. This project focussed on identifying mechanisms that led to numerical CIN, rather than structural CIN.

The final aim was to investigate the role of PIK3CA pathway activation during the early stages of tumourigenesis, given the body of evidence demonstrating the prevalence of this alteration in many cancer types. This project aimed to utilise various models to investigate the impact of upregulation of WT and mutated PIK3CA on mitotic processes.

Chapter 2: Materials & Methods

2.1 Cell Culture

RPE1 cells were obtained from ATCC and maintained in Dulbeccos's Modified Eagle Medium F12 (DMEM/F12, Sigma), supplemented with fetal bovine serum to a final concentration of 10% (Sigma), 2 mM L-glutamine (Gibco), and 1X Penicillin/Streptomycin (Gibco). HEK293FT cells were obtained from Thermofisher and maintained in DMEM (high glucose, pyruvate), supplemented with fetal bovine serum to a final concentration of 10%, 2mM L-glutamine, 1X Penicillin/Streptomycin, 0.1 mM MEM Non-Essential Amino Acids, and 0.5 mg/ml Geneticin. MCF10A cells were obtained from ATCC and maintained in DMEM/F12 supplemented with horse serum to a final concentration of 5%, 20 ng/ml EGF (Peprotech), 0.5 mg/ml Hydrocorticone (Sigma), 100 ng/ml Cholera Toxin (Sigma), 10 μg/ml Insulin (Sigma), and 1X Penicillin/Streptomycin.

2.2 Transfections & Transductions

2.2.1 siRNA Transfections

Forward transfections were performed by seeding $2x10^5$ cells the day before transfection. The following day, transfection mixes were prepared: 2.5 μl siRNA (10 μM) diluted in 125 μl opti-mem (Gibco), and 9 μl RNAiMAX diluted in 125 μl opti-mem (Thermo Fisher Scientific). After 5 minutes, the two mixtures were combined, incubated at room temperature for 15 minutes, and added to cells dropwise. After 7 hours the medium was removed, and fresh medium added.

Reverse transfections were performed by firstly preparing the transfection mixes: 12.5 μl siRNA (1 μM) diluted in 100 μl opti-mem combined, and 2.7 μl RNAiMAX diluted in 100 μl opti-mem. After 5 minutes, the two mixtures were combined, incubated at room temperature for 15 minutes, and added to an empty well dropwise. $5x10^5$ cells were then added to each well in 1 ml of medium. After 16 hours the medium was removed, and fresh medium added.

2.2.2 Virus Production

Virus production was performed using HEK293FT cells below passage 16, according to the ViraPower Lentiviral Expression Systems protocol (Thermofisher). $5x10^5$ cells were seeded in 10 cm tissue culture dishes the day before transfection. The following day, transfection mixes were prepared: 9 μg ViraPower packaging mix and 3 μg pLenti expression plasmid diluted in 1.5 ml opti-mem, and 36 μl Lipofectamine 2000 diluted in 1.5 ml opti-mem. After 5 minutes, the two mixtures were combined, incubated at room temperature for 20 minutes, and added to cells dropwise. After 16 hours the medium was removed, and fresh medium added. This protocol was also used in a scaled-down format for producing smaller lentiviral stocks using 1.9 cm tissue culture dishes.

2.2.3 Transduction

On the day before transduction cells were seeded in 6-well plates such that they reach 30-50% at the time of transduction. The following day, transduction mixes were prepared: the desired number of infectious units (IFU) of lentivirus were diluted in 1 ml complete medium, containing polybrene (Thermofisher) at a final concentration of 6 ug/ml. Culture medium was removed for each well, and replaced with 1 ml of the transduction mix. After 24 hours, the medium was removed, and fresh medium added.

2.2.4 Virus Titering

Lentiviral titers were initially calculated using a colony formation assay, and quantification of a fluorescent marker (H2B-mRFP), Figure 2.1a. Transduction mixes consisting of a 10 fold serial dilution ranging from 10^{-1} to 10^{-5} were prepared. For the colony formation assay, cells were trypsinized and seeded at

A.

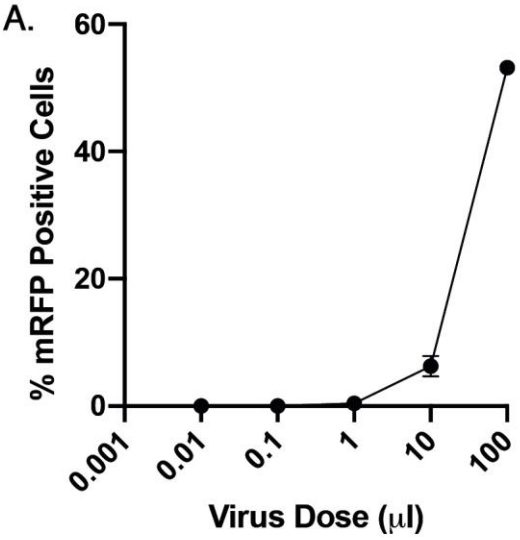

B.

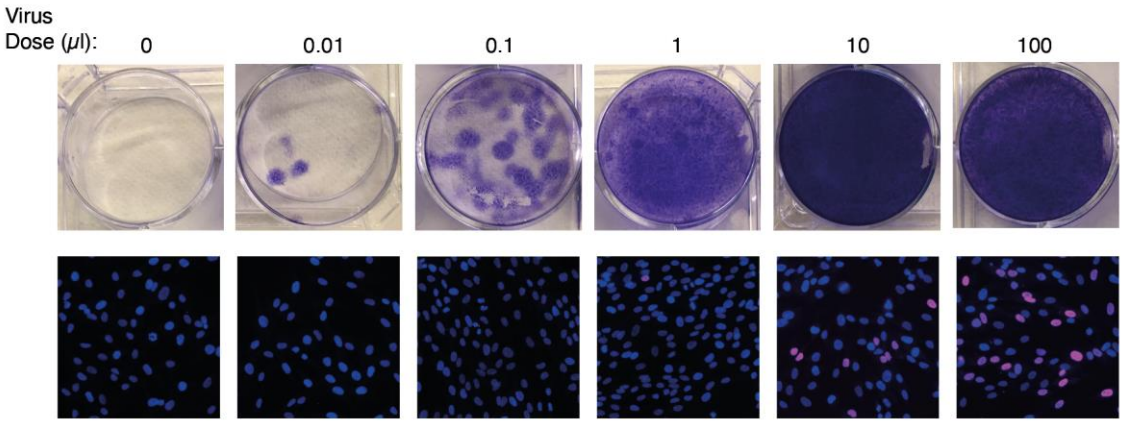

C.

Construct	Fluorescence Titer (IFU/ml)	Colony Formation Titer (IFU/ml)	Lenti-X Go Stix Value
pLVX-CMV-H2B-mRFP	1.52×10^6	1.39×10^6	2516

Figure 2.1 Virus Titering Using Colony Formation and Fluorescence Measurements **A.** The percentage of H2B-mRPF positive cells after transduction with virus at varying concentrations of IFU/ml. **B.** Example images showing crystal violet staining of colonies (top panel), and identification of H2B-mRFP positive cells using microscopy (bottom panel). **C.** Table detailing the titers calculated for each different method, and the Lenti-X Go Stix Value that these relate to. N = 2.

a 1:4 dilution 48 hours post-transduction. The following day, selection media containing 0.5 mg/ml geneticin was added to each well. Selection media was changed every 2-3 days. After 12 days, each well was fixed and staining with crystal violet to visualise colonies, Figure 2.1b. For fluorescence quantification, cells were trypsinized and seeded on cover slips 48 hours post-transduction. The following day, cells were fixed and DAPI stained, Figure 2.1b. Images were analysed using a nuclei quantification macro on FIJI.

Once a titer was confirmed using these methods for the H2B-mRFP lentivirus, it was also measured using Lenti-X GoStix (Takara Bio), which provide a quantitative value calculated from the amount of p24 present in the viral supernatant. H2B-mRFP lentivirus was used as a reference virus to relate the GoStix value to an IFU/ml value, Figure 2.1c, such that an IFU/ml measurement for other viral stocks could be obtained using solely the Lenti-X GoStix method.

2.3 CRISPR Activation

To perform CRISPR gene activation using the SAM system (Konermann *et al*. 2015), a stable cell line was generated expressing pLenti-MPH. The pLenti-SAM construct expressing the dCas9 and gRNA was transduced into the MPH cell line, and gene expression was measured by qPCR or western blotting at least 48 hours post-transduction.

2.4 RT-qPCR

Extraction of RNA was performed using Qiagen RNeasy kits (mini or micro, sample size dependant), with on-column digestion of DNA using the Qiagen DNase kit. RNA concentration was quantified using a NanoDrop (Thermo Fisher Scientific). cDNA synthesis was performed with 500 ng RNA, using SuperScript IV VILO Master Mix according to manufacturer instructions (Thermo Fisher Scientific). qPCR was performed according to manufacturer instructions using Power SYBR Green Master Mix (Applied Biosystems), Quantitect primers specific to the target gene (Qiagen), and 1 μl cDNA as a template. Experiments were performed in an Eppendorf Realplex 4 thermocycler. The ΔΔCT method was used to quantify relative gene expression levels, normalised to the house-keeping gene GAPDH.

2.5 Western Blotting

Cat#	*Supplier*	*Reported Target*	*Host*	*WB Dilution*	*IF Dilution*
32-2500	ThermoFisher Scientific	α-Tubulin	Mouse	1:5000	1:500

ab52866	Abcam	α-Tubulin	Rabbit		1:500
ab13939	Abcam	CENPA	Mouse		1:200
15-234-0001	Antibodies Incorporated	CREST	Human		1:300
ab4448	Abcam	Pericentrin	Rabbit		1:2000
NB500-181	Novus Biologicals	KIF11	Rabbit	1:1000	1:1000
ab172620	Abcam	KIFC1	Rabbit	1:1000	
MAB1618	Sigma Aldrich	DIC	Mouse	1:1000	
MA1-202	ThermoFisher Scientific	Cas9	Mouse	1:1000	
48818S	Cell Signalling Technologies	P53	Mouse	1:1000	
MABE866	Millipore UK	MAD2L1	Rabbit	1:1000	1:500
31430 GαM	ThermoFisher Scientific	Mouse IgG	Goat	1:5000	
31460 GαR	ThermoFisher Scientific	Rabbit IgG	Goat	1:5000	
926-32212 IRDye 800CW DαM	LI-COR	Mouse IgG	Donkey	1:5000	
926-32213 IRDye 800CW DαR	LI-COR	Rabbit IgG	Donkey	1:5000	
926-68072 IRDye 680RD DαM	LI-COR	Mouse IgG	Donkey	1:5000	
926-68073 IRDye 680RD DαR	LI-COR	Rabbit IgG	Donkey	1:5000	
A-11029 Alexa 488 GαM	ThermoFisher Scientific	Mouse IgG	Goat		1:1000
A-11034 Alexa 488 GαR	ThermoFisher Scientific	Rabbit IgG	Goat		1:1000
A-11013 Alexa 488 GαH	ThermoFisher Scientific	Human IgG	Goat		1:1000
A-11032 Alexa 594 GαM	ThermoFisher Scientific	Mouse IgG	Goat		1:1000
A-11037 Alexa 594 GαR	ThermoFisher Scientific	Rabbit IgG	Goat		1:1000
A-11014 Alexa 594 GαH	ThermoFisher Scientific	Human IgG	Goat		1:1000
A-21052 Alexa 633 GαM	ThermoFisher Scientific	Mouse IgG	Goat		1:1000
A-21071 Alexa 633 GαR	ThermoFisher Scientific	Rabbit IgG	Goat		1:1000
A-21091 Alexa 633 GαH	ThermoFisher Scientific	Human IgG	Goat		1:1000

Table 2.1 Details of Antibodies Used in this Project

Cells were collected by centrifugation, cell pellets were washed in PBS, and lysed in mammalian protein extraction reagent M-PER (Thermofisher) supplemented with Halt protease and phosphatase inhibitor cocktail (Thermofisher). Protein concentration was determined using the Direct Detect assay (Millipore). Protein samples were run on 4–15% Mini-PROTEAN TGX gels (Bio-Rad), and transferred onto nitrocellulose membranes (Thermofisher). Membranes were blocked with 5 % milk/TBS-T and incubated with primary antibodies diluted in 5 % milk/TBS-T overnight at 4^{o}C, Table 2.1. For chemiluminescent visualisation,

membranes were incubated with horseradish peroxidase-conjugated secondary antibodies (1:5000, GE Healthcare). Protein bands were visualised using SuperSignal™ West Pico PLUS Chemiluminescent Substrate (Thermofisher), and an ImageQuant LAS 4000 image analyser (GE Healthcare). For fluorescenct visualisation, membranes were incubated with IRDye 680RD or IRDye 800CW secondary antibody (Li-COR), and imaged using an Odyssey CLx system (Li-COR), Table 2.1.

2.6 Immunofluorescence

2.6.1 Basic Staining Protocol

Cells were grown on 22 x 22 mm cover slips in 6-well plates. Cover slips were washed in PBS and fixed according to the cellular structures to be imaged Table 2.2. Coverslips were then washed in PBS and blocked in 3% BSA, 1 hour at RT. Primary antibody was diluted according to Table 2.1 in 3% BSA, and 100 μl pipetted onto parafilm per cover slip. Cover slips were then transferred onto the

Cellular Structure	*Fixation Method*
General protocol	4% PFA 10 minutes, 0.2% Triton-X 10 minutes, at RT.
Kinetochores/centromeres	PTEMF (20 mM PIPES pH 6.8, 10 mM EGTA, 0.2% Triton X-100, 1 mM $MgCl_2$, 4% paraformaldehyde), 20 minutes, at RT.
Microtubules	-20°C 100% Methanol 6 minutes, at -20°C.

Table 2.2 Fixation Methods Detailing the different chemical fixation methods used during immunofluorescence staining and the cellular structures they are optimised for.

antibody solution cell-side down and incubated for 1 hour at RT. Cover slips were then transferred back to the 6-well plate and washed 3 x PBS for 30 minutes. Secondary antibody incubation was performed using the same method, followed by 3 x PBS washes for 30 minutes. Cover slips were stained with 1 μg/ml 4',6-diamidino-2-phenylindole (DAPI) for 5 minutes, washed 2 x PBS, left to air dry in the dark, and mounted onto glass slides in DAKO mounting medium (Agilent).

2.6.2 EdU Staining

The Click-iT EdU Cell Proliferation Alexa 647 kit (Thermofisher) was used to identify S phase cells. Cells were incubated in culture medium containing EdU at a final concentration of 10 μM for 20 minutes. EdU staining was subsequently performed according to manufacturer's instructions.

2.6.3 Cold Stable

Cells were grown on 22 x 22 mm cover slips in 6-well plates. 1 ml of ice-cold medium was added to each well, and the plate was incubated on ice for 3 minutes. Cells were then fixed in -20°C 100% methanol, 6 minutes at -20°C.

2.6.4 Metaphase Spreads

All centrifugation steps were performed at 1200 rpm for 8 minutes. Cells were treated with 100 ng/ml nocodazole for 16 hours, and metaphase-arrested cells harvested by mitotic shake off. Cells were centrifuged and resuspended in 5 ml hypotonic solution (75 mM KCl) for 25 minutes at 37°C. Cells were centrifuged and resuspended in Carnoy's fixative (3:1 methanol: acetic acid) and incubated at RT for 15-30 minutes. Cells were centrifuged and resuspended in Carnoy's fixative a second time, incubated at RT for 15-30 minutes. Cells were centrifuged and resuspended in 50-200 μl Carnoy's fixative. 12 μl of the cell solution was dropped from a height of 1 cm onto a glass slide, which was immediately placed in a covered 50°C water bath for 2 minutes for drying in a humidified environment, to improve chromosome spreading (Deng *et al*. 2003). Once dry, slides were staining with 1 μg/ml DAPI and a cover slip mounted in DAKO mounting medium.

2.7 Microscopy

2.7.1 Mitotic Error Quantification

Mitotic cells were imaged on a 3i Spinning Disk Confocal microscope, acquiring approximately 30 z-stacks of 0.2 μm using a 63X 1.4 numerical aperture

objective. Image analysis was performed using Slidebook and Fiji. In some older experiments, mitotic cells were imaged on an Olympus Deltavision microscope (Applied Precision LLC) equipped with a CoolSnap HQ camera, acquiring approximately 30 z-stacks of 0.2 μm using a 40X 1.3 numerical aperture objective. Images were deconvolved using conservative settings for 10 cycles using Softworx, and then exported for further analysis in Fiji.

2.7.2 Signal Intensity Quantification

To investigate protein levels in mitosis, metaphase cells were imaged on a 3i Spinning Disk Confocal microscope, acquiring approximately 30 z-stacks of 0.2 μm using a 63X 1.4 numerical aperture objective. When performing a cold stable assay to measure microtubule stability, cells were stained for α-tubulin, PCN and DAPI. Images were analysed using Fiji, a ROI was drawn around the whole spindle, and mean intensity values recorded for α-tubulin and PCN. When investigating KIF11 spindle localisation, cells were stained for KIF11, α-tubulin, and DAPI. Images were analysed in Fiji, where various ROIs were drawn, and the mean intensity values recorded for KIF11 and α-tubulin.

To investigate p53 expression, cells were stained for p53 and DAPI, and imaged on a on a 3i Spinning Disk Confocal microscope, acquiring a single plane image using a 40X 1.3 numerical aperture objective. Images were analysed in Slidebook, using the inbuilt tools to perform background subtraction, segment nuclei, filter nuclei, and measure p53 mean signal intensity.

2.7.3 High Content Screening of Centromeres

Cells were stained in CellCarrier-Ultra 96 well plates (Perkin Elmer). To capture CENPA foci in interphase cells a z-stack of 30 planes with a 0.3 μm step size was acquired, using a 63X 1.15 numerical aperture water immersion objective, on an Opera Phenix HCS imaging system. A large z-stack was acquired to account for variation in the central z position at different locations across the plate. Channels were imaged consecutively to minimise bleed through.

2.7.4 Live-Cell Imaging

All live cell imaging was performed on a 3i Spinning Disk Confocal Microscope, fitted with an environmental chamber maintained at 37^{o}C, and supplied with 5% CO_2.

To capture chromosomes during mitosis, live cells were seeded in glass-bottomed Nunc Lab-Tek chambers (Thermofisher). 3 hours prior to imaging, fresh medium was added containing SiR-DNA dye (Spirochrome) to a final concentration of 100 nM. A z-stack of 7 planes with a 2 μm step size was acquired, taking an image every 3 minutes using either the 63X or 40X objective. Cells were imaged for 12 hours. The same protocol was followed to capture the spindle during mitosis, instead using the SiR-Tubulin dye (Spirochrome) to a final concentration of 100 nM. Movies were analysed in Fiji or Slidebook, with manual quantification of mitotic timings and errors.

To capture Centrin 1 foci during mitosis, RPE1 eGFP-Centrin 1 cells were imaged, acquiring a z-stack of 28 planes with a 0.5 μm step size, taking an image every 40 seconds using a 100X 1.46 numerical aperture objective. Cells were imaged for up to 1 hour. Centrin 1 foci were tracked KiT2, a previously published software (Armond *et al*. 2016) using the manual spot detection method, and using custom built code to process the data, generate the centrosome trajectories, and extract the Euclidean distance between the centrosomes at each time point.

To capture EB1 dynamics during interphase, HeLa K-EB1-eGFP/RPE1 EB1-tRFP were imaged, acquiring a single plane image with a time interval of 500 ms, using a 100X 1.46 numerical aperture objective. Cells were imaged for 50 seconds.

To capture kinetochores during metaphase, RPE1-mNeonGreen-CENPA cells were imaged, acquiring a z-stack of 28 planes with a 0.5 μm step size, taking an image every 1.6 seconds using a 100X 1.46 numerical aperture objective. Cells were imaged for 5 minutes.

2.7.5 Kinetochore Microtubule Depolymerisation Assay

Cells were incubated with 100 nM SiR-Tubulin for 4 hours before imaging. 30 minutes before imaging, medium containing 100 nM SiR-Tubulin and 10 μM MG132 was added to prevent cells from transitioning to anaphase. Metaphase cells were identified using either DIC or eGFP-Centrin 1, and immediately before imaging medium was removed and replaced with medium containing 100 nM SiR-Tubulin, 10 μM MG132 and 200 ng/ml nocodazole. A z-stack of 28 planes with a 2 μm step size, taking an image every 1 minute using a 100X 1.46 numerical aperture objective was acquired. Cells were imaged for 15 minutes. Movies were analysed in Fiji by generating a sum intensity projection to extract total intensity within a ROI over time.

2.8 Phosphoproteomic Analysis

2.8.1 Sample Preparation

RPE1 cells were harvested and lysed in in 500 μl urea lysis buffer (Roche, 11873580001) and sonicated until clear. Protein samples were reduced, alkylated, and digested with LysC, followed by a trypsin digest. Phosphoenrichment was performed using TiO_2 beads (GL Sciences #5020-75010). Multiple wash steps were performed before phosphopeptides were eluted into columns for desalting according to manufacturers instructions (The Nest Group, HUM S18V). Samples were dried and stored at -80^{o}C. Immediately before analysis samples were resuspended in 10% formic acid.

2.8.2 Mass Spectrometric Analysis

Non-scale liquid chromatographic tandem mass spectrometry (nLC-MS/MS) was performed on a Q-Exactive Orbitrap Plus interfaced to a NANOSPRAY FLEX ion source and coupled to an Easy-nLC 1000 (Thermo Scientific).

2.8.3 Peptide Identification & Statistical Analysis

MaxQuant (version 1.5.5.1) software was used to identify peptides using the human UniProt database. To ensure accurate identifications, phosphopeptides were filtered at <1% false discovery rate (FDR). A custom-built R script was used to process the output files generated from MaxQuant, and the MSstats R package was used to perform statistical analysis. Data was log2 transformed, quantile normalised, and a linear mixed-effects model fitted. P values were generated using the group comparison function and adjusted to control for FDR using the Benjamini-Hochberg method.

Chapter 3: High-Throughput Automated Image Analysis Pipeline to Screen for CIN & Aneuploidy

This chapter describes the development, validation and implementation of a novel method to screen for chromosome instability and aneuploidy in fixed cells. A high-throughput image analysis pipeline was developed that employs customized software run using MATLAB, Python, and PyTorch to count centromeres in cells as a readout of aneuploidy, and micronuclei (MN), as a readout of chromosome segregation errors. These methods are superior to existing methods used to measure aneuploidy and chromosome instability in cells, as they greatly reduce the analysis time required per cell. Firstly, using the Opera Phenix High Content Screening (HCS) system, imaging protocols can be set up that run on 96 well plates, rather than hours spent on a microscope identifying and imaging mitotic cells on traditional slides. This allows for a larger number of conditions to be assessed in the same time frame. Secondly, time is also saved at the analysis stage. Rather than spending hours classifying mitotic errors in images, the researcher just sets off the analysis pipeline, which takes a matter of minutes to set up. Finally, the analysis methods identify conditions that give rise to true aneuploid cells, rather than identifying lagging chromosomes that are likely to be resolved and correctly segregated before the completion of mitosis.

The methodology was implemented to screen a number of genes to identify whether their upregulation causes CIN in the normal, non-transformed cell line RPE1, after they were identified to be overexpressed or involved in copy number amplification events during the early stages of tumourigenesis. Data from two main studies was used to collate a list of genes for screening (Table 3.1), focusing on gene upregulation during the early stages of lung cancer. These include the TRACERx clinical study (Jamal-Hanjani *et al*. 2017), and the microarray-based study investigating gene expression in pre-cancerous lung lesions (Teixeira *et al*. 2019). By sampling different regions of tumours, the TRACERx study has revealed an important understanding of tumour evolution. A key observation was that CIN and aneuploidy were widespread in late stage tumours, however it was

Source	*Gene*
TRACERx Lung Adenocarcinoma (Jamal-Hanjani *et al*. 2017)	FOXA1

TRACERx Lung Adenocarcinoma (Jamal-Hanjani *et al*. 2017)	EGFR
TRACERx Lung Adenocarcinoma (Jamal-Hanjani *et al*. 2017)	HEY1
TRACERx Lung Adenocarcinoma (Jamal-Hanjani *et al*. 2017)	NKX2-1
TRACERx Lung Adenocarcinoma (Jamal-Hanjani *et al*. 2017)	RSPO2
TRACERx Lung Adenocarcinoma (Jamal-Hanjani *et al*. 2017)	COX6C
TRACERx Lung Adenocarcinoma (Jamal-Hanjani *et al*. 2017)	KRAS
TRACERx Lung Adenocarcinoma (Jamal-Hanjani *et al*. 2017)	EIF3E
TRACERx Lung Adenocarcinoma (Jamal-Hanjani *et al*. 2017)	PPFIBP1
TRACERx Lung SCC (Jamal-Hanjani *et al*. 2017)	SOX2
TRACERx Lung SCC (Jamal-Hanjani *et al*. 2017)	PIK3CA
TRACERx Lung SCC (Jamal-Hanjani *et al*. 2017)	FGFR1
TRACERx Lung SCC (Jamal-Hanjani *et al*. 2017)	MYC
TRACERx Lung SCC (Jamal-Hanjani *et al*. 2017)	CCND1
TRACERx Lung SCC (Jamal-Hanjani *et al*. 2017)	FOXL2
TRACERx Lung SCC (Jamal-Hanjani *et al*. 2017)	CD79A
TRACERx Lung SCC (Jamal-Hanjani *et al*. 2017)	AKT2
TRACERx Lung SCC (Jamal-Hanjani *et al*. 2017)	IL7R
TRACERx Lung SCC (Jamal-Hanjani *et al*. 2017)	HOOK3
TRACERx Lung SCC (Jamal-Hanjani *et al*. 2017)	CEBPA
TRACERx Lung SCC (Jamal-Hanjani *et al*. 2017)	IKBKB
TRACERx Lung SCC (Jamal-Hanjani *et al*. 2017)	REL
TRACERx Lung SCC (Jamal-Hanjani *et al*. 2017)	TERT
TRACERx Lung SCC (Jamal-Hanjani *et al*. 2017)	LSM14A
Pre-invasive CIS Study (Teixeira *et al*. 2019)	ACTL6A
Pre-invasive CIS Study (Teixeira *et al*. 2019)	NEK2
Pre-invasive CIS Study (Teixeira *et al*. 2019)	NCAPD2
Pre-invasive CIS Study (Teixeira *et al*. 2019)	CENPH
Pre-invasive CIS Study (Teixeira *et al*. 2019)	ELAVL1
Pre-invasive CIS Study (Teixeira *et al*. 2019)	OIP5
Pre-invasive CIS Study (Teixeira *et al*. 2019)	SMC3
Pre-invasive CIS Study (Teixeira *et al*. 2019)	SMC4
Mitotic Genes Frequently Upregulated in Cancer (Zhang *et al*. 2010; Li *et al.* 2020)	KIF18A
Mitotic Genes Frequently Upregulated in Cancer (Gao *et al*. 2020; Li *et al*. 2020)	KIF18B
Mitotic Genes Frequently Upregulated in Cancer (Venere *et al*. 2015; Jiang *et al*. 2017; Zhou *et al*, 2021; Li *et al.* 2020).	KIF11
Positive Control (Sotillo *et al*. 2007)	MAD2
Positive Control (Shinmura *et al.* 2014)	PLK4
Positive Control (Zhang *et al*. 2008)	ESPL1
Positive Control (Hadjihannas *et al*. 2006)	AXIN2

Table 3.1 List of Genes for CRISPR Upregulation CIN Screening Showing the sources from which each gene was identified as upregulated in cancer. Green highlight identifies genes that were successfully run through all stages of the experimental workflow, including CRISPR upregulation, qPCR, imaging, and automated image analysis. Purple highlight identifies genes for which CRISPR upregulation failed. No highlight identifies genes where qPCR either failed, or the gene was not expressed in RPE1 cells.

unclear how these

processes were initiated. Many copy number and chromosome arm level changes were identified as clonal, indicating their development during the early stages of tumourigenesis and suggesting CIN is an ongoing event that contributes to tumour evolution. A small number of mitotic genes that are frequently found upregulated in cancer were also included in the screening list,

in addition to 4 positive control genes, that should cause CIN upon upregulation, Table 3.1. This work investigates the hypothesis that upregulation of oncogenes early on during tumourigenesis initiates chromosome instability in cells.

Elina Vladimirou and Jonathan Armond built the software and developed the computational image analysis pipeline presented in this chapter.

3.1 CRISPR Upregulation as a Gene Overexpression Tool

To model the copy number amplifications and gene overexpression identified in the aforementioned studies, the synergistic activation mediators (SAM) CRISPR upregulation system was employed, to upregulate gene expression to physiologically relevant levels. This system targeted the endogenous genetic loci, achieving between 2- and 20-fold upregulation, dependent on the gene involved and the gRNA design. Two lentiviral plasmids were required, one expressing the gRNA and the nuclease dead (d)Cas9 conjugated to VP64 (pLenti-SAM), and another expressing the MPH activators P65 and HSF1 conjugated to an MS2 binding domain (pLenti-MPH; Figure 3.1a). When transduced into cells, the dCas9-VP64 and gRNA localize upstream of the promoter of the gene of interest. The MPH activators are recruited through the MS2 loop binding domain, and this complex promotes recruitment of the general transcription machinery driving higher levels of gene expression (Figure 3.1b).

In some instances, expression of pLenti-SAM with a suitable gRNA was sufficient to drive increased gene expression in the absence of pLenti-MPH. gRNAs designed to target the promoter of *MAD2* were cloned into pLenti-SAM. However, transduction into cells in the absence of pLenti-MPH did not increase expression of *MAD2* compared to empty vector (EV) control (Figure 3.1c). When the pLenti-MPH was co-transduced alongside *MAD2*-targetting pLenti-SAM, gene expression reached up to 15-fold greater than EV (Figure 3.1c). From this

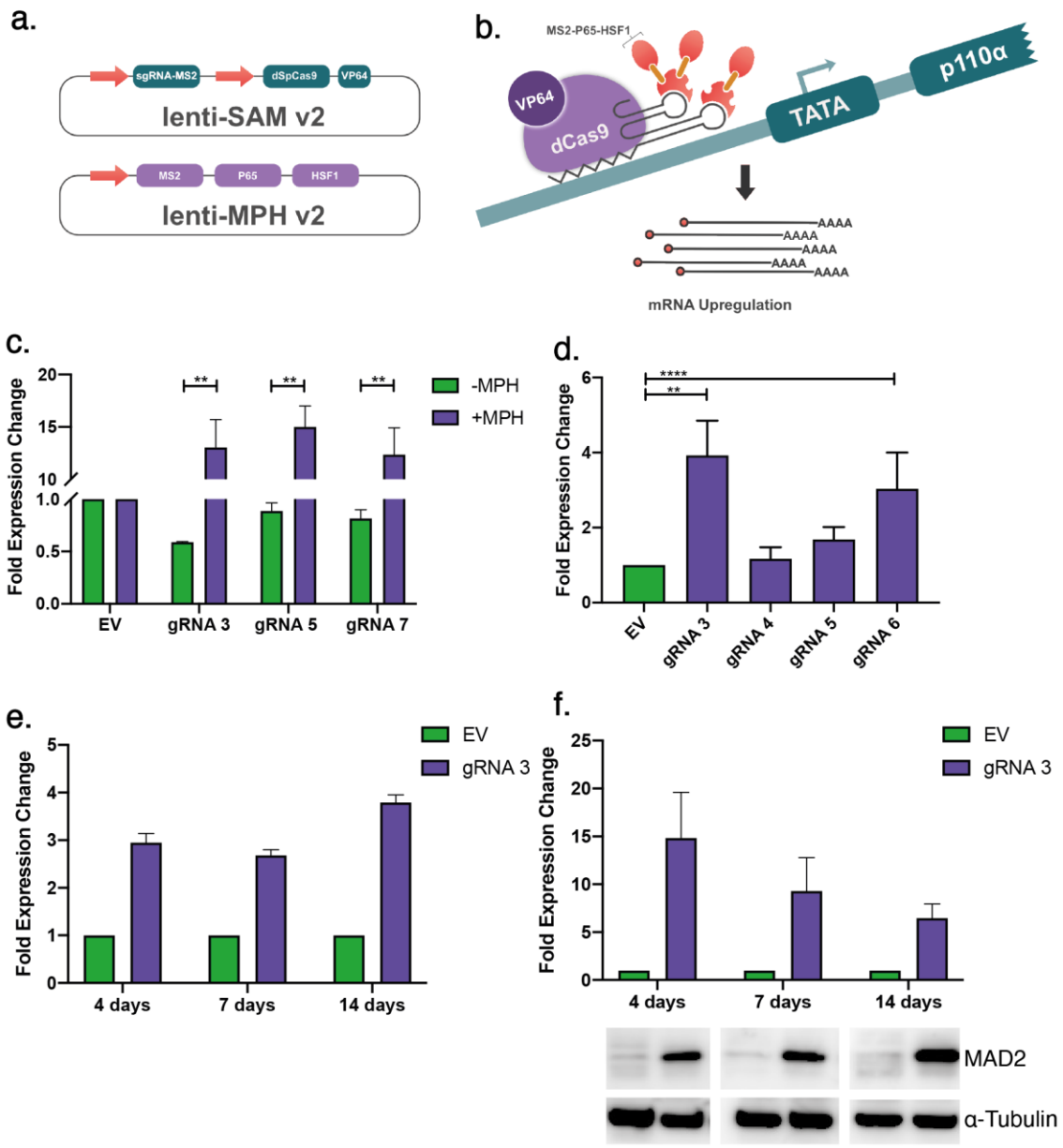

Figure 3.1 Optimisation of SAM CRISPR Activation as a Tool for Gene Upregulation **a.** Schematic showing the two constructs and **b.** how the system upregulates gene expression. **c.** Comparison of MAD2 upregulation in RPE1 cells, either with or without co-transduction of pLenti-MPH. N = 3 (-MPH), N = 2 (+MPH), Student's T-test, error bars = SEM. **d.** Comparison of the efficacy of four different gRNAs targetting MAD2, in RPE1-MPH. N = 3, one-way ANOVA with Dunnett's multiple comparisons test, error bars = SEM. **e.** Timecourse showing sustained upregulation of KIF11 for up to 14 days post-transduction, at the mRNA level and **f.** protein level. N = 3, error bars = SEM.

data it was clear that pLenti-MPH would be important for effective gene upregulation, therefore a clonal RPE1 cell line stably expressing the construct was generated (RPE1-MPH). Transduction of RPE1-MPH with *MAD2*-targetting pLenti-SAM resulted in successful upregulation of gene expression to a maximum of 4-fold, less than that observed when a co-transduction was performed.

Here out, RPE1-MPH were used when performing CRISPR upregulation. Use of a clonally selected cell line gave a more reliable baseline for the screening experiments. It was important to limit the amount of background CIN and aneuploidy in the cell line so that subtle phenotypes could be detected by the image analysis pipeline. It also presented an easier and more reproducible approach, as it removed any potential variation caused by transduction of the pLenti-MPH construct. Lastly, it also spread the amount of virus cells received over two transductions, improving viability.

Due to variation in the efficacy of the different gRNAs, between 6-8 were designed and cloned for each gene. Out of the 4 tested for MAD2, gRNA 3 was chosen for future experiments (Figure 3.1d). To confirm that CRISPR activation remained stable in cells over time, RPE1-MPH were transduced with pLenti-SAM containing *MAD2* targeting gRNA 3, and samples taken at 4, 10, and 14 days post transduction. qPCR showed that *MAD2* mRNA remained stably upregulated at all timepoints (Figure 3.1e). Western blotting revealed that upregulation at the protein level was higher than that of mRNA, however this diminished over a period of two weeks. At 14 days, however, there remained over 6-fold upregulation of *MAD2* at the protein level, confirming that CRISPR activation was suitable for use in experiments within this time period.

3.2 Development of the Automated Image Analysis Pipeline

3.2.1 Analysis Pipeline Stages

The automated image analysis pipeline is a multistep process which extracts information from the images in a high throughput manner (Figure 3.2a). The pipeline requires images stained with DAPI to identify nuclei and MN, CENPA to label centromeres, and EdU to identify cells in S phase (Figure 3.2b). The images are first segmented based on DAPI, using a deep learning approach with convolutional neural networks based on U-Net (Ronneberger *et al*. 2015), to fix a 3D mask to each nucleus (Figure 3.2c). This approach improves the accuracy of

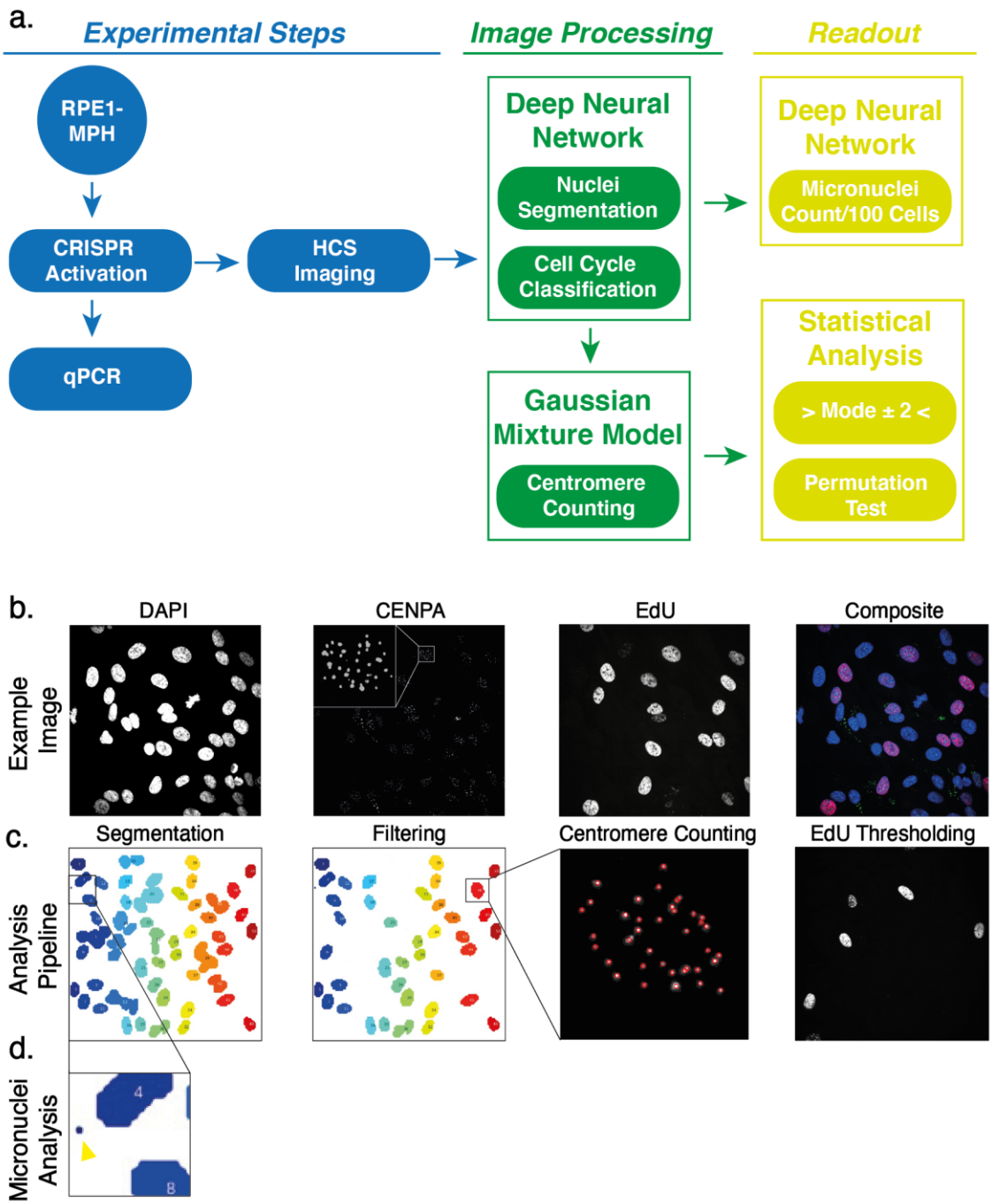

Figure 3.2 An Automated High-throughput Imaging Pipeline to Screen for Aneuploidy and CIN **a.** Flow chart detailing the different stages within the pipeline. **b.** Example images showing DAPI, CENPA and EdU staining. **c.** Images describing the segmentation, filtering, centromere counting, and EdU thresholding stages of image analysis. **d.** Example image showing micronuclei identification.

nuclei identification, despite there being variation in size, shape, signal intensity, and varying amounts of noise in the image.

The nuclei segments are then passed through a filtering step to identify and remove mitotic cells, multiple cells touching, and other erroneous segments that would give false aneuploid centromere counts (Figure 3.2c). This step uses

machine learning (ML); a gradient boosted decision trees ML algorithm using the LightGBM library was trained using a manually labelled dataset to classify segments by their identity. The algorithm feeds images through decision trees where parameters such as size, intensity, and circularity are used to make decisions on the identity of the segment.

After filtering, the number of CENPA spots in each segment are counted, using a 3D mixture model that identifies 3D gaussian peaks (Figure 3.2c). The algorithm can distinguish overlapping spots by taking into account their brightness. It uses a Gaussian mixture model to cluster spots by intensity into singlet, doublet or occasionally triplet intensity levels. If the intensity is more than double the average spot intensity, then one count is added as this is likely two fully overlapping centromeres. Similarly, two counts are added for triplets

The last stage of the pipeline identifies and counts MN (Figure 3.2d). This approach utilises freely available ML code developed by Google, that distinguishes shapes in images using a pre-trained neural network, MobileNetV2. This is modified into a custom deep neural network which outputs an MN count based on an input image. A training dataset was generated using 2160 images where each MN was labelled, and its coordinates stored in the metadata of the image. This was used to train the algorithm to identify MN in screening datasets. Using the image segmentation to derive a cell count, this analysis provides a readout of the number of MN/100 cells.

3.2.2 Validating the CIN Screening Experimental Approach

A diploid, normal human cell line was required for the CIN screening, such that any changes observed could be attributed to the gene upregulation, rather than inherent instability of the cell line. RPE1 cells were chosen as they show a near-diploid phenotype, whilst remain easy to work with and manipulate in culture. Metaphase spreads revealed a modal chromosome count of 46 in RPE1 (Figure 3.3a). After transduction of pLenti-MPH and generation of the RPE1-MPH cell

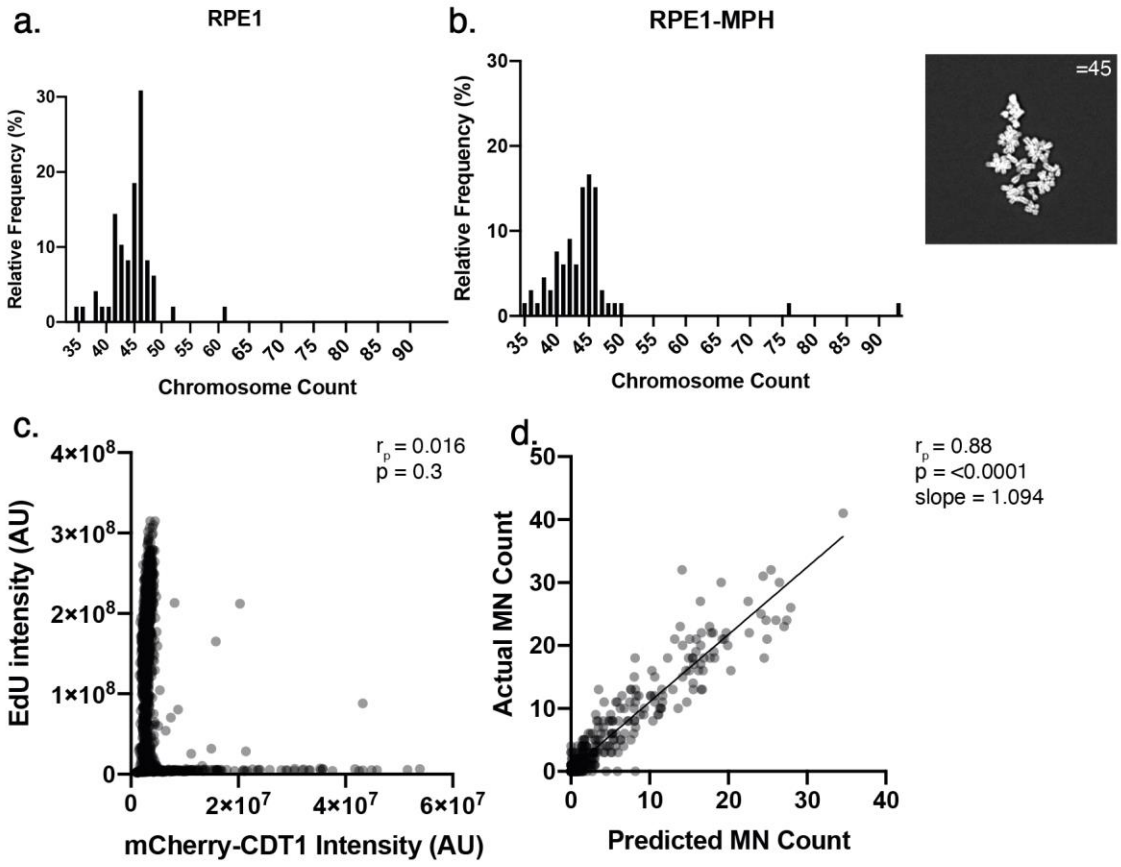

Figure 3.3 Validating the Screening Approach a. Histograms showing chromosome counts after metaphase spreads were performed on RPE1 and RPE1-MPH. **b.** Plot showing the correlation between EdU signal intensity and mCherry-CDT1, Pearson's correlation coefficient. **c.** MN counting of RPE1 cells transduced with increasing amounts of empty vector (EV) virus. **d.** Plot of the predicted MN count vs the actual MN count, measured from a set of labelled images. Pearson's correlation coefficient.

line, a small degree of aneuploidy was introduced, shown by the widening of the histogram in (Figure 3.3b). The modal chromosome count was 45, and there was no significant difference when comparing chromosome counts with the parental RPE1 cells by T-test ($p>0.05$), so the RPE1-MPH cell line was used for screening.

An accurate cell cycle marker was required such that only G1 cells were analysed for centromere counts. If S phase cells were included in the analysis, then gene upregulations that promote proliferation and increase the proportion of S phase cells could give a false impression of increased aneuploidy. Initially, the G1 marker mCherry-CDT1 was considered, and an RPE1 cell line expressing the construct was generated. However, expression was unstable, and the positive population was lost over time, suggesting toxicity. Labelling of RPE1-mCherry-CDT1 with EdU showed that both markers were accurate, as they were mutually

exclusive in cells (Figure 3.3c). To minimize interference with the RPE1-MPH cell line and any potential CIN caused by mCherry-CDT1 expression, EdU was chosen as a cell cycle marker. This could then be used to identify changes in the proliferation rate in response to gene upregulation.

Similarly, if gene upregulation increased the proportion of G2 cells, it could give a false impression of a tetraploid population. To combat this, an algorithm that grouped centromeres in nearest-neighbour pairs and calculated the distance between them was implemented to identify cells with paired KTs, indicative of G2. This removes G2 cells, enabling detection of a true tetraploid population.

To validate the MN counting algorithm, it was run on labelled images to generate matched visual and automated counts. The counts predicted automatically showed a high correlation with the actual count, determined manually ($p<0.0001$, Pearson's correlation coefficient), and gave a mean absolute error of 1.4 (Figure 3.3d). The slope of the regression line fitted to the data shows that on average the algorithm predicts very similar counts to what has been determined manually, without over or underestimating the number of MN.

3.2.3 Statistical Analysis of the Centromere Counting Results

Frequently up to 2000-3000 individual cells are processed by the analysis pipeline for a single condition, and the raw data can be plotted in a histogram, showing the distribution of centromere counts. While the algorithm underwent extensive development, there remains a moderate level of noise, with rare counts appearing below 30 and up to 100 centromeres for untreated RPE1 (Figure 3.4a). The modal centromere count lies very close to the expected value of 45, however, which is in line with the results from metaphase spreads of the RPE1-MPH cell line. Given this observation, deviation from the modal centromere count was used as a readout of the degree of aneuploidy, providing a more sensitive method to detect low levels of aneuploidy than assessing changes to the mode, which by

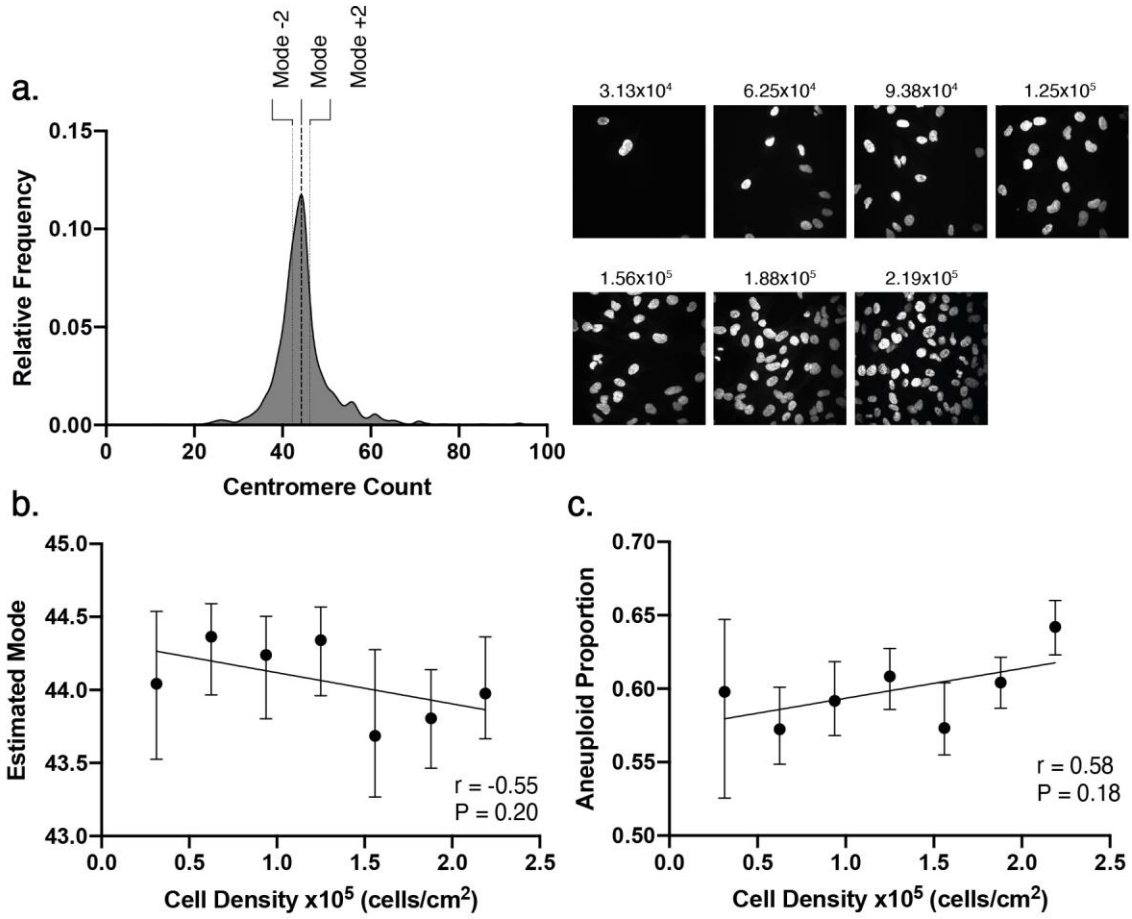

Figure 3.4 Interpreting Results from the Automated Image Analysis Pipeline a. An example output histogram of centromere counts measured from untreated RPE1 cells, showing a visual representation of the modal deviation analysis method (determining the proportion of cells outside of the mode ± 2). Kernel density smoothing was applied. **b.** The estimated mode after kernel smoothing. N = 2, Pearson's correlation coefficient. **c.** Calculation of the aneuploid proportion using the modal deviation method, for untreated RPE1 cells at different seeding densities. N = 2, Pearson's correlation coefficient.

definition, will only change when the majority of cells experience changes in chromosome number. Specifically, the proportion of cells with centromere counts lying outside of the modal count ± 2 was determined (an approximate 10% window around 46), and this value was used as a measure of aneuploidy. This method, here out referred to as modal deviation (MD) analysis, is an extension of that used by Bakhoum and colleagues to assess the percentage of cells that deviate from the modal chromosome number when assessing aneuploidy with chromosome specific FISH probes (Bakhoum *et al*. 2009c).

To accurately measure the statistical significance of the results, firstly a kernel density estimate of the histogram is fitted, to minimise the contribution to variation from stochastic noise generated by the automated analysis processes. A non-

parametric permutation test was then run, taking 10,000 samples from each dataset. This test provides an estimated p value based on the difference observed between the centromere counts in the control condition (empty vector, for example) vs a test condition, after sampling 10,000 different permutations of the data. Given the high number of cells within each condition and the high rate of sampling, this test provides an accurate estimate of the p value. Finally, bootstrapping was performed to determine the 95% confidence intervals, using a similar method of data resampling for each condition. These are used to compute error bars in plots showing the proportion of cells outside the modal centromere count ± 2.

RPE1 cells were seeded in multiple wells at varying densities, to test the robustness of this approach. The estimated mode after kernel smoothing of the histogram showed very minimal variation between the conditions, ranging from 43.7 to 44.4 (Figure 3.4b). There was no significant correlation between the modal count and the seeding density ($p>0.05$, Pearson's correlation coefficient). The modal deviation method was then used to calculate the aneuploid proportion, which again showed no correlation with seeding density ($p>0.05$, Figure 3.4b). The approach proved reproducible in untreated cells, therefore the pipeline was further implemented to detect CIN.

3.3 Implementing the Automated Image Analysis Pipeline

3.3.1 Chemical Induction of CIN as a Positive Control

As a positive control for CIN and aneuploidy, cells were treated with drugs commonly used to generate chromosome segregation errors. These conditions were used to test the sensitivity and accuracy of the centromere and MN counting algorithms. Firstly, increasing doses of reversine were used, at 0.15, 0.3, and 0.45 μM, inducing chromosome segregation errors and MN (Figure 3.5a). For both RPE1 and RPE1 $p53^{-/-}$, MD analysis of the centromere counting results showed a significant increase in the aneuploid proportion at 0.3 and 0.45 μM,

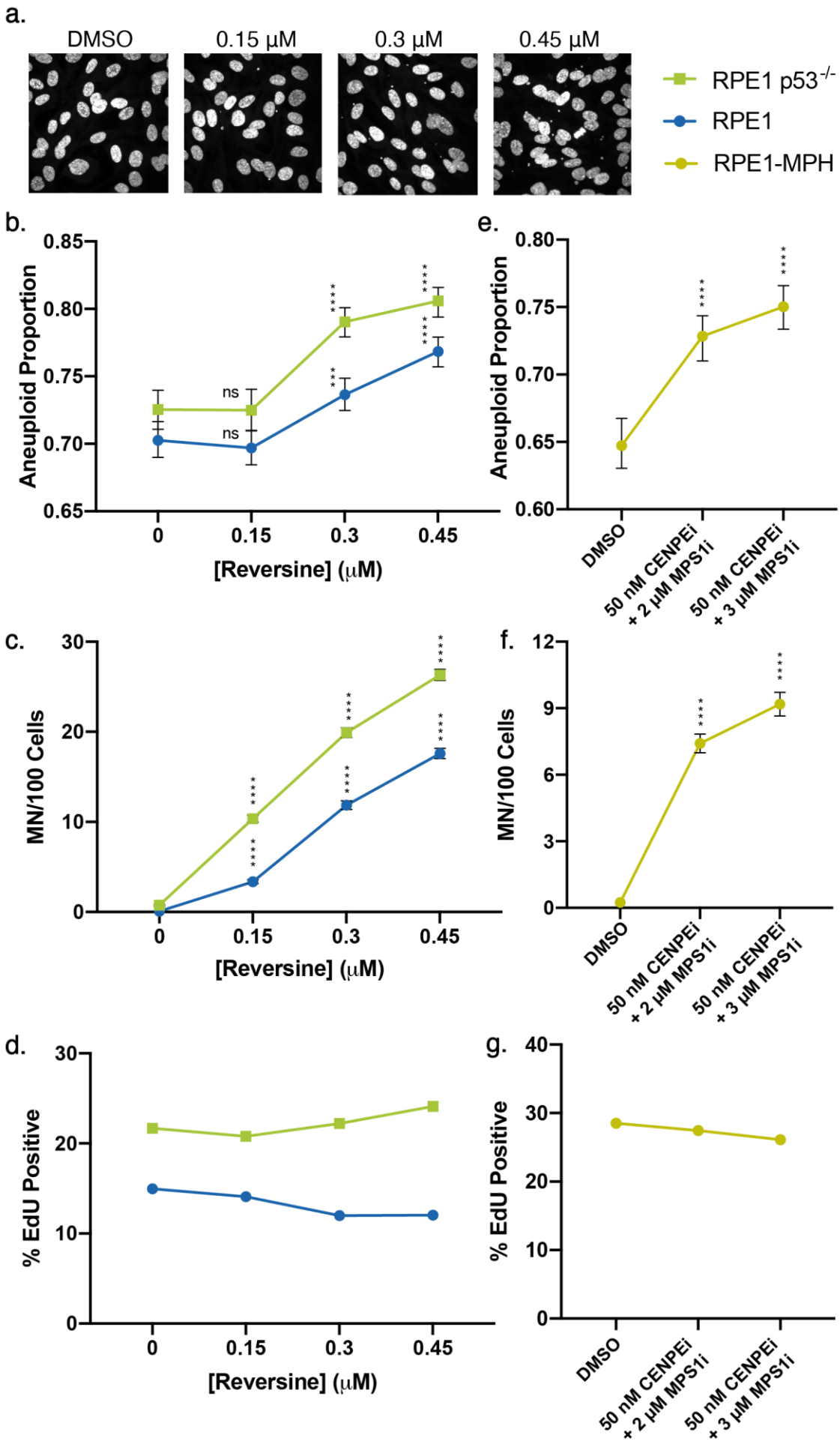
a.
DMSO
0.15 µM
0.3 µM
0.45 µM
RPE1 p53-/-
RPE1
RPE1-MPH
b.
Aneuploid Proportion
0.85
0.80
0.75
0.70
0.65
ns
ns
0
0.15
0.3
0.45
[Reversine] (µM)
e.
Aneuploid Proportion
0.80
0.75
0.70
0.65
0.60
DMSO
50 nM CENPEi + 2 µM MPS1i
50 nM CENPEi + 3 µM MPS1i
c.
MN/100 Cells
30
20
10
0
0
0.15
0.3
0.45
[Reversine] (µM)
f.
MN/100 Cells
12
9
6
3
0
DMSO
50 nM CENPEi + 2 µM MPS1i
50 nM CENPEi + 3 µM MPS1i
d.
% EdU Positive
30
20
10
0
0
0.15
0.3
0.45
[Reversine] (µM)
g.
% EdU Positive
40
30
20
10
0
DMSO
50 nM CENPEi + 2 µM MPS1i
50 nM CENPEi + 3 µM MPS1i

Figure 3.5 Chemical Induction of CIN as a Positive Control **a.** Images of individual fields showing increasing numbers of mincronuclei as the reversine concentration increases. Calculation of **b.** the modal deviation to determine the aneuploid proportion, **c.** the number of MN/100 cells, and **d.** the proportion of EdU positive cells after reversine treatment. Calculation of the **e.** modal deviation to determine the aneuploid proportion, **f.** the number of MN/100 cells, and **g.** the proportion of EdU positive cells after CENPE and MPS1 inhibition. **b & e.** N = 2, p values determined using a 10,000 sample permutation test with FDR adjustment, error bars = 95% confidence intervals determined by 1000 sample bootstrapping. **c & d.** N = 2, statistical analysis was performed on a per field basis (n > 230 for each condition), using a one-sided students T-test followed by FDR adjustment. Error bars = SEM.

while the 0.15 μM dose did not induce high enough levels of chromosome mis-segregation to cause significant deviation from the modal chromosome number ($p<0.001$, $p<0.001$, $p>0.05$, respectively, permutation test; Figure 3.5b). These results correlate with the MN counting results, which show increasing numbers of MN/100 cells as the reversine dose is increased (Figure 3.5c). The MN counting results show a significant increase in MN/100 cells detected at 0.15 μM reversine, however (0.09-3.37 MN/100 cells, $p<0.0001$, T-test), suggesting this assay is more sensitive. When calculating the proportion of EdU positive cells, RPE1 showed a subtle decreasing trend, suggesting higher doses of reversine promote cell cycle arrest (Figure 3.5d). The RPE1 $p53^{-/-}$ cell line, however, showed a subtle increasing trend.

A second method to chemically induce CIN was also tested; a combination of CENPE and MPS1 inhibitors (GSK923295 and NMS-P715, respectively), as this was shown to more specifically induce numerical CIN while causing less disruption to mitosis compared to reversine (Soto *et al*. 2017). Both doses tested caused a significant increase in the aneuploid proportion, similar to that observed at 0.3 μM reversine (Figure 3.5e). MN counting revealed a significant increase from 0.24 to around 7-9 MN/100 cells, again to similar levels as seen with 0.3 μM reversine (Figure 3.5f). Only very subtle changes to the proportion of EdU positive cells were observed (Figure 3.5g).

3.3.2 Screening a Library of Genes Using SAM CRISPR Upregulation

After successfully applying the automated image analysis pipeline and MD analysis of centromere counts to identify CIN and aneuploidy after chemical

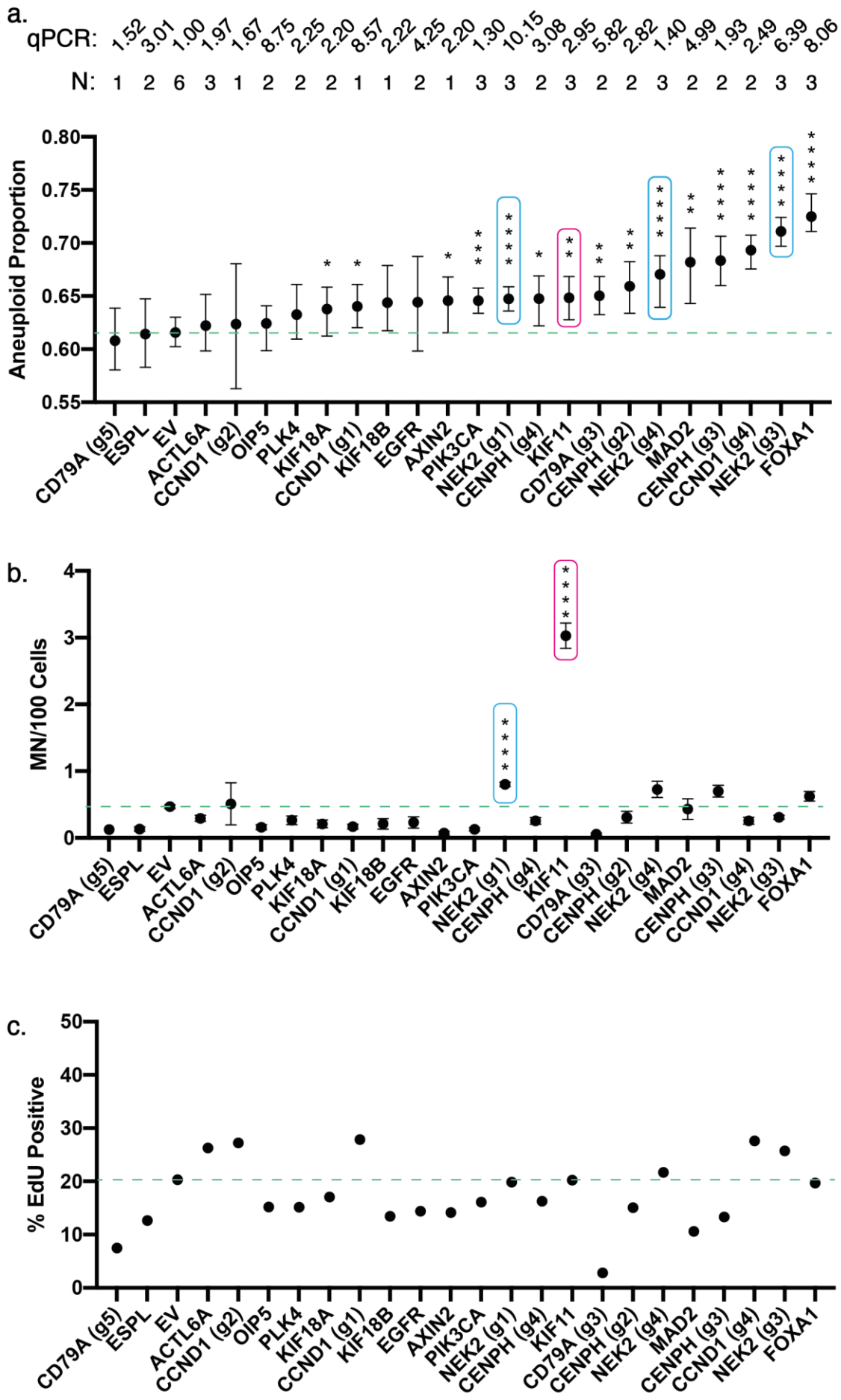
a.
qPCR: 1.52 3.01 1.00 1.97 1.67 8.75 2.25 2.20 8.57 2.22 4.25 2.20 1.30 10.15 3.08 2.95 5.82 2.82 1.40 4.99 1.93 2.49 6.39 8.06
N: 1 2 6 3 1 2 2 2 1 1 2 1 3 3 2 3 2 2 3 2 2 2 3 3
Aneuploid Proportion
0.80
0.75
0.70
0.65
0.60
0.55
CD79A (g5) ESPL EV ACTL6A CCND1 (g2) OIP5 PLK4 KIF18A CCND1 (g1) KIF18B EGFR AXIN2 PIK3CA NEK2 (g1) CENPH (g4) KIF11 CD79A (g3) CENPH (g2) NEK2 (g4) MAD2 CENPH (g3) CCND1 (g4) NEK2 (g3) FOXA1
b.
MN/100 Cells
4
3
2
1
0
CD79A (g5) ESPL EV ACTL6A CCND1 (g2) OIP5 PLK4 KIF18A CCND1 (g1) KIF18B EGFR AXIN2 PIK3CA NEK2 (g1) CENPH (g4) KIF11 CD79A (g3) CENPH (g2) NEK2 (g4) MAD2 CENPH (g3) CCND1 (g4) NEK2 (g3) FOXA1
c.
% EdU Positive
50
40
30
20
10
0
CD79A (g5) ESPL EV ACTL6A CCND1 (g2) OIP5 PLK4 KIF18A CCND1 (g1) KIF18B EGFR AXIN2 PIK3CA NEK2 (g1) CENPH (g4) KIF11 CD79A (g3) CENPH (g2) NEK2 (g4) MAD2 CENPH (g3) CCND1 (g4) NEK2 (g3) FOXA1

Figure 3.6 Implementing the CIN Screen Following CRISPR Upregulation Calculation of **a.** the modal deviation to determine the aneuploid proportion, **b.** the number of MN/100 cells, and **c.** the proportion of EdU positive cells after CRISPR upregulation of target genes. qPCR values for each gene are given, alongside the number of biological replicates. Blue boxes identify NEK2, pink boxes identify KIF11, green dashed line represents EV result. **a.** p values determined using a 10,000 sample permutation test with FDR adjustment, error bars = 95% confidence intervals determined by 1000 sample bootstrapping. **b.** Statistical analysis was performed on a per field basis (n > 230 for each condition), using a one-sided students T-test followed by FDR adjustment. Error bars = SEM.

induction of CIN, these methods were applied to a collated list of genes, Table 3.1, to investigate the effect of CRISPR gene upregulation. In the subset of genes for which CRISPR upregulation was successful, the modal deviation was plotted in comparison to EV. This identified a number of genes that significantly increased the modal deviation when upregulated (Figure 3.6a). As expected, MAD2 upregulation caused significant modal deviation ($p<0.01$, permutation test). Three different gRNAs targeting NEK2 and inducing varied levels of upregulation significantly increased the modal deviation ($p<0.0001$), a strong indication that NEK2 causes CIN when overexpressed.

MN analysis confirmed NEK2 as a hit gene, however only gRNA 1 caused a significant increase in MN/100 cells ($p<0.0001$, T-test; Figure 3.6b). This gRNA caused the highest upregulation of the three tested, at 10.15. It is possible that NEK2 increases the aneuploid population by separate mechanisms from those that cause MN, demonstrating the benefit of the dual readout. KIF11 upregulation showed a striking phenotype in the MN analysis, increasing the MN/100 cells around 6 fold that seen in EV treated cells (Figure 3.6b). Given that significant phenotypes were observed in both assays, KIF11 and NEK2 were identified as priority hits for further investigation. In the screening experiments, the proportion of EdU positive cells varied and did not show any correlation to the changes in modal deviation or MN/100 cells (Figure 3.6c).

3.4 Further Screening of KIF11 Upregulation

Following the identification of *KIF11* as a hit gene in the centromere counting approach, and the striking phenotype observed in the MN counting approach, upregulation of this gene was investigated further at additional time points of 3

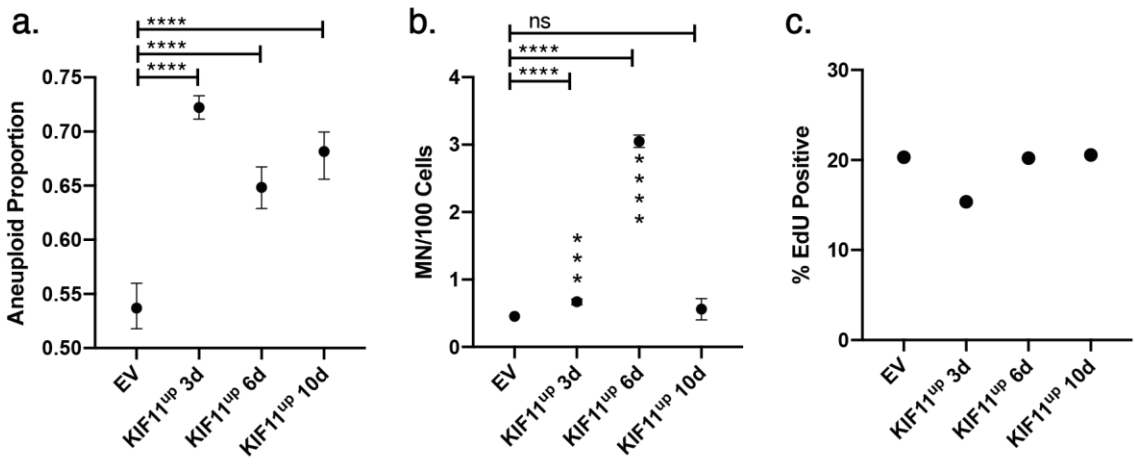

Figure 3.7 Investigating of the Effects of KIF11 Upregulation Over Time Calculation of **a.** the modal deviation to determine the aneuploid proportion, **b.** the number of MN/100 cells, and **c.** the proportion of EdU positive cells after CRISPR upregulation of KIF11. Statistical analysis was performed as in Figure 3.6.

and 10 days post transduction. MD analysis showed a significant increase in the proportion of aneuploid cells at all time points ($p<0.0001$, permutation test). The MN analysis showed a subtle but significant increase at 3 days from 0.46 to 0.67 MN/100 cells, a lot less than the increase to 3.05 MN/100 cells seen at 6 days. At 10 days, there is no significant change to MN numbers. These data suggest aneuploidy is maintained over time after *KIF11* upregulation, whereas chromosome segregation errors that cause MN are not. This time course does not provide information on whether a transient period of *KIF11* upregulation induces CIN that subsequently propagates further mitotic errors in the absence of upregulation; the CRISPR upregulation system is constitutively switched on, and therefore *KIF11* constitutively upregulated. An inducible system would be required to test whether transient *KIF11* upregulation can induce a persistent CIN phenotype in cells.

3.5 Discussion

3.5.1 CRISPR Upregulation

CRISPR upregulation was employed to model gene overexpression. This system allowed overexpression of the gene at the endogenous loci, to between 1.2-10 fold the expression level of normal RPE1 cells. This was beneficial in that genome wide screens can be performed using the relevant library of gRNAs, as

demonstrated by Konermann *et al* in a screen to identify genes that provide resistance to the BRAF inhibitor PLX-4720. In this study, upregulation of key cancer genes including *TERT*, *SOX2*, and *MYC* only reached around 5 fold increased gene expression, which is in striking contrast to the ~11,000 fold activation of Interleukin 1B (*IL1B),* and ~3000 fold activation of Hemoglogin Subunit Gamma 1 (*HGB1*) that was obtained (Konermann *et al*. 2015). This shows how variable and gene-specific the results of CRISPR upregulation can be.

The genes selected for CRISPR upregulation and CIN screening include well known oncogenes (e.g. *PIK3CA*), key mitotic regulators whose protein levels are tightly controlled (e.g. *KIF18A*), and genes that may not even be expressed in a non-transformed, differentiated cell line such as RPE1 (e.g. *SOX2;* (Ma et al. 2009). It is therefore not surprising that for 11 genes, CRISPR upregulation was unsuccessful, despite testing between 6 and 8 gRNAs for each gene, Table 3.1. In these instances, a standard expression vector system may be more appropriate for achieving gene upregulation, with the caveat that expression levels may not remain physiological. The CRISPR upregulation system was attractive in its low level of gene upregulation, and the potential for multiplexing to target multiple genes simultaneously. This approach was tested in an effort to upregulate both *PIK3CA* and *SOX2*, which occurs during amplification of the 3q chromosome arm. The poor upregulation seen for both *PIK3CA* and *SOX2* meant this was not possible, however. Other approaches to investigate the role of 3q amplification on tumourigenesis, and specifically whether this causes CIN and aneuploidy, are required.

3.5.2 Automated Detection of MN

The MN counting approach proved to accurate and sensitive. With little to no re-training of the ML algorithm, this approach could be applied to different cell lines and sample types to aid researchers in determining whether a set of experimental conditions induce MN. For example, this approach would be suited to screening patient derived cancer cell lines for MN, or tracking the development of CIN over time. Assessing MN in patient tissue samples would be more difficult as these are not suited to HCS imaging using the opera phenix, and the algorithm would

have to be re-trained on the different type of images obtained, but in theory this would be possible. The MN counting approach would be an informative readout for any type of screening experiment performed in cell lines to assess CIN.

The sensitivity of MN counting is demonstrated by the reversine treatments. DMSO treated cells exhibited 0.087 MN/100 (RPE1) cells, while 0.15 μM reversine caused 3.37 MN/100 cells, with an adjusted p value of $5.71x10^{-66}$. Given the linear relationship observed between the dose of reversine and number of MN/100 cells, this suggests the approach would be able to detect significant increases in MN at a dose of reversine 10 fold lower, 0.015 μM. In this project, between 230-1470 individual fields were analysed for MN per condition. The imaging was limited by the exposure time for three different channels (DAPI, EdU, CENPA), and the large stack acquired. If only performing the MN analysis, the amount of data acquired within the same imaging time could be increased around 6 fold, if a smaller stack was acquired with only the DAPI channel. This means the number of cells could increase from 1000-3000 to around 6000-18,0000 per condition, increasing the sensitivity and accuracy of MN detection. Previously, FISH against two chromosomes was used to determine mis-segregation rates after reversine treatments ranging from 0.25 - 1 μM, by manual quantification of up to 3734 cells (Sansregret *et al*. 2017). The MN approach presents an increase in sensitivity, as lower doses of reversine can be used, and accuracy, as more cells can be quantified.

Automated detection of MN is not a novel method, however. Various studies have employed either existing image analysis software or custom-built software to detect MN, in images of giemsa or DAPI stained cells, and imaging flow cytometry data. Early studies, using Metafer MNScore, PathFinder, and Cell Profiler 2.0 respectively, developed analysis methods that proved as reproducible as manual quantification, (Varga *et al*. 2004; Decordier *et al*. 2009; Ramadhani and Purnami 2013). Automated counts using Metafer MNScore were around 35% less than visual counts, however. Recently, a more advanced method employing custom-built algorithms was developed to overcome the problem of varied staining intensity and background signal (Bahreyni Toossi *et al*. 2017). This improved the sensitivity of MN detection, however automated counts were still 18% less than manual counts. A method for detection of MN in images taken from imaging flow

cytometry has been developed recently, using a deep learning approach which is able to detect more subtle differences in image features (Rodrigues *et al*. 2021). Imaging flow cytometry will always have a lower resolution than confocal microscopy, however, as the random orientation of cells within the imaging chamber could result in the main nucleus obscuring the MN. The automated MN counting algorithm designed in this study has both a high accuracy and high throughput, providing advancements to the field.

3.5.3 Automated Centromere Counting

It is important to note that not all types of CIN will give rise to MN, and hence solely counting MN may lead to phenotypes being missed. For example, gene upregulations that cause genome doubling would be picked up by centromere counting, increasing the modal deviation, but these cells may not have increased numbers of MN. Sister chromatid nondisjunction could also lead to aneuploidy in the absence of MN, and some conditions may even increase the incidence of lagging chromosomes without increasing MN, if they can be resolved quickly and segregated to the main daughter nuclei. Indeed, RPE1 resolve lagging chromosomes very efficiently, with a recent study showing that only around 10% remain uncorrected and form MN (Sen *et al*. 2021). While the MN detection approach has a higher accuracy and lower noise, the centromere counting approach can detect a more diverse range of mechanisms that result in aneuploidy, therefore these assays are most powerful when used together.

The centromere counting approach provides a measure of aneuploidy in cells, by counting all chromosomes in interphase cells based on CENPA staining, taking into account all potential karyotypes and states of polyploidy. This is a novel approach; to date, there are no other studies that have attempted this. This is advantageous as it has been demonstrated that different chromosomes mis-segregate at different rates, with 1 and 2 showing an increased incidence of lagging after nocodazole washout (Worrall *et al*. 2018). It is not known, however, if this phenotype translates to different mechanisms that induce lagging chromosomes, or whether this is only seen in response to induction of extremely high levels of CIN by the drug treatment (40% of cells show lagging chromosomes, with an average of around 3 per cell). It is therefore prudent to

assess all chromosomes. Studies that only assess the mis-segregation of one or two chromosomes using methods such as FISH (Sansregret *et al*. 2017), chromosome labelling (Belmont and Straight 1998), or the HAC assay (Liskovykh *et al*. 2019), have a reduced sensitivity, as any mis-segregations of other chromosomes will not be detected. It is worth noting that while there are disadvantages associated with identification of only one or two chromosomes by FISH, the centromere counting assay developed in this project would be highly amenable to identifying single FISH foci. If all human chromosomes mis-segregated at an equal rate and only the status of one was being assessed, then only 1/46 of mis-segregation events would be detected. Theoretically this means that assessing all chromosomes increases assay sensitivity by 46 fold.

However, the centromere counting assay has a basal level of noise that compromises sensitivity, which is not found in manual assays where the readout is a small number of FISH foci, corresponding to one or two chromosomes. The metaphase spreads performed also show variation in chromosome count around the mode (Figure 3.3a, 3.3b), so it is likely that at least a proportion of this noise reflects real phenotypes. Indeed, the centromere counting assay was not as sensitive as MN counting, as it did not detect a significant change in aneuploidy at 0.15 μM reversine, which generated 3.37 MN/100 cells. Advanced statistical modelling of the centromere counting data was not possible, as varying amounts of noise between experiments meant the model did not always fit the data well. Full width half max (FWHM) of the centromere count histograms was also performed, however this was not sensitive enough to detect significant differences. The modal deviation method worked well, however the ‘Aneuploid Proportion’ calculated is an estimate only, as this population of data also contains most of the noise. The analysis therefore overestimates the size of the aneuploid population, and this represents a caveat of the approach. The exact cause of the extremely low counts around 20 is not clear. One important experiment to validate the results obtained from centromere counting by CENPA staining would be to use an all-centromere FISH probe, using a different staining protocol but the same imaging protocol and centromere counting algorithm. This would confirm that CENPA staining identifies all centromeres within the cell.

Single cell whole genome sequencing (scWGS) is becoming increasingly popular as a method for characterising CIN, with the advantage of being able to detect structural CIN. One study developed tools to analyse sequencing data to identify copy number variation of whole chromosomes or chromosome fragments (Bakker *et al*. 2016). Array comparative genomic hybridisation (aCGH) was used as a control, which gives a readout of the average copy number from a bulk population, while scWGS was able to resolve the intratumour heterogeneity present. Recently, the accuracy of FISH and scWGS was investigated using trisomic fibroblast cell lines (Andriani *et al*. 2019). This study found that using a single FISH probe to quantify aneuploidies led to increased false positives, which could be solved by quantifying a second probe, while low coverage scWGS was more prone to false negatives. There are many studies using scWGS to detect complex structural CIN, including rearrangements (Sanders *et al*. 2020), breakage-fusion-bridge cycles (Umbreit *et al*. 2020), and chromothripsis (Cortés-Ciriano *et al*. 2020). In comparison, the centromere counting approach only measures whole chromosome aneuploidy and will never be able to provide information on structural CIN. Using the centromere count as a measure of whole chromosome aneuploidy may result in an overestimation, as structural events that disrupt centromere number such as dicentric chromosome formation would cause false positive readings of numerical CIN. Performing scWGS on hits identified by centromere and MN counting would be ideal to profile the exact chromosomal changes observed after a particular gene upregulation.

3.6 Conclusions

The work in this chapter led to the development of a novel automated image analysis pipeline to identify CIN and aneuploidy in cells, that improves on current methods used to detect these phenotypes. This segments images, applies ML-based filters to isolate non-contacting G1 cells, performs spot counting, and detects MN using deep neural networks. Using drugs to chemically induce CIN, the pipeline was demonstrated to accurately detect changes in chromosome number by counting centromeres in cells stained with CENPA, and MN formed by chromosome segregation errors. Applying these methods to a CRISPR upregulation screen identified *KIF11* and *NEK2* as significant hit genes, that cause CIN and aneuploidy when upregulated. In particular, KIF11 caused a

striking increase in MN/100 cells and was therefore taken forward for further phenotypic investigation.

Further investigation of the *NEK2* phenotype was not performed. Firstly, the *NEK2* data were obtained at a later stage in the project, and thus it was chosen to focus on *KIF11* in the interest if time. Secondly, overexpression of NEK2 has long been known to induce premature centrosome splitting, increased mitotic duration, and lagging chromosomes (Fry *et al*. 1998a; Lee and Gollahon 2013). In comparison, the cellular effects of *KIF11* overexpression were less well studied, therefore representing a more novel finding.

Chapter 4: Mechanistic Investigation of *KIF11* Upregulation

KIF11 is a mitotic kinesin with functions throughout all stages of mitosis, reviewed in section 1.4. This chapter describes the identification of specific phenotypes observed upon KIF11 upregulation, using a range of microscopy techniques. The fate of *KIF11^{up}* cells was investigated, to determine how this impacts cells. Investigation into the molecular mechanism was performed, to determine the exact cause of CIN and aneuploidy in these cells.

4.1 Fixed Imaging of *KIF11^{up}* Cells Identifies Mitotic Catastrophe, Lagging, and Misaligned Chromosomes upon KIF11 Upregulation

To investigate *KIF11* as a target gene causing aneuploidy and MN upon CRISPR upregulation, cells were fixed and stained for DAPI, α-tubulin, CREST and pericentrin (PCNT; Figure 4.1a). An immediate observation in *KIF11^{up}* cells was the presence of cells with fragmented nuclei, which appeared to have undergone mitotic catastrophe. *KIF11^{up}* cells showed significantly more interphase nuclei with this phenotype ($p<0.0001$, Fisher's Exact test; Figure 4.1b).

To further investigate this phenotype, mitotic cells were analysed (Figure 4.2a). qPCR firstly confirmed a significant increase in KIF11 mRNA level, similar to that achieved in the cells analysed using the HCS pipeline (Figure 4.2b). Inspection of these slides revealed metaphase cells showing disordered DAPI staining, indicating chromosomes were not being aligned properly at the metaphase plate. Analysis of metaphases revealed that the proportion of *KIF11^{up}* cells with misaligned chromosomes was over 3-fold higher than that of EV cells (4.45% vs 16.72%, $p<0.001$, Fisher's Exact test; Figure 4.2c). Inspection of PCNT staining revealed that *KIF11^{up}* cells were likely experiencing fragmentation of the PCM, as cells with multiple PCNT foci were frequently observed. Quantification showed the proportion of cells with >2 PCNT foci significantly increased in *KIF11^{up}* cells during metaphase ($p<0.001$; Figure 4.2d). The presence

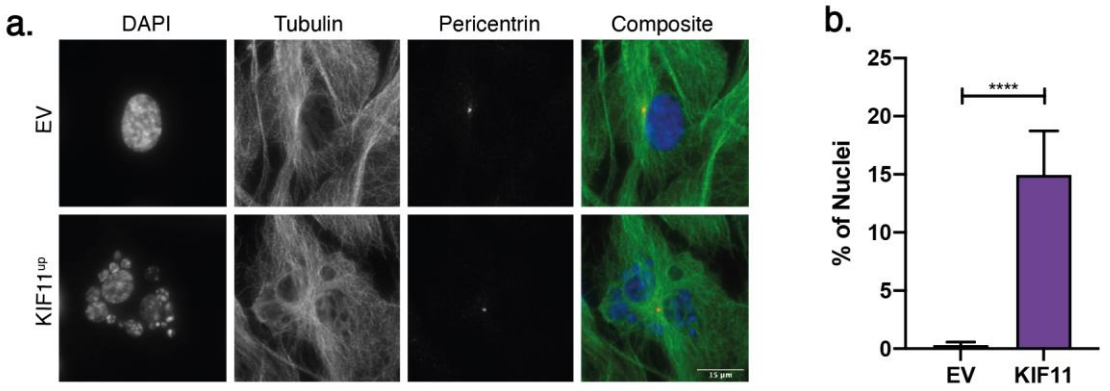

Figure 4.1 Mitotic Catastrophe upon KIF11 Upregulation a. Example images, showing fragmented nuclei with multiple micronuclei upon KIF11 upregulation, indicative of mitotic catastrophe. Scale bar = 15 µm. **b.** Quantification of the percentage of cells displaying the mitotic catastrophe phenotype. To avoid cells containing micronuclei from lagging chromosomes, only those with at least 3 seperate nuclear bodies were scored positive. N = 3, n >1100 cells, Fisher's Exact test,

of cells with misaligned chromosomes suggests there may be increased SAC activity in *KIF11^{up}* cells due to kMT attachment errors. To confirm this hypothesis, cells were fixed in PTEMF and stained for CENPA and MAD2 (Figure 4.2e). As expected, significantly more *KIF11^{up}* cells had MAD2 positive kinetochores when compared to EV ($p<0.01$, Fisher's Exact test; Figure 4.2f). Within the MAD2 positive proportions, there was no difference in the individual number of MAD2 foci per cell when comparing *KIF1^{up}* and EV cells.

Prometaphase cells were also imaged to assess PCNT foci. Preliminary data from two repeats showed a significant increase in *KIF11^{up}* cells with >2 PCNT foci compared to EV ($p<0.05$, Fisher's Exact test), suggesting that spindle pole fragmentation happens during or before prometaphase. However, 12% of *KIF11^{up}* prometaphase cells show fragmentation, compared to 23.5% of *KIF11^{up}* metaphase cells, suggesting that fragmentation also occurs in late prometaphase/early metaphase.

Anaphase cells were also subjected to phenotypic analysis. *KIF11^{up}* anaphase cells showed similar PCNT staining, with a significant proportion of cells exhibiting >2 PCNT foci ($p<0.001$; Figure 4.3a, 3b). Inspection of the images showed there was often two bright PCNT foci forming what looked to resemble a bipolar spindle, however many smaller PCNT foci were visible dispersed near the cell cortex, which remained able to nucleate microtubule formation, (small asters

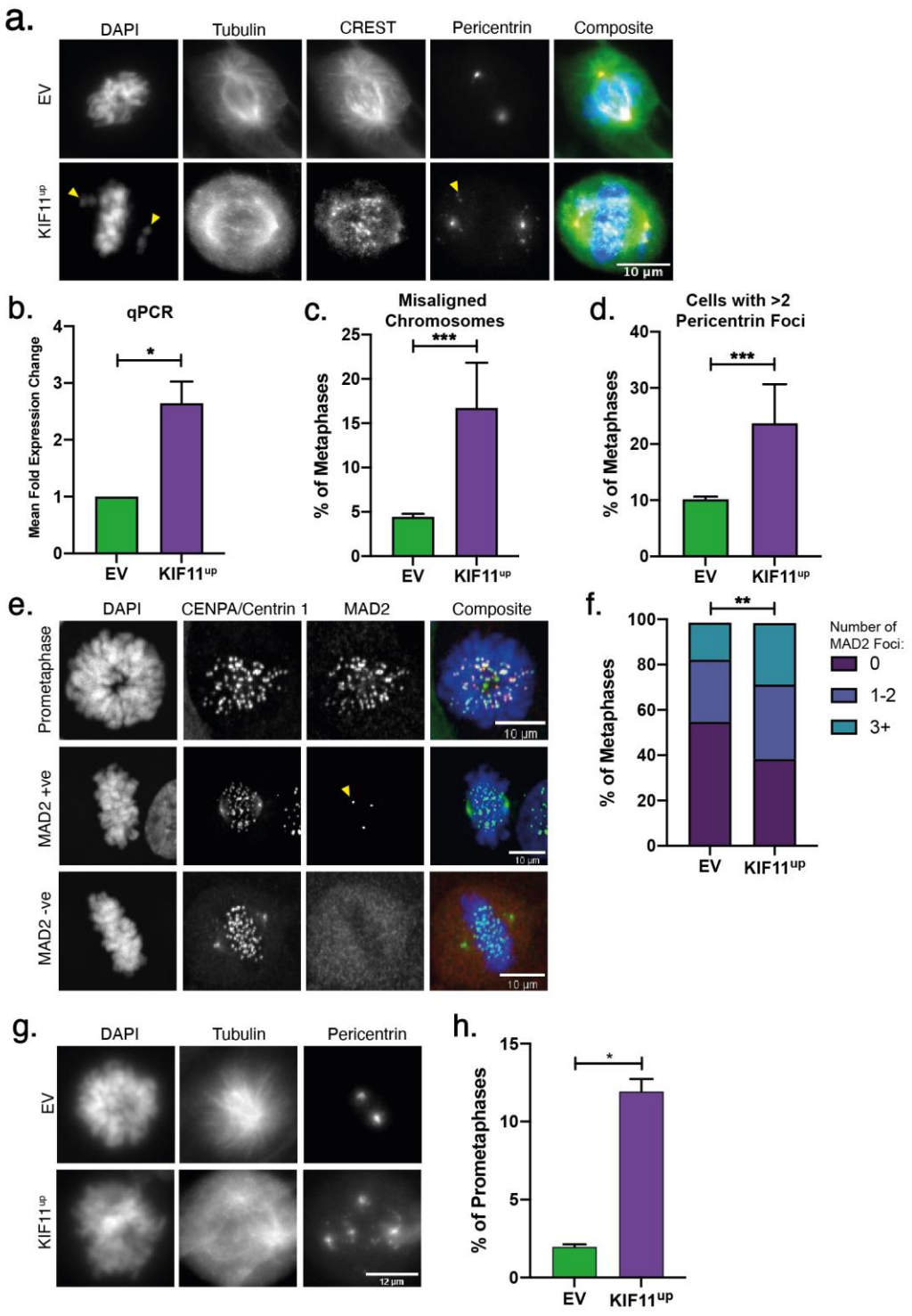

Figure 4.2 KIF11 Upregulation Causes Erroneous Metaphase a. Example images, showing dispersed pericentrin staining and erroneous chromosome segregation, due to multiple spindle poles. **b.** qPCR quantification of CRISPR gene upregulation of KIF11, N=3, error bars = SEM, paired student's T-test. **c.** Quantification of metaphase cells presenting with chromosome congression errors. **d.** Quantification of metaphase cells with >2 pericentrin foci, n >300 cells, N=3, Fisher's Exact test, error bars = SEM. **e.** Example images of mitotic cells stained for MAD2 and CENPA. **f.** Quantification of the number of MAD2 positive kinetochores in EV and KIF11^{up} cells, n > 120 cells, N=3, Fisher's Exact test. **g.** Example images of prometaphase cells with normal and fragmented PCNT. Quantification of prometaphase cells presenting with >2 pericentrin foci. **h.** N = 2, n > 80 cells, Fisher's Exact test, error bars = SEM.

can be seen in the lower panel images; Figure 4.3a). This increased PCNT foci phenotype was often associated with lagging chromosomes and multipolar spindles as shown in the example image; however lagging chromosomes were also observed in anaphases with 2 PCNT foci, where centrosome integrity was unaffected. Quantification showed a significant increase in both centric ($p<0.05$) and acentric ($p<0.001$) lagging chromosomes (Figure 4.3c and 3d, respectively).

To further support these results, *KIF11^{up}* cells were stained for CENPA, and images were taken of cells with up to 2 micronuclei. Any cells that had undergone mitotic catastrophe were avoided, as these most likely represented cells that had

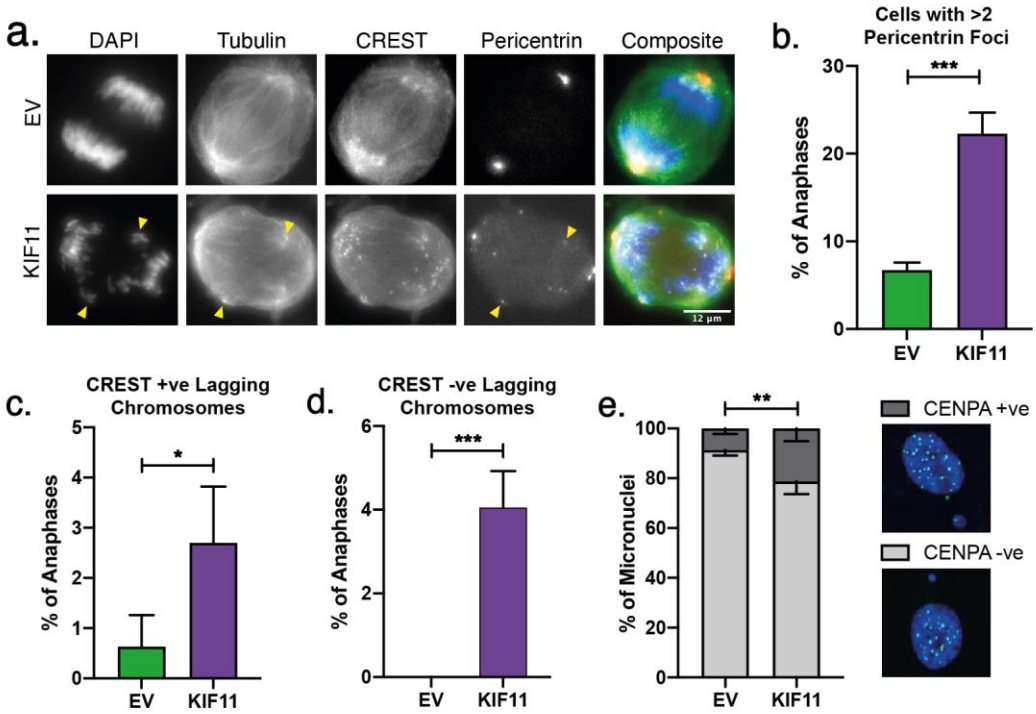

Figure 4.3 KIF11 Upregulation Causes Erroneous Anaphase a. Example images, showing dispersed pericentrin staining and erroneous chromosome segregation, due to multiple spindle poles. Scale bar = 12 µm. **b.** Quantification of anaphase cells with >2 pericentrin foci. **c.** Quantification of anaphase cells with CREST-positive lagging chromosomes and, **d.** CREST-negative. **b-d.** n >300 cells, N=3, Fisher's Exact test, error bars = SEM. **e.** Quantification of CENPA-positive vs CENPA-negative micronuclei, n >130 micronuclei, N=3, Fishers Exact test, error bars = SEM.

experienced spindle pole fragmentation, which increases centric lagging chromosomes. Quantification of CENPA foci within micronuclei revealed a significant increase in the proportion of CENPA positive micronuclei ($p<0.01$, Fisher's Exact test), suggesting KIF11 upregulation increases the amount of centric lagging chromosomes. Unexpectedly, for both EV and *KIF11^{up}* cells the

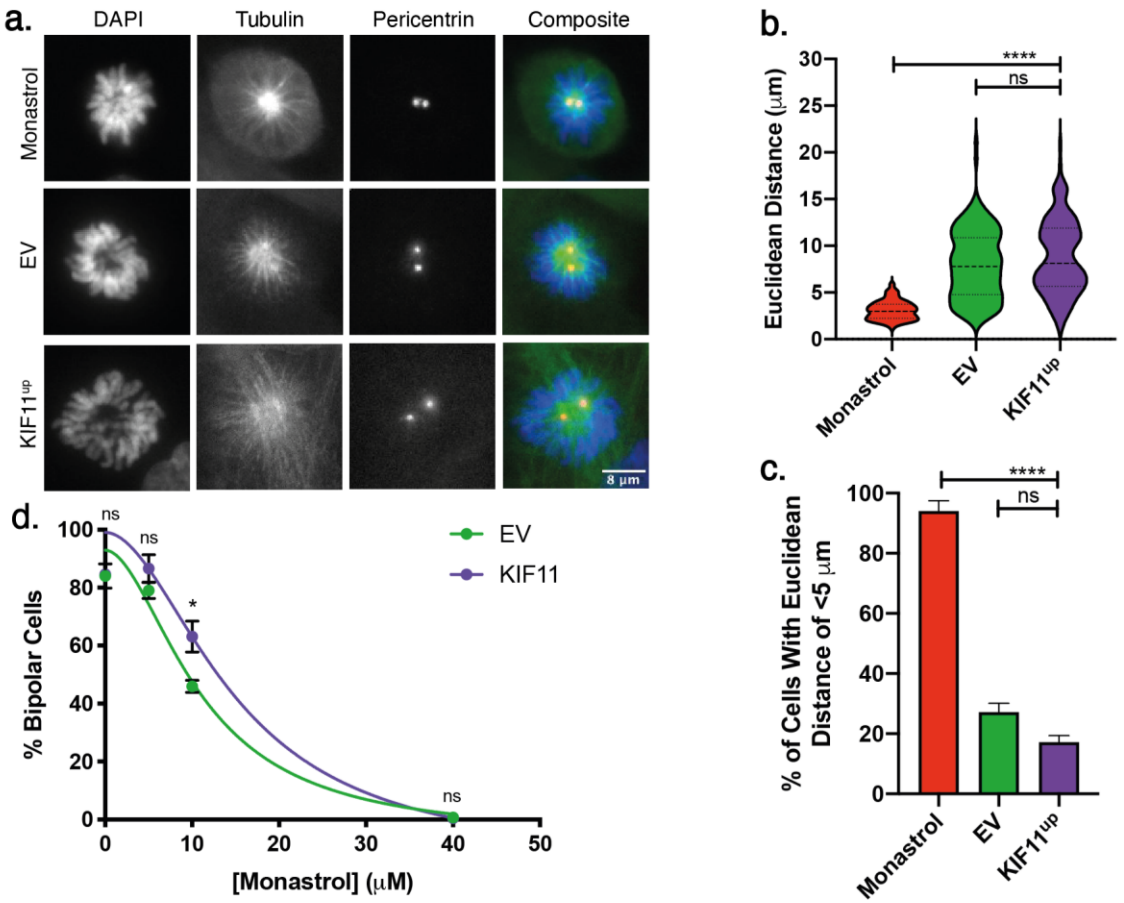

Figure 4.4 KIF11 Upregulation does not Increase Monopolar Spindle Formation in RPE1 Cells a. Example images, showing a positive control monopolar spindle induced by monastrol treatment, alongside potential monopolar spindles from EV and KIF11^{up} cells. Scale bar = 8 µm. **b.** Quantification of the euclidean distance (distance between centrosomes), measured through XYZ. N = 3, n = >150 cells, one-way ANOVA with Tukey's multiple comparisons test. **c.** Quantification of the percentage of cells with a euclidean distance <5 µm. Chi^2 followed by pairwise Fisher's Exact tests, with bonferroni p value correction for multiple comparisons, error bars = SEM. **d.** Plot showing the proportion of bipolar cells with increasing doses of monastrol. Curves were fitted using logistic regression, however IC50 values were not accurrate due to insufficient datapoints, and hence not reported. N = 2, n >100 cells, error bars = SD, two-way ANOVA with Šidák's multiple comparisons test.

majority of micronuclei were CENPA negative, (98.33% and 78.73% respectively; Figure 4.3e), which does not fit with the observation of similar numbers of CREST-positive vs CREST-negative lagging chromosomes observed previously (compare Figure 4.3c and 3d, purple bars).

Previous work by Castillo *et al* has shown that 4- to 9-fold overexpression of *KIF11* causes an increase in monopolar spindle formation in transgenic MEFs. To confirm whether CRISPR upregulation of KIF11 also induces this phenotype in epithelial cells, RPE1 were stained for PCNT and tubulin to visualise spindle formation (Figure 4.4a). Monastrol was used as a positive control for monopolar spindles. As these spindles were indistinguishable from prometaphase spindles,

cells were selected for imaging in a non-biased fashion based on ring-like DAPI staining. Measurement of the Euclidean distance between the centrosomes showed no significant difference between EV and *KIF11^{up}* cells ($p>0.05$, one-way ANOVA with Tukey's multiple comparisons tests; Figure 4.4b, suggesting CRISPR upregulation of KIF11 does not affect monopolar spindle formation. There was also no significant difference in the proportion of cells that had a Euclidean distance of <5 μm between EV and *KIF11^{up}* (Figure 4.4c).

Finally, monastrol was also used to test sensitivity to monopolar spindle formation in EV and *KIF11^{up}* cells. Cells were treated with increasing doses of monastrol for 16 hours, and then fixed for imaging, selecting and classifying cells with ring-like DAPI staining as monopolar. At 10 μM monastrol, *KIF11^{up}* cells showed a higher proportion of bipolar spindles than monopolar spindles compared to EV (63.1 vs 45.9%, respectively, $p<0.05$, two-way ANOVA with Šídák's multiple comparisons tests; Figure 4.4d). This suggests *KIF11^{up}* cells are able to overcome sub-optimal doses of monastrol more easily.

4.2 Live Imaging *KIF11^{up}* Cells Identifies Mitotic Catastrophe, Lagging and Misaligned Chromosomes upon *KIF11* Upregulation

To gain further insight as to how *KIF11* upregulation perturbs mitosis, *KIF11^{up}* cells were imaged overnight to capture mitosis, using the SiR-DNA dye to visualise chromosomes. As expected in light of the data from fixed cells showing unaligned chromosomes and increased MAD2 positive cells, *KIF11^{up}* cells took significantly longer to complete mitosis compared with EV. This held true when cells were imaged 48 hours after transduction (20.91 minutes vs 25.83 minutes, $p<0.01$, Student's T-test), and 1 week after transduction (21.56 minutes vs 23.95 minutes, $p<0.01$; Figure 4.5d). At 48 hours post-transduction two cells had extreme difficulty aligning chromosomes, taking 321 and 93 minutes respectively to complete mitosis. The maximum duration observed in *KIF11^{up}* cells 1-week post-transduction was 54 minutes, suggesting cells with extreme phenotypes are not viable, and do not proliferate beyond 1-week post-transduction.

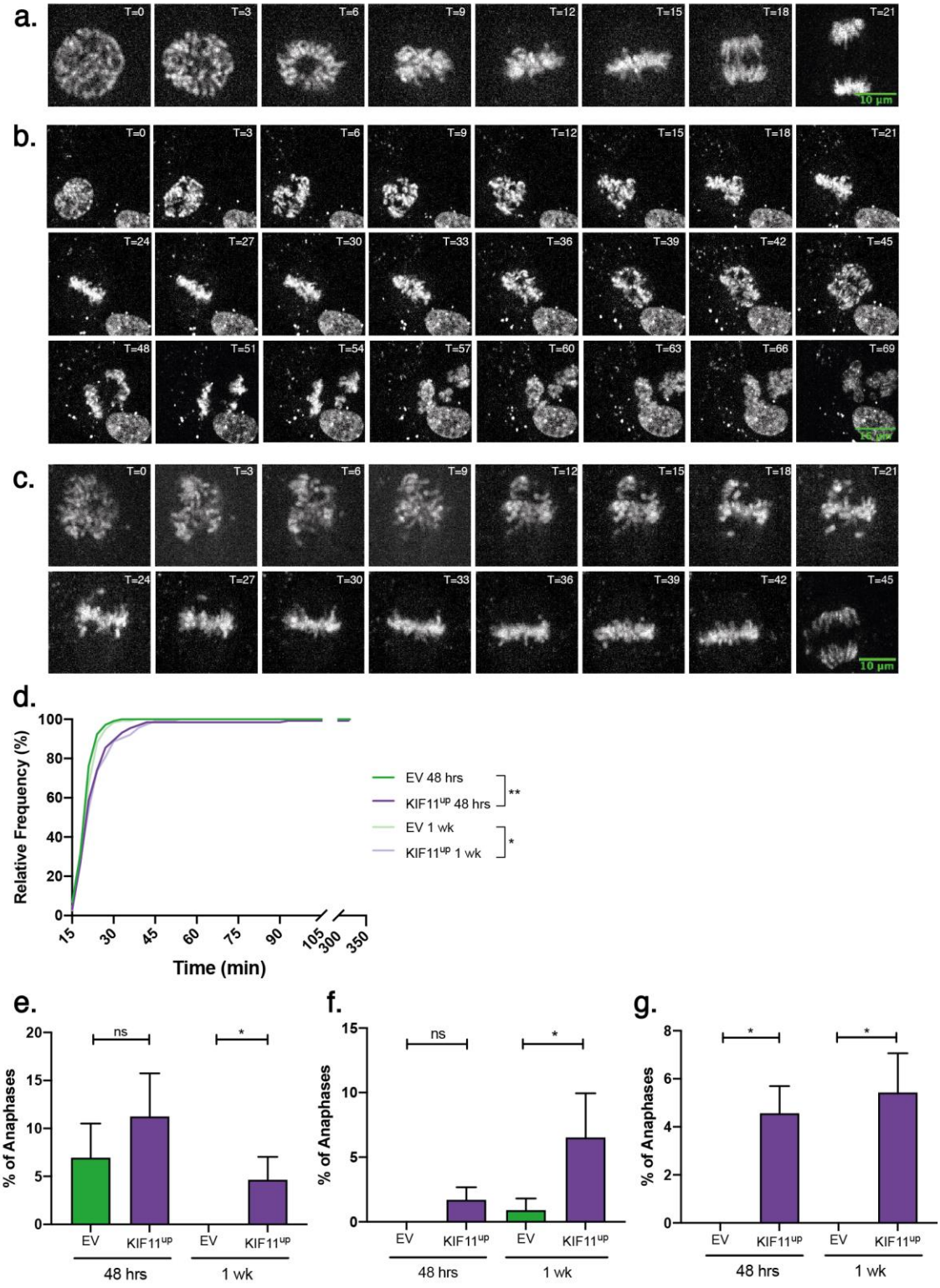

Figure 4.5 Live Imaging of KIF11^{up} Cells Identifies Erroneous Mitosis Example images from timelapse movies showing cells stained with SiR-DNA and undergoing **a.** normal mitosis, **b.** mitotic catastrophe, and **c.** delayed chromosome congression. **d.** Mitotic timings of EV and KIF11^{up} cells, 48 hours and 1-week post-transduction, N = 3, n >100 cells, Mann-Whitney test. **e.** Quantification of the number of cells experiencing lagging chromosomes that swere not associated with mitotic catastrophe. **f.** Quantification of the number of cells experiencing misaligned chromosomes. **g.** Quantification of the number of cells experiencing mitotic catastrophe. **e-g.** N=3, n >100 cells, Fisher's Exact test, error bars = SEM.

Consistent with data from fixed cells, there was an increase in cells with lagging chromosomes in the live cell imaging, and an increase in the proportion of cells experiencing a delay to chromosome alignment (Figures 4.5e and 4.5f, respectively). There was also an increase in cells that experienced an aberrant anaphase that led to mitotic catastrophe (Figure 4.5g. These data support the hypothesis of spindle pole fragmentation leading to mitotic catastrophe. During anaphase, bundles of chromosomes appeared to be pulled in different directions, resulting in an interphase cell with a fragmented nucleus (Figure 4.5b, Supplementary Movie 1a & 1b).

To confirm that cells were experiencing mitotic catastrophe and investigate cell fate, *KIF11^{up}* cells were imaged for a period of 60 hours using SiR-DNA to identify chromosomes and differential interference contrast to visualise the cytoplasm and cell cortex. Mitotic cells within the first 24 hours of imaging were tracked, to investigate the mitotic phenotype of the two daughter cells (Figure 4.6a). As expected, over 93% of EV mother cells divided normally during the first division, and 97.9% of their daughter cells went on to also divide normally, with the remaining 2.1% arresting in interphase (Figure 4.6b & 4.6c). In contrast, in the 5% of EV mother cells that experienced lagging DNA, only 80% of the daughter cells went on to divide normally, with 20% arresting in interphase (Figure 4.6b & 4.6d).

80% of *KIF11^{up}* mother cells divided normally, and of these, 79.8% of the daughter cells divided normally, 2.81 experienced mitotic catastrophe, 1.7% experienced lagging DNA, and 11.2% arrested in interphase (Figure 4.6e & 4.6f). This is higher than the equivalent rate of arrested cells observed in EV daughter cells that arose from normal mother cell divisions, 2.1%, suggesting that *KIF11^{up}* could be delaying the cell cycle even in the absence of visible spindle pole defects or lagging chromosomes. Indeed, quantification of cell cycle timings showed that *KIF11^{up}* daughter cells had significantly longer cell cycles than EV daughter cells, ($p<0.05$, Welch's T-test, Figure 4.6i).

None of the *KIF11^{up}* daughter cells that arose from mother cells that experienced mitotic catastrophe went on to divide normally. 77.4% experienced arrest, 19.4%

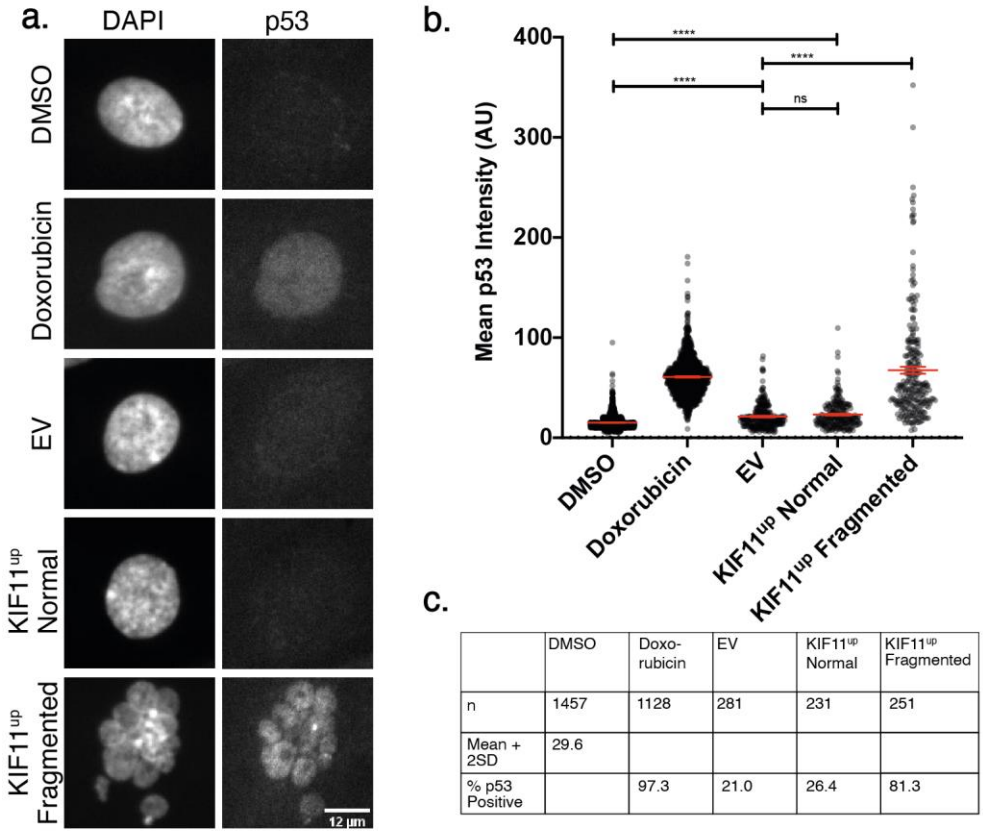

c.

	DMSO	Doxo-rubicin	EV	KIF11up Normal	KIF11up Fragmented
n	1457	1128	281	231	251
Mean + 2SD	29.6				
% p53 Positive		97.3	21.0	26.4	81.3

Figure 4.7 KIF11^{up} Cells that Undergo Mitotic Catastrophe Activate p53 **a.** Example images of cells stained for p53 after treatment with DMSO or Doxorubicin, or transduction with EV or KIF11^{up} lentivirus. Scale bar = 12 µm. **b.** Quantification of the mean nuclear p53 signal intensity. N = 3, n > 200 cells EV/KIF11^{up}, >1000 cells DMSO/Doxorubicin, error bars = mean + SEM, one-way ANOVA with Tukey's multiple comparison's test. **c.** comparis Table showing individual n numbers and the percentage of cells that are p53 positive, calculated as the percentage of cells with signal intensities higher than the mean + two standard deviations of DMSO treated cells.

experienced apoptosis (characterised by morphological rounding and condensation of DNA), and a small number (3.2%) of cells were able to re-enter the cell cycle and experienced mitotic catastrophe again. In these daughter cells, the mother cells experienced more subtle defects in anaphase with a less severe nuclear fragmentation, thus escaping p53 activation and cell cycle arrest/cell death.

Finally, it is worth noting that lagging DNA and mitotic catastrophe phenotypes occurred in a mutually exclusive fashion. None of the *KIF11^{up}* mother cells that experienced lagging chromosomes gave rise to daughter cells that experienced mitotic catastrophe, and the same is true in reverse, none of the *KIF11^{up}* mother cells that experienced mitotic catastrophe gave rise to daughter cells that experienced lagging chromosomes. These data provide evidence in support of

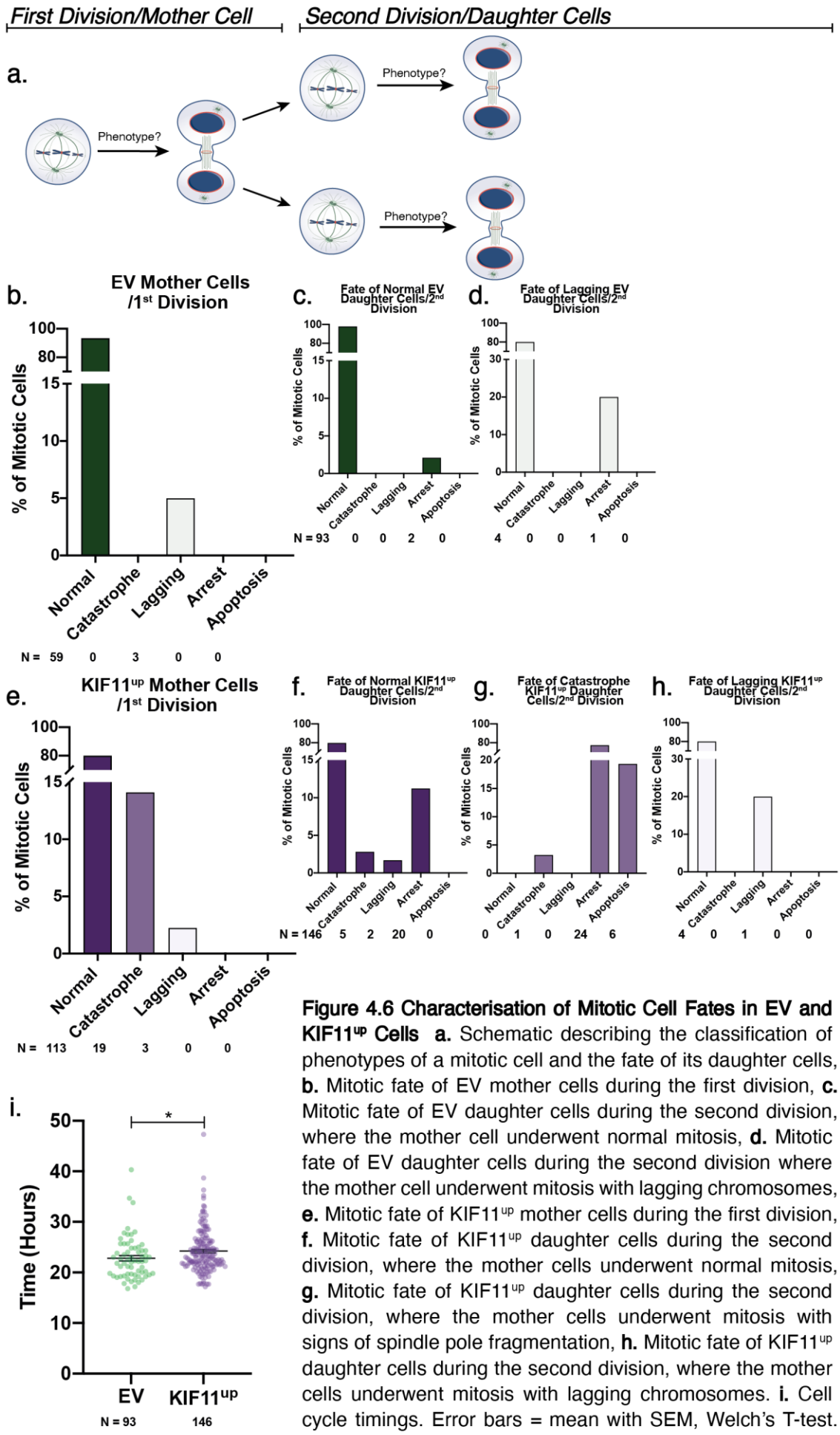

Figure 4.6 Characterisation of Mitotic Cell Fates in EV and KIF11^{up} Cells **a.** Schematic describing the classification of phenotypes of a mitotic cell and the fate of its daughter cells, **b.** Mitotic fate of EV mother cells during the first division, **c.** Mitotic fate of EV daughter cells during the second division, where the mother cell underwent normal mitosis, **d.** Mitotic fate of EV daughter cells during the second division where the mother cell underwent mitosis with lagging chromosomes, **e.** Mitotic fate of KIF11^{up} mother cells during the first division, **f.** Mitotic fate of KIF11^{up} daughter cells during the second division, where the mother cells underwent normal mitosis, **g.** Mitotic fate of KIF11^{up} daughter cells during the second division, where the mother cells underwent mitosis with signs of spindle pole fragmentation, **h.** Mitotic fate of KIF11^{up} daughter cells during the second division, where the mother cells underwent mitosis with lagging chromosomes. **i.** Cell cycle timings. Error bars = mean with SEM, Welch's T-test.

KIF11 functioning by two separate mechanisms to cause the observed phenotypes.

After the observation of cell cycle arrest following mitotic catastrophe in *KIF11^{up}* cells, immunofluorescence was performed to identify whether this was a p53-dependant arrest. DMSO and doxorubicin treated cells were used as negative and positive controls for p53 expression, respectively. Fragmented *KIF11^{up}* cells exhibited brighter p53 staining, which was significantly increased compared to EV cells ($p<0.001$, one-way ANOVA with Tukey's multiple comparisons tests; Figure 4.7). However, EV and normal *KIF11^{up}* cells showed significantly increased p53 staining compared to DMSO ($p<0.0001$, $p<0.0001$). There was no significant difference between EV and normal *KIF11^{up}* cells ($p>0.05$), suggesting that the transduction itself causes p53 activation.

Using DMSO treated cells as a control for p53 negative nuclei, the percentage of p53 positive cells was calculated. As expected, after doxorubicin treatment 97.3% of cells were p53 positive. In comparison, only 81.3% of the fragmented *KIF11^{up}* cells were p53 positive, suggesting that mitotic catastrophe does not always result in p53 activation.

4.3 Identification and Characterisation of *KIF11^{up}* Induced Spindle Pole Fragmentation

To confirm whether the observed phenotype is indeed spindle pole fragmentation, eGFP-Centrin 1 was introduced into the RPE1-MPH cell line. As the efficiency of CRISPR activation dropped over time in RPE1-MPH, and it had already undergone one round of clonal selection, a bulk population expressing the eGFP-Centrin1 marker was isolated by FACS. The RPE1-MPH-eGFP-Centrin 1 cell line could then be used for *KIF11* upregulation and investigation of centrosome phenotypes.

RPE1-MPH-eGFP-Centrin 1 *KIF11^{up}* cells were stained for DAPI, KIF11, and α-tubulin, which allowed for direct measurement of spindle pole fragmentation by assessing whether spindle poles were eGFP-Centrin 1-positive or -negative (Figure 4.8a). Analysis of a total 53 *KIF11^{up}* cells with multiple spindle poles

identified that 71.70% were due to spindle pole fragmentation, 22.64% were due to supernumerary centrosomes, and 5.66% were due to a combination of the two phenotypes (Figure 4.8b).

These images were subsequently used to quantify KIF11 intensity at different stages during mitosis; the different ROIs used are summarised in Figure 4.8c. These were chosen based on the known functions of KIF11, namely centrosome separation during prometaphase, and sliding of antiparallel microtubules during metaphase and anaphase. At the centrosomes of prometaphase cells and in the cytoplasm of metaphase cells, there was no significant difference in the KIF11: α-Tubulin ratio between EV and *KIF11*^{up} cells ($p>0.05$, one-way ANOVA with Tukey's multiple comparisons tests; Figure 4.8d). A significant increase in the KIF11: α-Tubulin ratio was observed between EV and *KIF11*^{up} multipolar cells in the whole anaphase spindle ($p<0.0001$), and the interpolar region in anaphase ($p<0.0001$). However, there was no significant difference between EV and *KIF11*^{up} bipolar cells for these same ROIs ($p>0.05$; Figures 4.8e, 4.5g, 4.8h). In the metaphase whole spindle ROI, there was a significant increase in the KIF11: α-Tubulin ratio between both EV and *KIF11*^{up} bipolar cells ($p<0.0001$), and EV

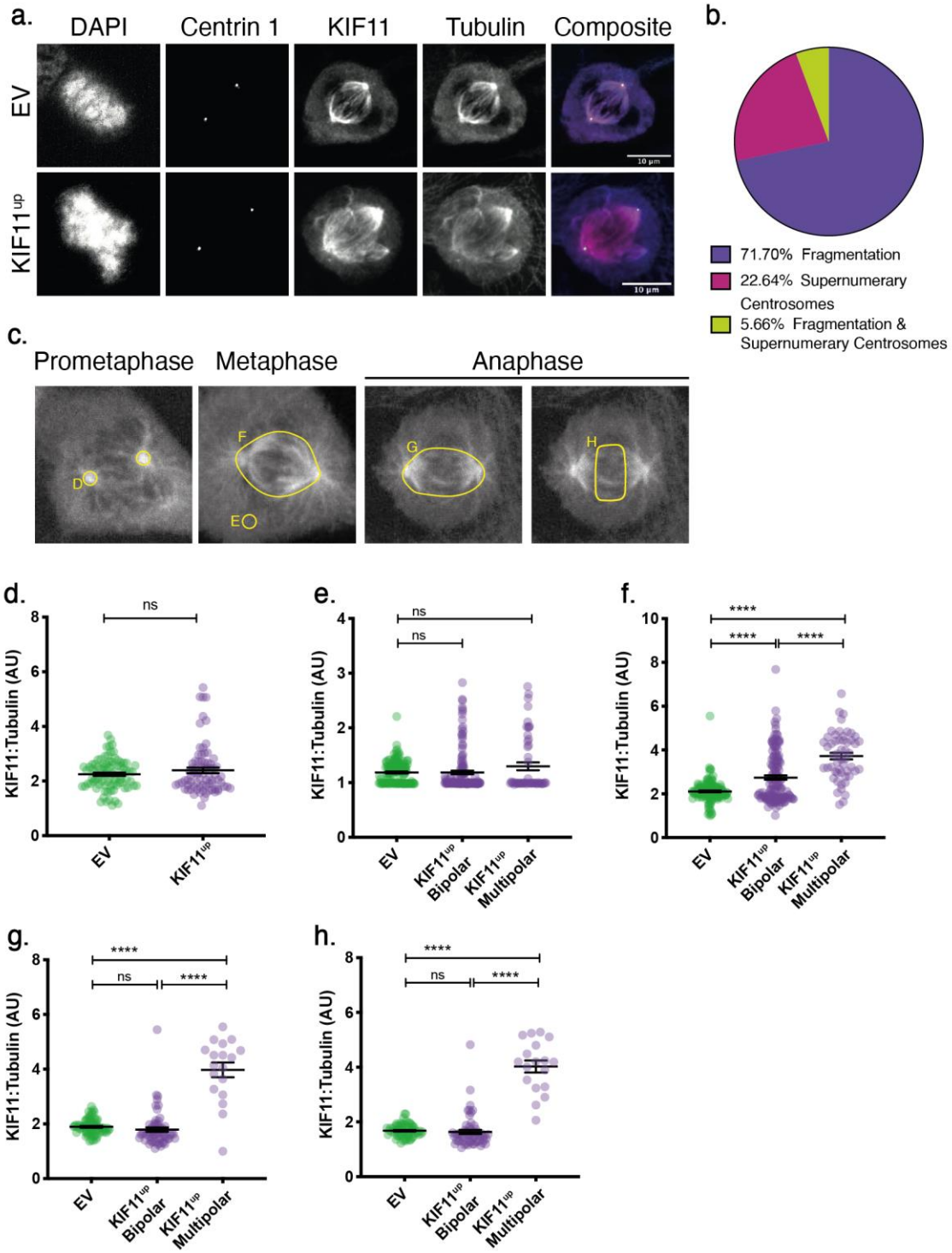

Figure 4.8 KIF11 Upregulation Increases the Amount of KIF11 on Metaphase and Anaphase Spindles a. example images showing cells with DAPI, Centrin 1, KIF11 and α-Tubulin staining, **b.** Phenotype analysis of cells with >2 spindle poles, **c.** example images showing the different regions of interest (ROIs) from which KIF11 signal intensity was measured, **d-h.** Graphs showing the ratio of KIF11:Tubulin signal measured in **d.** Prometaphase centrosomes (ROI D, N=3, error bars = SEM, Student's T-test), **e.** Cytoplasm of metaphase cells (ROI E), **f.** Metaphase whole spindle (ROI F), **g.** Anaphase whole spindle (ROI G), **h.** Anaphase interpolar microtubules (ROI H). N = 3, one-way ANOVA with Tukey's multiple comparisons test, error bars = SEM.

a.

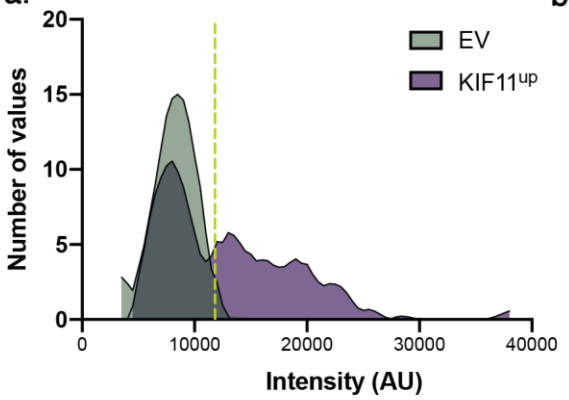

b.

Mean KIF11 intensity in EV cells	8213.9
SD	1804.8
Mean + 2SD	11823.5
% of KIF11^{up} cells where KIF11 intensity > 11823.5	45.3

Figure 4.9 KIF11 is Upregulated in 45.3% of KIF11^{up} Cells **a.** Histogram showing KIF11 signal intensity values measured in EV cells (metaphase whole spindle ROI), shown with second order smoothing, using a 7-sample moving average. Line at mean + 2 Standard Deviations (SD) of EV KIF11 intensity values. **b.** table of statistics used to calculate the proportion of KIF11^{up} cells that show significant upregulation of KIF11 compared to EV cells.

and *KIF11^{up}* multipolar cells (p<0.0001; Figure 4.8f). EV cells in prometaphase, metaphase and anaphase show KIF11 colocalisation with α-tubulin, suggesting that KIF11 localises across the entire mitotic spindle. These results confirmed that the excess KIF11 in *KIF11^{up}* cells does indeed result in increased KIF11 loading onto the spindle during mitosis.

This dataset allowed for calculation of the percentage of cells that significantly upregulate *KIF11* compared to EV cells. The values measured from the metaphase whole spindle ROI in EV cells were plotted in a histogram, and the mean and standard deviation calculated (Figure 4.9a). An intensity cut off of the mean + 2 standard deviations (11823.5) was set, and values above this measured from *KIF11^{up}* cells were classified as significantly upregulating *KIF11*. After smoothing the histogram using a moving average, this cut off lines up well with the second peak observed in the histogram of KIF11 intensity values measured in *KIF11^{up}* cells. These calculations showed that *KIF11* upregulation at the protein level was observed in 45.3% of cells (Figure 4.9b).

After better characterising spindle pole fragmentation in fixed cells, the RPE1-MPH-eGFP-Centrin 1 cell line was employed to observe the phenotype in live cells (Figure 4.10a, Supplementary Movie 2). RPE1-MPH-eGFP-Centrin 1 *KIF11^{up}* cells were imaged overnight, using SiR-Tubulin to visualise the spindle. 16 cells with spindle pole fragmentation were identified, based on the presence

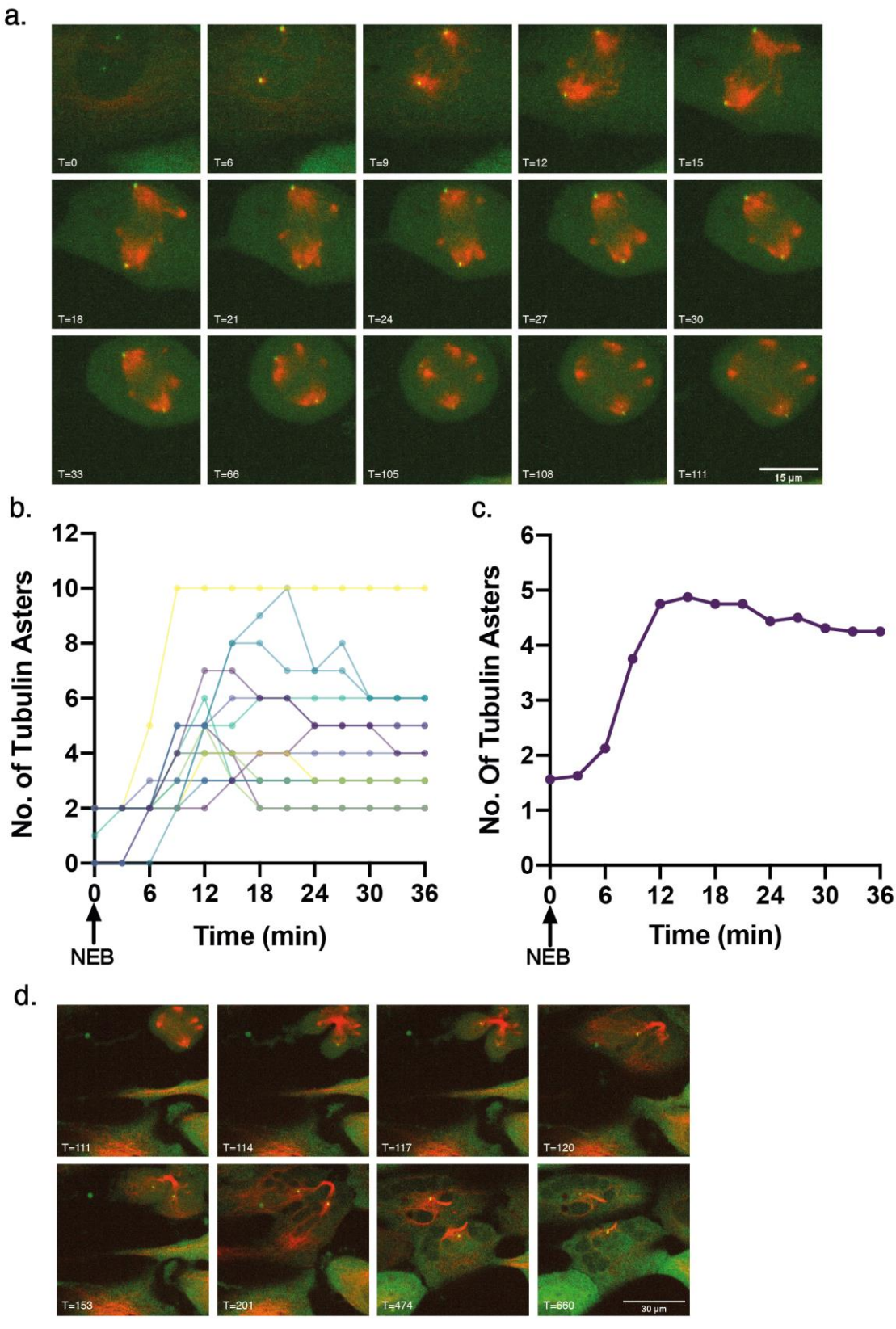

Figure 4.10 Direct Observation of Spindle Pole Fragmentation and Mitotic Catastrophe in KIF11^{up} Cells a. Example images from a timelapse, showing a cell with spindle pole fragmentation, **b.** Quantification of the number of tubulin asters with respect to time, aligned at NEB. n = 16 **c.** Average number of tubulin asters with respect to time **d.** Example images from a timelapse showing a cell undergoing mitotic catastrophe in anaphase due to spindle pole fragmentation. **a & d.** siR-Tubulin shown in red, eGFP-Centrin 1 shown in green, T = time in minutes.

of eGFP-Centrin 1 negative tubulin asters. Using the background fluorescence from eGFP-Centrin 1 to identify NEB, the timing of spindle pole fragmentation was quantified (Figure 4.10b). In all 16 cells, fragmentation was not observed until after NEB, taking an average of 9.75 minutes for fragmentation to become visible. The degree of fragmentation varied, with some cells developing up to 10 tubulin asters. These data confirm that spindle pole fragmentation is dependent on spindle formation. A degree of clustering was observed: when measuring the average number of spindle poles over time, the maximum average number of poles per cell, 4.88, is reached 15 minutes after NEB, however this stably reduces to 4.25 poles 33 minutes after NEB (Figure 4.10c).

This imaging was also able to confirm a direct link between spindle pole fragmentation and mitotic catastrophe. Observation of the 16 *KIF11*^{up} cells that experienced fragmentation showed that when cells attempted anaphase, this resulted in formation of fragmented interphase nuclei in the daughter cells, indicative of mitotic catastrophe (Figure 4.10d).

4.4 *HSET* Upregulation Partially Rescues KIF11 Induced Spindle Pole Fragmentation

Data from phenotypic analysis of fixed and live cells show that upregulation of *KIF11* increases the amount loaded onto the spindle during metaphase and anaphase, leading to spindle pole fragmentation. This could be due to disruption of the balance of forces within the spindle; excess KIF11 could generate excess outward pushing force on antiparallel microtubules. To investigate this hypothesis *HSET*, the molecular motor that opposes KIF11 activity (Mountain 1999), was upregulated simultaneously to KIF11 using CRISPR upregulation. Increased levels of HSET on the spindle should in theory increase the inward pulling forces on antiparallel microtubules, balancing the effect of increased KIF11.

A double transduction protocol was optimised to achieve similar levels of upregulation of each gene (Figure 4.11a), as upregulation could not be achieved when performing a simultaneous co-transduction of gRNAs targeting both *KIF11*

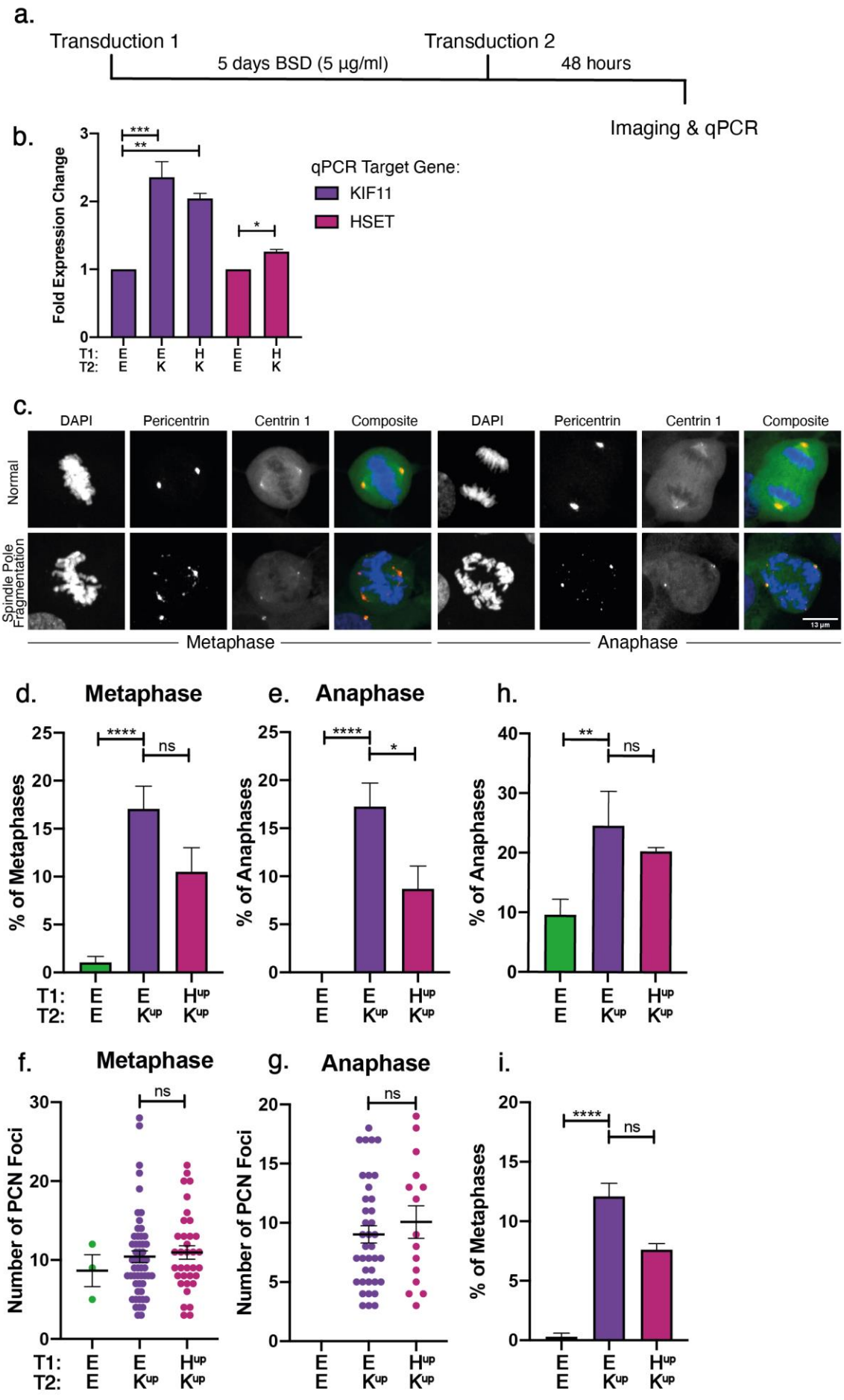
a.
Transduction 1
5 days BSD (5 µg/ml)
Transduction 2
48 hours
Imaging & qPCR
b.
Fold Expression Change
qPCR Target Gene:
KIF11
HSET
T1:
T2:
c.
DAPI
Pericentrin
Centrin 1
Composite
Normal
Spindle Pole Fragmentation
Metaphase
Anaphase
d. Metaphase
% of Metaphases
e. Anaphase
% of Anaphases
h.
% of Anaphases
f. Metaphase
Number of PCN Foci
g. Anaphase
Number of PCN Foci
i.
% of Metaphases
ns

Figure 4.11 CRISPR Upregulation of HSET Partially Rescues Spindle Pole Fragmentation in KIF11^{up} Cells a. Schematic showing the optimised experimental protocol for acheiving co-upregulation of two genes, **b.** quantification by qPCR of gene upregulation performed using the double transduction protocol, N = 3, one-way ANOVA with Tukey's/Student's T-test, E: Empty Vector, K: KIF11^{up}, H: HSET^{up}. **c.** Example images showing spindle pole fragmentation in metaphase and anaphase cells. **d.** Quantification of the percentage of cells with spindle pole fragmentation in metaphase and **e.** anaphase, **f.** Quantification of the number of PCN foci in metaphase cells with > 2 foci and **g.** anaphase cells with > 2 foci. **h.** Quantification of the percentage of anaphase cells with a normal spindle pole phenotype and lagging DNA, **i.** Quantification of the percentage of metaphase cells with misaligned chromosomes, **d, e, h & i.** N = 3, n > 200 cells, Chi^2 followed by pairwise Fisher's exact tests, with bonferroni p value correction for multiple comparisons, error bars = SEM, **f & g.** N = 3, Student's T-test, error bars = SEM.

and *HSET*. This involved an initial transduction (T1) followed by 5 days of selection, and a second transduction (T2), before harvesting of samples 48 hours later. Multiple gRNAs targeting the *HSET* promoter were tested but this gene proved difficult to activate. Targeting of *HSET* during T1 and *KIF11* during T2 resulted in a respective 1.26- and 2-fold increase in gene expression compared to control (EV/EV cells; $p<0.05$, Student's T-test; $p<0.01$, one-way ANOVA with Tukey's multiple comparisons tests; Figure 4.11b). Despite this difference, the level of *KIF11* upregulation was similar between EV/*KIF11^{up}* and *HSET^{up}*/*KIF11^{up}* cells, therefore enabling investigation of whether the small degree of *HSET* upregulation could partially rescue spindle pole fragmentation.

The double transduction protocol was performed in RPE1-MPH-eGFP-Centrin 1, which were then stained for PCNT to identify fragmented spindle poles (Figure 4.11c). Quantification of the proportion of cells with fragmentation showed a significant increase between EV/EV cells and EV/*KIF11^{up}* cells, in both metaphase and anaphase ($p<0.0001$, $p<0.0001$, Fisher's Exact test with Bonferroni p value correction; Figure 4.11d, 4.11e). When comparing EV/*KIF11^{up}* and *HSET^{up}*/*KIF11^{up}*, there were significantly less cells showing fragmentation in anaphase ($p<0.05$), and although not statistically significant, a similar reduction was observed in metaphase ($p>0.05$). The reduction is approximately half, suggesting that there was indeed a partial rescue of the phenotype. As HSET is known for its centrosome clustering function, the number of PCNT foci in cells with spindle pole fragmentation was quantified, to identify whether *HSET^{up}* reduces the severity of *KIF11^{up}* induced spindle pole fragmentation. However, no significant difference in the number of PCNT foci was observed in either metaphase or anaphase when comparing EV/*KIF11^{up}* and *HSET^{up}*/*KIF11^{up}*, ($p>0.05$, Student's T-test; Figure 4.11f, 4.11g).

This dataset was also used to investigate whether *HSET*^{up} was able to rescue the lagging and misaligned chromosome phenotypes. Quantification of lagging chromosomes in cells with normal spindle pole phenotypes, including both centric and acentric, showed no significant difference between EV/*KIF11*^{up} and *HSET*^{up}/*KIF11*^{up} cells ($p>0.05$, Fisher's Exact test, Figure 4.3e). This suggests *KIF11*^{up} causes lagging chromosomes via a mechanism separate from disruption of the spindle force balance. The proportion of cells exhibiting lagging chromosomes was higher in all conditions in this experiment compared to the single transduction, suggesting that the transduction itself induces CIN. The single transduction EV control caused only 0.6% of cells to show lagging chromosomes, whereas this increased to 9.6% in the double transduction EV/EV control (compare Figure 4.3c and 4.3d with Figure 4.11h).

Quantification of misaligned chromosomes showed a small insignificant decrease in *HSET*^{up}/*KIF11*^{up} cells compared to EV/*KIF11*^{up} (Figure 4.11f). These data suggest that *KIF11*^{up} exerts multiple effects during mitosis which cause separate phenotypes: firstly, a disruption to the balance of forces that causes spindle pole fragmentation, and a second unknown effect causing lagging and misaligned chromosomes. A likely candidate mechanism for this second effect is altered microtubule dynamics, which could account for both the lagging and misaligned chromosomes. To further investigate these hypotheses, mechanistic live cell imaging experiments were performed.

4.5 Investigation of the Mechanistic Basis of *KIF11*^{up}-Induced Phenotypes

To test the hypothesis that *KIF11* upregulation alters microtubule dynamics and/or stability giving rise to increased lagging and misaligned chromosomes, EV and *KIF11*^{up} cells were cold treated to depolymerise unstable microtubules. Cells were stained for α-Tubulin and PCNT, and the ratio of α-Tubulin: PCNT signal intensity was measured for the whole spindle (Figure 4.12a). In control conditions, there was no significant difference between EV, *KIF11*^{up} bipolar, or *KIF11*^{up} multipolar cells ($p>0.05$, one-way ANOVA with Tukey's multiple comparisons test, Figure 4.12b). After treatment with cold media, the signal intensities of α-Tubulin: PCNT were reduced, as expected. However, while not

statistically significant, *KIF11^{up}* multipolar cells showed some resistance to cold treatment; the signal intensity was higher than that of EV and *KIF11^{up}* bipolar after cold treatment ($p>0.05$, Figure 4.12b). These results suggest increased microtubule stability in *KIF11^{up}* multipolar cells.

To further investigate these results, a microtubule depolymerisation assay was performed in live cells, (Wilhelm *et al*. 2019). Mitotic cells labelled with SiR-tubulin were subject to nocodazole treatment, and the subsequent microtubule depolymerisation and spindle collapse was recorded (Figure 4.12c, Supplementary Movie 3). The rate of microtubule depolymerisation was measured by quantifying total SiR-tubulin intensity, plotted as a percentage of the spindle intensity at T=0. A two-phase decay model was used to fit the data to a curve and extract parameters describing the two populations of microtubules: fast depolymerising (non-kinetochore-bound) and slow depolymerising (kinetochore-microtubules; Figure 4.12d). Statistically testing the parameters extracted on a per cell basis identified a significant decrease between the half-lives of fast microtubules for EV compared to *KIF11^{up}* bipolar cells, and EV compared to *KIF11^{up}* multipolar cells (2.40 vs 1.94, $p<0.01$, and 2.40 vs 1.62 minutes, $p<0.0001$, respectively; one-way ANOVA with Tukey's multiple comparisons tests, Figure 4.12g). Analysis of the kinetics of the slow microtubules was not possible, as there was a large variation of half-lives. Analysis of the distribution of microtubules showed that there was no difference in the proportion of fast vs slow microtubules when comparing EV to *KIF11^{up}* bipolar cells (82.5% vs 80%, $p>0.05$); however, *KIF11^{up}* multipolar cells had significantly fewer fast microtubules compared to EV cells (82.5% vs 62.5%, $p<0.0001$). These results corroborate the findings from the cold stable assay, suggesting that microtubule dynamics are not altered in *KIF11^{up}* bipolar cells, and in *KIF11^{up}* multipolar cells there is an increase in stability and/or the number of kMTs.

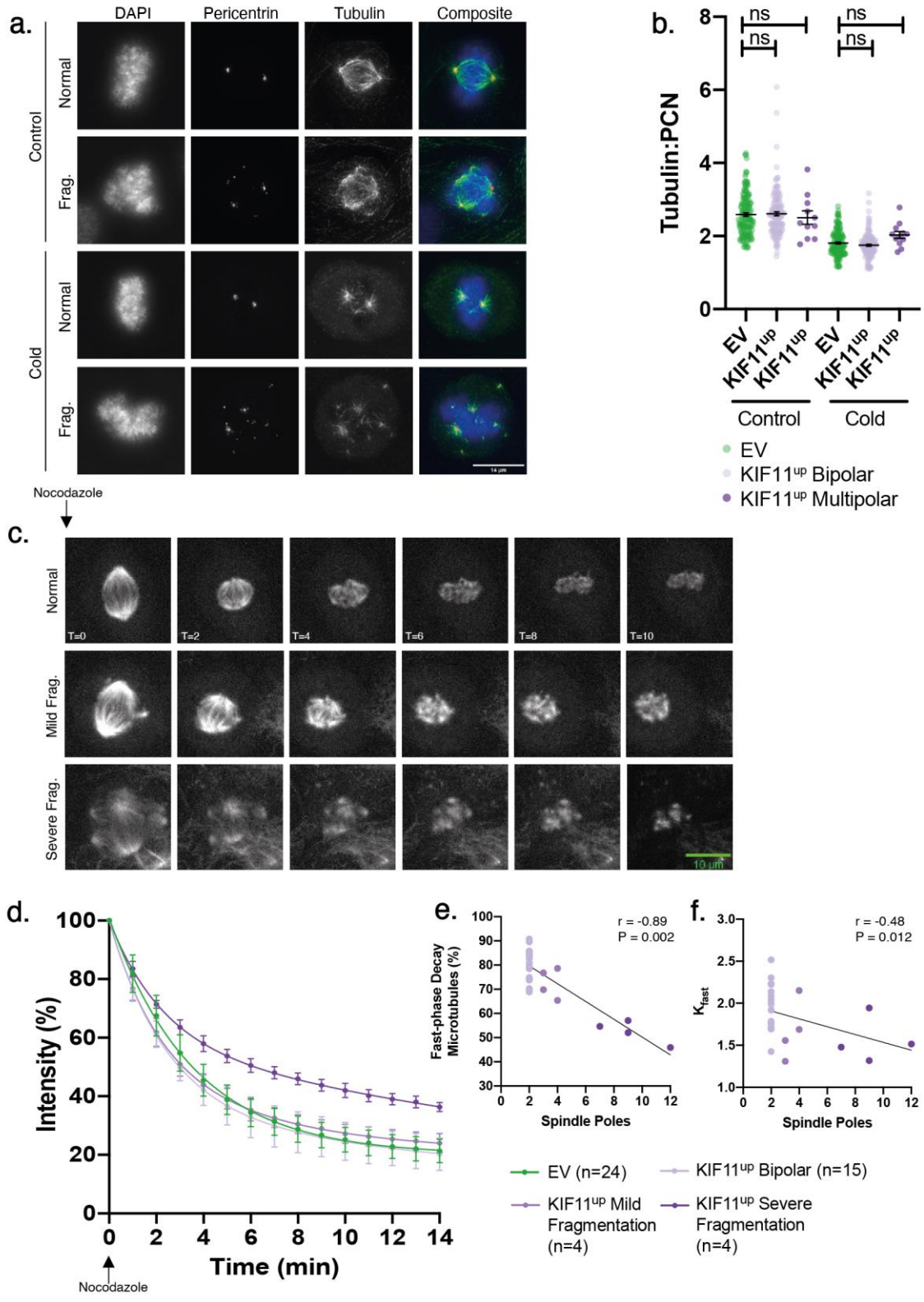

g.

	Mean Half-Life Fast (min)	Adj. p-val (vs EV)	Mean Half-Life Slow (min)	Adj. p-val (vs EV)	Mean % Fast	Adj. p-val (vs EV)
EV	2.40		1.95×10^{-12}		82.59	
KIF11up Bipolar	1.94	0.0017 **	4.69×10^{-11}	0.45 ns	80.09	0.49 ns
KIF11up Multipolar	1.62	<0.0001 ****	29.31	0.45 ns	62.52	<0.0001 ****

Figure 4.12 Multipolar but not Bipolar KIF11^{up} Cells show Increased Microtubule Stability **a.** Example images of control and cold treated EV and KIF11^{up} cells. Scale bar = 14 µm. **b.** Quantification of the tubulin signal intensity, normalised to pericentrin. N = 3, Welch's T-test, error bars = SEM. **c.** Example images from timelapse movies showing spindle collapse in cells with normal, mild and severe spindle pole fragmentation phenotypes, after addition of nocodazole. Scale bar = 10 µm. **d.** Quantification of spindle intensity as a percentage of that at T = 0, curves fitted using a two-phase decay model. Error bars = SD. **e.** Correlation between the number of spindle poles and the percentage of fast-phase decay microtubles. **f.** Correlation between the number of spindle poles and the half-life of the fast-phase microtubules. **e & f.** Spearman's rank correlation coefficient. **g.** Table of statistics extracted using the two-phase decay model. N = 3, one-way ANOVA with Tukey's multiple comparison's test.

The results from the cold stable assay suggest that the observed phenotype of increased microtubule stability is indeed caused by changes to microtubule dynamics, as if the difference was an artefact caused by more α-Tubulin staining in cells with multiple spindle poles, it would be observed in the control cells as well as cold-treated. There is no equivalent control in the microtubule depolymerisation assay, however. To better understand the relationship between microtubule depolymerisation and spindle pole fragmentation, the percentage of fast microtubules and their half-lives were plotted against the number of spindle poles (Figure 4.12e and 4.12f, respectively). These plots show a statistically significant negative correlation between the number of spindle poles and the percentage of fast depolymerising microtubules, suggesting that the more spindle poles present, the higher the proportion of kinetochore microtubules. There is also a negative correlation between the number of spindle poles and the half-life of the fast microtubules, suggesting that the more spindle poles present, the faster non-kinetochore bound microtubules depolymerise in the presence of nocodazole.

To test the hypothesis that *KIF11* upregulation alters the balance of forces during mitosis causing spindle pole fragmentation, RPE1-MPH-eGFP-Centrin 1 *KIF11^{up}* cells were imaged during mitosis to track centrosomes (Figure 4.13a). Centrosome tracking was performed to identify whether a force imbalance could be detected by measuring the rate of centrosome separation during prometaphase and anaphase.

Cells were selected for imaging based on the presence of bright tubulin asters at the centrosomes, indicating spindle formation had just begun and the cell was

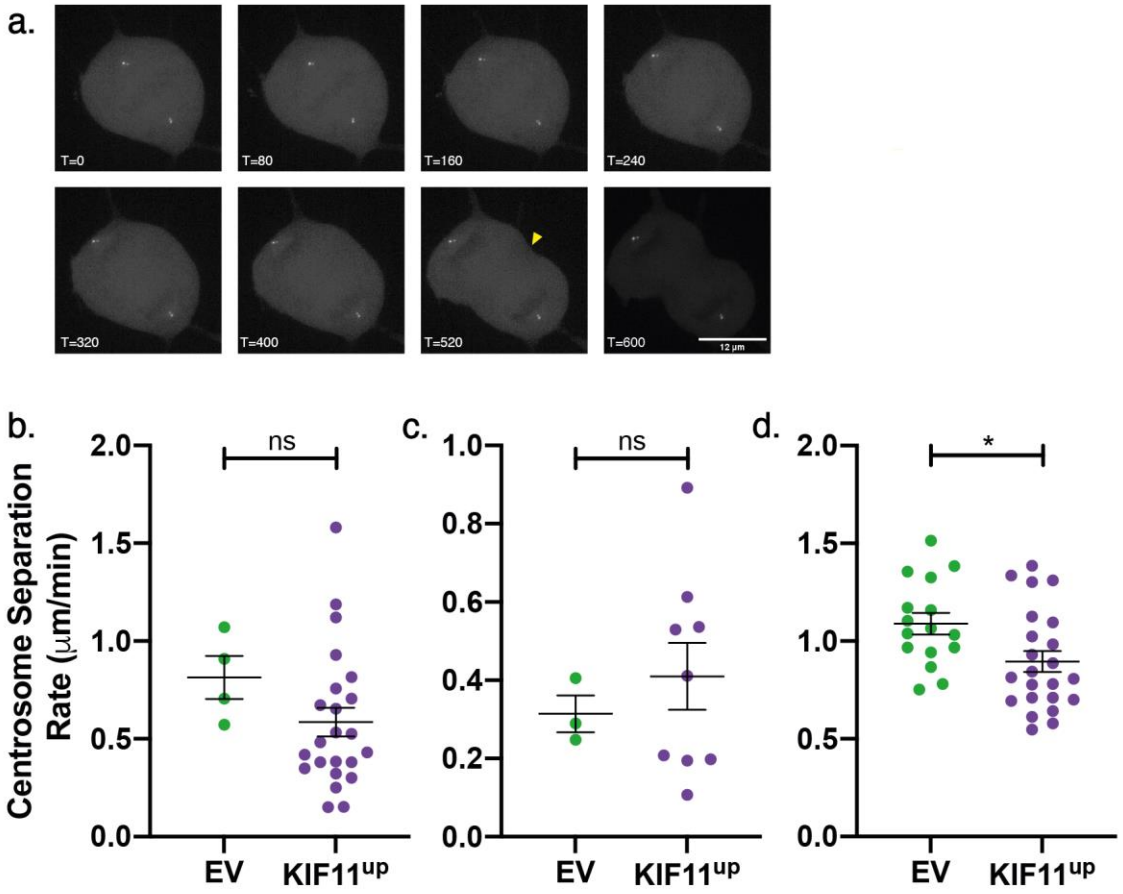

Figure 4.13 KIF11 Upregulation Reduces the Rate of Centrosome Separation During Anaphase
a. Centrosome separation rate of prometaphase cells where centrosomes move closer before establishing a bipolar spindle (plotted as inverse values). Scale bar = 12 µm. **b.** Centrosome separation rate in prometaphase cells where centrosomes move apart. **c.** Centrosome separation rate during anaphase. N = 3, Welch's T-test, error bars = SEM, T = time in minutes.

about to undergo NEB. This captured the movement of centrosomes through prometaphase, anaphase, and cytokinesis, however it was not able to reliably capture the entirety of prophase. In prometaphase, centrosomes either moved towards each other or away from each other before a stable metaphase spindle was established). In either case, there was no significant difference in the rate of centrosome movement in EV compared to *KIF11^{up}* cells ($p>0.05$, Welch's T-test; Figure 4.13b, 4.13c). Identification of cells at the correct stage proved difficult, however, and n numbers were insufficient to draw conclusions.

A second approach was taken of selecting metaphase cells for imaging, to measure the rate of centrosome separation during anaphase. Since metaphase cells are easy to identify, higher n numbers were collected for each condition. There was a significant decrease in the rate of centrosome separation during

anaphase in *KIF11*^{up} cells compared to EV (1.09 vs 0.90 μm/min, $p<0.05$), when centrosomes were tracked from anaphase onset until the first frame showing cleavage furrow ingression (Figure 4.13d). The data describe the rate of movement of the centrosomes away from each other during anaphase B but do not provide information on anaphase A, as the RPE1-MPH-eGFP-Centrin 1 cell line does not contain a suitable KT marker. The slower rate of separation measured in *KIF11*^{up} cells is consistent with the theory that outward pushing force from KIF11 crosslinking of interpolar microtubules does not directly contribute to separation of centrosomes during anaphase, but instead acts as a brake on centrosome separation, creating frictional forces between interpolar microtubules.

4.6 Discussion

4.6.1 *KIF11* Upregulation Causes Functionally Distinct Phenotypes

The data presented in this chapter demonstrates that upon *KIF11* upregulation cells experience spindle pole fragmentation, while the population that retain spindle pole integrity exhibit increased centric and acentric lagging chromosomes. The results from measuring KIF11 signal intensity on metaphase spindles support a model whereby the more extreme fragmentation phenotype is caused by higher levels of gene upregulation, while lagging chromosomes are caused by low to moderate levels of upregulation. There is likely a threshold at which the force imbalance becomes too great, resulting in spindle pole fragmentation. In this work no evidence could be found to suggest that lagging chromosomes in the *KIF11*^{up} bipolar class were caused by changes in MT stability. Further experiments would be required to determine the mechanism causing lagging chromosomes, for example, assessing kinetochore structure to confirm the presence of merotelic attachments in *KIF11*^{up} cells.

When classifying anaphase cells, similar amounts of centric and acentric lagging chromosomes were observed. When assessing micronuclei in interphase cells, however, there were around 4 times the amount of CENPA negative compared to CENPA positive, suggesting a greater proportion of lagging chromosomes are acentric. This is likely because centric lagging chromosomes are more often able

to segregate and integrate into the main daughter cell nucleus. Assuming they are due to merotelic kMT attachments, once this has been resolved the correct attachment is present for chromosome segregation, whereas acentric chromosome do not have any kMTs. One study suggested that 78% of U2OS cells with a lagging chromosome in anaphase form a micronucleus in at least one daughter cell (Thompson and Compton 2011), however more recently this was found to be an overestimation. RPE1 and U2OS were shown to spontaneously exhibit lagging chromosomes in 9% and 44% of anaphases, respectively, however these only resulted in micronuclei 6% and 14% of the time, respectively (Orr *et al*. 2021).

Centric and acentric chromosomes upon *KIF11* upregulation is a novel phenotype that has not been demonstrated previously. While spindle pole fragmentation in response to *KIF11* upregulation has not been directly demonstrated and thoroughly investigated, there is a body of evidence supporting this observation. Castillo *et al* observed a ~3% increase in multipolar spindles in MEFs, but it was not confirmed whether this was due to fragmentation or supernumerary centrosomes. There are likely differences in how different cell types deal with excess KIF11; it would be important to assay for this phenotype in a variety of normal and transformed cell lines, to investigate the importance of *KIF11*^{up} in mitosis. Compelling evidence for the force imbalance hypothesis is demonstrated by dynein or NuMA knockout (Hueschen *et al*. 2019; Neahring *et al*. 2021) which caused similar phenotypes to that demonstrated in this study. Inhibition of KIF11 in dynein or NuMA depleted cells rescued the phenotype, while cells lacking both dynein and KIF11 maintained spindle pole integrity. This demonstrates that the outward forces of KIF11 are balanced by dynein and NuMA mediated spindle pole focussing forces.

4.6.2 Centrosome Fragmentation & Separation

An interesting question addressed by the data in this study is when spindle pole fragmentation begins in *KIF11*^{up} cells with regards to centrosome separation. Live cell imaging of *KIF11*^{up} cells expressing eGFP-Centrin 1 and stained with SiR-tubulin shows that fragmentation is dependent on spindle formation, occurring an average of 9.75 minutes after NEB, just before an established metaphase spindle

can be observed. Given that RPE1 always separate centrosomes to the opposite side of the nucleus either vertically or horizontally before NEB (Magidson *et al*. 2011), it is puzzling that fragmentation is never seen before NEB. These observations suggest that fragmentation occurs during the late stages of prometaphase, when the spindles have established enough microtubules that a threshold of KIF11 loading is reached, causing a force imbalance that results in fragmentation. This hypothesis fits with the observation that 12% of prometaphase cells show spindle pole fragmentation.

When quantifying KIF11 signal intensity on metaphase spindles (Figure 4.8f), many cells with bipolar spindles show similar levels of *KIF11*^{up} compared to those with multipolar spindles. However, this is not seen during prometaphase and anaphase. This could be explained by the regulation of KIF11s affinity for microtubules via phosphorylation. Upon entry to mitosis, T926 phosphorylation increases the microtubule binding affinity, while the phosphatase PP2A negatively regulates this site, promoting mitotic exit. It is likely that the metaphase spindle intensity measurements show increased KIF11 staining compared to anaphase as this is when KIF11 has the greatest affinity for microtubules, and therefore the phenotype is more pronounced.

It is unclear why only a small proportion of *KIF11*^{up} cells undergo spindle pole fragmentation, when around 45% of the population show upregulation, and during metaphase similar spindle intensities are observed between bipolar and multipolar cells. Instead of measuring signal intensity in cells fixed at various stages of mitosis, using a KIF11 knock-in and performing upregulation would give a much more accurate picture of protein levels throughout the cell cycle. Generation of a knock-in cell line was attempted however tagging of *KIF11* with RFP could not be achieved due to poor transfection efficiency of the editing constructs. This could be used to test the hypothesis that cells with high levels of upregulation experience spindle pole fragmentation, while cells with more subtle phenotypes exhibit lagging chromosomes.

4.6.3 Alternative Methods to Rescue KIF11 Spindle Pole Fragmentation

The findings presented by Hueschen *et al* and Nearhing *et al* suggest dynein and NuMA are attractive targets for rescue of *KIF11*^{up} mediated spindle pole fragmentation. However, in these studies an inducible CRISPR knockout system was used to achieve a full depletion of the dynein heavy chain (DHC). Previous work has shown that siRNA knockdown of DHC causes a much less severe loss of spindle pole integrity, with spindles establishing a barrel-like shape that remains bipolar (Tanenbaum *et al*. 2008). In this project, successful depletion of DHC was achieved, however this did not induce any visible changes in spindle structure. It was therefore concluded that siRNA knockdown was not an appropriate method to induce sufficient changes in protein level that could mediate rescue of spindle pole fragmentation in *KIF11*^{up} cells.

Dynein also localises to multiple structures during mitosis, and performs different functions during the different stages, which would confound results when used in rescue experiments. In prophase/prometaphase, dynein functions in conjunction with KIF11 to separate centrosomes, therefore knockdown/knockout would in theory improve the force balance, showing rescue of the spindle pole fragmentation phenotype. In metaphase, however, dynein is localised on the cell cortex, where it pulls the centrosomes outwards, at the kinetochores where it pulls the centrosomes inwards, and at the centrosomes where it focusses MT minus ends. Knockdown/knockout of dynein would therefore have complex effects on the forces during metaphase and would not be a suitable model to rescue the force imbalance upon *KIF11*^{up}.

Monastrol could have been used to rescue spindle pole fragmentation in *KIF11*^{up} cells. A dose titration like the experiment in Figure 4.4d would have to have been performed to identify a dose that does not cause monopolar spindle formation, but still partially inhibits KIF11. However, while this experiment would be

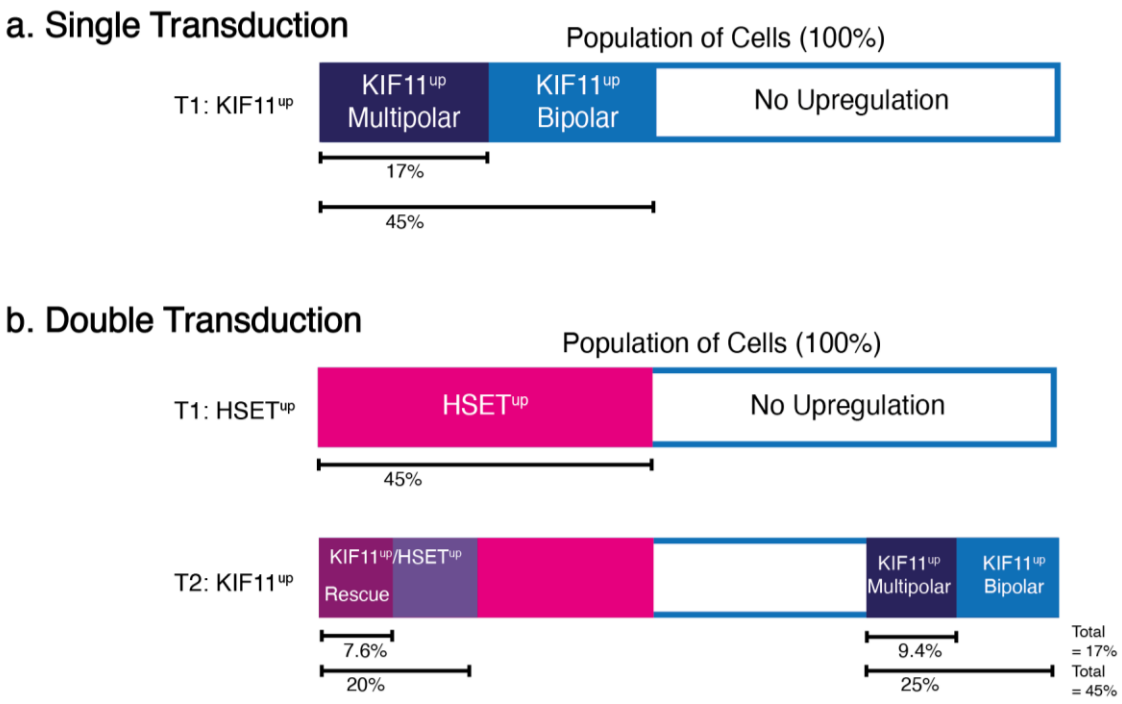

Figure 4.14 Heterogeneity Among Cell Populations after Gene Upregulation a. Model of the cell population after a single transduction to upregulate KIF11. Based on data measuring KIF11 spindle intensity in fixed cells, 45% of cells show upregulation. 17% of cells showed spindle pole fragmentation after gene upregulation. **b.** Model of the cell population after the double transduction protocol. In the first transduction (T1), 45% of cells upregulate HSET. In the second transduction, 45% of cells upregulate KIF11. Assuming these transductions are independent and after T1 cells that are successfully transduced in T2 are randomly distributed, then 20% of HSET^{up} cells would be successfully transduced. Within this population, 7.6% of cells would be expected to undergo spindle pole fragmentation, and are therefore classified as showing phenotype rescue. Within the 25% of cells that were unsuccessfully transduced in T1, but successfully transduced in T2, 9.4% would be expected to undergo spindle pole fragmentation due to increased KIF11 and no change in HSET. This model fits the data presented in Figure 4.11.

important to confirm the phenotypes observed are dependent on KIF11, it does not provide any mechanistic information on the force imbalance. In conclusion, *HSET* upregulation provides the most direct method of investigating the force balance in mitosis after *KIF11^{up}*, by increasing the forces that directly oppose KIF11.

While there is a clear reduction in the proportion of mitotic cells that show spindle pole fragmentation after upregulation of both *HSET* and *KIF11*, the severity of fragmentation based on the number of PCNT foci was unchanged (Figure 4.11). Given the role of HSET in centrosome clustering, this is a surprising result. It would be important to confirm whether this was due to the lower level of upregulation achieved for *HSET* (1.3-fold), compared to *KIF11* (2.5-fold). This phenotype could also be due to heterogeneity in the transduction efficiency within

the cell population. For *KIF11^{up}*, 45% of cells showed successful gene upregulation after transduction, and 17% show spindle pole fragmentation (Figure 4.14a). If the same transduction efficiency applies to *HSET^{up}*, then after both transductions around 20% of the population would have successfully upregulated both genes. Assuming the lentiviral transduction process is completely random, *KIF11^{up}* in *HSET^{up}* cells shows complete phenotype rescue, and *HSET^{up}* in cells without *KIF11^{up}* has no effect on mitosis, this would explain why there is a partial phenotypic rescue with no change in the number of PCNT foci in the *KIF11^{up}*/*HSET^{up}* cells that show fragmentation. Figure 4.14b shows a schematic interpretation of this theory, describing how the data fits this model.

4.6.4 Cellular Impact of *KIF11^{up}* Phenotypes

Analysis of *KIF11^{up}* cells showed that 81.3% of the cells with fragmented/multinucleated interphase nuclei were positive for p53, a finding consistent with the observation that 77.4% of daughter cells from cell divisions showing mitotic catastrophe undergo cell cycle arrest. Only 19.4% of cells underwent apoptosis after a division showing mitotic catastrophe, suggesting these cells can remain arrested in the cell cycle for over 36 hours. Cells were imaged for a total of 60 hours, and the daughter cells of those dividing within the first 24 hours tracked and analysed. Imaging for longer would be important to determine whether these cells do eventually undergo apoptosis, or if they are able to re-enter the cell cycle, propagating aneuploidy and CIN. One cell in this experiment showed a mild mitotic catastrophe-like phenotype in the first round of cell division, giving rise to a daughter cell that also showed mitotic catastrophe, an observation also found in other live imaging experiments. This poses the question of whether the *KIF11^{up}* cells experience apoptosis after mitotic catastrophe, or senescence. Immunofluorescent staining or for markers of both phenotypes would confirm the fate of cells that experience mitosis with a mitotic catastrophe-like phenotype.

That propagation of this phenotype was observed through multiple generations suggests that *KIF11^{up}* poses a threat to genomic stability. This likely occurs when KIF11 levels are increased only a small amount, giving rise to only a small degree of fragmentation and less severe chromosome segregation errors. Indeed, it has

been observed that not all numerical segregation errors induce p53 (Soto *et al*. 2017). In addition, in *KIF11^{up}* cells that show a normal division with lagging chromosomes, 1 out of 5 cells gave rise to a daughter cell that also experienced a lagging chromosome, suggesting that the type of errors induced by *KIF11^{up}* do not cause p53 activation and propagate CIN across generations. These observations provide evidence in support of a role for *KIF11^{up}* in promoting and propagating aneuploidy and CIN, that could be harnessed by cancer cells.

While various centrosome abnormalities have been found in cancer, there are no reports of spindle pole fragmentation caused by overexpression of *KIF11*. It is unclear whether cancer cells that upregulate *KIF11* experience lagging chromosomes, spindle pole fragmentation, or mitotic catastrophe as a direct consequence, and how this effects the cell population. Given the high prevalence of *TP53* loss in cancer, it is tempting to speculate that this phenotype is less toxic, as cells may not undergo cell cycle arrest following mitotic catastrophe. Most studies investigating *KIF11* upregulation in cancer are using it as a biomarker (Beer *et al*. 2008; Venere *et al*. 2015; Daigo *et al*. 2017; Jiang *et al*. 2017; Zhou *et al*. 2021), and there are no reports where its functional role in cancer has been mechanistically investigated. This kind of study would be extremely difficult, as determining the impact of excess KIF11 in a cancer cell line would require reducing KIF11 protein levels back to that seen in a normal, non-transformed version of the cell type involved, as complete inhibition or protein loss results in a cell division block. The finding that *KIF11* expression level correlates with poor patient survival in clinical studies suggests that it does indeed contribute to cancer progression, and the aneuploidy and CIN generated helps to accelerate tumour evolution and drug resistance.

4.6.5 Centrosome Tracking

The centrosome tracking experiments, while not providing meaningful data on the effects of *KIF11* upregulation during prometaphase and metaphase, revealed an insight into the function of KIF11 during anaphase. Older work in yeast identified that the kinesin-5 family member Cin8p generates outward forces important for centrosome separation in anaphase (Straight, 1998). However, studies in mammalian cells have shown the antiparallel sliding force generated

by KIF11 is dispensable for anaphase, that inhibition does not affect the rate of centrosome separation in anaphase B, and that KIF11 acts as a brake reducing the speed of centrosome separation (Collins *et al*. 2014b; Vukušić *et al*. 2017; Vukušić *et al*. 2021). A recent extensive study investigating the control of anaphase A and B by molecular motors identified a redundancy between KIF4A and KIF11: genetic/chemical ablation of both proteins completely inhibits chromosome segregation, while single ablations do not significantly reduce the speed of centrosome separation (Vukušić *et al*. 2021). These data suggest that in the absence of KIF4A, the outward sliding force generated by KIF11 is essential for chromosome segregation. In this work it has been demonstrated that 2-fold upregulation of KIF11 significantly reduces the rate of centrosome separation in anaphase B, a finding consistent with Collins *et al*, and the hypothesis that increased KIF11 on central spindle and interpolar microtubules increases the friction during anaphase, slowing centrosome separation.

Given the well-known function of KIF11 in centrosome separation during prophase and prometaphase, alongside with the observed timing of spindle pole fragmentation at 9.75 minutes after NEB, it is most likely fragmentation occurs during the period of KIF11 activity at prometaphase centrosomes. However, the data do not suggest increased outward forces are applied to the centrosomes at any point in mitosis, due to increased amounts of KIF11. The measurements collected during centrosome tracking and analysis of spindle lengths focus on the eGFP-Centrin 1 positive centrosomes after fragmentation has occurred, which could make the results misleading in multiple ways. Firstly, it is possible that due to the combined activity of the many kinesins involved in regulating the force balance during mitosis, alongside dynein, there is no change in forces at the main Centrin 1-positive centrosomes, which often nucleate the bulk of the microtubules. There may be increased outward force applied to microtubules nucleated by the fragmented pericentriolar material, which were not measured in these assays. Secondly, it is possible that a force imbalance is present early on during mitosis while centrosomes are being separated before NEB, which leads to fragmentation. Again, the assays performed in this study were not able to capture sufficient centrosome movement before NEB to draw meaningful conclusions. This imbalance may be corrected early on in mitosis and thus missed in the centrosome tracking assays. Thirdly, there may indeed be

increased outward force applied to the centrosome throughout mitosis, but due to the activity of opposing motors such as HSET, this may not necessarily translate to measurable differences in the rate of centrosome separation or spindle lengths during metaphase and/or anaphase.

4.7 Conclusions

This work has demonstrated that upregulation of KIF11 gene expression to 2.5-fold that in normal RPE1 cells induces spindle pole fragmentation in mitosis, leading to mitotic catastrophe. In the subset of cells that exhibit normal spindle poles, there is a small but significant increase in both centric and acentric lagging chromosomes. A thorough investigation into the mechanisms that cause these phenotypes and their consequences in cells was performed to identify how this could impact cancer cells that overexpress KIF11. While it was demonstrated that spindle pole fragmentation is caused by a force imbalance exerted on the mitotic spindle, the mechanism causing lagging chromosomes could not be identified. Both phenotypes can have dangerous consequences in cells, which may contribute to the generation and maintenance of CIN and aneuploidy in cancer. In RPE1 cells, mitotic catastrophe was a highly toxic event, with most cells undergoing a p53 induced cell cycle arrest, although some cells were able to re-enter the cell cycle and mitosis. In the future, it will be important to investigate the impact of this phenotype in a cancer context, where it may be less toxic to cells and cause a greater degree of aneuploidy due to the absence of functional p53.

Chapter 5: Oncogenic *PIK3CA* Expression Causes Supernumerary Centrosomes

In chapter 3 a CRISPR upregulation system was used to model gene overexpression and screen for CIN. This system resulted in robust transcriptional activation for many of the genes tested, however oncogenes with tightly regulated transcriptional programs proved difficult to upregulate. Despite testing multiple gRNAs, only 1.3-fold upregulation of *PIK3CA* gene expression was achieved.

While this result was highly reproducible and represents a 30% increase in gene expression, this is less than what is observed in patients (Keraite *et al*. 2020). This project also sought to investigate the role of oncogenic activating mutations in *PIK3CA*, for which CRISPR activation in a WT system could not be used. Alternative models were sought to investigate the role of oncogenic PIK3CA signalling in the development of CIN.

In this chapter cell lines expressing *PIK3CA*^{H1047R} through CRISPR/Cas9 genome editing of the endogenous genetic loci were employed, to investigate whether expression of *PIK3CA*^{H1047R}, a mutation frequently occurring clonally during the early stages of tumourigenesis, effects CIN and centrosome maintenance. H1047R is an oncogenic activating point mutation that constitutively activates PIK3CA, permanently switching on the signalling pathway. The results presented here build on the findings from the study by Berenjeno *et al*, demonstrating that expression of *PIK3CA*^{H1047R} in MEFs causes centrosome amplification and promotes their clustering into a pseudobipolar mitotic spindle. However, using expression vectors driven by CMV promoters leads to high levels of *PIK3CA*^{H1047R} expression, which is not an accurate model for cancer patients harbouring a point mutation at one or two PIK3CA alleles within their genome. Here, centrosome amplification and clustering in clonal MCF10A cell lines that underwent genome editing to introduce either a heterozygous or homozygous knock-in of the H1047R mutation have been assessed. These cellular models express similar levels of *PIK3CA*^{H1047R} as is seen in patients with homo or heterozygous point mutations. Clones where editing failed, and the genotype remained wild type at both genomic loci, were used as controls. These cell lines were generated by Evelyn Lau and made available for use in this project by Bart Vanhaesbroek. Maria Carriera contributed to the quantification of supernumerary centrosomes in these cell lines.

5.1 *PIK3CA*^{H1047R} Does Not Cause Numerical CIN or Aneuploidy

To investigate whether the cell lines expressing *PIK3CA*^{H1047R} are more error prone during mitosis, cells were fixed and stained with α-Tubulin, CREST, and PCNT (Figure 5.1a). The cell lines were characterised at ~10 passages post genome editing. Minimal numbers of centric and acentric lagging chromosomes

were observed across all cell lines analysed, with only 0.5-4% of anaphases exhibiting the phenotype (Figure 5.1b). There was no significant difference in the number of anaphases with lagging chromosomes between the WT and heterozygous ($p>0.05$, pairwise Fisher's exact test with Bonferroni p value correction), or WT and homozygous cell lines ($p>0.06$). Multipolar anaphases were also rarely seen, with only 1-4% of anaphases for all cell lines exhibiting the phenotype (Figure 5.1b). When quantifying anaphases exhibiting a chromatin bridge, however, the homozygous *PIK3CA*^{H1047R} cell lines showed significantly higher rates compared to the WT cell lines (3.7% vs 9.2%, $p<0.0001$, Figure 5.1d). This data could indicate that homozygous expression of *PIK3CA*^{H1047R} causes replication stress in MCF10A, whereas heterozygous expression does not. Although oncogene induced replication stress is well established in cancer, there is limited evidence to suggest that PIK3CA activation alone can induce this phenotype.

The micronuclei counting assay developed in Chapter 1 was employed to screen for CIN in these cell lines. For this assay, cell lines at passage ~50 post genome editing were used. None of the *PIK3CA*^{H1047R} cell lines showed any significant increase in MN compared to WT cell lines ($p>0.05$, two sample T-test, Figure 5.1e). These data suggest that cell lines expressing *PIK3CA*^{H1047R} do not exhibit increased chromosome segregation errors and MN formation. The proportion of EdU positive cells was increased in the *PIK3CA*^{H1047R} cell lines, consistent with PIK3CA activation functioning to promote cell proliferation (Figure 5.1f).

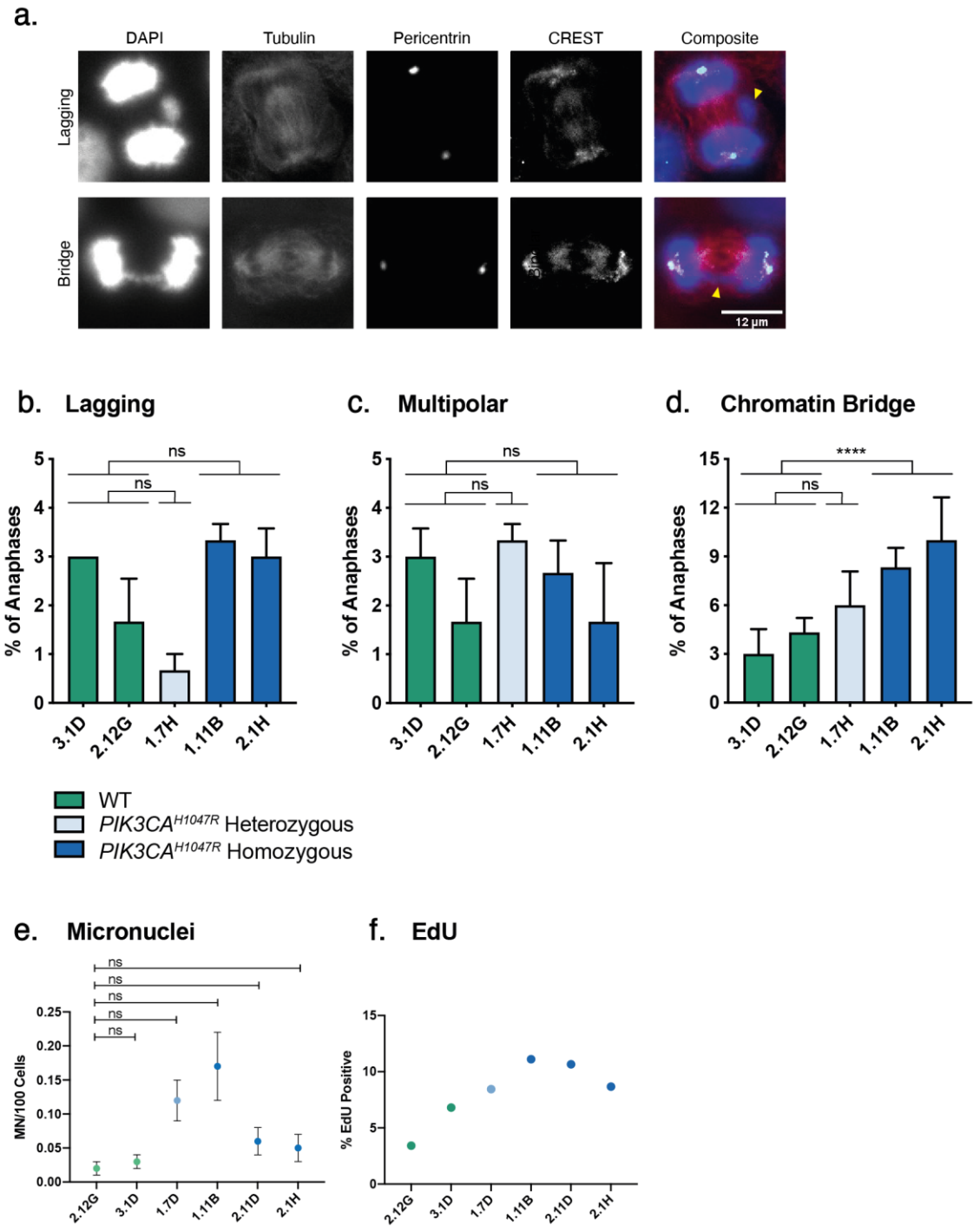

Figure 5.1 Cell Lines Expressing *PIK3CA*^{H1047R} Exhibit Increased Chromatin Bridges during Anaphase a. Example images showing cells with a lagging chromosome (top panel), and chromatin bridge (bottom panel). Quantification of the proportion of anaphases exhibiting **b.** lagging DNA, **c.** a multipolar spindle, and **d.** a chromatin bridge. N = 3, n = 300 cells per cell line, error bars = SEM. Data were pooled by genotype and Chi^2 followed by pairwise Fisher's exact tests performed, with bonferroni p value correction for multiple comparisons. **e.** Calculation of the number of micronuclei per 100 cells. N = 1, n > 57 fields, error bars = SEM, two-sample T-test performed on a per field basis. **f.** Calculation of the proportion of EdU positive cells as a measure of proliferation.

5.2 *PIK3CA*^{H1047R} Expression and Supernumerary Centrosomes

Metaphase cells were imaged, and supernumerary centrosomes were identified based on PCNT staining (Figure 5.2a). Bright PCNT foci that showed microtubule nucleation were counted as individual centrosomes, as the centrin antibodies tested did not stain the centrosomes specifically enough to be distinguished from background signal. The heterozygous and homozygous *PIK3CA*^{H1047R} cell lines had significantly more centrosomes compared to WT, when quantifying total centrosome numbers ($p<0.0001$, Kruskall-Wallis test followed by Dunn's multiple comparisons test, Figure 5.2b). These data show a dose dependant effect of *PIK3CA*^{H1047R}, as the heterozygous cell line exhibits an intermediate phenotype compared to the WT and homozygous cell lines. As additional controls, plain MCF10A (pre-genome editing) and Clone A4 (a clonal MCF10A cell line selected for genome editing, that showed minimal mitotic errors) were analysed for supernumerary centrosomes. Interestingly, the WT cell lines had significantly more centrosomes than Clone A4 ($p<0.0001$), suggesting the plasmid transfection and processes associated with genome editing effect mechanisms by which cells acquire supernumerary centrosomes (Figure 5.2b).

Four cell lines underwent quantification of supernumerary centrosomes at passage 50, in addition to passage 10, providing information on the evolution of the centrosome phenotype over time (Figure 5.2c). There were no significant changes to centrosome counts in p10 vs p50 for the two WT clones (3.1D and 2.12G), or the homozygous *PIK3CA*^{H1047R} clone (2.1H; pairwise Mann-Whitney tests, $p>0.05$). The heterozygous clone however showed a significant reduction in centrosome count from p10 to p50, with the majority of cells at p50 exhibiting a normal phenotype with two centrosomes. It is unclear whether *PIK3CA*^{H1047R} itself effects the proliferation of cells with supernumerary centrosomes, however these data shows that evolution of the cell line in culture can indeed change the centrosome phenotype over time.

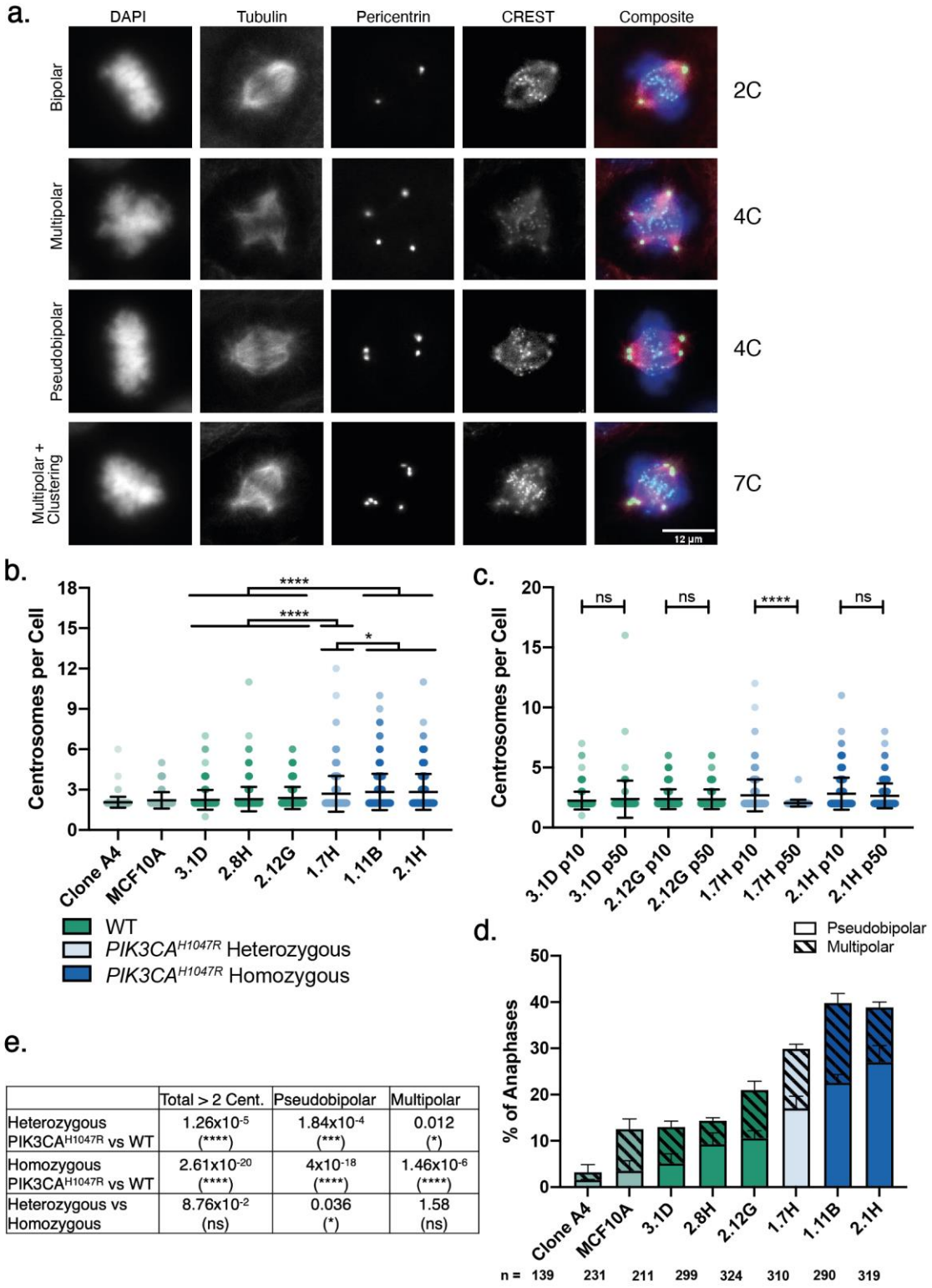

e.

	Total > 2 Cent.	Pseudobipolar	Multipolar
Heterozygous PIK3CA^{H1047R} vs WT	$1.26x10^{-5}$ (****)	$1.84x10^{-4}$ (***)	0.012 (*)
Homozygous PIK3CA^{H1047R} vs WT	$2.61x10^{-20}$ (****)	$4x10^{-18}$ (****)	$1.46x10^{-6}$ (****)
Heterozygous vs Homozygous	$8.76x10^{-2}$ (ns)	0.036 (*)	1.58 (ns)

Figure 5.2 Cell Lines Expressing *PIK3CA^{H1047R}* show Increased Incidence of Supernumerary Centrosomes **a.** Example images showing cells stained with PCNT and α-Tubulin to identify centrosomes. **b.** Quantification of the number of centrosomes per metaphase cell at passage ~10. Centrosome counts were pooled by genotype and analysed by Kruskal-Wallis test followed by Dunn's multiple comparisons test. **c.** Comparison of the number of centrosomes per metaphase cell in passage ~10 and ~50. Mann-Whitney test, error bars = Mean and SD. **d.** Quantification of the proportion of metaphase cells with >2 centrosomes, showing the proportion of cells with multipolar spindles in the striped bars, and pseudobipolar spindles in the solid bars. N = 2/3, error bars = SEM. **e.** Table of statistics; Chi^2 followed by pairwise Fisher's exact tests, with bonferroni p value correction for multiple comparisons.

The polarity of mitotic spindles was also quantified in all cell lines at passage 10. Figure 5.2d shows the proportion of multipolar metaphases (striped bars), pseudobipolar metaphases (solid bars), and proportion of metaphases exhibiting supernumerary centrosomes (striped + solid bars). A dose-dependent trend can be seen when comparing the proportion of metaphases exhibiting supernumerary centrosomes, with the homozygous cell lines showing higher rates than the WTs, and the heterozygous cell line showing an intermediate phenotype. These differences are significant when pooling and comparing against the WT cell lines, ($p<0.0001$ and $p<0.0001$, pairwise Fisher's exact tests with Bonferroni p value correction; Figure 5.2e). The same trend can be clearly seen for the proportion of pseudobipolar cells across the different cell line genotypes (Figure 5.2d solid bars) and is weakly present for the multipolar cells.

Two methods were employed to quantify centrosome clustering in cells. Simply comparing the incidence of pseudobipolar spindles among cell lines of different genotypes alone would be inaccurate, as it would not account for the higher incidence of supernumerary centrosomes observed in the *PIK3CA*^{H1047R} cell lines. Firstly, a ratio of the proportion of multipolar spindles: pseudobipolar spindles was calculated, giving a simple measure of the proportion of cells with supernumerary centrosomes that can form a pseudobipolar spindle (Figure 5.3a). This is method of analysis is stringent, quantifying only cells that have clustered all centrosomes. The results for the WT cell lines showed a high variability, and no clear trend could be identified from the data. When pooling cell lines by genotype and comparing WT against the heterozygous and homozygous cell lines, there was no significant difference in the multipolar: pseudobipolar ratio ($p>0.05$, pairwise Fisher's exact test with Bonferroni p value correction).

As fixing only captures the phenotype of the cells during a snapshot of mitosis, a second method was employed: for each cell line, the proportion of cells exhibiting clustering at one or more pole was quantified in metaphases with supernumerary centrosomes (Figure 5.3b). This method may better represent clustering efficiency, as multipolar spindles are often only an intermediate state. However, there was no clear trend between the WT, homozygous, or heterozygous cell lines. Due to Clone A4 showing low numbers of cells with supernumerary

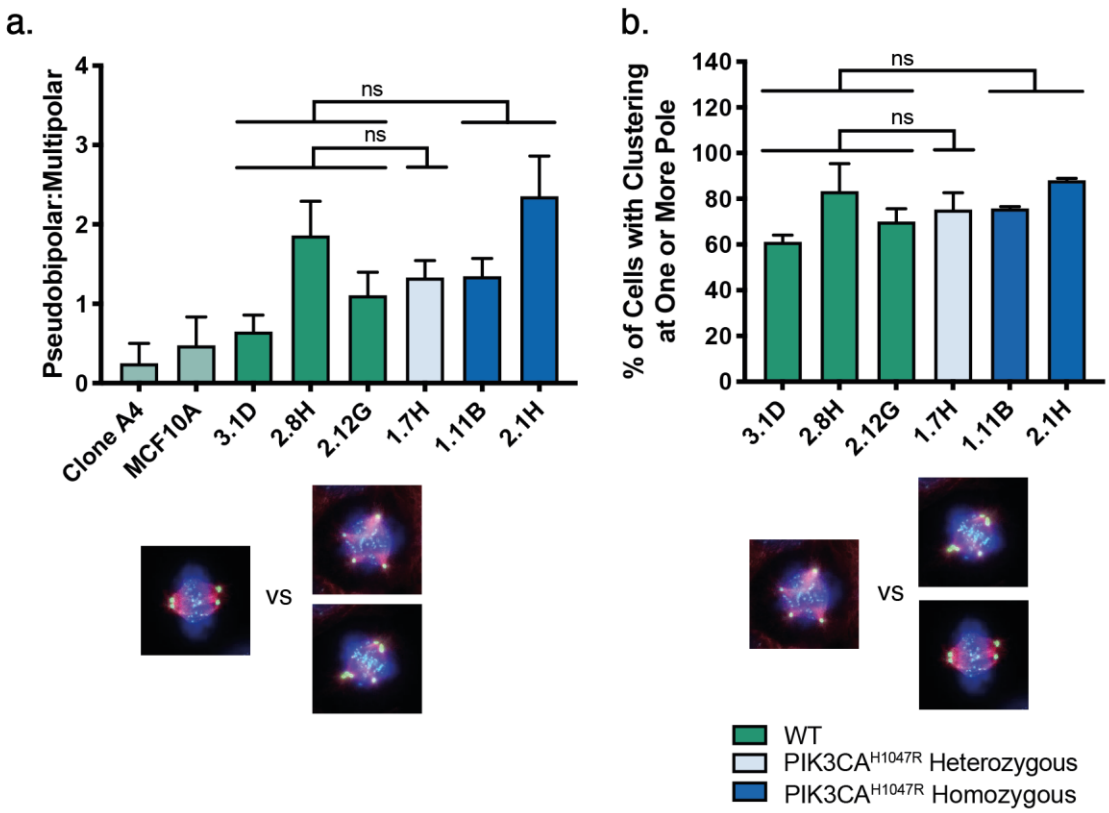

Figure 5.3 Quantifying Clustering Efficiency in WT and PIK3CA^{H1047R} Cell Lines **a.** Quantification of clustering efficiency by taking the ratio of pseudobipolar cells: multipolar metaphase cells. Ratios for each experimental repeat (N = 3) were pooled by genotype, and a one-way ANOVA performed with Dunnett's multiple comparisons test, error bars = SEM. **b.** Quantification of clustering efficiency by identifying metaphase cells that show clustering at one or more spindle pole. Cells with 2 centrosomes were excluded from this analysis. Data were pooled by genotype, and Chi^2 followed by pairwise Fisher's exact tests performed, with Bonferroni p value correction. Error bars = SEM.

centrosomes (4 cells compared to a minimum of 27 in all other cell lines), these were excluded from analysis. When pooling cell lines by genotype, there were no significant differences in the proportion of cells showing clustering at one or more pole ($p>0.05$, pairwise Fisher's exact test with Bonferroni p value correction). These data suggest that expression of *PIK3CA^{H1047R}* in MCF10A does not increase clustering efficiency, and that the increased proportion of pseudobipolar spindles observed in the heterozygous and homozygous cell lines (Figure 5.2d) are simply a result of higher proportions of cells with supernumerary centrosomes.

5.3 Live Cell Imaging of *PIK3CA^{H1047R}* Cell Lines

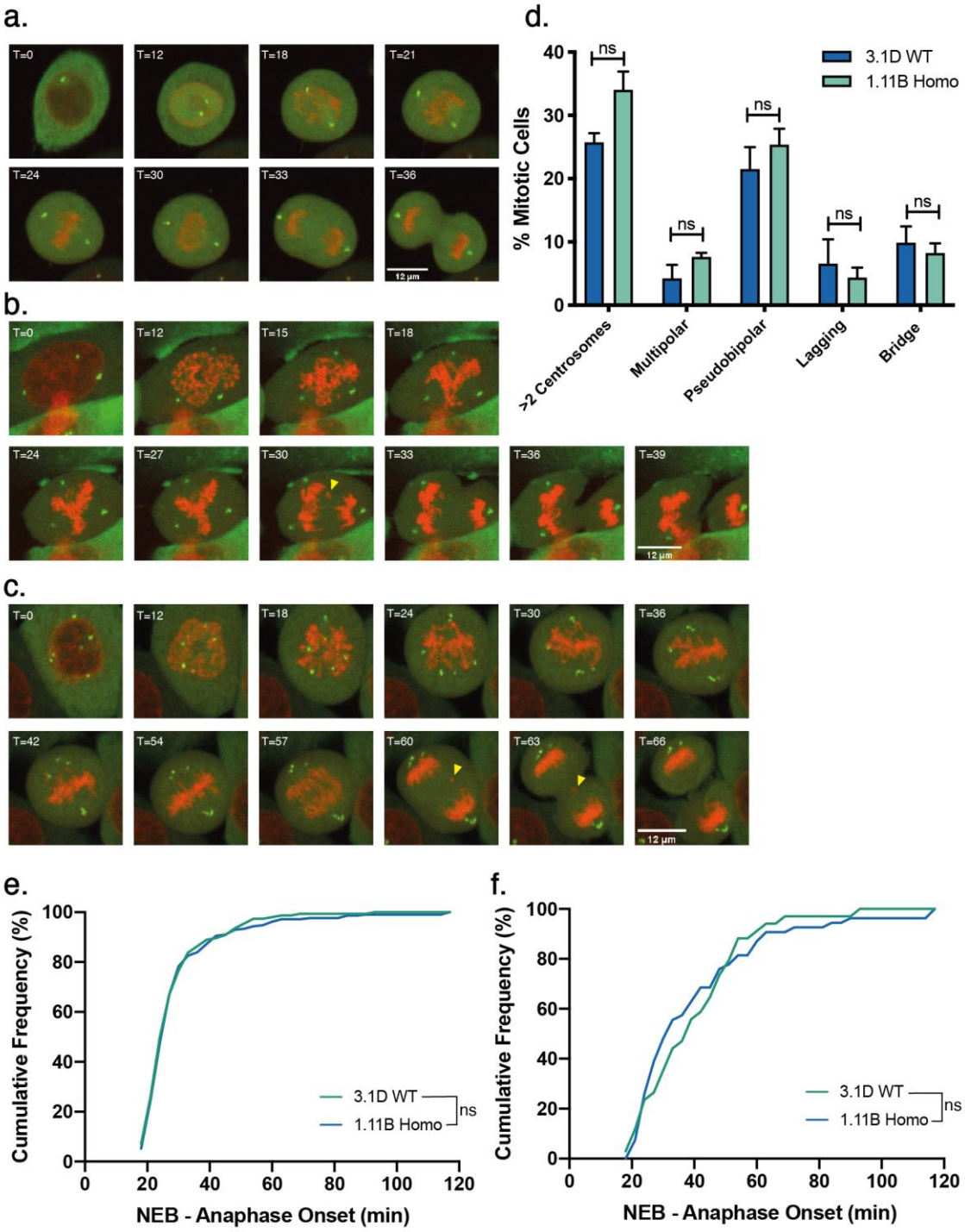

Figure 5.4 Analysis of Mitotic Errors and Centrosome Clustering in Live Cells Example images from time-lapse movies showing 3.1D cells expressing eGFP-Centrin 1 and stained with SiR-DNA undergoing: **a.** normal mitosis, **b.** multipolar mitosis with lagging DNA, giving rise to two daughter cells, **c.** centrosome clustering to form a psuedobipolar spindle, undergoing a bipolar anaphase with lagging DNA. **d.** Quantification of mitotic errors. N = 3, n = 154 (3.1D), 213 (1.11B), Fisher' Exact test, error bars = SEM. **e.** Mitotic timings of 3.1D and 1.11B expressing eGFP-Centrin 1, Welch's T-test. **f.** Mitotic timings of the subset of cells forming a pseudobipolar spindle, Welch's T-test.

To further investigate centrosome clustering in cells expressing *PIK3CA*^{H1047R}, the eGFP-Centrin 1 marker was introduced to the WT 3.1D and the homozygous *PIK3CA*^{H1047R} 1.11B cell line at passage ~10. A bulk positive population was isolated by FACS, to avoid selecting for aberrant phenotypes during clonal selection. Cells were imaged overnight using SiR-DNA to visualise chromosomes, which alongside the eGFP-Centrin 1 marker, allowed for identification of multipolar and pseudobipolar cells and visualisation of centrosome clustering (Figure 5.4, Supplementary Movie 4). In comparison to the fixed cell imaging where there were significantly increased proportions of cells exhibiting >2 centrosomes and chromatin bridges, no significant differences in these phenotypes were observed in live cells ($p>0.05$, Fisher's exact test; Figure 5.4d). Furthermore, there was no difference in the proportions of cells exhibiting lagging chromosomes, multipolar spindles, or pseudobipolar spindles.

Mitotic timings were measured between the two cell lines, quantifying the time taken from NEB to anaphase onset. There was no significant difference between 3.1D (WT) and 1.11B (homozygous) when including measurements from all cells, (mean of 28.8 ± 10.9 vs 30.0 ± 14.4 minutes, $p>0.05$, Welch's T-test; Figure 5.4e). To test whether clustering is achieved faster in 1.11B compared to 3.1D, mitotic timings were plotted for the subset of cells forming a pseudobipolar spindle (Figure 5.4f). However, there remained no significant difference between 3.1D and 1.11B (mean of 40.3 ± 16.4 vs 40.9 ± 22.2 minutes, respectively, $p>0.05$). This data is in agreement with the results from fixed cell imaging, suggesting that *PIK3CA*^{H1047R} does not impact centrosome clustering in MCF10A cells.

5.4 Discussion

5.4.1 *PIK3CA*^{H1047R} Increases Anaphase Chromatin Bridge Formation

One of the most striking phenotypes observed in the *PIK3CA*^{H1047R} cell lines was a dose-dependent increase in the incidence of chromatin bridges in anaphase. This phenotype is distinct from lagging chromosomes and suggests that *PIK3CA*^{H1047R} impacts pre-mitotic processes that result in mitotic errors, for example, by causing replication stress. This can result in chromatids remaining connected during mitosis due to incomplete DNA replication, or incomplete

untangling of supercoiled DNA by topoisomerases, resulting in a chromatin bridge. It is well known that oncogene activation can induce replication stress by various mechanisms, such as deregulating the cell cycle and perturbing pathways that regulate DNA replication (Primo and Teixeira 2020). Oncogenic Ras causes oxidative stress and increases transcription, causing collisions between the replication and transcription machinery (Primo and Teixeira 2020). However, there is limited evidence for a direct role of PIK3CA signalling.

PIK3CA positively regulates various metabolic processes, including nucleotide and protein synthesis. It is therefore unlikely that replication stress is caused by insufficient levels of the molecular components required for DNA synthesis, including polymerases, histones and nucleotides. One study found that MCF10A expressing *PIK3CA*^{H1047R} alongside *HER2* overexpression showed enrichment for pathways related to DNA replication stress, including checkpoint kinase 1 (CHK1) signalling, while expression of *PIK3CA*^{H1047R} or *HER2* alone did not (Dong *et al*. 2017). Under normal conditions cells would detect faulty DNA replication during S phase through CHK1 activation, resulting in a cell cycle delay that provides time for DNA damage and replication errors to be repaired. It is possible that PIK3CA^{H1047R} interferes with CHK1 signalling, promoting progression through S phase in the presence of aberrant DNA structures that lead to anaphase bridges in mitosis. Whether CHK1 signalling is disrupted in the CRISPR *PIK3CA*^{H1047R} cell lines, which do not have any other known alterations, would require further investigation.

The DNA fibre assay is the gold standard for assessing replication stress, providing a readout of the replication fork rate. Performing this assay in the CRISPR cell lines would elucidate whether *PIK3CA*^{H1047R} caused a reduction or increase in replication fork speed compared to WT cell lines, however it would not provide any information on the mechanism. Sequencing the genomes of the cell lines would be confirm whether there is an increase in structural CIN, and would identify translocations, chromothripsis, and chromosome arm loss/gain events (Umbreit *et al*. 2020). Future experiments could assess the fate of cells that experience a chromatin bridge, as these commonly result in p53 activation due to DNA damage. *PIK3CA*^{H1047R} may promote survival of the daughter cells

rather than cell cycle arrest, however neither this study nor others have found evidence to suggest that *PIK3CA*^{H1047R} provides tolerance to CIN.

5.4.2 *PIK3CA*^{H1047R} Does not Induce Numerical CIN or Aneuploidy

There was no evidence of whole chromosome segregation errors in the *PIK3CA*^{H1047R} cell lines. There was no significant increase in micronuclei or lagging chromosomes observed in anaphase cells, suggesting that *PIK3CA*^{H1047R} does not directly affect mitotic processes. This contrasts with the findings of Berenjeno *et al*, using MEFs homozygous for *PIK3CA*^{H1047R}. The MEF cell lines derived were unstable, however, spontaneously transforming *in vitro* and developing a tetraploid population through unknown mechanisms (Borel *et al*. 2002). MCF10A, which are a normal, non-transformed cell line do not exhibit spontaneous genome doubling, and thus the effect of *PIK3CA*^{H1047R} on the tolerance to this phenotype cannot be determined. A simple experiment to address this issue would be to induce tetraploidy by treatment with DCB, and assess cell survival, proliferation, and development of aneuploidy in the different cell lines. However, DCB treatment would also generate supernumerary centrosomes, so it would become difficult to delineate the effects of *PIK3CA*^{H1047R} on tolerance to genome doubling and the stresses this applies to protein synthesis and mitosis, versus tolerance to supernumerary centrosomes. Treatment of these cell lines with reversine or the MPS1i and CENPEi combination to induce numerical CIN would provide a good model system for assessing the role of *PIK3CA*^{H1047R} on tolerance to aneuploidy.

It is interesting that despite the high incidence of supernumerary centrosomes in cell lines of all genotypes (18% WT, 30% heterozygous *PIK3CA*^{H1047R}, 40% homozygous *PIK3CA*^{H1047R}), the incidence of lagging chromosomes was <3.5% across all cell lines. Induction of supernumerary centrosomes in RPE1 cells led to 12% of cells mis-segregating a chromosome (Ganem *et al*. 2009), demonstrating that only a small number of cells actually experience errors, which is in line with the results from the MCF10A cell lines tested in this study. However, if supernumerary centrosomes increased merotelic attachments and lagging chromosomes, then one would expect to see a correlation between the two phenotypes. This is not the case for the MCF10A cell lines, as the WT and

homozygous cell lines had a similar incidence of segregation errors despite the homozygous cell line showing around double the incidence of supernumerary centrosomes compared to WT.

5.4.3 *PIK3CA^{H1047R}* Cell Lines Show Supernumerary Centrosomes

In this study, the homozygous and heterozygous cell lines showed a significant increase in the proportion of cells with supernumerary centrosomes. The WT cell lines also showed an average of 14.4% cells with supernumerary centrosomes, which is higher than expected for a normal, non-transformed cell line. However, analysis of MCF10A that had not undergone the CRISPR protocol showed an incidence of 12.5% supernumerary centrosomes. While it was clone A4 that was used for generating the *PIK3CA^{H1047R}* cell lines, where only 1.6% of cells exhibited supernumerary centrosomes, these results suggest a basal level of centrosome amplification in MCF10A that is maintained over time. It is likely that once clone A4 was expanded in culture, the incidence of supernumerary centrosomes increased and stabilised at that seen in the bulk MCF10A population.

In the study by Berenjeno *et al*, overexpression of either WT, *PIK3A^{H1047R}* or *PIK3CA^{E545K}* increased the incidence of supernumerary centrosomes from 3% in vector control to around 11% in MCF10A. In this model the gene is likely expressed to a higher level than in the CRISPR cell lines, as there are multiple copies present under the control of a CMV promoter, compared to only 1 or 2 copies under the control of an endogenous promoter. This confirms that a single copy of activated *PIK3CA* can cause the phenotype, demonstrating that this is a physiologically relevant phenotype. A key difference between the models used to investigate *PIK3CA^{H1047R}* mediated centrosome amplification is that inducible expression from an expression vector and inducible expression in the MEF cell lines derived from mice are performed at much shorter timescales of 3-5 days, whereas the CRISPR MCF10A cell lines were in culture constitutively expressing *PIK3CA^{H1047R}* up to passage 50. For two WT lines and a homozygous line, there was no difference in the incidence of supernumerary centrosomes at passage 10 compared to passage 50, suggesting the phenotype is stable and does not increase in severity over time, or undergo negative selection. The heterozygous

cell line showed a strong reduction in supernumerary centrosomes at passage 50, however, suggesting that these cells were selected against. It would be useful to perform longer term experiments with an inducible system to assess how this phenotype evolves in vitro. It would also be useful to determine whether centrosome amplification is occurring continuously, followed by cell death to maintain a stable incidence of supernumerary centrosomes over time, or whether centrosome amplification occurs during the early stages of *PIK3CA*^{H1047R} expression followed by survival and maintenance of the cell population, and downregulation of pathways that cause centrosome amplification.

One limitation of these results in that PCNT was used as the sole marker for centrosomes in fixed cell, without a centriole marker. Berenjeno *et al* previously showed that centrosomes were positive for the PCM marker γ-tubulin, as well as centrin 2. The size and intensity of PCNT foci in these cells was extremely consistent compared to the foci observed after KIF11 mediated centrosome fragmentation. Nonetheless, use of a centriole marker such as centrin 1 or centrin 2 would improve the reliability of these results.

5.4.4 *PIK3CA*^{H1047R} Cell Lines do not Show Increased Centrosome Clustering Efficiency

In disagreement with the published literature, no evidence for an increased centrosome clustering efficiency in *PIK3CA*^{H1047R} cell lines could be detected. For all genotypes, around 75% of cells showed clustered centrosomes at one or more pole, suggesting that multipolar metaphases were transient, and clustering was achieved in the majority of mitoses with supernumerary centrosomes. In support of this, only a very small proportion of cells underwent multipolar anaphase, (2-3.5% for all genotypes; Figure 5.1c). These results are also in disagreement with the finding that MCF10A cells are poor at centrosome clustering, exhibiting clustering in only ~40% of mitoses (Rhys *et al*. 2017). Loss of E-cadherin in MCF10A increased the clustering efficiency to ~70%, which may explain the high degree of clustering observed across all cell lines. Indeed, it has been reported that MCF10A can experience partial EMT-like changes in culture including switching of E-cadherin expression to N-cadherin, in response to low density

seeding (Sarrió *et al*. 2008). Future experiments could employ western blotting to assess E-cadherin levels in the cell lines to confirm this hypothesis.

One clear observation was the dose-dependent effect of *PIK3CA*^{H1047R} expression on the formation of pseudobipolar spindles (Figure 5.2d, solid bars). These results suggest that cells expressing *PIK3CA*^{H1047R} can cluster centrosomes into a pseudobipolar spindle faster, while WT cells exhibit a transient multipolar spindle for longer time periods before clustering is achieved. Live cell imaging of a WT and homozygous *PIK3CA*^{H1047R} cell line was performed, however there was no significant difference in the mitotic timings of cells with supernumerary centrosomes in WT vs the homozygous cell line. The supernumerary centrosome phenotype was also lost in this experiment, with the WT clone 3.1D showing a 12.75% increase, while the homozygous clone showed a 4.9% decrease compared to the results from fixed cells. Both cell lines did not show any changes to in centrosome number between passage 10 and 50, suggesting the inconsistent result is not due to evolution in culture (Figure 5.2c). This could be due to the different markers used between the fixed and live experiments (PCNT vs eGFP-Centrin 1). The live imaging protocol and low exposure required to avoid phototoxicity meant that eGFP-Centrin 1 foci were not always clear, punctate foci, and potential signal artefacts were present in the movies. However, this would not explain why the WT phenotype increased in severity, while the homozygous phenotype decreased; the same degree of change would be expected for both cell lines.

5.4 Conclusions

This work has demonstrated that CRISPR cell lines edited to express *PIK3CA*^{H1047R} either hetero- or homozygously show an increased incidence of supernumerary centrosomes in mitosis. Despite investigation of clustering in fixed and live cells, however, there was no evidence that *PIK3CA*^{H1047R} increased clustering efficiency on cells with supernumerary centrosomes. These cell lines were useful for assessing the centrosome phenotypes in a normal cell line, that expressed physiologically relevant levels of *PIK3CA*^{H1047R}, over long periods of time. However, the lack of inducibility meant that it was difficult to assess the mechanism causing supernumerary centrosomes and led to concerns of

phenotype evolution in culture. This work has also demonstrated that expression of *PIK3CA*^{H1047R} does not lead to numerical CIN and aneuploidy in MCF10A cells. Interestingly there was an increase in anaphase chromatin bridges, suggesting that *PIK3CA*^{H1047R} could play a role in propagating structural CIN. Further investigation of this phenotype might further elucidate the role of *PIK3CA*^{H1047R} in cancer, and how this mutation could be affecting replication to cause chromatin bridges.

Chapter 6: Investigating the Effects of Chemical PIK3CA Activation on Mitosis

The work presented in this chapter made use of a novel small molecule activator of PIK3CA ('1938'), which induces constitutive activation of the catalytic subunit. As the *PIK3CA*^{H1047R} knock-in cell lines used in Chapter 5 constitutively expressed mutant *PIK3CA*, using 1938 provided an ideal model system to investigate upregulation of PIK3CA signalling over shorter timescales. 1938 was beneficial in that it allowed for simple experimental set-ups, which enabled extensive high spatio-temporal imaging on many samples. By using 1938 either alone or in combination with a PIK3CA inhibitor (BYL719) as a 'rescue', the effect of chemical PIK3CA activation on CIN, centrosome maintenance and MT dynamics was investigated. Sarah Conduit performed the phosphoproteomic and western blotting analysis, with contribution from Amandeep Bhamra and Silvia Surinova; Maria Carriera contributed to the cold stable assay; Maria Carriera and Elina Vladimirou contributed to the EB1 tracking; Maria Carriera and Elina Vladimirou performed the kinetochore tracking experiments and statistical analysis; Jonathan Armond performed the force inference analysis of the metaphase kinetochore oscillations using a previously developed mathematical model.

6.1 Chemical PIK3CA Activation Causes Significant Changes to the Phosphorylation Status of Mitotic Genes

To validate that 1938 activates the PIK3CA signalling pathway, western blotting was performed to identify phosphorylation of downstream targets (Figure 6.1a). RPE1 cells were serum starved for 24 hours before stimulation with 1938. A strong induction of pAKT-S473, pAKT-T308, and pPRAS40 can be observed at all time points, however pathway activation is strongest after 15 minutes of stimulation, and weakest after 4 hours of stimulation. Serum starvation arrests cells in G1 and switches off PIK3CA signalling, due to the lack of growth factors. This allows for measurement of the amount of 1938 dependent pAKT formed

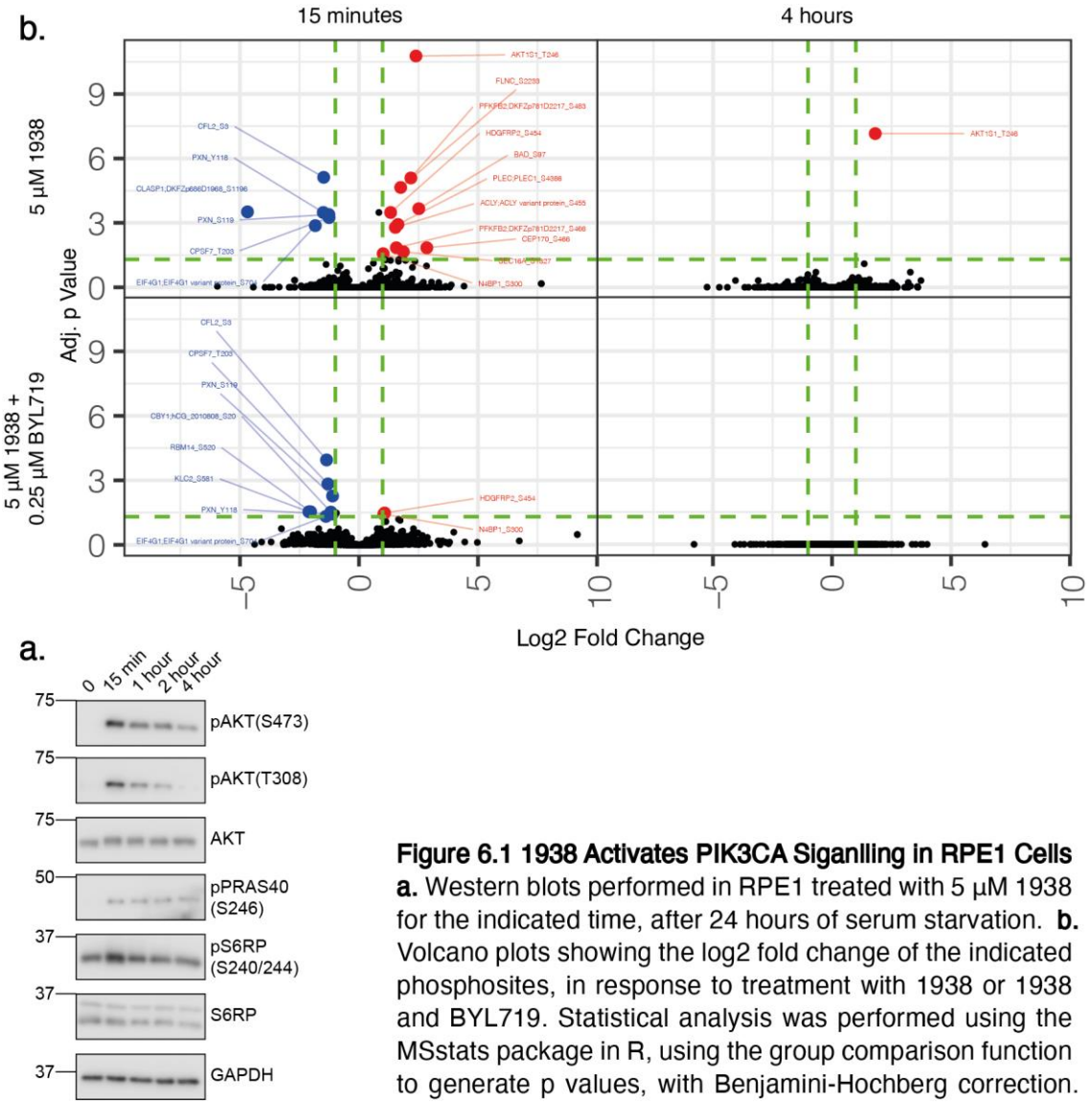

Figure 6.1 1938 Activates PIK3CA Siganlling in RPE1 Cells
a. Western blots performed in RPE1 treated with 5 µM 1938 for the indicated time, after 24 hours of serum starvation. **b.** Volcano plots showing the log2 fold change of the indicated phosphosites, in response to treatment with 1938 or 1938 and BYL719. Statistical analysis was performed using the MSstats package in R, using the group comparison function to generate p values, with Benjamini-Hochberg correction.

upon addition of the drug, as the cells do not contain any pre-existing pAKT formed in response to growth factor signalling.

Phosphoproteomic analysis was subsequently performed, to identify genes that are differentially phosphorylated or dephosphorylated in response to 1938 treatment. RPE1 cells were serum starved for 24 hours, treated with 1938 or insulin as a positive control, and samples were harvested for processing and phosphoproteomic analysis. Phosphosites with >2-fold change and with p-values <0.05 were considered significantly altered (Figure 6.1b). After treatment of cells with insulin for 15 minutes or 4 hours, a significantly increased amount of pCEP170-S466 can be observed. Treatment with 1938 for 15 minutes or 4 hours also identifies pCEP170-S466 as an upregulated phosphosite, and in addition identifies pCLASP1-S1196 as significantly downregulated. As expected, co-

treatment with 0.25 μM BYL719 abolished the effects on these phosphosites. Subjecting MEFs to the same drug treatments identified upregulation of pCEP170-S1150 and pKIF21a-S65, and downregulation of pMAP2-T1623, but no significant change to any CLASP1 phosphosites.

6.2 Chemical PIK3CA Activation does not cause CIN or Centrosome Changes

To identify whether chemical activation of the PIK3CA pathway causes the same supernumerary centrosome phenotype as seen after genetic activation, RPE1-eGFP-Centrin 1 cells were treated with 10 μM 1938 for 72 hours, to allow for approximately three cell cycles. This time scale should in theory allow for the accumulation of significant numbers of cells with an abnormal supernumerary centrosome phenotype, whether the supernumerary centrosomes were caused by PIK3CA induced centrosome amplification or induction of tetraploidy. However, there was no significant difference in the number of cells with >2 centrosomes between DMSO and 1938 ($p>0.05$, Fisher's exact test; Figure 6.2a).

Next, cells were treated with 1938 to investigate whether chemical activation of PIK3CA causes chromosome segregation errors and CIN. RPE1 were treated with 10 μM 1938 for 24 hours, before overnight imaging with SiR-DNA. Fresh medium containing 1938 and SiR-DNA was added 2 hours before imaging. There were no significant differences between DMSO and 1938 in the proportion of mitotic cells exhibiting lagging DNA or a multipolar spindle ($p>0.05$, Fisher's exact test, Figure 6.2b). This data shows that chemical activation of PIK3CA does not induce CIN.

Using the centromere and micronuclei counts as a readout of CIN and aneuploidy, a simple assay was designed using co-treatment of cells of 1938 and reversine, to identify whether activation of the PIK3CA pathway could provide a protective effect against chromosome instability. RPE1 cells treated with 0.3 μM of reversine alone showed a significant increase in the proportion of aneuploid

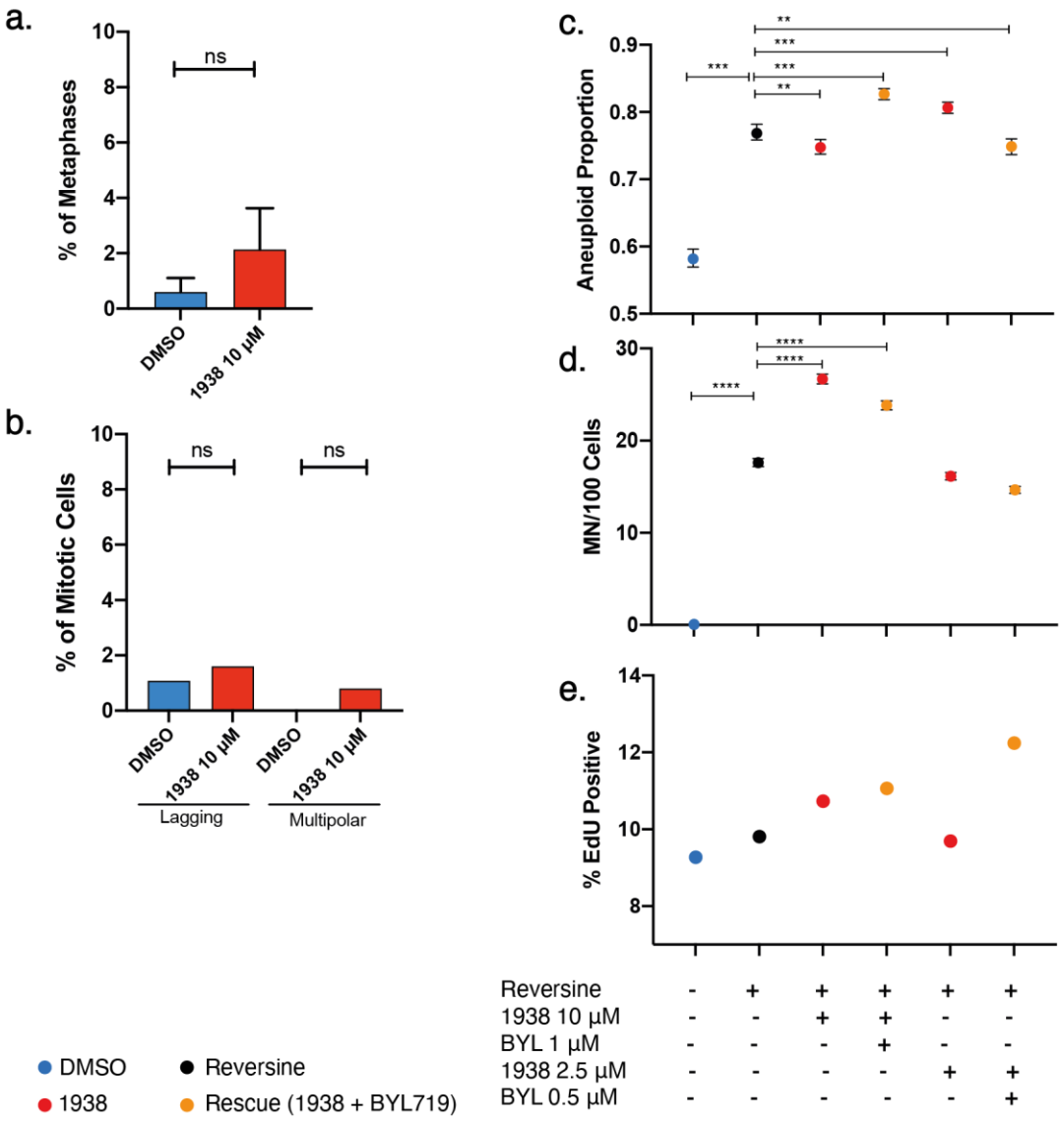

Figure 6.2 Chemical PIK3CA Activation does not Cause Mitotic Errors or Supernumerary Centrosomes a. Quantification of supernumerary centrosomes in RPE1-eGFP-Centrin 1 cells treated with DMSO or 10 μM 1938 for 72 hours. N = 3, n > 300 cells, Fisher's Exact test, error bars = SEM. **b.** Quantification of lagging DNA and multipolar mitoses from live cell imaging of RPE1 cells treated with DMSO or 10 μM 1938 for 24 hours. N = 3, n > 300 cells, Fisher's Exact test, error bars = SEM. Calculation of: **c.** the modal deviation to determine the aneuploid proportion, p values determined using a 10,000 sample permutation test with FDR adjustment, error bars = 95% confidence intervals determined by 1000 sample bootstrapping. **d.** the number of MN/100 cells, Statistical analysis was performed on a per field basis (n > 230 for each condition), using a one-sided students T-test followed by FDR adjustment. Error bars = SEM. **e.** Quantificantion of the proportion of EdU positive cells after the indicated treatment.

cells and MN/100 cells (Figure 6.2c, 6.2d). Two doses of 1938 were then tested in combination with reversine, as well as the appropriate rescue condition with BYL719. While significant differences are observed, these are small in magnitude, and do not reduce the phenotypes to the levels observed in DMSO treated cells. Both the reversine + 10 μM 1938, and reversine + 10 μM 1938 + 1

μM BYL719 treatments caused a significant increase in MN/100 cells compared to reversine alone (Figure 6.2d). These data suggest that at high doses the drug treatments may compromise genome stability, increasing formation of MN from reversine induced lagging chromosomes. This effect could potentially be due to general drug toxicity at the high 1938 dose. The proportion of EdU positive cells shows minimal variation in this experiment (Figure 6.2e).

6.3 Chemical PIK3CA Activation Alters Mitotic Timing

Time-lapse imaging RPE1 cells labelled with SiR-DNA was performed after treatment with 10 μM 1938 for 24 hours, and the time from NEB – anaphase onset calculated. This revealed a significant delay in 1938 treated cells compared to DMSO, which took an average of 21.9 ± 4.1 minutes to complete mitosis, compared to 26.1 ± 5.9 minutes (mean ± SD, $p<0.001$, Student's T test, Figure 6.3c). This difference was due to cells spending longer in metaphase (mean of 11.7 ± 5.2 minutes compared to 8.0 ± 4.0 minutes; Figure 6.3e), while there was no difference in the time taken from NEB – metaphase onset, Figure 6.3d). Visual inspection of the time-lapse movies revealed that 1938 treated cells showed more obvious metaphase plate thinning before anaphase onset compared to DMSO. These results suggest that 1938 could cause changes to MT dynamics during metaphase, resulting in a subtle metaphase arrest phenotype, whilst MT dynamics during prometaphase and the mitotic machinery required for chromosome congression are not affected.

Throughout the time-lapse movies, a globular background signal developed in the SiR-DNA channel in 1938 treated cells, resembling the morphology of lysosomes. This signal slowly became stronger throughout the 12-hour time-lapse. To confirm this signal was from lysosomes, cells treated with DMSO or 1938 for 36 hours (to match the 24 hour treatment plus 12 hours of imaging in Figure 6.3) were incubated with lysotracker to label the lysosomes (Figure 6.4a). A striking difference could be seen, with 1938 treated cells exhibiting enlarged lysosomes with brighter staining (Figure 6.4b). To identify whether this lysosome phenotype was impacting mitosis, the time taken from NEB – anaphase onset

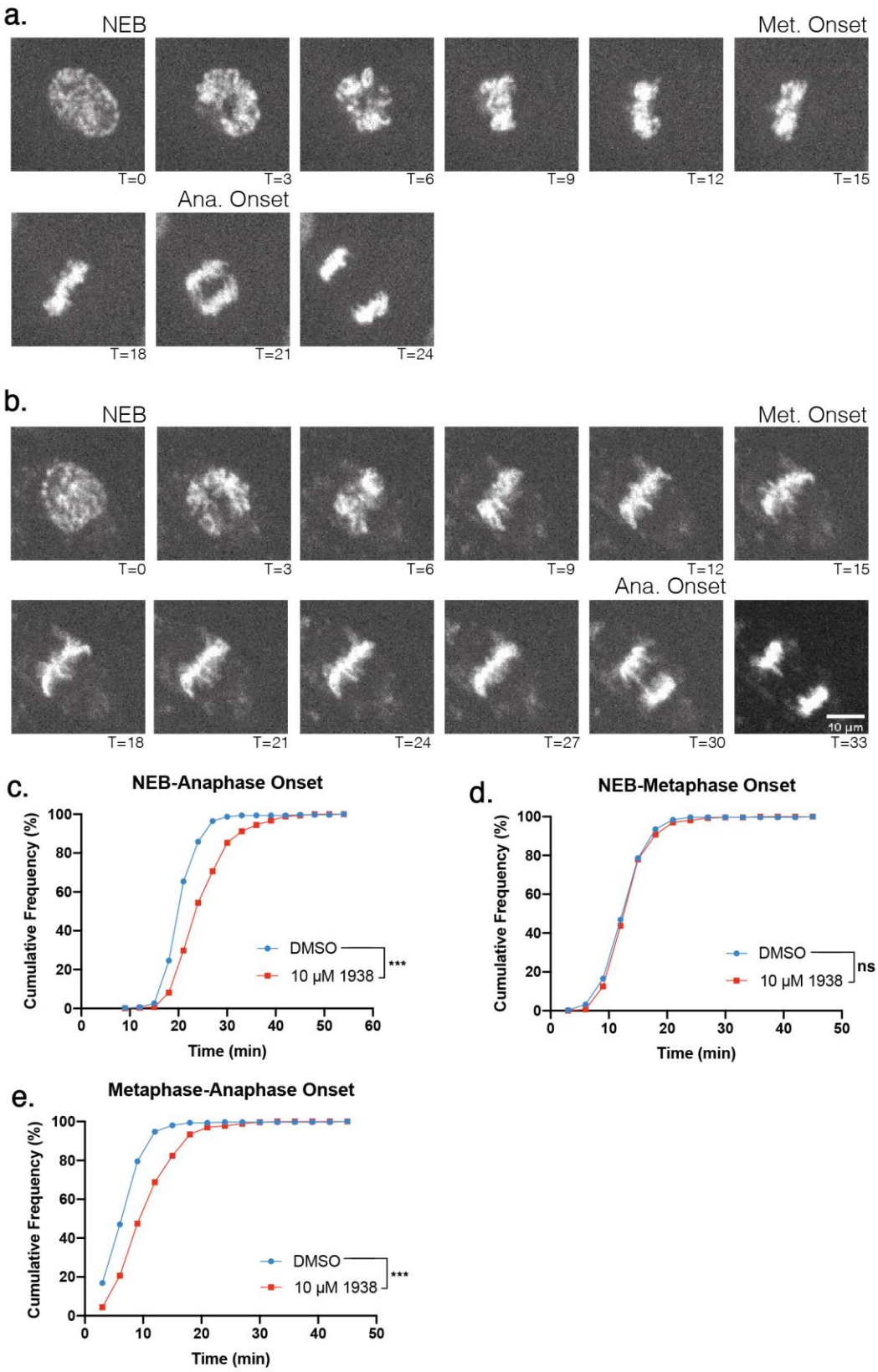

Figure 6.3 Chemical PIK3CA Activation Alters Mitotic Timing Example images from time-lapse movies of RPE1 cells treated with **a.** DMSO or, **b.** 10 µM 1938 for 24 hours. Quantification of the time taken from **c.** NEB - anaphase onset, **d.** NEB - metaphase onset, and **e.** metaphase - anaphase onset. N = 3, n > 300 cells, Student's T-test.

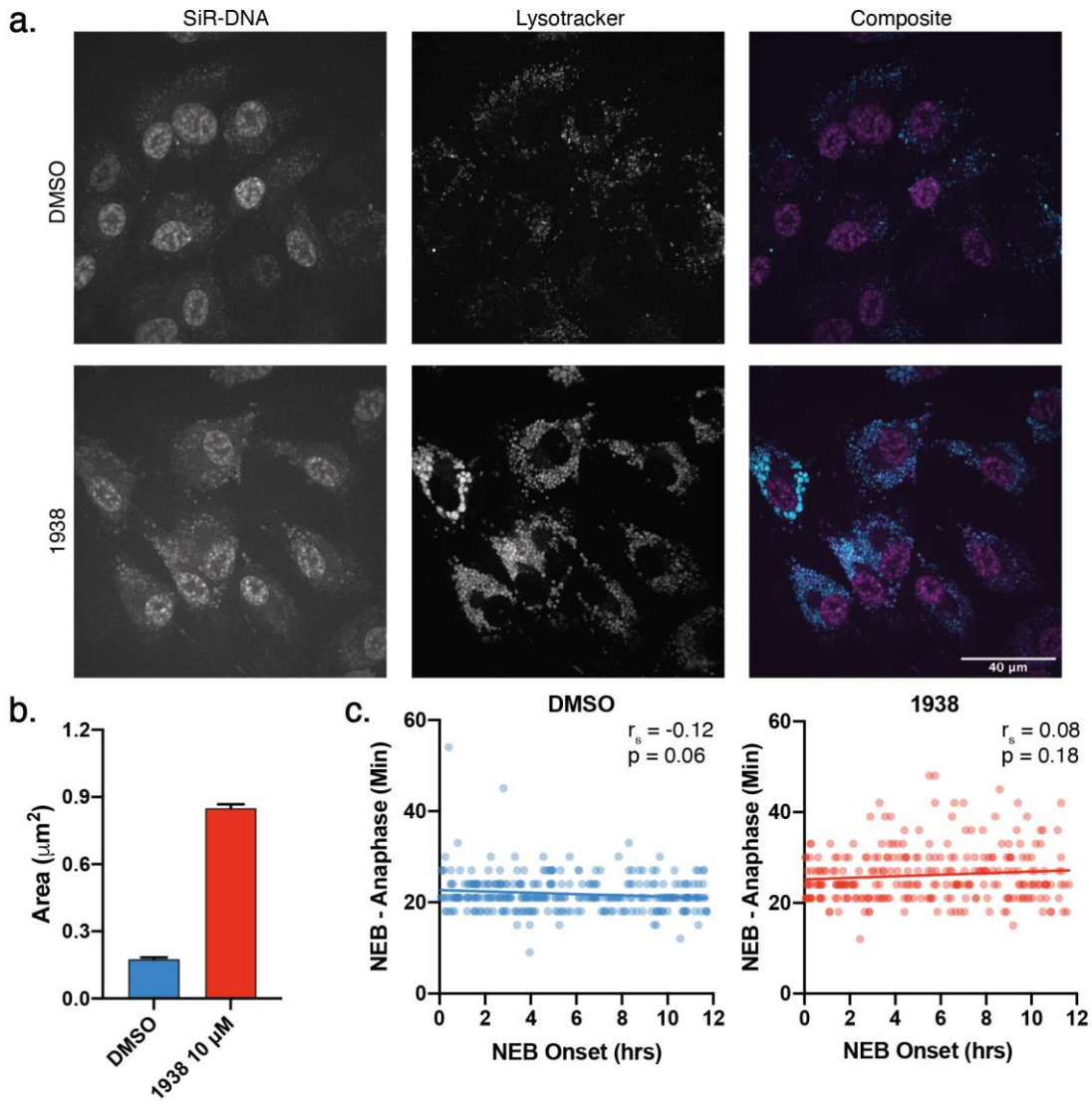

Figure 6.4 1938 Treatment Increases Lysosome Size in RPE1 Cells a. Example images of live cells treated with either DMSO or 10 µM 1938 for 36 hours, and labelled with SiR-DNA and lysotracker. **b.** Quantification of lysosome area. N = 1, n > 100 cells per condition, error bars = SEM. **c.** Correlation between the time taken from NEB - anaphase and the time after imaging began at which cells underwent NEB and entered mitosis. Spearman's correlation coefficient.

was plotted against the frame in which the cell underwent NEB and entered mitosis (Figure 6.4c). This confirmed that there was no correlation between mitotic timing and the length of exposure to the drug (Spearman's correlation coefficient). Due to the effects observed, the dose of 1938 was lowered in future experiments.

6.4 Investigating the Effect of Chemical PIK3CA Activation on Interphase Microtubule Dynamics

As the phosphoproteomic analysis identified phosphosites on proteins involved in regulating MT function (CLASP1, CEP170, and MAP2) as significantly altered in response to 1938, and given the importance of PIK3CA signalling at the cell cortex for cell motility (Onishi *et al*. 2007), the effect of chemical PIK3CA activation on MT dynamics was investigated next. EB1-tagRFP was introduced in RPE1 cells and 2D time-lapse movies of interphase cells were captured after the various drug treatments (Figure 6.5a). For these experiments, the focal plane was set at the bottom of the cell, to capture EB1 comets at the cell cortex, which was very close to the surface of the cover slip. U-track was used to automatically track EB1 comets in MATLAB, providing a measure of the MT growth speed and MT growth lifetime.

MT dynamics across the whole cell were analysed first. The growth speed was significantly increased after treatment with 1938 compared to DMSO (mean of 27.1 ± 3.8 vs 28.7 ± 4.1 μm/min, $p<0.05$, one-way ANOVA with Dunnett's multiple comparisons test), and significantly reduced after BYL719 compared to DMSO (mean of 27.1 ± 3.8 vs 25.0 ± 2.2 μm/min, $p<0.0001$; Figure 6.5b). There was no significant difference between DMSO and the rescue condition, where cells were treated with both 1938 and BYL719, indicating that this phenotype is indeed dependent on PIK3CA signalling. There were no significant changes to the lifetime of EB1 comets in any condition, with an average lifetime around 9 seconds observed for all conditions (p values >0.05; Figure 6.5c). This suggests that chemical activation of PIK3CA increases the rate of tubulin polymerisation but does not affect the MT stability.

Specific ROIs were then implemented to isolate the leading and rear edges of the cell (Figure 6.5a). At the leading edge, treatment with 1938 again significantly increases the growth speed compared to DMSO (mean of 20.8 ± 3.9 vs 24.2 ± 2.4 μm/min, $p<0.01$, Figure 6.5d). However, BYL719 treatment does not significantly affect growth speed ($p>0.05$), and there is no rescue effect seen in the combined treatment (Figure 6.5d). As seen in the whole cell measurements, 1938 treatment does not change EB1 comet lifetime at the leading edge, however it is significantly reduced after BYL719 treatment, which is in line with previously

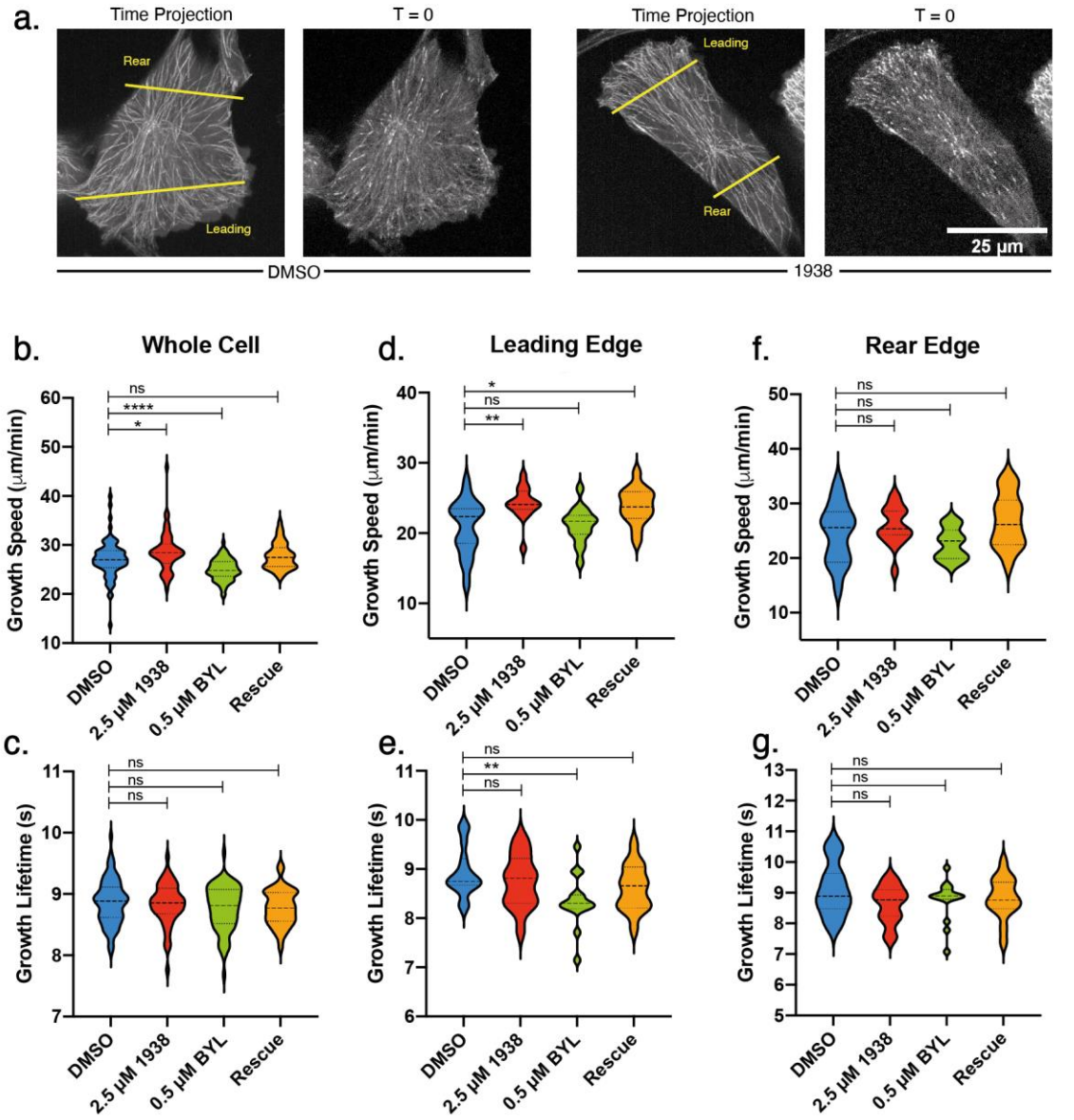

Figure 6.5 Chemical PIK3CA Activation Increases Growth Speed at Microtubule Plus Ends **a.** Example images from DMSO and 1938 treated cells showing EB1-tagRFP comets. Projection of the 50 second movie through time shows comet trajectories. Quantification of: **b.** MT growth speed across the whole cell, **c.** MT growth lifetime across the whole cell, **d.** MT growth speed at the leading edge, **e.** MT growth lifetime at the leading edge, **f.** MT growth speed at the rear edge, **g.** MT growth lifetime at the rear edge. **b & c.** N = 3, n > 40 cells, one-way ANOVA with Dunnett's multiple comparisons test. **d-g.** N = 3, n = 15 cells, one-way ANOVA with Dunnett's multiple comparisons test, lines show median and interquartile range.

published findings (Figure 6.5e, green population, $p<0.01$; (Onishi et al. 2007). However, the evidence supporting this hypothesis is weak, as activation with 1938 does not produce a concordant increase in EB1 comet lifetime.

At the rear edge, there are no significant changes to either growth speed or lifetime with any of the treatments ($p>0.05$). These results are in line with the established role for PIK3CA and AKT functioning at the leading edge of cells.

Overall, the growth speeds were lower at the leading and rear edges compared to the entire cell, with speeds around 22.5, 25, and 27 μm/min, respectively. This suggests that MT polymerization is faster in the centre of the cell, which is consistent with previously published findings (Waterman-Storer and Salmon 1997; Matov *et al*. 2010).

6.5 Investigating the Effect of Chemical PIK3CA Activation on Microtubule Dynamics during Mitosis

To investigate whether chemical PIK3CA activation alters MT dynamics during mitosis, several alternative approaches were taken, as the original u-Track software used for tracking of EB1 comets was developed for 2D movies. Firstly, cells were fixed under normal conditions following a 4 hour drug treatment (Figure 6.6a), and intensity of α-Tubulin measured normalized to PCNT. Treatment with 1938 had no significant effect on the ratio of α-Tubulin: PCNT signal intensity ($p>0.05$, one-way ANOVA with Dunnett's multiple comparisons test; Figure 6.6b). Treatment with BYL719, however, significantly increased the ratio ($p<0.0001$). Analysis of the raw mean grey values measured for α-Tubulin and PCNT showed that this was due to differences observed in α-Tubulin intensity, as no significant differences were observed in PCNT staining across all conditions. These data suggest inhibition of PIK3CA promotes increased MT polymerization in mitosis.

A cold stable assay was then performed, to determine whether kMTs showed increased cold resistance after PIK3CA activation/inhibition. Treatment with 1938 alone resulted in a significant reduction in the ratio of α-Tubulin: PCNT signal intensity, compared to DMSO ($p<0.05$; Figure 6.6c). This suggests activation of PIK3CA destabilizes mitotic spindle MTs, resulting in more catastrophe events in response to cold treatment. BYL719 treated cells caused a significant increase in the α-Tubulin: PCNT ratio ($p<0.01$), similar to that seen under normal conditions, while the rescue showed no significant difference with DMSO ($p>0.05$; Figure 6.6c).

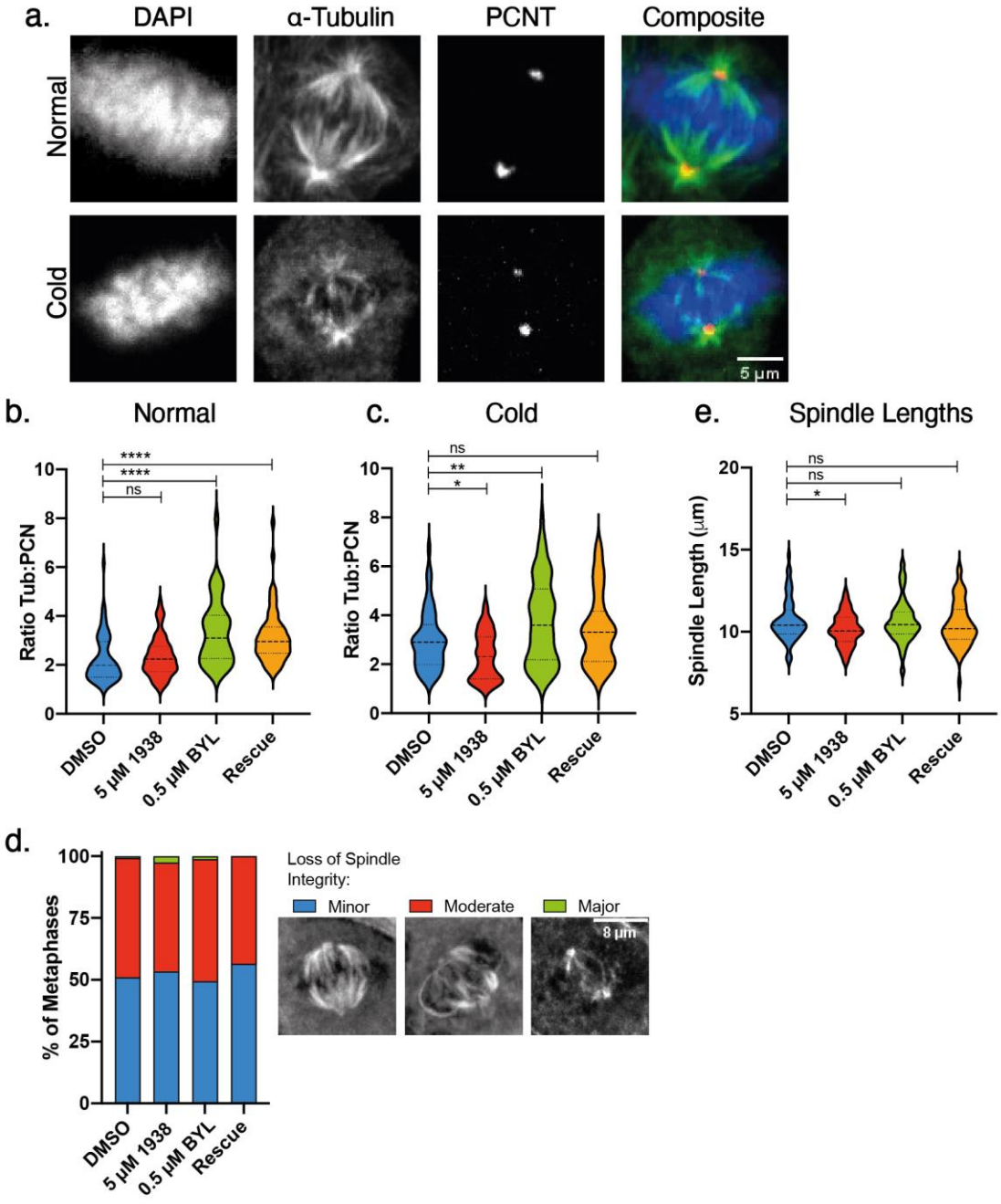

Figure 6.6 Mitotic Microtubule Stability after Chemical PIK3CA Activation and Inhibition **a.** Example images of DMSO treated cells under normal and cold conditions. Quantification of α-Tubulin signal intensity normalised to PCNT under **b.** normal conditions, following 4 hour drug treatments, **c.** cold conditions, following 4-hour drug treatments. **d.** Classification of spindle integrity after 4 hour drug treatments and cold media incubation. **e.** Spindle lengths measured under normal conditions, following 4 hour drug treatments. N = 3, n > 30 cells, one-way ANOVA with Dunnett's multiple comparisons test, lines show median and interquartile range.

Finally, spindle lengths were also measured in cells treated with the various drugs, under normal conditions (Figure 6.6e). Whilst there were no obvious changes to the spindle structure, this revealed a small yet significant reduction in spindle length after treatment with 1938 ($p<0.05$). This effect was absent in BYL719 and rescue conditions, suggesting that co-treatment with BYL719

successfully rescued this phenotype. This data supports the theory that 1938 can indeed alter MT dynamics, however it does not provide any further information on the mechanistic basis of the effect.

To further investigate MT dynamics in mitotic cells, a MT depolymerization assay was performed to directly monitor spindle MT stability. This assay provides information on the rate of catastrophe in response to low dose nocodazole, in non-KT MTs that depolymerise rapidly, and k-MTs that depolymerise slowly. SiR-Tubulin intensity is measured in the 15 minutes following addition of nocodazole (Figure 6.7a). The data was plotted and fitted to a curve using a two-phase decay model (Figure 6.7b), from which the half-lives of the fast population of MTs (non-KT MTs) and the slow population (k-MTs) can be extracted. No significant differences were observed in rate of tubulin signal decay between DMSO, 1938, or BYL719 treated cells for either the fast or slow MT populations ($p>0.05$, one-way ANOVA with Dunnett's multiple comparisons tests).

Given the observation of reduced pCLASP1-S1196 in response to 1938 treatment, combined with the established role for CLASP1 of promoting turnover of MT plus ends, KT oscillations were probed after PIK3CA activation or inhibition. RPE1 expressing mNeonGreen-CENPA were treated with either DMSO, 1938, or BYL719, and then imaged for 5 minutes with high spatio-temporal resolution to capture KT movement in metaphase cells (Figure 6.8a, Supplementary Movie 5). Movies were analysed using the KiT software to track sister-KTs (Figure 6.8b). Plotting the autocorrelation of sister-KT centre positions allows for identification of the rate at which KTs switch direction (the oscillatory half period), given by the minimum of the curve. Both 1938 and BYL719 treatment reduce the half period to around 48 seconds, while in DMSO treated cells KTs oscillate with a half period of 60 seconds (Figure 6.8c). This means that KTs switch their direction of travel on average 12 seconds sooner in 1938 and BYL719 treated cells compared to DMSO, suggesting changes in the rate at which MTs switch from a growing state to a depolymerizing state.

a.

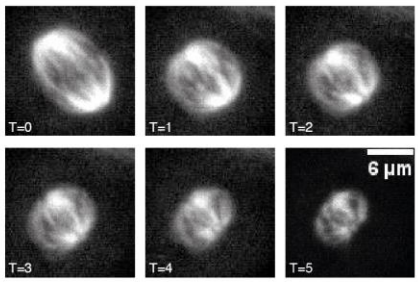

b.

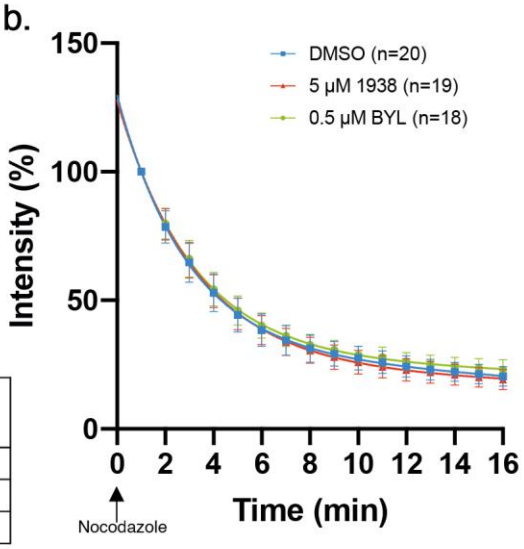

c.

Treatment	Mean Half-Life (Fast)	Adjusted p-val (vs DMSO)	Mean Half-Life (Slow)	Adjusted p-val (vs DMSO)
DMSO	2.06	-	5.20×10^{-8}	-
5 µM 1938	2.21	0.73	2.66×10^{-12}	0.14
0.5 µM BYL	2.14	0.92	4.23×10^{-10}	0.99

Figure 6.7 Chemical PIK3CA Activation and Inhibition does not Effect Microtubule Depolymerisation in Response to Nocodazole **a.** Example images from timelapse movies showing spindle collapse in DMSO-treated cells after addition of nocodazole. **b.** Quantification of spindle intensity as a percentage of that at T = 0, curves fitted using a two-phase decay model. Error bars = SD. **c.** Table of statistics calculated using the two phase decay model. Two phase decay curves were fitted and half-lives calculated on a per cell basis. N = 3, n >18 cells, one way ANOVA with Dunnett's multiple comparisons test performed on the half-lives measured from each cell.

Further statistical analysis of the KT trajectories was performed using CupL software to extract additional parameters that describe KT movements at metaphase. Compared to DMSO, the speed at which KTs oscillate was significantly reduced after treatment with either 1938 or BYL719, (means of 2.09 ± 0.5, 1.85 ± 0.48, and 1.94 ± 0.52 µm/min, respectively. Mean ± SD, $p<0.0001$, $p<0.0001$, one-way ANOVA with Dunnett's multiple comparisons tests, Figure 6.8d). The speed of KT movement during oscillations also describes the rate of MT growth and depolymerisation, depending on the direction of travel. For BYL719, these results are consistent with the EB1 tracking results, which showed a reduction in MT growth speed. For 1938 however, these results are not consistent with the EB1 tracking data. It is unclear how both activation and inhibition of the pathway could result in the same phenotype, and future work using orthogonal approaches might further describe these phenotypes.

Compared to DMSO, the inter-sister distance was significantly increased after treatment with either 1938 or BYL719, (means of 0.93 ± 0.11, 0.96 ± 0.11, and 1.04 ± 0.19 µm/min, respectively, $p<0.001$, $p<0.0001$; Figure 6.8e). The probability

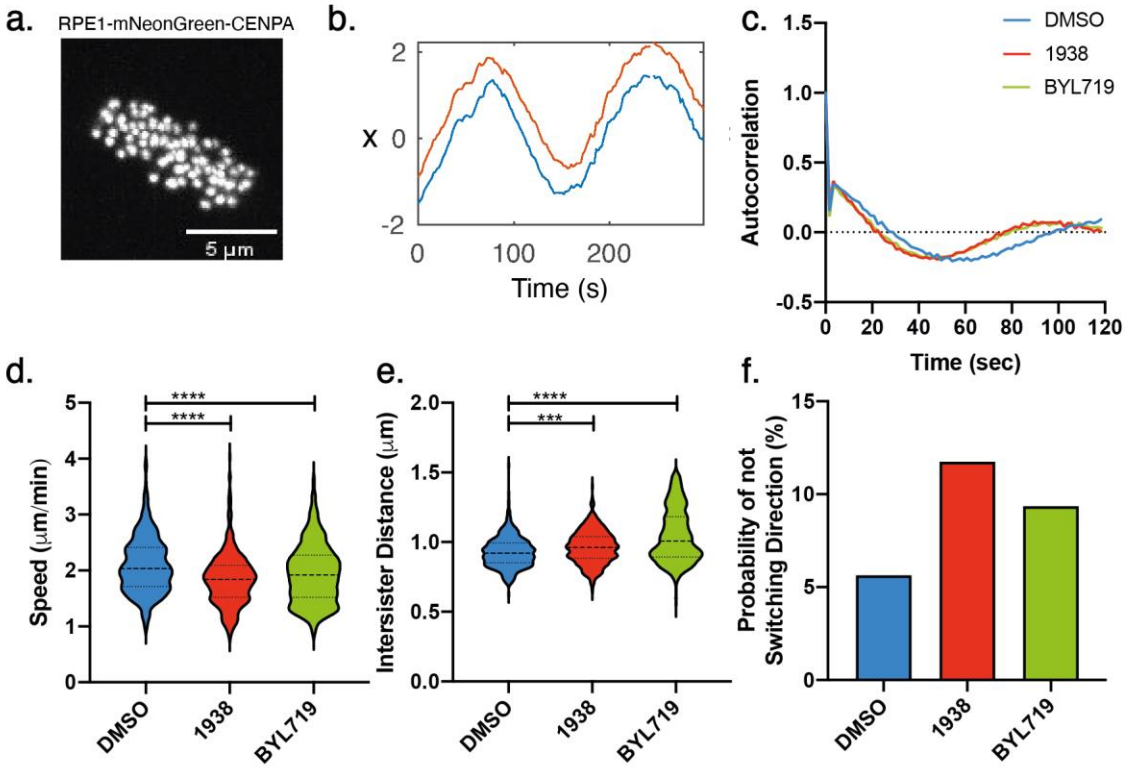

Figure 6.8 Chemical PIK3CA Activation and Inhibition Alters Metaphase Kinetochore Oscillations **a.** Example projection through z in a DMSO treated cell at T = 0. **b.** Example plot showing the oscillations of a single sister-KT pair. KT positions were plotted through time. **c.** Autocorrelation between sister-KTs with respect to time. N = 2, n = 20 cells (DMSO), n = 18 cells (1938), n = 15 cells (BYL), from which >440 sister-KT pairs were tracked. **d.** Sister-KT oscillation speed. **e.** Distance between each sister-KT. **f.** Probability of switching direction. **d & e.** one-way ANOVA with Dunnett's multiple comparisons test.

that KTs do not switch direction was increased for both 1938 and BYL719 treatment (Figure 6.8f). These data suggest there could be increased pulling forces on either KT, perhaps due to reduced poleward flux. Again, it is unclear why PIK3CA inhibition and activation induce the same phenotype. One explanation for these observations is that the drugs impact the polymerising and depolymerising populations within the k fiber differently, but the overall effect on KT oscillations is the same (Armond *et al*. 2015).

6.6 Discussion

6.6.1 Multiple Models for Investigating PIK3CA Pathway Activation

Multiple models to investigate PIK3CA pathway activation have been utilized in this project: genetic upregulation of WT *PIK3CA* via CRISPR activation, knock-in of *PIK3CA*^{H1047R} at the WT locus in MCF10A, and chemical activation using 1938.

Chemical activation is a model closer to oncogenic activating point mutations rather than overexpression, however the metabolic processes associated with uptake and breakdown of the drug mean the effects on cellular physiology are very different. Compared to CRISPR gene upregulation, chemical activation and the CRISPR knock-in cell lines have the benefit of being independent of regulation by p85. When upregulating PIK3CA the results will be confounded by the effect of p85 regulation, as in a model where p85 levels are limiting, excess PIK3CA could be unstable and degraded before any changes in signalling pathway dynamics are observed (Luo and Cantley 2005). It is not known whether p85 is expressed in excess of PIK3CA in RPE1 cells, or how rapidly monomeric PIK3CA is degraded. Determination of gene expression and protein ratios by qPCR and western blotting, respectively, could enable a better understanding of protein interactions upon upregulation of PIK3CA.

6.6.2 1938 Dose Toxicity

Various doses and treatment regimens have been used in this work, as new information came to light part way through the study implicating toxicity at doses above 5 μM. This is a limitation of the work, preventing comparison of results from different experiments. Ideally, all work should be repeated at a dose <5 μM, applied to cells for <4 hours, to ensure there is no toxicity and the phenotype is measured within the window of increased pAKT. The western blotting performed in Figure 6.1a employed serum starvation so that only 1938-induced pAKT was measured. In the presence of serum, only very small changes in pAKT levels are observed when treating cells with 1938. None of the experiments in this study were performed in serum starvation, as this would have led to a rapid cell cycle arrest in RPE1 and no mitotic cells in the control conditions. This could explain why the phenotypes measured are so subtle, as in the presence of serum only subtle changes in pathway signalling are observed. A quantitative measure of pathway expression in the presence of serum would help interpret these results.

Potential drug toxicity presents another limitation of this work. The dramatic increase in lysosome volume after 1938 treatment at 10 μM for 36 hours suggests that metabolic processes are altered at high doses. The high dose of 1938 likely results in a strong induction of mTOR activity, and a subsequent increase in

protein synthesis. It has been shown that overactivation of mTOR causes an accumulation of unfolded proteins in the endoplasmic reticulum (ER) causing ER stress (Ozcan *et al*. 2008), which in turns activates autophagy, a cellular recycling mechanism that breaks down damaged or excessive proteins and organelles to generate energy (Fu *et al*. 2017). The lysosome phenotype observed is likely due to an upregulation of autophagy, meaning more cellular components are rapidly delivered to lysosomes for degradation, resulting in their enlargement. Prolonged ER stress can lead to apoptosis; in PC-3 cells, tunicamycin treatment to induce ER stress caused apoptosis in 14.3% of cells after 72 hours, increasing to 53.7% of cells after 96 hours. During the first 48 hours of treatment there was no detectable apoptosis (Guha *et al*. 2017). Future experiments might investigate whether high doses of 1938 can cause apoptosis at later time points such as 96 hours, to determine the impact of the drug toxicity observed during the live cell imaging (when cells were treated with 10 μM 1938 and imaged for up to 36 hours).

Despite the effects observed on lysosome homeostasis suggesting drug toxicity, analysis of the time lapse movies revealed there was no change in the proportion of cells entering mitosis late in the movie, when the lysosome phenotype became more severe. There was also no increase in the mitotic duration of cells entering mitosis late in the movie (Figure 6.4c), suggesting that the lysosome phenotype does not affect mitosis. There were no signs of apoptosis evident from SiR-DNA staining.

6.6.3 Chemical PIK3CA Activation & Microtubule Dynamics

Activation of PIK3CA has been shown to stabilize MTs at the leading edge of fibroblasts. Results from EB1 comet tracking in non-contacting RPE1 cells partially support these findings, however not all results were consistent. The MT lifetime provides a good measure of MT stability, describing the length of time an MT can persist before it undergoes catastrophe. In contrast, the growth speed describes processes at the plus tip that regulate tubulin polymerization. PIK3CA inhibition with BYL719 resulted in a decrease in MT lifetime at the leading edge, which is in line with published results (Onishi *et al*. 2007), however 1938 treatment did not induce the expected increase in MT lifetime (Figure 6.5e).

BYL719 is a well-characterized drug that has been shown to effectively inhibit phosphorylation of AKT after a 1 μM treatment for 48 hours (Keam *et al*. 2015), therefore the treatment regimen used for the EB1 tracking experiments (0.5 μM, 24 hours) likely resulted in effective pathway inhibition. The pathway dynamics for 1938 differ dramatically, however. After 15 minutes, a strong induction of pAKT is observed but this drops significantly at 4 hours (Figure 6.1a). If pAKT levels at 24 hours dropped even lower than what is observed at 4 hours, then pathway activation may be too subtle to observe the MT stabilization phenotype at the leading edge at this time point. A reduction in levels of pAKT at later time points is expected due to the intrinsic feedback mechanisms that shut down signalling through the pathway after a period of activation (Figure 1.7a). In this work, the time scale on which these pathways function in response to 1938 has not been characterized. Future experiments using a 15 minute drug treatment would test this hypothesis.

Microtubule stability was also measured in mitosis, to identify whether chemical PIK3CA activation could induce a similar MT stabilization phenotype as that in migrating cells. These experiments were performed on the shorter timescale of 4 hours, therefore negating the concern of negative feedback causing a reduction in pAKT levels. The intensity measurements from spindles treated with normal and cold media gave subtle but significant changes in the signal intensity of tubulin normalized to PCNT. Both the BYL719 and rescue treatments resulted in increased spindle intensity under normal conditions, while 1938 treatment had no significant effect. Under normal conditions, an increased spindle intensity could be explained by increased nucleation of MTs at the spindle poles, which is mediated by CLASPs. Current evidence in the literature suggests that PIK3CA can modulate CLASP activity through GSK3-mediated phosphorylation, however the exact mechanism and which phosphorylation sites are involved in regulating CLASP association with kinetochore, the MT body, and spindle poles have not been elucidated.

The cold-treated cells again showed subtle phenotypic changes, however when classifying spindle integrity between the different conditions, no differences in MT stability could be observed. This was confirmed by the results from the MT depolymerization assay with nocodazole. Tracking of kinetochores in mitosis

revealed changes in their oscillatory behaviour in response to activation and inhibition of PIK3CA, which could reflect changes to the rates of polymerization and depolymerization of kMTs (Figure 6.8). The data presented in this project suggest a model where PIK3CA signalling modulates MT polymerization without effecting MT stability.

6.6.4 Experimental Results in the Context of Phosphoproteomic Data

All links between PIK3CA signalling and CLASPs in this study are based on the observation of negative regulation of pCLASP1-S1196 in response to 15 minute and 4 hour treatment with 5 μM 1938, and what has previously been shown in the literature (Akhmanova *et al*. 2001). S1196 resides in an unstructured region of CLASP1, between the TOG3 and CLIP-ID domains, which have been implicated in tubulin and lattice MT binding (Figure 6.9). As yet, there are no studies investigating the importance of this phosphorylation site in the function of CLASP1. Western blotting for phosphorylated CLASPs, and in particular pCLASP1-S1196, in mitotic fractions after activation and inhibition of PIK3CA signalling would confirm whether they are indeed regulated by this pathway. Staining mitotic cells for CLASPs and measuring their intensity at kinetochores and spindle poles, as well as colocalization with tubulin staining, could elucidate whether modulation of PIK3CA signalling effects CLASP localization in mitosis. Finally, generation of a non-phosphorylatable mutant at S1196 in CLASP1 and investigating its effects on mitotic processes would provide mechanistic

Figure 6.9 Protein Domain Structure of CLASP1 Showing the location of the S1196 residue.

information, and an insight into the importance of this residue and its regulation by PIK3CA.

As no increase in segregation errors could be observed nor any other detrimental effects on the fidelity of mitosis, even if PIK3CA does regulate the function of CLASP1 in mitosis through the S1196 phosphorylation site, this may not be of

any functional consequence. Given the lack of any clear phonotypes in this study, there is little motivation to further investigate the role of PIK3CA signalling on CLASP function. Perhaps in a cancer context alongside additional alterations that modulate MT stability and mitotic fidelity, this pathway could have more pronounced effects in either promoting or repressing chromosome segregation errors, however this would be a difficult hypothesis to investigate.

pCEP170-S466 was identified as a positively regulated phosphosite in response to 15 minute and 4 hour treatment with 5 μM 1938. The significance of this residue is unknown, as it was shown that the N-terminal region (residues 2-754) were dispensable for localization to both MTs and centrosomes. Overexpression of *CEP170* was shown to increase bundling and cause long and wavy MTs, a phenotype similar to that observed with *EB1* overexpression (Guarguaglini *et al*. 2005). As the S466 residue does not reside in the regions of the protein required for MT and centrosome localization, it is unlikely to directly affect CEP170 binding, however it may indirectly cause changes to the protein structure. Expression of a non-phosphorylatable mutant at S466 would provide an insight into its function, but given the lack of any clear phentotypes observed in this study with regards to MT dynamics, there is insufficient evidence to motivate this work.

CEP170 interacts with the MT depolymerase KIF2b, one of the three kinesin 13 isoforms alongside KIF2a and MCAK, increasing its binding to spindle MTs (Welburn and Cheeseman 2012). KIF2b localises to centrosomes, MTs, and unaligned chromosomes, where its functions are essential for mitosis. Depletion results in monopolar spindles, altered MT dynamics, and cytokinesis failure if cells attempt anaphase (Manning *et al*. 2007). If phosphorylation of CEP170 at S466 by the PIK3CA pathway was important for its interaction with KIF2b, then treatment with BYL719 would be expected to perturb mitosis, inducing similar phenotypes to KIF2b depletion. It is possible that regulation of S466 finely tunes the affinity of CEP170 for KIF2b and/or MTs, which could contribute to MT instability and the correction of merotelic attachments, similar to the function of MCAK. In this study, there was no evidence to suggest that either activation or inhibition of PIK3CA signalling results in lagging chromosomes, or aids in their resolution when cells are treated with reversine. Differential phosphorylation of

CEP170-S466 may however play a role in the altered MT dynamics observed in the kinetochore tracking results (Figure 6.8).

While pCEP170-S466 was identified as differentially regulated in response to both insulin and 1938, pCLASP1-S1196 was only identified in response to 1938 (Figure 6.1b). This could reflect a normal pathway response at the CEP170 phosphorylation site, whereas CLASP1 is only targeted in the presence of aberrant, constitutively active PIK3CA pathway signalling. Performing phosphoproteomics in an RPE1 cell line with inducible PIK3CA^{H1047R} and WT PIK3CA as a control would test this hypothesis.

6.7 Conclusions

Despite investigating CIN, aneuploidy, centrosome biology, and MT dynamics in mitotic and interphase cells, no clear phenotypes implicating PIK3CA in these processes were observed. In RPE1 cells, chemical activation of PIK3CA does not cause CIN, prevent lagging chromosome and MN formation in the presence of reversine, or promote the survival of aneuploid cells. 1938 treatment was not able to induce centrosome amplification in RPE1 cells, despite using a dose high enough to cause significant changes to lysosome morphology (10 μM 1938, 72 hours). Small changes were observed to MT dynamics in interphase cells; most notably, BYL719 treatment reduced EB1 comet lifetime at the leading edge of migrating cells. The data concerning MT dynamics in mitotic cells were inconclusive, however the MT depolymerisation assay (the most robust method, performed in live cells with multiple measurements taken over time), showed no change in MT stability after treatment with either 1938 or BYL719 treatment. Further investigation into the role of PIK3CA signalling in mitosis is required to elucidate its significance, as well as the significance of the differentially regulated phosphosites on CLASP1 and CEP170.

Chapter 7: General Discussion

7.1 Meeting the Project Aims

Overall, the results presented in this thesis effectively meet the initial aims of the project. A screening approach combining CRISPR gene upregulation, automated centromere counting, and automated MN detection was successfully developed and validated with commonly used drugs that cause chromosome segregation errors. This pipeline was implemented to screen 39 target genes to investigate their ability to induce CIN and aneuploidy when upregulated. 17 genes were successful through all stages of the pipeline and hits were identified. Extensive investigation of cellular phenotypes induced by KIF11 upregulation was then performed, identifying spindle pole fragmentation and mitotic catastrophe as a consequence of the force imbalance caused by excess KIF11. A secondary phenotype of centric and acentric lagging chromosomes was also observed, and although the molecular mechanism was not elucidated, this may be of functional significance in cancer.

Using various tools, the role of PIK3CA pathway activation in mitosis was thoroughly investigated, addressing the aims to investigate chromosome segregation, MT dynamics, and centrosome biology. These studies identified a novel potential role of the oncogenic *PIK3CA* mutant *PIK3CA*^{H1047R} in structural CIN, as cell lines expressing this mutant show an increased incidence of chromatin bridges. There was no evidence to suggest that cell lines expressing *PIK3CA*^{H1047R} experience increased numerical CIN, as no increase in chromosome segregation errors or MN could be detected by the assays used. Finally, using a chemical activation of PIK3CA to investigate phenotypes on a shorter time scale led to the observation of changes to MT dynamics, most notably abberant KT oscillations during metaphase.

7.2 Investigating the Early Causes of CIN

An overarching aim of this project was to investigate the causes of CIN during the early stages of tumourigenesis. It is well established that whilst mutations or downregulation of mitotic checkpoint genes can initiate CIN and tumourigenesis

in mouse models, these alterations are not observed in human cancers. In fact, CIN^+ cancers often upregulate checkpoint genes, resulting in a stronger checkpoint response during mitosis as opposed to a weakening. In particular, SAC components are often upregulated in cancer, including *MAD2L1*, and *BUB1*, and kinetochore components such as *CENPE* and *NDC80*. Mitotic and SAC genes that have been identified as perturbed (up or downregulated) in human cancers have been summarised (Schvartzman *et al*. 2010), alongside their ability to cause tumour formation in mouse models, providing evidence that these alterations play a role in both the initiation of CIN and tumourigenesis. However, there is not always a direct causative link, and it is unclear whether SAC upregulation is a cause of CIN, or a consequence of CIN development, to improve survival and proliferation and reduce mitotic errors.

Profiling precancerous lesions provides a more accurate insight on genetic alterations that occur early in tumourigenesis, as performed in the recent study by Teixiera *et al*, (Teixeira *et al*. 2019). This study followed the patients over time, taking tissue samples, to identify alterations associated with progressive vs regressive lesions. This study suggests that CIN is present in precancerous lesions, where it is associated with progression to cancer. However, it cannot identify causative links between early genetic alterations and the development of CIN. Another study investigated expression of mitotic spindle checkpoint genes in a panel of breast cancer samples, identifying significant deregulation of 49/76 genes (Bièche *et al*. 2011). This study used normal breast tissue as a control, and benign, invasive carcinoma (grade I), and invasive carcinoma (grade III) to investigate gene expression changes over the course of tumour progression. Nine genes showed significant overexpression in benign samples, including *NDC80*, suggesting they contribute to CIN in the early stages of tumourigenesis. This study provides strong evidence in support of the theory that upregulation of mitotic spindle and SAC genes initiate CIN.

The work presented in this thesis aimed to bridge the gap between identification of genes that were associated with CIN and proving a causative link. The centromere and MN counting assays developed enabled thorough investigation of 17 target genes, providing evidence as to whether their upregulation can

directly cause CIN. As these genes were previously identified to be associated with CIN, it was likely that hits would be identified from this small pool of targets. Indeed, many genes showed significant changes to the aneuploid proportion in the centromere counting assay, and *KIF11* and *NEK2* were additionally validated in the MN assay. Future work could seek to validate the other hits identified solely by the centromere counting assay, including *CENPH*, *CCND1*, and *FOXA1*, as there are diverse mechanisms by which these could be altering the centromere count yet not causing MN.

The work in this thesis was carried out using two cell lines, RPE1 and MCF10A, which are both non-transformed chromosomally stable near-diploid cell lines. These cell lines provide a good model of normal cells, but they are immortalised with hTERT to survive extended passages in culture. It would be interesting to test the effects of gene upregulation on CIN and aneuploidy in a primary human cell line, to investigate, for example, whether KIF11 upregulation results in a similar p53 response after mitotic catastrophe. As much of the data that informed the gene selection process came from studies in lung cancer patients, primary human bronchial epithelial cells represent an even better model system for investigating the initiation of CIN and aneuploidy (Hynds *et al*. 2019). For the work in this thesis, RPE1 cells were chosen as they are widely used in the mitosis field (and hence well characterised) and are easy to culture and manipulate.

7.3 Can Driver Genes Cause CIN?

There have been no studies directly assessing the contribution to CIN and aneuploidy of more general cancer driver genes that are not involved in mitosis. Mitosis is a robust process that proceeds error-free over many cell cycles, however certain aspects of the molecular machinery are regarded as ‘fragile’. Minor perturbations of proteins (as small as a 20% reduction) can impair signalling, causing errors (Heinrich *et al*. 2013). Mitotic fidelity could therefore be impacted by cancer driver genes that have downstream mitotic targets. These may only cause very low levels of CIN, requiring high sensitivity analysis methods for detection. However, the few cells that experience these errors could be more dangerous, accelerating tumourigenesis.

There are examples of classical cancer driver events impacting the fidelity of mitosis through downstream targets. Many mitotic checkpoint genes are under transcriptional control by the E2F transcription factors and are subsequently deregulated by loss of the retinoblastoma pathway (Rb). *MAD2L1* overexpression has been demonstrated in response to Rb knockdown, leading to CIN and aneuploidy in HCT116 cells (Hernando *et al*. 2004). The work in this thesis sought to investigate a number of classical cancer driver genes, including *EGFR*, *TERT*, and *KRAS*. One problem experienced was that often these genes were the most difficult to successfully overexpress using CRISPR upregulation. While we did not observe any significant change to the aneuploid proportion after EGFR upregulation, further implementation of the centromere counting and MN assays using different model systems for gene upregulation and a greater number of target genes would enable a more detailed investigation of this hypothesis.

7.4 The Role of p53

All experiments performed in this study used a p53 proficient cell line, to study the effects of gene upregulation in WT background. This was important as not all cancers show loss of *TP53*, and it is not always a prerequisite for CIN and aneuploidy. Profiling of the NCI-60 cancer cell lines revealed that there was no change in numerical karyotype complexity between the subset of $p53^-$ and $p53^+$ cells lines (Roschke *et al*. 2003). There is strong evidence to suggest that p53 limits the proliferation of aneuploid cells and those that experience chromosome segregation errors, however (Thompson and Compton 2010; Soto *et al*. 2017). Future experiments performing the same analysis in a p53 deficient cell line could identify CIN phenotypes that are suppressed by p53, and therefore not detectable in the experiments performed in this project. If a particular alteration caused a very mild phenotype, then use of a p53 deficient background could provide a synergistic effect that enables identification of an otherwise undetectable phenotype.

Investigation of the effects of *KIF11* upregulation in a p53 deficient cell line would provide important information on the impact of this phenotype to cells, and its role in tumourigenesis. *KIF11* upregulation causes spindle pole fragmentation and mitotic catastrophe in a subset of cells, leading to p53 activation in 81.3% of those

cells, suggesting loss of *TP53* would increase the number of proliferating aneuploid cells. *TP53* loss may also show synergism with *KIF11* upregulation and increase the incidence of centric and acentric lagging chromosomes. It would be interesting to investigate the ability of *KIF11* upregulation alone to induce transformation of RPE1 cells, compared to a combination of *KIF11* upregulation and *TP53* loss.

Knocking out *TP53* in the *PIK3CA*^{H1047R} cell lines could provide a more detailed insight into the effects of the mutation on mitotic fidelity, as aberrant phenotypes would not be eliminated from the population. Whilst *PIK3CA*^{H1047R} did not affect the survival of aneuploid cells after treatment with reversine, the picture may be different in a *TP53* deficient background. In mouse models of breast cancer, expression of *PIK3CA*^{H1047R} is sufficient to induce mammary tumours. Expression of *PIK3CA*^{H1047R} in combination with *TP53* loss accelerated tumour development, and reduced survival, demonstrating the cooperative effects of these alterations (Adams *et al*. 2011).

7.5 Future Work

There are numerous ways the work presented in this thesis could be expanded on in the future. Exploring different applications of the CIN assay, identifying further hits, and investigating the other hit genes would be of priority. A key avenue to investigate regarding the mechanism of KIF11 mediated centrosome fragmentation is the relationship between chromosome congression and centrosome fragmentation. It would be interesting to determine whether fragmentation occurs before or after misaligned chromosomes appear in live cells upregulating KIF11. It would also be interesting to determine the precise mechanism causing congression errors in the absence of spindle pole fragmentation. Finally, development of an inducible model to study centrosome amplification and chromosome instability in cells with PIK3CA pathway activation would be important, to draw more established conclusions to the hypotheses addressed in this work.

7.6 Conclusion

The work in this thesis effectively meets the aims set out at the start of the project. The centromere and MN counting assays provide technological advancements to computational image analysis methods. Others in the mitosis field will be able to use the methods directly, or in further development of similar image analysis techniques. The discovery that *KIF11* upregulation causes spindle pole fragmentation and lagging chromosomes in cells contributes to the understanding of the function of KIF11, and its interplay with other proteins in mitosis. This finding raises interesting questions as to the role of KIF11 overexpression in cancer, and the physiological effects of upregulation in these patients. The finding of increased incidence of supernumerary centrosomes in *PIK3CA*^{H1047R} cell lines without any increase in clustering efficiency furthers previously published results, raising questions as to the cell-type specific functions of *PIK3CA*^{H1047R} in the formation and clustering of supernumerary centrosomes. Observation of increased chromatin bridges in *PIK3CA*^{H1047R} cell lines suggests a novel link between expression and structural CIN. Finally, use of the chemical activator enabled investigation of whether PIK3CA plays a role in the regulation of mitotic MT dynamics. This builds on previous results studying the regulation of cytoplasmic MT dynamics, demonstrating a novel role for PIK3CA in altering metaphase KT oscillations.

Appendix

Appendix 1: Supplementary Movies

Supplementary Move 1a & 1b: Examples of mitotic catastrophe likely due to spindle pole fragmentation after *KIF11* upregulation. Maximum intensity projection.

Supplementary Movie 2: Example of a cell undergoing mitosis labelled with eGFP-Centrin 1 and SiR-Tubulin, experiencing spindle pole fragmentation after *KIF11* upregulation. Maximum intensity projection.

Supplementary Movie 3: Example movie of an EV cell stained with SiR-Tubulin and treated with nocodazole, undergoing spindle collapse. Sum intensity projection.

Supplementary Movie 4: Example of centrosome clustering in the homozygous *PIK3CA*^{H1047R} cell line (clone 3.1D). Cell is labelled with eGFP-Centrin 1 and SiR-Tubulin. Maximum intensity projection.

Supplementary Movie 5: Example of RPE1 expressing mNeonGreen-CENPA, showing KT oscillations. Maximum intensity projection.

Appendix 2: List of gRNAs used for CRISPR upregulation

Gene	Sense Sequence (5' to 3')	Antisense Sequence (5' to 3')
SOX2	caccGGCCGCGCGGGGGAGGCCGG	aaacCCGGCCTCCCCCGCGCGGCC
SOX2	caccGGCGGGGCCTCCCGCGCCGC	aaacGCGGCGCGGGAGGCCCCGCC
SOX2	caccGGAGGAGGGGGCAGGCGAGG	aaacCCTCGCCTGCCCCCTCCTCC
SOX2	caccGCGAGGCTGGGCTCGAGTGG	aaacCCACTCGAGCCCAGCCTCGC
SOX2	caccgTCTAGCGACCAATCAGCGCG	aaacCGCGCTGATTGGTCGCTAGAc
SOX2	caccGGGGGCTGTCAGGGAATAAA	aaacTTTATTCCCTGACAGCCCCC
SOX2	caccGCCGGGTTTTGCATGAAAGG	aaacCCTTTCATGCAAAACCCGGC
PIK3CA	caccGCGGCACGGCCCCCGCCTCC	aaacGGAGGCGGGGGCCGTGCCGC
PIK3CA	caccgAGCGGCGGGGGAGAGGGGCC	aaacGGCCCCTCTCCCCCGCCGCTc
PIK3CA	caccgCGGGCCCGGCCGGGCAGCTC	aaacGAGCTGCCCGGCCGGGCCCGc
PIK3CA	caccgTGCCGCGGCCGCTGGGACTG	aaacCAGTCCCAGCGGCCGCGGCAc
PIK3CA	caccgCGACACCTCAGCGGCCGCAG	aaacCTGCGGCCGCTGAGGTGTCGc
PIK3CA	caccgCTGGGGCCGCCGGCGAGGCA	aaacTGCCTCGCCGGCGGCCCCAGc
PIK3CA	caccGAAGTAGAAAGCGGCAGTTC	aaacGAACTGCCGCTTTCTACTTC
FGFR1	caccGGCCCCGGCTGGGCTGCGGC	aaacGCCGCAGCCCAGCCGGGGCC
FGFR1	caccgTCCCGAGCGGCCCCCGGCGC	aaacGCGCCGGGGGCCGCTCGGGAc
FGFR1	caccgCGGCGAGCGGAGGGAGGCGC	aaacGCGCCTCCCTCCGCTCGCCGc
FGFR1	caccgAGCGCGCAGCCGGGAGGCTC	aaacGAGCCTCCCGGCTGCGCGCTc
FGFR1	caccGGTAAGAGCCGCGGCGCCCC	aaacGGGGCGCCGCGGCTCTTACC

FGFR1	caccGCCAAGCCCGCCCCAGATCC	aaacGGATCTGGGGCGGGCTTGGC
FGFR1	caccgAGCCACGGCGGACTCTCCCG	aaacCGGGAGAGTCCGCCGTGGCTc
FGFR1	caccgCGGAACCTCCACGCCGAGCG	aaacCGCTCGGCGTGGAGGTTCCGc
MYC	caccGAGGGTGGGGAGGGTGGGGA	aaacTCCCCACCCTCCCCACCCTC
MYC	caccgTTCCCCCACGCCCTCTGCTT	aaacAAGCAGAGGGCGTGGGGGAAc
MYC	caccGAACCCGGGAGGGGCGCTTA	aaacTAAGCGCCCCTCCCGGGTTC
MYC	caccGGTGGGGAGGAGACTCAGCC	aaacGGCTGAGTCTCCTCCCCACC
MYC	caccgTCTCGCTAATCTCCGCCCAC	aaacGTGGGCGGAGATTAGCGAGAc
MYC	caccgTCCAGACCCTCGCATTATAA	aaacTTATAATGCGAGGGTCTGGAc
MYC	caccgAGCTAGAGTGCTCGGCTGCC	aaacGGCAGCCGAGCACTCTAGCTc
CCND1	caccGGGGGCGGGGGCGGGCGCAG	aaacCTGCGCCCGCCCCCGCCCCC
CCND1	caccGCTCTGCCCCTCGCTGCTCC	aaacGGAGCAGCGAGGGGCAGAGC
CCND1	caccGGGGCGCGGGCGCCAAACGC	aaacGCGTTTGGCGCCCGCGCCCC
CCND1	caccGGCAGAGAATGGGAGCGGGA	aaacTCCCGCTCCCATTCTCTGCC
CCND1	caccgACTCCGCCGCAGGGCAGGCG	aaacCGCCTGCCCTGCGGCGGAGTc
CCND1	caccGCGCCTCAGGGATGGCTTTT	aaacAAAAGCCATCCCTGAGGCGC
CCND1	caccGTTAAGCAAAGATCAAAGCC	aaacGGCTTTGATCTTTGCTTAAC
CCND1	caccgCTATGAAAACCGGACTACAG	aaacCTGTAGTCCGGTTTTCATAGc
FOXL2	caccgAGGCCGGTCCAGGCTGTGCG	aaacCGCACAGCCTGGACCGGCCTc
FOXL2	caccgCCCCCGCCCAGCGAGCCTCA	aaacTGAGGCTCGCTGGGCGGGGGc
FOXL2	caccgCGTGAGCCTGGCTGTCGGCT	aaacAGCCGACAGCCAGGCTCACGc
FOXL2	caccgCACCGAGTTCCGCTTGCGTC	aaacGACGCAAGCGGAACTCGGTGc
FOXL2	caccgTGAACTCGCCCGTGCGCGGC	aaacGCCGCGCACGGGCGAGTTCAc
FOXL2	caccgGGCGTTTACAAAAAGTGACT	aaacAGTCACTTTTTGTAAACGCCc
FOXL2	caccGGCGCCTTCGCCCCTATAGC	aaacGCTATAGGGGCGAAGGCGCC
CD79A	caccGGCTGCTTGGGTGGGGGAAG	aaacCTTCCCCCACCCAAGCAGCC
CD79A	caccgAGCCTAGGGAACCTGAGTCC	aaacGGACTCAGGTTCCCTAGGCTc
CD79A	caccGAAACTGCTCCCTGCACCTG	aaacCAGGTGCAGGGAGCAGTTTC
CD79A	caccGCTTGACCTCTCCCCCTGCC	aaacGGCAGGGGGAGAGGTCAAGC
CD79A	caccgCCTGCCCATGACACATGCCC	aaacGGGCATGTGTCATGGGCAGGc
CD79A	caccGTGGCCACAATTCCCCTGAG	aaacCTCAGGGGAATTGTGGCCAC
CD79A	caccGCTCGTCACTGCTGAGCCTT	aaacAAGGCTCAGCAGTGACGAGC
AKT2	caccGCGCAAGAGCAGGGCAGAGA	aaacTCTCTGCCCTGCTCTTGCGC
AKT2	caccGGCCTCGCTAGGCCGTGGGG	aaacCCCCACGGCCTAGCGAGGCC
AKT2	caccgCTTCCTGTTTGTGGCGCGAG	aaacCTCGCGCCACAAACAGGAAGc
AKT2	caccGGGCCTGTGTGGGTTAGAGA	aaacTCTCTAACCCACACAGGCCC
AKT2	caccGCTCTCTCAGAGTTCGTCTC	aaacGAGACGAACTCTGAGAGAGC
AKT2	caccgCTGCGCACATTAGACAACTT	aaacAAGTTGTCTAATGTGCGCAGc
IL7R	caccgTGATGTAAGCACAGTAAGTG	aaacCACTTACTGTGCTTACATCAc
IL7R	caccgTCTGAAATTATTGTTCCTCC	aaacGGAGGAACAATAATTTCAGAc
IL7R	caccGGGGGCTGCAGGGAATATCC	aaacGGATATTCCCTGCAGCCCCC
IL7R	caccgAGAAGGCAAGTTCCAGAAAC	aaacGTTTCTGGAACTTGCCTTCTc
IL7R	caccgTACTTATCTAACCACAGACA	aaacTGTCTGTGGTTAGATAAGTAc
IL7R	caccgAGTATTGCTGCTGTAAGCAG	aaacCTGCTTACAGCAGCAATACTc

HOOK3	caccGGCGGCGGCGGCGGCGGCGG	aaacCCGCCGCCGCCGCCGCCGCC
HOOK3	caccGGTGTGGGCGGCCGGGGGCG	aaacCGCCCCCGGCCGCCCACACC
HOOK3	caccGGCGCGCCCGGCGGCAGCGG	aaacCCGCTGCCGCCGGGCGCGCC
HOOK3	caccGCGGCGGCGCTGGGGAGGAG	aaacCTCCTCCCCAGCGCCGCCGC
HOOK3	caccgCGCGGCGGCGCGGGTCGGCC	aaacGGCCGACCCGCGCCGCCGCGc
HOOK3	caccgCTCGGCCTCGGCTCCAGCCA	aaacTGGCTGGAGCCGAGGCCGAGc
HOOK3	caccgCACTGCGCACGCTCGCGCCC	aaacGGGCGCGAGCGTGCGCAGTGc
HOOK3	caccgACGCAGCGAACTGGTGGCGG	aaacCCGCCACCAGTTCGCTGCGTc
CEBPA	caccGCGCCGCGCCGCCGCAGCCC	aaacGGGCTGCGGCGGCGCGGCGC
CEBPA	caccgCTGGGCGCGCTGGAGGCGGT	aaacACCGCCTCCAGCGCGCCCAGc
CEBPA	caccgACCGCCTCCAGCGCGCCCAG	aaacCTGGGCGCGCTGGAGGCGGTc
CEBPA	caccGCCGCGCGCTAGGACCCAGC	aaacGCTGGGTCCTAGCGCGCGGC
CEBPA	caccgTCCGAGGCGGCCTCTGTCCC	aaacGGGACAGAGGCCGCCTCGGAc
CEBPA	caccGCGTTGCGCCGCGGCCTGCC	aaacGGCAGGCCGCGGCGCAACGC
CEBPA	caccGCTGGTTCGCCGCCCCATGC	aaacGCATGGGGCGGCGAACCAGC
IKBKB	caccGGGCGACTCCCCCGGGGCGG	aaacCCGCCCCGGGGGAGTCGCCC
IKBKB	caccGGCCGCGGCCGCTCTTAAAG	aaacCTTTAAGAGCGGCCGCGGCC
IKBKB	caccgCCTGTCCCGGGACCCTCGAC	aaacGTCGAGGGTCCCGGGACAGGc
IKBKB	caccGCACTCGCAGCATCCGGACC	aaacGGTCCGGATGCTGCGAGTGC
IKBKB	caccgCTCCCGGCGCGAGGCAGACC	aaacGGTCTGCCTCGCGCCGGGAGc
IKBKB	caccgTTCTTTTAAATCGGTGAGCA	aaacTGCTCACCGATTTAAAAGAAc
IKBKB	caccGTGTGGTCTCTAGACAACTG	aaacCAGTTGTCTAGAGACCACAC
REL	caccgTCGCGCGCGCGGCGGCCGCG	aaacCGCGGCCGCCGCGCGCGCGAc
REL	caccgCAGGGGCGGGGCGCTGGGGG	aaacCCCCCAGCGCCCCGCCCCTGc
REL	caccgCGGGAGCCAGGGGCAGGGGG	aaacCCCCCTGCCCCTGGCTCCCGc
REL	caccGTCGCCCCGCCCACGCCTCC	aaacGGAGGCGTGGGCGGGGCGAC
REL	caccGAGCGGGGAGAGCCGAGTGC	aaacGCACTCGGCTCTCCCCGCTC
REL	caccgCCGACGCAGCAACCCTCACC	aaacGGTGAGGGTTGCTGCGTCGGc
REL	caccGGCGGGAGGGGAATTTCCCG	aaacCGGGAAATTCCCCTCCCGCC
REL	caccgCAGCCGAGAGGCGAGCAGCC	aaacGGCTGCTCGCCTCTCGGCTGc
TERT	caccGGCGGAGGGACTGGGGACCC	aaacGGGTCCCCAGTCCCTCCGCC
TERT	caccGGGGGCTGGGCCGGGGACCC	aaacGGGTCCCCGGCCCAGCCCCC
TERT	caccGAGGGGCTGGGAGGGCCCGG	aaacCCGGGCCCTCCCAGCCCCTC
TERT	caccgCGCCCCGTCCCGACCCCTCC	aaacGGAGGGGTCGGGACGGGGCGc
TERT	caccgCCGCGCGGAGGAGGCGGAGC	aaacGCTCCGCCTCCTCCGCGCGGc
TERT	caccGGCGGGGCCGCGGAAAGGAA	aaacTTCCTTTCCGCGGCCCCGCC
TERT	caccGGAAGGTGAAGGGGCAGGAC	aaacGTCCTGCCCCTTCACCTTCC
TERT	caccgCCAGGACCGCGCTTCCCACG	aaacCGTGGGAAGCGCGGTCCTGGc
LSM14A	caccGGCGGCGGCGCGGGGCATGC	aaacGCATGCCCCGCGCCGCCGCC
LSM14A	caccGGCCGCGCTCTCGCGAGACT	aaacAGTCTCGCGAGAGCGCGGCC
LSM14A	caccGGACTACGGTGGTGGTCTTG	aaacCAAGACCACCACCGTAGTCC
LSM14A	caccGGCCGCGTGAGAGGAACTTC	aaacGAAGTTCCTCTCACGCGGCC
LSM14A	caccGAAGTTCCTCTCACGCGGCC	aaacGGCCGCGTGAGAGGAACTTC
LSM14A	caccGGGACCGGCTGAGTGCCTCG	aaacCGAGGCACTCAGCCGGTCCC

LSM14A	caccgCCCGGCAGCGCTTGTTGGCC	aaacGGCCAACAAGCGCTGCCGGGc
LSM14A	caccgCCCGAGGCCACGAATGAGCC	aaacGGCTCATTCGTGGCCTCGGGc
FOXA1	caccGGCGGCGGCGGCGGCGCGGC	aaacGCCGCGCCGCCGCCGCCGCC
FOXA1	caccGCGGGGGCAGCGCCGGGGGC	aaacGCCCCCGGCGCTGCCCCCGC
FOXA1	caccGCTGCGGGGCGCGGCGTGCG	aaacCGCACGCCGCGCCCCGCAGC
FOXA1	caccGCTGCCGCGGAGCGCGGCGC	aaacGCGCCGCGCTCCGCGGCAGC
FOXA1	caccgTGGGGAGAGGACGAGGAGGT	aaacACCTCCTCGTCCTCTCCCCAc
FOXA1	caccgCTTCCCGCGGAGGCGCTCCC	aaacGGGAGCGCCTCCGCGGGAAGc
FOXA1	caccCAACTGCACTTGCCTCGCAG	aaacCTGCGAGGCAAGTGCAGTTG
EGFR	caccGGGCCGAGGCGCGGGGAGGC	aaacGCCTCCCCGCGCCTCGGCCC
EGFR	caccgCCGATCCCTCCTCCGCCGCC	aaacGGCGGCGGAGGAGGGATCGGc
EGFR	caccGGGCGGGAGGAGGAGGGACC	aaacGGTCCCTCCTCCTCCCGCCC
EGFR	caccgCAGAGGAGGAGGAGAATGCG	aaacCGCATTCTCCTCCTCCTCTGc
EGFR	caccgCCACCGCTGTCCACCGCCTC	aaacGAGGCGGTGGACAGCGGTGGc
EGFR	caccGACCCAAGGCCAGCGGCCGC	aaacGCGGCCGCTGGCCTTGGGTC
EGFR	caccGGAGGGAGGAGAACCAGCAG	aaacCTGCTGGTTCTCCTCCCTCC
EGFR	caccGCCCGGACGTCTAGCTCGCG	aaacCGCGAGCTAGACGTCCGGGC
HEY1	caccGGGGCGGGCGCGGAGGGCGG	aaacCCGCCCTCCGCGCCCGCCCC
HEY1	caccGCCTCGCTCCCGCCCCTCCC	aaacGGGAGGGGCGGGAGCGAGGC
HEY1	caccgCGGGCGAGGGGGCGGAGAGG	aaacCCTCTCCGCCCCCTCGCCCGc
HEY1	caccgCCGACGCACCGCCGCCGGGC	aaacGCCCGGCGGCGGTGCGTCGGc
HEY1	caccgCCAGGGCAACAGCCGCCCCC	aaacGGGGGCGGCTGTTGCCCTGGc
HEY1	caccgCGCTGATTGGCAGCCGCTCC	aaacGGAGCGGCTGCCAATCAGCGc
HEY1	caccgCGCGAGAAACCGGATTGGCC	aaacGGCCAATCCGGTTTCTCGCGc
HEY1	caccGCGCGGTCCGCTAGAGCCCT	aaacAGGGCTCTAGCGGACCGCGC
NKX2-1	caccGGAAAGGGGGCGGGGAGCAG	aaacCTGCTCCCCGCCCCCTTTCC
NKX2-1	caccGGGCGGAGGGGGCGCTGAGT	aaacACTCAGCGCCCCCTCCGCCC
NKX2-1	caccGGGTTGTGGCTCGGGGATCC	aaacGGATCCCCGAGCCACAACCC
NKX2-1	caccgAAACCCCTGAGCTGCGGGGG	aaacCCCCCGCAGCTCAGGGGTTTc
NKX2-1	caccgCTCTCTTCTGCCGCCGTCAG	aaacCTGACGGCGGCAGAAGAGAGc
NKX2-1	caccGGGGATCGACTGCCTCCCGG	aaacCCGGGAGGCAGTCGATCCCC
NKX2-1	caccgCTCGGATTCTCTCCGGTAGG	aaacCCTACCGGAGAGAATCCGAGc
NKX2-1	caccgTCTCAAAGAGAGAGAGAGAG	aaacCTCTCTCTCTCTCTTTGAGAc
RSPO2	caccgAGCTGCCAGGCGCTCCCAGC	aaacGCTGGGAGCGCCTGGCAGCTc
RSPO2	caccgTCGGGCGGCGCGGCCTCCCT	aaacAGGGAGGCCGCGCCGCCCGAc
RSPO2	caccGGAGCGGCGGGTGCAGCCAC	aaacGTGGCTGCACCCGCCGCTCC
RSPO2	caccGGCGACGCCAGGCAGGAGCG	aaacCGCTCCTGCCTGGCGTCGCC
RSPO2	caccGCGGTGCTCCATCCCGGGCT	aaacAGCCCGGGATGGAGCACCGC
RSPO2	caccgTGGAATTCCAGCGGCCGCCG	aaacCGGCGGCCGCTGGAATTCCAc
RSPO2	caccGGGGAAAAGTTTGCCGAGAC	aaacGTCTCGGCAAACTTTTCCCC
RSPO2	caccgCGAGCCGCTTGGTTAGCACG	aaacCGTGCTAACCAAGCGGCTCGc
COX6C	caccGTTTGTCTTTTTCATCTTCT	aaacAGAAGATGAAAAAGACAAAC
COX6C	caccgAAAACAAGGATTTTGAAGGA	aaacTCCTTCAAAATCCTTGTTTTc
COX6C	caccgTTCTCTACCTGGCAAAGCTG	aaacCAGCTTTGCCAGGTAGAGAAc

COX6C	caccGTAGCTGGGCCACGTCTCTG	aaacCAGAGACGTGGCCCAGCTAC
COX6C	caccgATAGAGGGGCGGTATTTTTG	aaacCAAAAATACCGCCCCTCTATc
COX6C	caccgTTAATACCGATCCCATGCAG	aaacCTGCATGGGATCGGTATTAAc
KRAS	caccGGAGAAGGAGGGGGCCGGGC	aaacGCCCGGCCCCCTCCTTCTCC
KRAS	caccgCTCTGCCCTCTGCGGCCGCC	aaacGGCGGCCGCAGAGGGCAGAGc
KRAS	caccGGGGAGGCAGCGAGCGCCGG	aaacCCGGCGCTCGCTGCCTCCCC
KRAS	caccGCGGTGTGGGAAGAGGGAAG	aaacCTTCCCTCTTCCCACACCGC
KRAS	caccgCGTACGAGAGGGAGCGGCTG	aaacCAGCCGCTCCCTCTCGTACGc
KRAS	caccGCGCTCGATTCTTCTTCAGA	aaacTCTGAAGAAGAATCGAGCGC
KRAS	caccgTCCGAGCACACCGATGAGTT	aaacAACTCATCGGTGTGCTCGGAc
EIF3E	caccgAACTGGCCTAAAGAAAGGGG	aaacCCCCTTTCTTTAGGCCAGTTc
EIF3E	caccGGGTTTACCCTGGAGAGCAG	aaacCTGCTCTCCAGGGTAAACCC
EIF3E	caccgCCACAGCACATGCGCAGTAC	aaacGTACTGCGCATGTGCTGTGGc
EIF3E	caccgAAACAGATCCCTCTATTTGT	aaacACAAATAGAGGGATCTGTTTc
EIF3E	caccGTTGTCCCACCCTTTGCGTT	aaacAACGCAAAGGGTGGGACAAC
EIF3E	caccGGATCTGTCTGTTCGTTTGT	aaacACAAACGAACAGACAGATCC
EIF3E	caccGGACAACGACGCATGCGCGC	aaacGCGCGCATGCGTCGTTGTCC
PPFIBP1	caccgAGCGGGCGCGCAGGCGCCCC	aaacGGGGCGCCTGCGCGCCCGCTc
PPFIBP1	caccgAGCCAGACTAGGGCTGGAAG	aaacCTTCCAGCCCTAGTCTGGCTc
PPFIBP1	caccGCCAAAGAGAGTCAGCAGTG	aaacCACTGCTGACTCTCTTTGGC
PPFIBP1	caccgAGCCGGGGAACGTCACTCAG	aaacCTGAGTGACGTTCCCCGGCTc
PPFIBP1	caccgCGAGGAATGCATAAAATTAG	aaacCTAATTTTATGCATTCCTCGc
PPFIBP1	caccgTGCCCTTCCTGCTATCTCTA	aaacTAGAGATAGCAGGAAGGGCAc
PPFIBP1	caccGGAACGGAGATAATCCGATG	aaacCATCGGATTATCTCCGTTCC
ACTL6	caccGCTGCGCCGCATCCCCGCCG	aaacCGGCGGGGATGCGGCGCAGC
ACTL6	caccGGGGGCGGAGCTTCCCGGGT	aaacACCCGGGAAGCTCCGCCCCC
ACTL6	caccgCAGCCATGGGGGCGGGAAAG	aaacCTTTCCCGCCCCCATGGCTGc
ACTL6	caccGAGTTGGGTTGCGGAGCTGG	aaacCCAGCTCCGCAACCCAACTC
ACTL6	caccGAAAGCGACAGCAGGACAGA	aaacTCTGTCCTGCTGTCGCTTTC
ACTL6	caccgCCTCCTATCAGCCAATCACT	aaacAGTGATTGGCTGATAGGAGGc
NEK	caccgCCAAACGGAGGGCGGGAGAG	aaacCTCTCCCGCCCTCCGTTTGGc
NEK	caccGGCCGCTTCGCCTCTCTCAT	aaacATGAGAGAGGCGAAGCGGCC
NEK	caccgAGCTCGCCGGGTTCTCCCAC	aaacGTGGGAGAACCCGGCGAGCTc
NEK	caccGAAGAACACAACAATACCCT	aaacAGGGTATTGTTGTGTTCTTC
NEK	caccgATTTTGGGAAAAGTGTCACT	aaacAGGGTATTGTTGTGTTCTTC
NEK	caccGTTAAAAGCAGACGCCGACG	aaacCGTCGGCGTCTGCTTTTAAC
NCAPD	caccGCAGTCAGGCTGAAATGAAA	aaacTTTCATTTCAGCCTGACTGC
NCAPD	caccgCAAAGGGCCGCCTCTGAGTC	aaacGACTCAGAGGCGGCCCTTTGc
NCAPD	caccGGCCAATCCCCGGCAGGCAG	aaacCTGCCTGCCGGGGATTGGCC
NCAPD	caccgAGATTTGAACTCGGTATTTG	aaacCAAATACCGAGTTCAAATCTc
NCAPD	caccgACAACACGCACCAATTAGCA	aaacTGCTAATTGGTGCGTGTTGTc
NCAPD	caccgTTTCAAGTCGGCGGAGAATC	aaacGATTCTCCGCCGACTTGAAAc
ELAVL	caccgCGCTCCGGGGCGCGCGGGAG	aaacCTCCCGCGCGCCCCGGAGCGc
ELAVL	caccgAATGGGCTCGCGCGCGGGGG	aaacCCCCCGCGCGCGAGCCCATTc

ELAVL	caccGGCGTGTCCGGGCCGCGGGC	aaacGCCCGCGGCCCGGACACGCC
ELAVL	caccgCTCCGCGGCCGGCGGAGACG	aaacCGTCTCCGCCGGCCGCGGAGc
ELAVL	caccgACTTCGCAGGCGGCGCCGAC	aaacGTCGGCGCCGCCTGCGAAGTc
ELAVL	caccgATTGGCCGGCGTAGCTGTCG	aaacCGACAGCTACGCCGGCCAATc
OIP	caccgCGGACTCGGACTCCAGTGCT	aaacAGCACTGGAGTCCGAGTCCGc
OIP	caccgTGCGTCCTCATTGGACATCA	aaacTGATGTCCAATGAGGACGCAc
OIP	caccgTGAAAAAAGCGCGCCTCTGT	aaacACAGAGGCGCGCTTTTTTCAc
OIP	caccgCGGGAAATCAGCCTTTCTAT	aaacATAGAAAGGCTGATTTCCCGc
OIP	caccGGTTAGAAACCCCGCCTTTG	aaacCAAAGGCGGGGTTTCTAACC
OIP	caccgACGAATACGCAGGCGCCAAA	aaacTTTGGCGCCTGCGTATTCGTc
SMC	caccgCTCGCCGAGAGGCGGGGTCT	aaacAGACCCCGCCTCTCGGCGAGc
SMC	caccgAATCCCTTCACCTCTGGACC	aaacGGTCCAGAGGTGAAGGGATTc
SMC	caccGAAGTATCGCGGGAAGAGGA	aaacTCCTCTTCCCGCGATACTTC
SMC	caccgCTCAAGTTCCAGGAAAGCGG	aaacCCGCTTTCCTGGAACTTGAGc
SMC	caccGTAACTCTTAGAAGTCACTA	aaacTAGTGACTTCTAAGAGTTAC
SMC	caccgACGCGGCACGTCATCCGAGT	aaacACTCGGATGACGTGCCGCGTc
SMC	caccgTGGGGGCGGAGTCCGCGCCT	aaacAGGCGCGGACTCCGCCCCCAc
SMC	caccgAACCACCTTGCAGCCTTCAC	aaacGTGAAGGCTGCAAGGTGGTTc
SMC	caccgCAGTCCTCCACAGCGTTTTT	aaacAAAAACGCTGTGGAGGACTGc
SMC	caccGAAGCTTTTGACTAAGTCTC	aaacGAGACTTAGTCAAAAGCTTC
SMC	caccGCGTAGGAGGAGTCAAGTTC	aaacGAACTTGACTCCTCCTACGC
CENP	caccGCGGAAGGGGCGGGGCCCTC	aaacGAGGGCCCCGCCCCTTCCGC
CENP	caccGGCGGAAAGGGTGGGGCCCT	aaacAGGGCCCCACCCTTTCCGCC
CENP	caccgACCACGGCAACCGAAAAACA	aaacTGTTTTTCGGTTGCCGTGGTc
CENP	caccgCTACGGGCTCCTCTTTCATC	aaacGATGAAAGAGGAGCCCGTAGc
CENP	caccGCAGACGGCTGGTAAAAAGT	aaacACTTTTTACCAGCCGTCTGC
CENP	caccGATGTGTAGAGTGCTGAGTT	aaacAACTCAGCACTCTACACATC
KIF11	caccGGAGCCCCGCCCCCGGAGCG	aaacCGCTCCGGGGGCGGGGCTCC
KIF11	caccgTGTCTGCTTGCTCCGGAACT	aaacAGTTCCGGAGCAAGCAGACAc
KIF11	caccGCTGAGGGAATTTTGGGCTA	aaacTAGCCCAAAATTCCCTCAGC
KIF11	caccgATGGGATGCAGTATCCTCAC	aaacGTGAGGATACTGCATCCCATc
KIF11	caccgCCTACGGGAACGTAAAGAGG	aaacCCTCTTTACGTTCCCGTAGGc
KIF11	caccGTGGAACTTTTAGCGTAGCG	aaacCGCTACGCTAAAAGTTCCAC
KIF11	caccgCAATTCTAGCGTCTCGGCTC	aaacGAGCCGAGACGCTAGAATTGc
KIF18A	caccGGCTAGGCCGGAGCTGCTGG	aaacCCAGCAGCTCCGGCCTAGCC
KIF18A	caccgCGCAGCCAGGCTGAGCTTCT	aaacAGAAGCTCAGCCTGGCTGCGc
KIF18A	caccgCCCACTTTGGCCACCGCCTC	aaacGAGGCGGTGGCCAAAGTGGGc
KIF18A	caccGCAACGCGCGCGGCCGTTTC	aaacGAAACGGCCGCGCGCGTTGC
KIF18A	caccgTGTCACGGCTCGCGGCAGCT	aaacAGCTGCCGCGAGCCGTGACAc
KIF18A	caccgTCTTTGCTTGCTCGTCACCG	aaacCGGTGACGAGCAAGCAAAGAc
KIF18A	caccgACGTGATGACATCACGCGAG	aaacCTCGCGTGATGTCATCACGTc
KIF18B	caccgCGCGGGTAGGGGAGGGTGTG	aaacCACACCCTCCCCTACCCGCGc
KIF18B	caccGCAAGGCGCCGGGTGGAGGT	aaacACCTCCACCCGGCGCCTTGC
KIF18B	caccGTGAGCAAGCCCACTGTGAA	aaacTTCACAGTGGGCTTGCTCAC

KIF18B	caccgAAACTGCAGCCGACAGGAAG	aaacCTTCCTGTCGGCTGCAGTTTc
KIF18B	caccgTTCAAATTAGCCGGGCGGGC	aaacGCCCGCCCGGCTAATTTGAAc
KIF18B	caccGAAACAGCCAATCAGCGATA	aaacTATCGCTGATTGGCTGTTTC
KIF18B	caccgCTCGCAACACTTTGTTACTT	aaacAAGTAACAAAGTGTTGCGAGc
KIF18B	caccGACCAATAGGAAGCACGGTC	aaacGACCGTGCTTCCTATTGGTC
KIFC1	caccGGTGGCGGCCGGAGGAGAAG	aaacCTTCTCCTCCGGCCGCCACC
KIFC1	caccGACCCGTGCCGGGAGACAGG	aaacCCTGTCTCCCGGCACGGGTC
KIFC1	caccGGCTCCAGCGCTGCCTCTCC	aaacGGAGAGGCAGCGCTGGAGCC
KIFC1	caccgCGCCTCCTGGTGACTGCAGT	aaacACTGCAGTCACCAGGAGGCGc
KIFC1	caccgAAATGACGCGTGCGCAAACG	aaacCGTTTGCGCACGCGTCATTTc
KIFC1	caccgCGCAACTGGCCAAGCGAAAC	aaacGTTTCGCTTGGCCAGTTGCGc
KIFC1	caccGTTTTCCGTCGACGTGATTG	aaacCAATCACGTCGACGGAAAAC
MAD2L1	caccgCCAACTGCGCCTGCGCGAAC	aaacGTTCGCGCAGGCGCAGTTGGc
MAD2L1	caccGGACCTGGTCGCGCTGTGCC	aaacGGCACAGCGCGACCAGGTCC
MAD2L1	caccGGAAGGCTGAGAGAAAGGGC	aaacGCCCTTTCTCTCAGCCTTCC
MAD2L1	caccgCTGCGTGGGGCTGGGCTTAA	aaacTTAAGCCCAGCCCCACGCAGc
MAD2L1	caccGGCCGCTCCCGCGACATCAC	aaacGTGATGTCGCGGGAGCGGCC
MAD2L1	caccGGTCTACTAGTTGGGGCCGA	aaacTCGGCCCCAACTAGTAGACC
MAD2L1	caccgTAGGATGTGTCTTCTGGTCG	aaacCGACCAGAAGACACATCCTAc
MAD2L1	caccgACCTACCGTAGTGTCACACC	aaacGGTGTGACACTACGGTAGGTc
AXIN2	caccGGCGGGGCGGGGCGGGCGCG	aaacCGCGCCCGCCCCGCCCCGCC
AXIN2	caccgCGTGCGGCGGGGGCGGGCCG	aaacCGGCCCGCCCCCGCCGCACGc
AXIN2	caccgCCCTCGGGGCCGCGGGGGGC	aaacGCCCCCCGCGGCCCCGAGGGc
AXIN2	caccgCAGGGGGCGGAGGAGAGGCC	aaacGGCCTCTCCTCCGCCCCCTGc
AXIN2	caccTTAAGGCGGGCGGCGCGGGC	aaacGCCCGCGCCGCCCGCCTTAA
AXIN2	caccGGGAAGGGTTAACGCGGGAG	aaacCTCCCGCGTTAACCCTTCCC
AXIN2	caccGCGGCTGTGATTGGCGCGGC	aaacGCCGCGCCAATCACAGCCGC
PLK4	caccgTCTGCCGCGCATGCGCGCCC	aaacGGGCGCGCATGCGCGGCAGAc
PLK4	caccGGTTCTAGACTTCGGGGCCA	aaacTGGCCCCGAAGTCTAGAACC
PLK4	caccgCTTCCTTTGCGGCCGGCCCA	aaacTGGGCCGGCCGCAAAGGAAGc
PLK4	caccGCAGAAGTTCTTCCGAGAGT	aaacACTCTCGGAAGAACTTCTGC
PLK4	caccgAAAAGAGCAGGCCTTAAAGA	aaacTCTTTAAGGCCTGCTCTTTTc
PLK4	caccgTAAACTCTCCGCAGCGCTTC	aaacGAAGCGCTGCGGAGAGTTTAc
PLK4	caccgTTCGGGCGGGAGGCTGTCTC	aaacGAGACAGCCTCCCGCCCGAAc
PLK4	caccgCACGAGACCGCTGTGGGAAG	aaacCTTCCCACAGCGGTCTCGTGc
ESPL1	caccgCGCCGCGCTGCGCGCTCCCG	aaacCGGGAGCGCGCAGCGCGGCGc
ESPL1	caccGCGGCGCAACGCCGGGCGCG	aaacATCCGCGGCTGCCAATCAGC
ESPL1	caccgATCCGCGGCTGCCAATCAGC	aaacGCTGATTGGCAGCCGCGGATc
ESPL1	caccGTTAGGGCCTCTTGGGGGTG	aaacCACCCCCAAGAGGCCCTAAC
ESPL1	caccgCAGAGCAGCAAGACCCTCCG	aaacCGGAGGGTCTTGCTGCTCTGc
ESPL1	caccgTTTGAAAGGAGGGTCTGGCG	aaacCGCCAGACCCTCCTTTCAAAc

References:

Adams, J.R. et al. 2011. Cooperation between Pik3ca and p53 Mutations in Mouse Mammary Tumor Formation. *Cancer Research* 71(7), pp. 2706–2717. doi: 10.1158/0008-5472.CAN-10-0738.

Afonso, O. et al. 2014. Feedback control of chromosome separation by a midzone Aurora B gradient. *Science (New York, N.Y.)* 345(6194), pp. 332–336. doi: 10.1126/science.1251121.

Akhmanova, A. et al. 2001. CLASPs Are CLIP-115 and -170 Associating Proteins Involved in the Regional Regulation of Microtubule Dynamics in Motile Fibroblasts. *Cell* 104(6), pp. 923–935. doi: 10.1016/S0092-8674(01)00288-4.

Amaral, N. et al. 2016. The Aurora-B-dependent NoCut checkpoint prevents damage of anaphase bridges after DNA replication stress. *Nature Cell Biology* 18(5), pp. 516–526. doi: 10.1038/ncb3343.

Amaro, A.C. et al. 2010. Molecular control of kinetochore-microtubule dynamics and chromosome oscillations. *Nature Cell Biology* 12(4), pp. 319–329. doi: 10.1038/ncb2033.

Andriani, G.A. et al. 2019. A direct comparison of interphase FISH versus low-coverage single cell sequencing to detect aneuploidy reveals respective strengths and weaknesses. *Scientific Reports* 9(1), p. 10508. doi: 10.1038/s41598-019-46606-w.

Antonin, W. and Neumann, H. 2016. Chromosome condensation and decondensation during mitosis. *Current Opinion in Cell Biology* 40, pp. 15–22. doi: 10.1016/j.ceb.2016.01.013.

Armond, J.W. et al. 2015. Probing microtubule polymerisation state at single kinetochores during metaphase chromosome motion. *Journal of Cell Science* 128(10), pp. 1991–2001. doi: 10.1242/jcs.168682.

Armond, J.W. et al. 2016. KiT: a MATLAB package for kinetochore tracking. *Bioinformatics* 32(12), pp. 1917–1919. doi: 10.1093/bioinformatics/btw087.

Auckland, P. et al. 2020. CENP-F stabilizes kinetochore-microtubule attachments and limits dynein stripping of corona cargoes. *Journal of Cell Biology* 219(e201905018). Available at: https://doi.org/10.1083/jcb.201905018 [Accessed: 7 June 2021].

Bahreyni Toossi, M.T. et al. 2017. Automatic detection of micronuclei by cell microscopic image processing. *Mutation Research/Fundamental and Molecular Mechanisms of Mutagenesis* 806, pp. 9–18. doi: 10.1016/j.mrfmmm.2017.07.012.

Bakhoum, S.F. et al. 2009a. Deviant kinetochore-microtubule dynamics underlie chromosomal instability. *Current biology : CB* 19(22), pp. 1937–1942. doi: 10.1016/j.cub.2009.09.055.

Bakhoum, S.F. et al. 2009b. Genome stability is ensured by temporal control of kinetochore-microtubule dynamics. *Nature cell biology* 11(1), pp. 27–35. doi: 10.1038/ncb1809.

Bakhoum, S.F. et al. 2014. DNA-Damage Response during Mitosis Induces Whole-Chromosome Missegregation. *Cancer Discovery* 4(11), pp. 1281–1289. doi: 10.1158/2159-8290.CD-14-0403.

Bakhoum, S.F. et al. 2015. Numerical chromosomal instability mediates susceptibility to radiation treatment. *Nature Communications* 6, p. 5990. doi: 10.1038/ncomms6990.

Bakker, B. et al. 2016. Single-cell sequencing reveals karyotype heterogeneity in murine and human malignancies. *Genome Biology* 17(1), p. 115. doi: 10.1186/s13059-016-0971-7.

Barisic, M. et al. 2014. Kinetochore motors drive congression of peripheral polar chromosomes by overcoming random arm-ejection forces. *Nature Cell Biology* 16(12), pp. 1249–1256. doi: 10.1038/ncb3060.

Baudoin, N.C. et al. 2020. Asymmetric clustering of centrosomes defines the early evolution of tetraploid cells. Available at: https://elifesciences.org/articles/54565 [Accessed: 29 June 2021].

Baudoin, N.C. and Cimini, D. 2018. A guide to classifying mitotic stages and mitotic defects in fixed cells. *Chromosoma* 127(2), pp. 215–227. doi: 10.1007/s00412-018-0660-2.

Beer, T.M. et al. 2008. Southwest Oncology Group phase II study of ispinesib in androgen-independent prostate cancer previously treated with taxanes. *Clinical Genitourinary Cancer* 6(2), pp. 103–109. doi: 10.3816/CGC.2008.n.016.

Belmont, A.S. and Straight, A.F. 1998. In vivo visualization of chromosomes using lac operator-repressor binding. *Trends in Cell Biology* 8(3), pp. 121–124. doi: 10.1016/S0962-8924(97)01211-7.

Berenjeno, I.M. et al. 2017. Oncogenic PIK3CA induces centrosome amplification and tolerance to genome doubling. *Nature Communications* 8(1), p. 1773. doi: 10.1038/s41467-017-02002-4.

Bickel, K.G. et al. 2017. Src family kinase phosphorylation of the motor domain of the human kinesin-5, Eg5. *Cytoskeleton (Hoboken, N.J.)* 74(9), pp. 317–330. doi: 10.1002/cm.21380.

Bièche, I. et al. 2011. Expression analysis of mitotic spindle checkpoint genes in breast carcinoma: role of NDC80/HEC1 in early breast tumorigenicity, and a two-gene signature for aneuploidy. *Molecular Cancer* 10(1), p. 23. doi: 10.1186/1476-4598-10-23.

Björkqvist, A.M. et al. 1998. DNA gains in 3q occur frequently in squamous cell carcinoma of the lung, but not in adenocarcinoma. *Genes, Chromosomes & Cancer* 22(1), pp. 79–82.

Borel, F. et al. 2002. Multiple centrosomes arise from tetraploidy checkpoint failure and mitotic centrosome clusters in p53 and RB pocket protein-compromised cells. *Proceedings of the National Academy of Sciences* 99(15), pp. 9819–9824.

Burrell, R.A. et al. 2013. Replication stress links structural and numerical cancer chromosomal instability. *Nature* 494(7438), pp. 492–496. doi: 10.1038/nature11935.

Cahu, J. et al. 2008. Phosphorylation by Cdk1 Increases the Binding of Eg5 to Microtubules In Vitro and in Xenopus Egg Extract Spindles. *PLoS ONE* 3(12). Available at: https://www.ncbi.nlm.nih.gov/pmc/articles/PMC2592692/ [Accessed: 2 June 2021].

Cameron, L.A. et al. 2006. Kinesin 5–independent poleward flux of kinetochore microtubules in PtK1 cells. *Journal of Cell Biology* 173(2), pp. 173–179. doi: 10.1083/jcb.200601075.

Cárcer, G. de et al. 2018. Plk1 overexpression induces chromosomal instability and suppresses tumor development. *Nature Communications* 9(1), p. 3012. doi: 10.1038/s41467-018-05429-5.

Castedo, M. et al. 2004a. Cell death by mitotic catastrophe: a molecular definition. *Oncogene* 23(16), pp. 2825–2837. doi: 10.1038/sj.onc.1207528.

Castedo, M. et al. 2004b. Mitotic catastrophe constitutes a special case of apoptosis whose suppression entails aneuploidy. *Oncogene* 23(25), pp. 4362–4370. doi: 10.1038/sj.onc.1207572.

Castillo, A. et al. 2007. Overexpression of Eg5 causes genomic instability and tumor formation in mice. *Cancer Research* 67(21), pp. 10138–10147. doi: 10.1158/0008-5472.CAN-07-0326.

Chattopadhyay, S. et al. 2015. Niche-Based Screening in Multiple Myeloma Identifies a Kinesin-5 Inhibitor with Improved Selectivity over Hematopoietic Progenitors. *Cell Reports* 10(5), pp. 755–770. doi: 10.1016/j.celrep.2015.01.017.

Cheeseman, I.M. and Desai, A. 2008. Molecular architecture of the kinetochore–microtubule interface. *Nature Reviews Molecular Cell Biology* 9(1), pp. 33–46. doi: 10.1038/nrm2310.

Chen, G.-Y. et al. 2017. Eg5 inhibitors have contrasting effects on microtubule stability and metaphase spindle integrity. *ACS chemical biology* 12(4), pp. 1038–1046. doi: 10.1021/acschembio.6b01040.

Chen, Y. and Hancock, W.O. 2015. Kinesin-5 is a microtubule polymerase. *Nature Communications* 6(1), p. 8160. doi: 10.1038/ncomms9160.

Chong, M.-L. et al. 2014. Phosphatidylinositol-3-kinase pathway aberrations in gastric and colorectal cancer: Meta-analysis, co-occurrence and ethnic variation. *International Journal of Cancer* 134(5), pp. 1232–1238. doi: 10.1002/ijc.28444.

Cimini, D. et al. 2006. Aurora kinase promotes turnover of kinetochore microtubules to reduce chromosome segregation errors. *Current biology: CB* 16(17), pp. 1711–1718. doi: 10.1016/j.cub.2006.07.022.

Cimini, D. 2007. Detection and Correction of Merotelic Kinetochore Orientation by Aurora B and its Partners. *Cell Cycle* 6(13), pp. 1558–1564. doi: 10.4161/cc.6.13.4452.

Clift, D. and Schuh, M. 2015. A three-step MTOC fragmentation mechanism facilitates bipolar spindle assembly in mouse oocytes. *Nature Communications* 6, p. 7217. doi: 10.1038/ncomms8217.

Clute, P. and Pines, J. 1999. Temporal and spatial control of cyclin B1 destruction in metaphase. *Nature Cell Biology* 1(2), pp. 82–87. doi: 10.1038/10049.

Collins, E. et al. 2014a. Eg5 restricts anaphase B spindle elongation in mammalian cells. *Cytoskeleton* 71(2), pp. 136–144. doi: https://doi.org/10.1002/cm.21158.

Cooper, G.M. 2000. The Eukaryotic Cell Cycle. *The Cell: A Molecular Approach. 2nd edition* . Available at: https://www.ncbi.nlm.nih.gov/books/NBK9876/ [Accessed: 16 June 2021].

Cortés-Ciriano, I. et al. 2020. Comprehensive analysis of chromothripsis in 2,658 human cancers using whole-genome sequencing. *Nature Genetics* 52(3), pp. 331–341. doi: 10.1038/s41588-019-0576-7.

Daigo, K. et al. 2017. Characterization of KIF11 as a novel prognostic biomarker and therapeutic target for oral cancer. *International Journal of Oncology* 52(1), pp. 155–165. doi: 10.3892/ijo.2017.4181.

Davoli, T. et al. 2017. Tumor aneuploidy correlates with markers of immune evasion and with reduced response to immunotherapy. *Science* 355(6322). Available at: https://science.sciencemag.org/content/355/6322/eaaf8399 [Accessed: 13 July 2021].

Decordier, I. et al. 2009. Automated image analysis of cytokinesis-blocked micronuclei: an adapted protocol and a validated scoring procedure for biomonitoring. *Mutagenesis* 24(1), pp. 85–93. doi: 10.1093/mutage/gen057.

DeLuca, J.G. et al. 2006. Kinetochore Microtubule Dynamics and Attachment Stability Are Regulated by Hec1. *Cell* 127(5), pp. 969–982. doi: 10.1016/j.cell.2006.09.047.

Deng, W. et al. 2003. A new method for improving metaphase chromosome spreading. *Cytometry Part A* 51A(1), pp. 46–51. doi: 10.1002/cyto.a.10004.

Dewhurst, S.M. et al. 2014. Tolerance of whole-genome doubling propagates chromosomal instability and accelerates cancer genome evolution. *Cancer Discovery* 4(2), pp. 175–185. doi: 10.1158/2159-8290.CD-13-0285.

Dong, L. et al. 2017. Cooperative oncogenic effect and cell signaling crosstalk of co-occurring HER2 and mutant PIK3CA in mammary epithelial cells. *International Journal of Oncology* 51(4), pp. 1320–1330. doi: 10.3892/ijo.2017.4108.

Du, Y. et al. 2010. The kinesin-8 Kif18A dampens microtubule plus-end dynamics. *Current biology: CB* 20(4), pp. 374–380. doi: 10.1016/j.cub.2009.12.049.

Dudka, D. et al. 2018. Complete microtubule–kinetochore occupancy favours the segregation of merotelic attachments. *Nature Communications* 9(1), p. 2042. doi: 10.1038/s41467-018-04427-x.

Duensing, S. et al. 2000. The human papillomavirus type 16 E6 and E7 oncoproteins cooperate to induce mitotic defects and genomic instability by uncoupling centrosome duplication from the cell division cycle. *Proceedings of the National Academy of Sciences of the United States of America* 97(18), pp. 10002–10007.

Even-Ram, S. et al. 2007. Myosin IIA regulates cell motility and actomyosin–microtubule crosstalk. *Nature Cell Biology* 9(3), pp. 299–309. doi: 10.1038/ncb1540.

Fava, L.L. et al. 2017. The PIDDosome activates p53 in response to supernumerary centrosomes. *Genes & Development* 31(1), pp. 34–45. doi: 10.1101/gad.289728.116.

Fenech, M. 2007. Cytokinesis-block micronucleus cytome assay. *Nature Protocols* 2(5), pp. 1084–1104. doi: 10.1038/nprot.2007.77.

Fry, A.M. et al. 1998a. A centrosomal function for the human Nek2 protein kinase, a member of the NIMA family of cell cycle regulators. *The EMBO Journal* 17(2), pp. 470–481. doi: 10.1093/emboj/17.2.470.

Fry, A.M. et al. 1998b. C-Nap1, a Novel Centrosomal Coiled-Coil Protein and Candidate Substrate of the Cell Cycle–regulated Protein Kinase Nek2. *Journal of Cell Biology* 141(7), pp. 1563–1574. doi: 10.1083/jcb.141.7.1563.

Fu, Y.-F. et al. 2017. Endoplasmic reticulum stress induces autophagy and apoptosis while inhibiting proliferation and drug resistance in multiple myeloma through the PI3K/Akt/mTOR signaling pathway. *Oncotarget* 8(37), pp. 61093–61106. doi: 10.18632/oncotarget.17862.

Fujimitsu, K. et al. 2016. Cyclin-dependent kinase 1–dependent activation of APC/C ubiquitin ligase. *Science* 352(6289), pp. 1121–1124. doi: 10.1126/science.aad3925.

Funabiki, H. and Murray, A.W. 2000. The Xenopus Chromokinesin Xkid Is Essential for Metaphase Chromosome Alignment and Must Be Degraded to Allow Anaphase Chromosome Movement. *Cell* 102(4), pp. 411–424. doi: 10.1016/S0092-8674(00)00047-7.

Funk, L.C. et al. 2016. Living in CIN: Mitotic Infidelity and Its Consequences for Tumor Promotion and Suppression. *Developmental Cell* 39(6), pp. 638–652. doi: 10.1016/j.devcel.2016.10.023.

Gaglio, T. et al. 1996. Opposing motor activities are required for the organization of the mammalian mitotic spindle pole. *Journal of Cell Biology* 135(2), pp. 399–414. doi: 10.1083/jcb.135.2.399.

Ganem, N.J. et al. 2009. A Mechanism Linking Extra Centrosomes to Chromosomal Instability. *Nature* 460(7252), pp. 278–282. doi: 10.1038/nature08136.

Ganem, N.J. et al. 2014. Cytokinesis Failure Triggers Hippo Tumor Suppressor Pathway Activation. *Cell* 158(4), pp. 833–848. doi: 10.1016/j.cell.2014.06.029.

Ganem, N.J. and Compton, D.A. 2004. The KinI kinesin Kif2a is required for bipolar spindle assembly through a functional relationship with MCAK. *The Journal of Cell Biology* 166(4), pp. 473–478. doi: 10.1083/jcb.200404012.

Ganem, N.J. and Compton, D.A. 2006. Functional roles of poleward microtubule flux during mitosis. *Cell Cycle (Georgetown, Tex.)* 5(5), pp. 481–485. doi: 10.4161/cc.5.5.2519.

Ganguly, A. et al. 2012. The Role of Microtubules and Their Dynamics in Cell Migration *. *Journal of Biological Chemistry* 287(52), pp. 43359–43369. doi: 10.1074/jbc.M112.423905.

Gao, T. et al. 2020. KIF18B promotes tumor progression in osteosarcoma by activating β-catenin. *Cancer Biology & Medicine* 17(2), pp. 371–386. doi: 10.20892/j.issn.2095-3941.2019.0452.

Gardner, M.K. et al. 2008. Chromosome congression by kinesin-5 motor-mediated disassembly of longer kinetochore microtubules. *Cell* 135(5), pp. 894–906. doi: 10.1016/j.cell.2008.09.046.

Gay, G. et al. 2012. A stochastic model of kinetochore–microtubule attachment accurately describes fission yeast chromosome segregation. *J Cell Biol* 196(6), pp. 757–774. doi: 10.1083/jcb.201107124.

Godek, K.M. and Compton, D.A. 2018. Quantitative Methods to Measure Aneuploidy and Chromosomal Instability. *Methods in cell biology* 144, pp. 15–32. doi: 10.1016/bs.mcb.2018.03.002.

Gregan, J. et al. 2011. Merotelic kinetochore attachment: causes and effects. *Trends in Cell Biology* 21(6), pp. 374–381. doi: 10.1016/j.tcb.2011.01.003.

Guarguaglini, G. et al. 2005. The Forkhead-associated Domain Protein Cep170 Interacts with Polo-like Kinase 1 and Serves as a Marker for Mature Centrioles. *Molecular Biology of the Cell* 16(3), pp. 1095–1107. doi: 10.1091/mbc.E04-10-0939.

Guerreiro, A. et al. 2021. WDR62 localizes katanin at spindle poles to ensure synchronous chromosome segregation. *Journal of Cell Biology* 220(8). Available at: https://doi.org/10.1083/jcb.202007171 [Accessed: 21 July 2021].

Guha, P. et al. 2017. Tunicamycin induced endoplasmic reticulum stress promotes apoptosis of prostate cancer cells by activating mTORC1. *Oncotarget* 8(40), pp. 68191–68207. doi: 10.18632/oncotarget.19277.

Habedanck, R. et al. 2005. The Polo kinase Plk4 functions in centriole duplication. *Nature Cell Biology* 7(11), pp. 1140–1146. doi: 10.1038/ncb1320.

Hadjihannas, M.V. et al. 2006. Aberrant Wnt/β-catenin signaling can induce chromosomal instability in colon cancer. *Proceedings of the National Academy of Sciences* 103(28), pp. 10747–10752. doi: 10.1073/pnas.0604206103.

Hadjihannas, M.V. et al. 2010. Conductin/axin2 and Wnt signalling regulates centrosome cohesion. *EMBO Reports* 11(4), pp. 317–324. doi: 10.1038/embor.2010.23.

Häfner, J. et al. 2014. Pre-anaphase chromosome oscillations are regulated by the antagonistic activities of Cdk1 and PP1 on Kif18A. *Nature Communications* 5(1), p. 4397. doi: 10.1038/ncomms5397.

He, J. et al. 2016. PTEN regulates EG5 to control spindle architecture and chromosome congression during mitosis. *Nature Communications* 7(1), p. 12355. doi: 10.1038/ncomms12355.

Heinrich, S. et al. 2013. Determinants of robustness in spindle assembly checkpoint signalling. *Nature Cell Biology* 15(11), pp. 1328–1339. doi: 10.1038/ncb2864.

Hernando, E. et al. 2004. Rb inactivation promotes genomic instability by uncoupling cell cycle progression from mitotic control. *Nature* 430(7001), pp. 797–802. doi: 10.1038/nature02820.

Hiruma, Y. et al. 2015. Competition between MPS1 and microtubules at kinetochores regulates spindle checkpoint signaling. *Science* 348(6240), pp. 1264–1267. doi: 10.1126/science.aaa4055.

Holdgaard, S.G. et al. 2019. Selective autophagy maintains centrosome integrity and accurate mitosis by turnover of centriolar satellites. *Nature Communications* 10(1), p. 4176. doi: 10.1038/s41467-019-12094-9.

Holm, C. et al. 1989. DNA topoisomerase II must act at mitosis to prevent nondisjunction and chromosome breakage. *Molecular and Cellular Biology* 9(1), pp. 159–168. doi: 10.1128/mcb.9.1.159-168.1989.

Howard, J. and Hyman, A.A. 2003. Dynamics and mechanics of the microtubule plus end. *Nature* 422, pp. 753–758. doi: 10.1038/nature01600.

Hoxhaj, G. and Manning, B.D. 2020. The PI3K–AKT network at the interface of oncogenic signalling and cancer metabolism. *Nature Reviews Cancer* 20(2), pp. 74–88. doi: 10.1038/s41568-019-0216-7.

Hoyt, M.A. et al. 1991. S. cerevisiae genes required for cell cycle arrest in response to loss of microtubule function. *Cell* 66(3), pp. 507–517. doi: 10.1016/0092-8674(81)90014-3.

Hueschen, C.L. et al. 2019. Microtubule End-Clustering Maintains a Steady-State Spindle Shape. *Current Biology* 29(4), pp. 700-708.e5. doi: 10.1016/j.cub.2019.01.016.

Hynds, R.E. et al. 2019. Expansion of Human Airway Basal Stem Cells and Their Differentiation as 3D Tracheospheres. *Methods in Molecular Biology (Clifton, N.J.)* 1576, pp. 43–53. doi: 10.1007/7651_2016_5.

Irvine, D.V. et al. 2004. Chromosome size and origin as determinants of the level of CENP-A incorporation into human centromeres. *Chromosome Research* 12(8), pp. 805–815. doi: 10.1007/s10577-005-5377-4.

Jamal-Hanjani, M. et al. 2017. Tracking the Evolution of Non–Small-Cell Lung Cancer. *New England Journal of Medicine* 376(22), pp. 2109–2121. doi: 10.1056/NEJMoa1616288.

Jaqaman, K. et al. 2010. Kinetochore alignment within the metaphase plate is regulated by centromere stiffness and microtubule depolymerases. *Journal of Cell Biology* 188(5), pp. 665–679. doi: 10.1083/jcb.200909005.

Ji, Z. et al. 2015. Kinetochore attachment sensed by competitive Mps1 and microtubule binding to Ndc80C. *Science* 348(6240), pp. 1260–1264. doi: 10.1126/science.aaa4029.

Jiang, M. et al. 2017. KIF11 is required for proliferation and self-renewal of docetaxel resistant triple negative breast cancer cells. *Oncotarget* 8(54), pp. 92106–92118. doi: 10.18632/oncotarget.20785.

Kajtez, J. et al. 2016. Overlap microtubules link sister k-fibres and balance the forces on bi-oriented kinetochores. *Nature Communications* 7(1), p. 10298. doi: 10.1038/ncomms10298.

Kapitein, L.C. et al. 2005. The bipolar mitotic kinesin Eg5 moves on both microtubules that it crosslinks. *Nature* 435(7038), pp. 114–118. doi: 10.1038/nature03503.

Kapoor, T.M. et al. 2000. Probing Spindle Assembly Mechanisms with Monastrol, a Small Molecule Inhibitor of the Mitotic Kinesin, Eg5. *The Journal of Cell Biology* 150(5), pp. 975–988.

Kapoor, T.M. and Mitchison, T.J. 2001. Eg5 is static in bipolar spindles relative to tubulin. *The Journal of Cell Biology* 154(6), pp. 1125–1134. doi: 10.1083/jcb.200106011.

Karki, M. et al. 2017. Precocious centriole disengagement and centrosome fragmentation induced by mitotic delay. *Nature Communications* 8, p. 15803. doi: 10.1038/ncomms15803.

Kaseda, K. et al. 2011. Dual pathway spindle assembly increases both the speed and the fidelity of mitosis. *Biology Open* 1(1), pp. 12–18. doi: 10.1242/bio.2011012.

Keam, B. et al. 2015. In Vitro Anticancer Activity of PI3K Alpha Selective Inhibitor BYL719 in Head and Neck Cancer. *ANTICANCER RESEARCH* , p. 8.

Keraite, I. et al. 2020. PIK3CA mutation enrichment and quantitation from blood and tissue. *Scientific Reports* 10(1), p. 17082. doi: 10.1038/s41598-020-74086-w.

Kheir, S.M. et al. 1988. Prognostic significance of DNA aneuploidy in stage I cutaneous melanoma. *Annals of Surgery* 207(4), pp. 455–461.

Kim, B.R. et al. 2016. SOX2 and PI3K Cooperate to Induce and Stabilize a Squamous-Committed Stem Cell Injury State during Lung Squamous Cell Carcinoma Pathogenesis. *PLOS Biology* 14(11), p. e1002581. doi: 10.1371/journal.pbio.1002581.

Kim, C.D. et al. 2019. Small molecule allosteric uncoupling of microtubule depolymerase activity from motility in human Kinesin-5 during mitotic spindle assembly. *Scientific Reports* 9(1), p. 19900. doi: 10.1038/s41598-019-56173-9.

Kim, K. and Rhee, K. 2011. The pericentriolar satellite protein CEP90 is crucial for integrity of the mitotic spindle pole. *Journal of Cell Science* 124(3), pp. 338–347. doi: 10.1242/jcs.078329.

King, R.W. et al. 1995. A 20s complex containing CDC27 and CDC16 catalyzes the mitosis-specific conjugation of ubiquitin to cyclin B. *Cell* 81(2), pp. 279–288. doi: 10.1016/0092-8674(95)90338-0.

Kinross, K.M. et al. 2012. An activating Pik3ca mutation coupled with Pten loss is sufficient to initiate ovarian tumorigenesis in mice. *The Journal of Clinical Investigation* 122(2), pp. 553–557. doi: 10.1172/JCI59309.

Konermann, S. et al. 2015. Genome-scale transcriptional activation by an engineered CRISPR-Cas9 complex. *Nature* 517(7536), pp. 583–588. doi: 10.1038/nature14136.

Korzeniewski, N. et al. 2011. The HPV-16 E7 oncoprotein induces centriole multiplication through deregulation of Polo-like kinase 4 expression. *Molecular Cancer* 10, p. 61. doi: 10.1186/1476-4598-10-61.

Krenn, V. and Musacchio, A. 2015. The Aurora B Kinase in Chromosome Bi-Orientation and Spindle Checkpoint Signaling. *Frontiers in Oncology* 5. Available at: https://www.frontiersin.org/articles/10.3389/fonc.2015.00225/full [Accessed: 16 June 2021].

Krzywicka-Racka, A. and Sluder, G. 2011. Repeated cleavage failure does not establish centrosome amplification in untransformed human cells. *The Journal of Cell Biology* 194(2), pp. 199–207. doi: 10.1083/jcb.201101073.

Kumar, P. et al. 2012. Multisite Phosphorylation Disrupts Arginine-Glutamate Salt Bridge Networks Required for Binding of Cytoplasmic Linker-associated Protein 2 (CLASP2) to End-binding Protein 1 (EB1)*. *Journal of Biological Chemistry* 287(21), pp. 17050–17064. doi: 10.1074/jbc.M111.316661.

Kwon, M. et al. 2008. Mechanisms to suppress multipolar divisions in cancer cells with extra centrosomes. *Genes & Development* 22(16), pp. 2189–2203. doi: 10.1101/gad.1700908.

Lamb, J.C. and Birchler, J.A. 2003. The role of DNA sequence in centromere formation. *Genome Biology* 4(5), p. 214. doi: 10.1186/gb-2003-4-5-214.

Lan, W. et al. 2004. Aurora B phosphorylates centromeric MCAK and regulates its localization and microtubule depolymerization activity. *Current biology: CB* 14(4), pp. 273–286. doi: 10.1016/j.cub.2004.01.055.

Lara-Gonzalez, P. et al. 2021. Spindle assembly checkpoint activation and silencing at kinetochores. *Seminars in Cell & Developmental Biology* . Available at: https://www.sciencedirect.com/science/article/pii/S1084952121001609 [Accessed: 12 July 2021].

Laughney, A.M. et al. 2015. Dynamics of Tumor Heterogeneity Derived from Clonal Karyotypic Evolution. *Cell Reports* 12(5), pp. 809–820. doi: 10.1016/j.celrep.2015.06.065.

Lee, H.-S. et al. 2013. A new assay for measuring chromosome instability (CIN) and identification of drugs that elevate CIN in cancer cells. *BMC Cancer* 13(1), p. 252. doi: 10.1186/1471-2407-13-252.

Lee, J. and Gollahon, L. 2013. Mitotic perturbations induced by Nek2 overexpression require interaction with TRF1 in breast cancer cells. *Cell Cycle* 12(23), pp. 3599–3614. doi: 10.4161/cc.26589.

Lee, K. and Rhee, K. 2012. Separase-dependent cleavage of pericentrin B is necessary and sufficient for centriole disengagement during mitosis. *Cell Cycle (Georgetown, Tex.)* 11(13), pp. 2476–2485. doi: 10.4161/cc.20878.

Lee, R.T. et al. 2008. A University of Chicago consortium phase II trial of SB-715992 in advanced renal cell cancer. *Clinical Genitourinary Cancer* 6(1), pp. 21–24. doi: 10.3816/CGC.2008.n.003.

Lens, S.M.A. and Medema, R.H. 2019. Cytokinesis defects and cancer. *Nature Reviews Cancer* 19(1), pp. 32–45. doi: 10.1038/s41568-018-0084-6.

Leontiadou, H. et al. 2018. Insights into the mechanism of the PIK3CA E545K activating mutation using MD simulations. *Scientific Reports* 8(1), p. 15544. doi: 10.1038/s41598-018-27044-6.

Li, J. et al. 2005. SAK, A New Polo-Like Kinase, Is Transcriptionally Repressed by p53 and Induces Apoptosis upon RNAi Silencing. *Neoplasia (New York, N.Y.)* 7(4), pp. 312–323.

Li, R. and Murray, A.W. 1991. Feedback control of mitosis in budding yeast. *Cell* 66(3), pp. 519–531. doi: 10.1016/0092-8674(81)90015-5.

Li, T.-F. et al. 2020. Overexpression of kinesin superfamily members as prognostic biomarkers of breast cancer. *Cancer Cell International* 20(1), p. 123. doi: 10.1186/s12935-020-01191-1.

Liskovykh, M. et al. 2019. A novel assay to screen siRNA libraries identifies protein kinases required for chromosome transmission. *Genome Research* 29(10), pp. 1719–1732. doi: 10.1101/gr.254276.119.

Liu, D. et al. 2012. Polo-like kinase-1 regulates kinetochore–microtubule dynamics and spindle checkpoint silencing. *J Cell Biol* 198(4), pp. 491–499. doi: 10.1083/jcb.201205090.

Liu, Y. et al. 2017. Protein Phosphatase 2A (PP2A) Regulates EG5 to Control Mitotic Progression. *Scientific Reports* 7(1), p. 1630. doi: 10.1038/s41598-017-01915-w.

Logarinho, E. et al. 2012. CLASPs prevent irreversible multipolarity by ensuring spindle-pole resistance to traction forces during chromosome alignment. *Nature Cell Biology* 14(3), pp. 295–303. doi: 10.1038/ncb2423.

Lombillo, V.A. et al. 1995. Antibodies to the kinesin motor domain and CENP-E inhibit microtubule depolymerization-dependent motion of chromosomes in vitro. *Journal of Cell Biology* 128(1), pp. 107–115. doi: 10.1083/jcb.128.1.107.

López, S. et al. 2020. Interplay between whole-genome doubling and the accumulation of deleterious alterations in cancer evolution. *Nature Genetics* 52(3), pp. 283–293. doi: 10.1038/s41588-020-0584-7.

López-García, C. et al. 2017. BCL9L Dysfunction Impairs Caspase-2 Expression Permitting Aneuploidy Tolerance in Colorectal Cancer. *Cancer Cell* 31(1), pp. 79–93. doi: 10.1016/j.ccell.2016.11.001.

Luo, J. and Cantley, L.C. 2005. Then Negative Regulation of Phosphoinositide 3-Kinase Signaling by p85 and Its Implication in Cancer. *Cell Cycle* 4(10), pp. 1309–1312. doi: 10.4161/cc.4.10.2062.

Ma, W. et al. 2009. Reprogramming RPE to differentiate towards retinal neurons with Sox2. *Stem cells (Dayton, Ohio)* 27(6), pp. 1376–1387. doi: 10.1002/stem.48.

Mackenzie, K.J. et al. 2017. cGAS surveillance of micronuclei links genome instability to innate immunity. *Nature* 548(7668), pp. 461–465. doi: 10.1038/nature23449.

Magidson, V. et al. 2011. The Spatial Arrangement of Chromosomes during Prometaphase Facilitates Spindle Assembly. *Cell* 146(4), pp. 555–567. doi: 10.1016/j.cell.2011.07.012.

Maia, A.R.R. et al. 2012. Cdk1 and Plk1 mediate a CLASP2 phospho-switch that stabilizes kinetochore–microtubule attachments. *The Journal of Cell Biology* 199(2), pp. 285–301. doi: 10.1083/jcb.201203091.

Maiato, H. et al. 2003a. How Do Kinetochores CLASP Dynamic Microtubules? *Cell Cycle* 2(6), pp. 511–514. doi: 10.4161/cc.2.6.576.

Maiato, H. et al. 2003b. Human CLASP1 Is an Outer Kinetochore Component that Regulates Spindle Microtubule Dynamics. *Cell* 113(7), pp. 891–904. doi: 10.1016/S0092-8674(03)00465-3.

Maiato, H. et al. 2004. Microtubule-Associated Proteins and Their Essential Roles During Mitosis. In: *International Review of Cytology*. Academic Press, pp. 53–153. Available at: https://www.sciencedirect.com/science/article/pii/S007476960441002X [Accessed: 7 June 2021].

Maiato, H. and Logarinho, E. 2014. Mitotic spindle multipolarity without centrosome amplification. *Nature Cell Biology* 16(5), pp. 386–394. doi: 10.1038/ncb2958.

Malumbres, M. 2014. Cyclin-dependent kinases. *Genome Biology* 15(6), p. 122. doi: 10.1186/gb4184.

Mandelker, D. et al. 2009. A frequent kinase domain mutation that changes the interaction between PI3Kα and the membrane. *Proceedings of the National Academy of Sciences* 106(40), pp. 16996–17001.

Manic, G. et al. 2017. Chapter Four - Molecular Regulation of the Spindle Assembly Checkpoint by Kinases and Phosphatases. In: Galluzzi, L. ed. *International Review of Cell and Molecular Biology*. Academic Press, pp. 105–161. Available at: https://www.sciencedirect.com/science/article/pii/S1937644816300739 [Accessed: 13 July 2021].

Manning, A.L. et al. 2007. The kinesin-13 proteins Kif2a, Kif2b, and Kif2c/MCAK have distinct roles during mitosis in human cells. *Molecular Biology of the Cell* 18(8), pp. 2970–2979. doi: 10.1091/mbc.e07-02-0110.

Marteil, G. et al. 2018. Over-elongation of centrioles in cancer promotes centriole amplification and chromosome missegregation. *Nature Communications* 9(1), p. 1258. doi: 10.1038/s41467-018-03641-x.

Mastronarde, D.N. et al. 1993. Interpolar spindle microtubules in PTK cells. *Journal of Cell Biology* 123(6), pp. 1475–1489. doi: 10.1083/jcb.123.6.1475.

Matov, A. et al. 2010. Analysis of Microtubule Dynamic Instability Using a Plus End Growth Marker. *Nature methods* 7(9), pp. 761–768. doi: 10.1038/nmeth.1493.

Mayer, T.U. et al. 1999. Small molecule inhibitor of mitotic spindle bipolarity identified in a phenotype-based screen. *Science (New York, N.Y.)* 286(5441), pp. 971–974. doi: 10.1126/science.286.5441.971.

Mazumdar, M. et al. 2004. Human chromokinesin KIF4A functions in chromosome condensation and segregation. *Journal of Cell Biology* 166(5), pp. 613–620. doi: 10.1083/jcb.200401142.

McAinsh, A.D. and Meraldi, P. 2011. The CCAN complex: Linking centromere specification to control of kinetochore–microtubule dynamics. *Seminars in Cell & Developmental Biology* 22(9), pp. 946–952. doi: 10.1016/j.semcdb.2011.09.016.

McEwen, B.F. et al. 1997. Kinetochore Fiber Maturation in PtK1 Cells and Its Implications for the Mechanisms of Chromosome Congression and Anaphase Onset. *The Journal of Cell Biology* 137(7), pp. 1567–1580.

McKinley, K.L. and Cheeseman, I.M. 2016. The molecular basis for centromere identity and function. *Nature Reviews Molecular Cell Biology* 17(1), pp. 16–29. doi: 10.1038/nrm.2015.5.

Mitchison, T.J. and Salmon, E.D. 1992. Poleward kinetochore fiber movement occurs during both metaphase and anaphase-A in newt lung cell mitosis. *The Journal of Cell Biology* 119(3), pp. 569–582. doi: 10.1083/jcb.119.3.569.

Moritz, M. et al. 1995. Microtubule nucleation by γ-tubulin-containing rings in the centrosome. *Nature* 378(6557), pp. 638–640. doi: 10.1038/378638a0.

Mountain, V. et al. 1999. The Kinesin-Related Protein, Hset, Opposes the Activity of Eg5 and Cross-Links Microtubules in the Mammalian Mitotic Spindle. *The Journal of Cell Biology* 147(2), pp. 351–366.

Musacchio, A. 2015. The Molecular Biology of Spindle Assembly Checkpoint Signaling Dynamics. *Current Biology* 25(20), pp. R1002–R1018. doi: 10.1016/j.cub.2015.08.051.

Neahring, L. et al. 2021. Opposing motors provide mechanical and functional robustness in the human spindle. *bioRxiv* , p. 2021.03.02.433652. doi: 10.1101/2021.03.02.433652.

Neumann, B. et al. 2010. Phenotypic profiling of the human genome by time-lapse microscopy reveals cell division genes. *Nature* 464(7289), pp. 721–727. doi: 10.1038/nature08869.

Nicholson, J.M. et al. 2015. Chromosome mis-segregation and cytokinesis failure in trisomic human cells. Pines, J. ed. *eLife* 4, p. e05068. doi: 10.7554/eLife.05068.

Nigg, E.A. and Holland, A.J. 2018. Once and only once: mechanisms of centriole duplication and their deregulation in disease. *Nature Reviews Molecular Cell Biology* 19(5), pp. 297–312. doi: 10.1038/nrm.2017.127.

Norden, C. et al. 2006. The NoCut Pathway Links Completion of Cytokinesis to Spindle Midzone Function to Prevent Chromosome Breakage. *Cell* 125(1), pp. 85–98. doi: 10.1016/j.cell.2006.01.045.

Onishi, K. et al. 2007. The PI3K-Akt pathway promotes microtubule stabilization in migrating fibroblasts. *Genes to Cells* 12(4), pp. 535–546. doi: https://doi.org/10.1111/j.1365-2443.2007.01071.x.

Orr, B. et al. 2021. An anaphase surveillance mechanism prevents micronuclei formation from mitotic errors. *bioRxiv* , p. 2021.02.26.433009. doi: 10.1101/2021.02.26.433009.

Orth, J.D. et al. 2008. Quantitative live imaging of cancer and normal cells treated with Kinesin-5 inhibitors indicates significant differences in phenotypic responses and cell fate. *Molecular cancer therapeutics* 7(11), pp. 3480–3489. doi: 10.1158/1535-7163.MCT-08-0684.

Owens, B. 2013. Kinesin inhibitor marches toward first-in-class pivotal trial. *Nature Medicine* 19(12), pp. 1550–1550. doi: 10.1038/nm1213-1550a.

Ozaki, T. et al. 2003. Chromosomal alterations in osteosarcoma cell lines revealed by comparative genomic hybridization and multicolor karyotyping. *Cancer Genetics and Cytogenetics* 140(2), pp. 145–152. doi: 10.1016/s0165-4608(02)00685-4.

Ozcan, U. et al. 2008. Loss of the Tuberous Sclerosis Complex Tumor Suppressors Triggers the Unfolded Protein Response to Regulate Insulin Signaling and Apoptosis. *Molecular Cell* 29(5), pp. 541–551. doi: 10.1016/j.molcel.2007.12.023.

Pardee, A.B. 1974. A Restriction Point for Control of Normal Animal Cell Proliferation. *Proceedings of the National Academy of Sciences* 71(4), pp. 1286–1290.

Pereira, A.L. et al. 2006. Mammalian CLASP1 and CLASP2 Cooperate to Ensure Mitotic Fidelity by Regulating Spindle and Kinetochore Function. *Molecular Biology of the Cell* 17(10), pp. 4526–4542. doi: 10.1091/mbc.e06-07-0579.

Petry, S. 2016. Mechanisms of Mitotic Spindle Assembly. *Annual review of biochemistry* 85, pp. 659–683. doi: 10.1146/annurev-biochem-060815-014528.

Polak, B. et al. 2017. PRC1-labeled microtubule bundles and kinetochore pairs show one-to-one association in metaphase. *EMBO reports* 18(2), pp. 217–230. doi: 10.15252/embr.201642650.

Primo, L.M.F. and Teixeira, L.K. [no date]. DNA replication stress: oncogenes in the spotlight. *Genetics and Molecular Biology* 43(1 Suppl 1), p. e20190138. doi: 10.1590/1678-4685-GMB-2019-0138.

Prosser, S.L. and Pelletier, L. 2017. Mitotic spindle assembly in animal cells: a fine balancing act. *Nature Reviews Molecular Cell Biology* 18(3), pp. 187–201. doi: 10.1038/nrm.2016.162.

Quinton, R.J. et al. 2021. Whole-genome doubling confers unique genetic vulnerabilities on tumour cells. *Nature* 590(7846), pp. 492–497. doi: 10.1038/s41586-020-03133-3.

Raaijmakers, J.A. et al. 2012. Nuclear envelope-associated dynein drives prophase centrosome separation and enables Eg5-independent bipolar spindle formation. *The EMBO Journal* 31(21), pp. 4179–4190. doi: 10.1038/emboj.2012.272.

Ramadhani, D. and Purnami, S. 2013. Automated Detection of Binucleated Cell and Micronuclei using CellProfiler 2.0 Software. *HAYATI Journal of Biosciences* 20(4), pp. 151–156. doi: 10.4308/hjb.20.4.151.

Rapley, J. et al. 2005. Coordinate Regulation of the Mother Centriole Component Nlp by Nek2 and Plk1 Protein Kinases. *Molecular and Cellular Biology* 25(4), pp. 1309–1324. doi: 10.1128/MCB.25.4.1309-1324.2005.

Rappel, W.-J. and Edelstein-Keshet, L. 2017. Mechanisms of cell polarization. *Current Opinion in Systems Biology* 3, pp. 43–53. doi: 10.1016/j.coisb.2017.03.005.

Rhys, A.D. et al. 2017. Loss of E-cadherin provides tolerance to centrosome amplification in epithelial cancer cells. *Journal of Cell Biology* 217(1), pp. 195–209. doi: 10.1083/jcb.201704102.

Rieder, C. and Salmon, E. 1994. Motile kinetochores and polar ejection forces dictate chromosome position on the vertebrate mitotic spindle. *Journal of Cell Biology* 124(3), pp. 223–233. doi: 10.1083/jcb.124.3.223.

Rieder, C.L. et al. 1994. Anaphase onset in vertebrate somatic cells is controlled by a checkpoint that monitors sister kinetochore attachment to the spindle. *The Journal of cell biology* 127(5), pp. 1301–1310. doi: 10.1083/jcb.127.5.1301.

Rieder, C.L. et al. 1995. The checkpoint delaying anaphase in response to chromosome monoorientation is mediated by an inhibitory signal produced by unattached kinetochores. *Journal of Cell Biology* 130(4), pp. 941–948. doi: 10.1083/jcb.130.4.941.

Rodrigues, M.A. et al. 2021. The in vitro micronucleus assay using imaging flow cytometry and deep learning. *npj Systems Biology and Applications* 7(1), pp. 1–12. doi: 10.1038/s41540-021-00179-5.

Ronneberger, O. et al. 2015. U-Net: Convolutional Networks for Biomedical Image Segmentation. In: Navab, N. et al. eds. *Medical Image Computing and Computer-Assisted Intervention – MICCAI 2015*. Lecture Notes in Computer Science. Cham: Springer International Publishing, pp. 234–241. doi: 10.1007/978-3-319-24574-4_28.

Roschke, A.V. et al. [no date]. Karyotypic Complexity of the NCI-60 Drug-Screening Panel., p. 15.

Rutledge, S.D. et al. 2016. Selective advantage of trisomic human cells cultured in non-standard conditions. *Scientific Reports* 6(1), p. 22828. doi: 10.1038/srep22828.

Sanders, A.D. et al. 2020. Single-cell analysis of structural variations and complex rearrangements with tri-channel processing. *Nature Biotechnology* 38(3), pp. 343–354. doi: 10.1038/s41587-019-0366-x.

Sansregret, L. et al. 2017. APC/C Dysfunction Limits Excessive Cancer Chromosomal Instability. *Cancer discovery* 7(2), pp. 218–233. doi: 10.1158/2159-8290.CD-16-0645.

Santaguida, S. et al. 2017. Chromosome Mis-segregation Generates Cell-Cycle-Arrested Cells with Complex Karyotypes that Are Eliminated by the Immune System. *Developmental Cell* 41(6), pp. 638-651.e5. doi: 10.1016/j.devcel.2017.05.022.

Sarrió, D. et al. 2008. Epithelial-Mesenchymal Transition in Breast Cancer Relates to the Basal-like Phenotype. *Cancer Research* 68(4), pp. 989–997.

Saunders, A.M. et al. 2007. Kinesin-5 acts as a brake in anaphase spindle elongation. *Current biology : CB* 17(12), pp. R453–R454. doi: 10.1016/j.cub.2007.05.001.

Sawin, K.E. et al. 1992. Mitotic spindle organization by a plus-end-directed microtubule motor. *Nature* 359(6395), pp. 540–543. doi: 10.1038/359540a0.

Sawin, K.E. and Mitchison, T.J. 1994. Microtubule flux in mitosis is independent of chromosomes, centrosomes, and antiparallel microtubules. *Molecular Biology of the Cell* 5(2), pp. 217–226. doi: 10.1091/mbc.5.2.217.

Sawin, K.E. and Mitchison, T.J. 1995. Mutations in the kinesin-like protein Eg5 disrupting localization to the mitotic spindle. *Proceedings of the National Academy of Sciences of the United States of America* 92(10), pp. 4289–4293.

Schvartzman, J.-M. et al. 2010. Mitotic chromosomal instability and cancer: mouse modelling of the human disease. *Nature reviews. Cancer* 10(2), pp. 102–115. doi: 10.1038/nrc2781.

Sen, O. et al. 2021. Kinetochore life histories reveal the origins of chromosome mis-segregation and correction mechanisms. *bioRxiv* , p. 2021.03.30.436326. doi: 10.1101/2021.03.30.436326.

Senturk, E. and Manfredi, J.J. 2013. p53 and Cell Cycle Effects After DNA Damage. *Methods in molecular biology (Clifton, N.J.)* 962, pp. 49–61. doi: 10.1007/978-1-62703-236-0_4.

Sheltzer, J.M. et al. 2017. Single-chromosome Gains Commonly Function as Tumor Suppressors. *Cancer Cell* 31(2), pp. 240–255. doi: 10.1016/j.ccell.2016.12.004.

Shinmura, K. et al. 2014. PLK4 overexpression and its effect on centrosome regulation and chromosome stability in human gastric cancer. *Molecular Biology Reports* 41(10), pp. 6635–6644. doi: 10.1007/s11033-014-3546-2.

Sidi, S. et al. 2008. Chk1 Suppresses a Caspase-2 Apoptotic Response to DNA Damage that Bypasses p53, Bcl-2, and Caspase-3. *Cell* 133(5), pp. 864–877. doi: 10.1016/j.cell.2008.03.037.

Silkworth, W.T. and Cimini, D. 2012. Transient defects of mitotic spindle geometry and chromosome segregation errors. *Cell Division* 7, p. 19. doi: 10.1186/1747-1028-7-19.

Simões-Sousa, S. et al. 2018. The p38α Stress Kinase Suppresses Aneuploidy Tolerance by Inhibiting Hif-1α. *Cell Reports* 25(3), pp. 749-760.e6. doi: 10.1016/j.celrep.2018.09.060.

Skibbens, R.V. et al. 1993. Directional instability of kinetochore motility during chromosome congression and segregation in mitotic newt lung cells: a push-pull mechanism. *The Journal of Cell Biology* 122(4), pp. 859–875. doi: 10.1083/jcb.122.4.859.

Skoufias, D.A. et al. 2006. S-trityl-L-cysteine is a reversible, tight binding inhibitor of the human kinesin Eg5 that specifically blocks mitotic progression. *The Journal of Biological Chemistry* 281(26), pp. 17559–17569. doi: 10.1074/jbc.M511735200.

Smith, E. et al. 2011. Differential control of Eg5-dependent centrosome separation by Plk1 and Cdk1. *The EMBO Journal* 30(11), pp. 2233–2245. doi: 10.1038/emboj.2011.120.

Soto, M. et al. 2017. p53 Prohibits Propagation of Chromosome Segregation Errors that Produce Structural Aneuploidies. *Cell Reports* 19(12), pp. 2423–2431. doi: 10.1016/j.celrep.2017.05.055.

Soto, M. et al. 2018. Chromosomes trapped in micronuclei are liable to segregation errors. *Journal of Cell Science* 131(13), p. jcs214742. doi: 10.1242/jcs.214742.

Starita, L.M. et al. 2004. BRCA1-Dependent Ubiquitination of γ-Tubulin Regulates Centrosome Number. *Molecular and Cellular Biology* 24(19), pp. 8457–8466. doi: 10.1128/MCB.24.19.8457-8466.2004.

Steblyanko, Y. et al. 2020. Microtubule poleward flux in human cells is driven by the coordinated action of four kinesins. *The EMBO Journal* 39(23). Available at: https://onlinelibrary.wiley.com/doi/10.15252/embj.2020105432 [Accessed: 22 January 2021].

Stopsack, K.H. et al. 2019. Aneuploidy drives lethal progression in prostate cancer. *Proceedings of the National Academy of Sciences* 116(23), pp. 11390–11395. doi: 10.1073/pnas.1902645116.

Straight, A.F. et al. 1996. GFP tagging of budding yeast chromosomes reveals that protein–protein interactions can mediate sister chromatid cohesion. *Current Biology* 6(12), pp. 1599–1608. doi: 10.1016/S0960-9822(02)70783-5.

Stumpff, J. et al. 2008. The Kinesin-8 Motor Kif18A Suppresses Kinetochore Movements to Control Mitotic Chromosome Alignment. *Developmental Cell* 14(2), pp. 252–262. doi: 10.1016/j.devcel.2007.11.014.

Sturgill, E.G. et al. 2016. Kinesin-5 inhibitor resistance is driven by kinesin-12. *Journal of Cell Biology* 213(2), pp. 213–227. doi: 10.1083/jcb.201507036.

Suzuki, A. et al. 2014. The Architecture of CCAN Proteins Creates a Structural Integrity to Resist Spindle Forces and Achieve Proper Intrakinetochore Stretch. *Developmental Cell* 30(6), pp. 717–730. doi: 10.1016/j.devcel.2014.08.003.

Tanenbaum, M.E. et al. 2008. Dynein, Lis1 and CLIP-170 counteract Eg5-dependent centrosome separation during bipolar spindle assembly. *The EMBO journal* 27(24), pp. 3235–3245. doi: 10.1038/emboj.2008.242.

Tanenbaum, M.E. et al. 2009. Kif15 Cooperates with Eg5 to Promote Bipolar Spindle Assembly. *Current Biology* 19(20), pp. 1703–1711. doi: 10.1016/j.cub.2009.08.027.

Tanenbaum, M.E. and Medema, R.H. 2010. Mechanisms of Centrosome Separation and Bipolar Spindle Assembly. *Developmental Cell* 19(6), pp. 797–806. doi: 10.1016/j.devcel.2010.11.011.

Taylor, W.R. and Stark, G.R. 2001. Regulation of the G2/M transition by p53. *Oncogene* 20(15), pp. 1803–1815. doi: 10.1038/sj.onc.1204252.

Teixeira, V.H. et al. 2019. Deciphering the genomic, epigenomic, and transcriptomic landscapes of pre-invasive lung cancer lesions. *Nature Medicine* 25(3), pp. 517–525. doi: 10.1038/s41591-018-0323-0.

Thompson, S.L. et al. 2010. Mechanisms of Chromosomal Instability. *Current biology : CB* 20(6), pp. R285–R295. doi: 10.1016/j.cub.2010.01.034.

Thompson, S.L. and Compton, D.A. 2010. Proliferation of aneuploid human cells is limited by a p53-dependent mechanism. *Journal of Cell Biology* 188(3), pp. 369–381. doi: 10.1083/jcb.200905057.

Thompson, S.L. and Compton, D.A. 2011. Chromosome missegregation in human cells arises through specific types of kinetochore–microtubule attachment errors. *Proceedings of the National Academy of Sciences of the United States of America* 108(44), pp. 17974–17978. doi: 10.1073/pnas.1109720108.

Tikhonenko, I. et al. 2008. Kinesin-5 is not essential for mitotic spindle elongation in Dictyostelium. *Cell Motility* 65(11), pp. 853–862. doi: 10.1002/cm.20307.

Tillement, V. et al. 2009. Spindle assembly defects leading to the formation of a monopolar mitotic apparatus. *Biology of the Cell* 101(1), pp. 1–11. doi: 10.1042/BC20070162.

Tirnauer, J.S. et al. 2002. EB1–Microtubule Interactions in Xenopus Egg Extracts: Role of EB1 in Microtubule Stabilization and Mechanisms of Targeting to Microtubules. *Molecular Biology of the Cell* 13(10), pp. 3614–3626. doi: 10.1091/mbc.e02-04-0210.

Uetake, Y. and Sluder, G. 2010. Prolonged prometaphase blocks daughter cell proliferation despite normal completion of mitosis. *Current biology : CB* 20(18), pp. 1666–1671. doi: 10.1016/j.cub.2010.08.018.

Umbreit, N.T. et al. 2020. Mechanisms generating cancer genome complexity from a single cell division error. *Science* 368(6488). Available at: https://science.sciencemag.org/content/368/6488/eaba0712 [Accessed: 23 June 2021].

Uteng, M. et al. 2008. Poleward transport of Eg5 by dynein-dynactin in Xenopus laevis egg extract spindles. *The Journal of Cell Biology* 182(4), pp. 715–726. doi: 10.1083/jcb.200801125.

van Heesbeen, R.G.H.P. et al. 2014. Balanced Activity of Three Mitotic Motors Is Required for Bipolar Spindle Assembly and Chromosome Segregation. *Cell Reports* 8(4), pp. 948–956. doi: 10.1016/j.celrep.2014.07.015.

Varga, D. et al. 2004. An automated scoring procedure for the micronucleus test by image analysis. *Mutagenesis* 19(5), pp. 391–397. doi: 10.1093/mutage/geh047.

Venere, M. et al. 2015. The Mitotic Kinesin KIF11 is a Central Driver of Invasion, Proliferation, and Self Renewal in Glioblastoma. *Science translational medicine* 7(304), p. 304ra143. doi: 10.1126/scitranslmed.aac6762.

Verdaasdonk, J.S. and Bloom, K. 2011. Centromeres: unique chromatin structures that drive chromosome segregation. *Nature Reviews Molecular Cell Biology* 12(5), pp. 320–332. doi: 10.1038/nrm3107.

Vladimirou, E. et al. 2013. Nonautonomous Movement of Chromosomes in Mitosis. *Developmental Cell* 27(1), pp. 60–71. doi: 10.1016/j.devcel.2013.08.004.

Vukušić, K. et al. 2017. Microtubule Sliding within the Bridging Fiber Pushes Kinetochore Fibers Apart to Segregate Chromosomes. *Developmental Cell* 43(1), pp. 11-23.e6. doi: 10.1016/j.devcel.2017.09.010.

Vukušić, K. et al. 2019. Force-generating mechanisms of anaphase in human cells. *Journal of Cell Science* 132(jcs231985). Available at: https://doi.org/10.1242/jcs.231985 [Accessed: 28 May 2021].

Vukušić, K. et al. 2021. Microtubule-sliding modules based on kinesins EG5 and PRC1-dependent KIF4A drive human spindle elongation. *Developmental Cell* 56(9), pp. 1253-1267.e10. doi: 10.1016/j.devcel.2021.04.005.

Wang, F. and Lin, S.L. 2014. Knockdown of kinesin KIF11 abrogates directed migration in response to epidermal growth factor-mediated chemotaxis. *Biochemical and Biophysical Research Communications* 452(3), pp. 642–648. doi: 10.1016/j.bbrc.2014.08.136.

Wang, R.W. et al. 2020. Aneuploid cells activate NF-κB to promote their immune clearance by NK cells. *bioRxiv* , p. 2020.06.25.172239. doi: 10.1101/2020.06.25.172239.

Waterman-Storer, C.M. and Salmon, E.D. 1997. Actomyosin-based Retrograde Flow of Microtubules in the Lamella of Migrating Epithelial Cells Influences Microtubule Dynamic Instability and Turnover and Is Associated with Microtubule Breakage and Treadmilling. *Journal of Cell Biology* 139(2), pp. 417–434. doi: 10.1083/jcb.139.2.417.

Watkins, T.B.K. et al. 2020. Pervasive chromosomal instability and karyotype order in tumour evolution. *Nature* 587(7832), pp. 126–132. doi: 10.1038/s41586-020-2698-6.

Welburn, J.P.I. and Cheeseman, I.M. 2012. The microtubule-binding protein Cep170 promotes the targeting of the kinesin-13 depolymerase Kif2b to the mitotic spindle. *Molecular Biology of the Cell* 23(24), pp. 4786–4795. doi: 10.1091/mbc.E12-03-0214.

Wilhelm, T. et al. 2019. Mild replication stress causes chromosome mis-segregation via premature centriole disengagement. *Nature Communications* 10(1), p. 3585. doi: 10.1038/s41467-019-11584-0.

Winey, M. et al. 1991. MPS1 and MPS2: novel yeast genes defining distinct steps of spindle pole body duplication. *Journal of Cell Biology* 114(4), pp. 745–754. doi: 10.1083/jcb.114.4.745.

Wittmann, T. and Waterman-Storer, C.M. 2005. Spatial regulation of CLASP affinity for microtubules by Rac1 and GSK3β in migrating epithelial cells. *Journal of Cell Biology* 169(6), pp. 929–939. doi: 10.1083/jcb.200412114.

Worrall, J.T. et al. 2018. Non-random Mis-segregation of Human Chromosomes. *Cell Reports* 23(11), pp. 3366–3380. doi: 10.1016/j.celrep.2018.05.047.

Wurzenberger, C. and Gerlich, D.W. 2011. Phosphatases: providing safe passage through mitotic exit. *Nature Reviews Molecular Cell Biology* 12(8), pp. 469–482. doi: 10.1038/nrm3149.

Yang, Z. et al. 2007. Kinetochore Dynein Is Required for Chromosome Motion and Congression Independent of the Spindle Checkpoint. *Current Biology* 17(11), pp. 973–980. doi: 10.1016/j.cub.2007.04.056.

Zeman, M.K. and Cimprich, K.A. 2014. Causes and Consequences of Replication Stress. *Nature cell biology* 16(1), pp. 2–9. doi: 10.1038/ncb2897.

Zhang, C. et al. 2010. Kif18A is involved in human breast carcinogenesis. *Carcinogenesis* 31(9), pp. 1676–1684. doi: 10.1093/carcin/bgq134.

Zhang, C.-Z. et al. 2015. Chromothripsis from DNA damage in micronuclei. *Nature* 522(7555), pp. 179–184. doi: 10.1038/nature14493.

Zhang, N. et al. 2008. Overexpression of Separase induces aneuploidy and mammary tumorigenesis. *Proceedings of the National Academy of Sciences* 105(35), pp. 13033–13038. doi: 10.1073/pnas.0801610105.

Zhou, Y. et al. 2021. KIF11 is upregulated in colorectal cancer and silencing of it impairs tumor growth and sensitizes colorectal cancer cells to oxaliplatin via p53/GSK3β signaling. *Journal of Cancer* 12(12), pp. 3741–3753. doi: 10.7150/jca.52103.

Zielke, N. et al. 2013. Endoreplication. *Cold Spring Harbor Perspectives in Biology* 5(1). Available at: https://www.ncbi.nlm.nih.gov/pmc/articles/PMC3579398/ [Accessed: 4 January 2019].